UNIVERSIDAD DE GRANADA

Departamento de Electrónica y Tecnología de Computadores

TESIS DOCTORAL

Printed sensor systems on flexible substrate

Dispositivos sensores impresos sobre sustrato flexible

Presented by:
Pablo Escobedo Araque

Supervisors:
Alberto José Palma López
Antonio Martínez Olmos

To apply for:
International PhD Degree in Information and Communication Technologies

Programa de Doctorado en Tecnologías de la Información y las Comunicaciones

Junio 2018

Nos esse quasi nanos gigantium humeris insidentes
(«Somos como enanos aupados a hombros de gigantes»)

Bernardo de Chartres, s. XII

A mis padres

Agradecimientos

La palabra *gracias* proviene del latín *gratia*, que a su vez deriva de *gratus* (agradable, agradecido), y en origen se refiere a la honra o alabanza que se tributa a otro en reconocimiento de un favor. Sirvan por tanto estas líneas que escribo a continuación para expresar mi honra, alabanza y sincero reconocimiento a todos aquellos que me han acompañado de una manera u otra durante esta etapa de mi vida.

Quiero comenzar agradeciendo a mis directores de tesis, Alberto y Antonio, por el trabajo, generosidad, tiempo e inteligencia que han dedicado desde el principio a mí y a este proyecto. Ambos tenían mi respeto y, durante este tiempo, se han ganado también mi admiración. Extiendo estas palabras de agradecimiento a Migue, que aunque no sea director «oficial» sobre el papel, sabe de sobra que para mí ha sido director «de corazón» como el que más. Gracias, *sosssio*, ya sabes que de mayor quiero ser como tú (versión 2.0 mejorada, a ser posible). Gracias también a Jesús, que fue de los primeros en apostar por mí y animarme a emprender esta aventura. Recuerdo que, tras la defensa de mi proyecto fin de carrera, hace ya cuatro años (o quizá uno más…), me dijo que en el futuro nos veríamos en la exposición de mi tesis, y su predicción está cada vez más cerca. Alberto, Antonio, Migue y Jesús: he tenido la suerte de encontrar en vosotros no solo maestros, sino mentores. Gracias de corazón por vuestra calidad profesional y personal.

También quiero dar las gracias al resto de compañeros de departamento: Diego, Antonio García, Encarni, Fran, Curro y a todos los demás, por hacerme sentir como en casa desde el primer momento. Muchas gracias a los compañeros y amigos con los que tuve la suerte de coincidir en el departamento, muy especialmente Sofía y Fernando, Nuria, Pepe y Almudena, aunque desafortunadamente ya no nos veamos tanto como me gustaría.

Esta tesis se ha realizado en estrecha colaboración con el departamento de Química Analítica de la Universidad de Granada. Por tanto, mi más sincero reconocimiento y agradecimiento en primer lugar a Luis Fermín Capitán, que ha sido otro pilar fundamental en el desarrollo de mi tesis. Gracias a Miguel (muchas veces compañero de fatigas en los laboratorios de Ciencias), a Isa (y su particular técnica de supervisar experimentos) y a Alfonso. También agradezco a Sara su alegría y su buena disposición.

Also, I would like to thank Professor Leena Ukkonen and Dr. Toni Björninen for giving me the opportunity to work with their research group at the Tampere University of Technology. Thank you (kiitos) for sharing your expertise, and for your guidance and time. Thank you also to the *crazy cat people* who I was lucky to meet in Tampere and made my stay there much more funny.

Gracias a mis compañeros de despacho del CITIC: Paco, Fermín, Gabriel, Marta, Rober, Diego e Ignacio. Por esos saludos mañaneros tan originales y porque haberlos conocido es una de las cosas buenas que me llevo al final de esta experiencia.

No quiero olvidarme de todos los familiares y amigos que a lo largo de estos años se han interesado por mi tesis, me han preguntado y se han preocupado por mí. Aunque no sería posible nombrar a todos y cada uno de vosotros, creedme que agradezco y valoro sinceramente vuestro interés y cariño.

Si hasta ahora he agradecido con sinceridad y franqueza, a partir de aquí lo hago con el corazón en la mano. Gracias a Dios por la familia que tengo, que ha sido un apoyo imprescindible desde la decisión inicial de comenzar la tesis doctoral hasta su punto final. Gracias a mis padres, Carmen y Juan Carlos, por una lista tan larga de cosas que merecerían más páginas que esta tesis. Intentando resumir, quiero darles las gracias por su amor, por su ejemplo, por educarnos a mí y a mis hermanos en valores como la bondad, la fe, la honradez, la responsabilidad y el esfuerzo, valores de los que ellos siempre han sido para mí ejemplo y guía. No tendré vida suficiente para agradecerles todo lo que me han dado y siguen dándome. Gracias a mis hermanos mayores, Teresa y Carlos, a mi hermana «pequeña» Carmen (aunque ya sea médico siempre será mi hermana pequeña), a mis cuñados y a mis sobrinos Pablo, Lucía y Marcos, que sin saberlo me hacen más feliz. Gracias a mi familia política, aunque no me gusta especialmente ese término porque los considero, directamente, familia sin más: a Dori y Jose María, por hacerme sentir como un hijo más, y a mi *cuñaílla* Clara, que es para mí como mi otra hermana «pequeña».

Por último, gracias a la persona con la que quiero compartir el resto de mi vida: Cristina. Por su apoyo incondicional, su optimismo y generosidad, por hacerme reír, por saber consolarme y animarme, por soportarme hasta cuando estoy insoportable, por creer en mí siempre y desde siempre, por hacerme sentir importante y capaz de cualquier cosa, por soñar conmigo en un futuro cada vez más cercano, por todo lo vivido y por todo lo que nos queda por vivir. En definitiva, gracias por hacerme feliz.

A todos, una vez más y siempre:

Gracias

Resumen

Motivación y objetivos

La monitorización de magnitudes ambientales tales como la temperatura, humedad, radiación ionizante y concentración de sustancias gaseosas o en disolución es una necesidad creciente en una amplia variedad de áreas que abarca desde el ámbito personal hasta el clínico o el industrial, incluyendo gran parte de los sectores socioeconómicos, entre los que cabe destacar aplicaciones en los ámbitos de Internet de las Cosas (Internet of Things, IoT), redes de sensores inalámbricos (Wireless Sensor Networks, WSN), inteligencia ambiental, envasado inteligente, monitorización biomédica y calidad de vida.

Por otro lado, la aparición en los últimos años de tecnologías de fabricación de circuitos electrónicos mediante técnicas de impresión directa ha propiciado el desarrollo de estos dispositivos sensores sobre sustratos flexibles de tipo celulósico, polimérico o textil. El uso de técnicas de impresión para la fabricación de circuitos eléctricos y electrónicos permite potencialmente una reducción de los costes de producción, además de que los dispositivos impresos pueden presentar interesantes ventajas como flexibilidad, ligereza, espesor reducido, transparencia, menor impacto medioambiental o facilidad de integración y adaptación a diferentes geometrías y superficies .

El desarrollo en paralelo de dispositivos sensores impresos, selectivos, sensibles, de respuesta rápida y bajo coste que se puedan desplegar ampliamente y, además, estar conectados de forma inalámbrica mediante tecnologías como RFID (Radio Frequency IDentification) o NFC (Near Field Communication) es una opción de gran interés científico y tecnológico. Por otra parte, es deseable el desarrollo de dispositivos sensores que permitan obtener información cuantitativa precisa sin necesidad de disponer de instrumentación dedicada, sino utilizando dispositivos ubicuos, con lo esto que supone de miniaturización, bajo consumo, bajo coste y capacidad de comunicación inalámbrica.

Aunando todo lo anterior, el principal objetivo de esta tesis es el desarrollo de sistemas de medida rápidos, de bajo coste y ubicuos, basados fundamentalmente en el uso de tecnologías de impresión sobre sustratos flexibles como principal proceso, si no único, de fabricación. Además, se propicia la presencia en un mismo sustrato de sensores químicos y físicos, así como elementos conductores impresos con capacidad de procesar y transmitir inalámbricamente las señales procedentes de dichos sensores. Por un lado, se plantean objetivos de tipo metodológico, consistentes en el estudio de las dos principales tecnologías directas de impresión utilizadas en electrónica impresa flexible: la serigrafía y la inyección por chorro de tinta. Como

continuación de este objetivo metodológico, se propone la caracterización de diferentes tipos de tratamientos post-impresión, necesarios para conseguir que las estructuras impresas sean eléctricamente conductivas. En este sentido, se analizarán dos procesos de sinterizado o curado: el térmico y el eléctrico. En cuanto a los objetivos de desarrollo, las estrategias de interés son las siguientes:

- Desarrollo de etiquetas RFID o NFC pasivas que incluyan sensores comerciales. Tan solo dispositivos y sensores de muy bajo consumo pueden incorporarse a este tipo de etiquetas sin batería de alimentación.

- Integración de sensores impresos en estructuras pasivas con capacidad de cosechamiento de energía en las que la información proveniente de los sensores se encuentre disponible al usuario a través de interfaces simples o tecnologías inalámbricas con RFID/NFC.

- Diseño de sistemas impresos en los que los propios constituyentes de la etiqueta básica posean o se hayan modificado para tener capacidad sensora.

- Desarrollo de plataformas sensoras basadas en dispositivos móviles como lectores ubicuos al alcance de cualquier usuario. Este objetivo incluye el diseño de aplicaciones móviles dedicadas que permitan la alimentación del sistema sensor a través de tecnología NFC, la comunicación bidireccional entre el sistema sensor y el dispositivo móvil, o el procesamiento de los datos provenientes de los sensores.

Existen diversos sustratos flexibles que cumplen los requisitos necesarios para su uso en electrónica imprimible. Entre los más comunes destacan el tereftalato de polietileno (PET), el naftalato de polietileno (PEN) y la poliimida (PI), cuyos espesores pueden variar entre las decenas y los cientos de µm. Las ventajas de PET y PEN radican en su alta transparencia óptica y bajo coste. Sin embargo, su resistencia a altas temperaturas es limitada. En cuanto a la poliimida, tiene la ventaja de resistir temperaturas más altas pero su coste se encarece. Además, la poliimida es un material sensible a la humedad, propiedad que puede aprovecharse para el desarrollo de sistemas sensores de dicha magnitud. Otros sustratos que pueden utilizarse para electrónica imprimible son el papel, el cristal flexible o materiales textiles.

En cuanto a las tintas conductoras, las más extendidas y mejor valoradas en el sector son las tintas conductivas compuestas por nanopartículas metálicas. Están formadas por materiales altamente conductores como la plata, el cobre, el oro o el aluminio. En nuestro caso, para la impresión mediante inyección por chorro de tinta se ha hecho uso de la tinta Suntronic U5603 de Sun Chemical, una tinta de nanopartículas con un contenido de plata sólida del 20%. Según el fabricante, la tinta puede alcanzar

resistividades entre 5 y 30 µΩ·cm tras su sinterizado térmico. En cuanto a serigrafía, en esta tesis se ha utilizado la tinta conductiva de plata SunTronic CRSN 2442, también de Sun Chemical. Su contenido sólido de plata es del 70% y promete resistividades entre 25 y 50 µΩ·cm tras el curado térmico.

Los dos tipos de curado o sinterizado estudiados en esta tesis han sido el térmico y el eléctrico. El sinterizado térmico es el método más común, y consiste en calentar los patrones impresos ya sea sobre una placa caliente o dentro de un horno. Se pueden alcanzar temperaturas de 200 °C o incluyo superiores. Durante el proceso, el disolvente de la tinta se evapora y las nanopartículas metálicas pierden su escudo aislante protector, fundiéndose para formar estructuras conductivas. En cuanto al curado eléctrico, el sinterizado se consigue al aplicar una tensión sobre el patrón impreso, que causa un flujo de corriente a través de la estructura. Este flujo de corriente genera un calentamiento local de la estructura impresa a causa del efecto Joule, que lleva a cabo el curado. Como paso previo al sinterizado eléctrico propiamente dicho, es necesario que la estructura posea una conductividad inicial, aunque sea muy baja, que permita el tránsito de corriente. Esto se consigue a través de una fase de pre-curado, que normalmente se realiza térmicamente a baja temperatura.

Resultados y Conclusiones

Una vez marcados los objetivos y tras el breve contexto teórico expuesto, a continuación se resumen las diversas contribuciones de esta tesis junto con los resultados más relevantes obtenidos y las conclusiones que se pueden extraer de ellos.

Como paso previo al desarrollo de dispositivos sensores impresos, se han estudiado, caracterizado y comparado dos de los principales métodos de curado de electrónica impresa: el térmico y el eléctrico. Para el estudio del curado térmico se ha diseñado una resistencia impresa simple fabricada mediante inyección por chorro de tinta. El proceso de caracterización del curado térmico ha consistido en monitorizar en tiempo real el cambio en la resistividad de la estructura impresa, estando dicha estructura en el interior de un horno de convección durante su curado térmico. Se han considerado dos procesos de curado térmico: una rampa de temperatura y un escalón de temperatura. En ambos casos, se han monitorizado los procesos térmicos para seis temperaturas finales de curado, de 100 a 200 °C en pasos de 20 °C. Tanto con rampa como con escalón de temperatura, se consigue mejor resistividad cuanto mayor es la temperatura de curado final, como cabría esperar. Para el mismo tiempo de curado, la resistividad de los patrones sufre un decremento de alrededor del 67 % si la temperatura final es de 200 °C con respecto a una temperatura final de 100 °C. Por otro lado, nuestro estudio ha demostrado que se obtienen mejores valores de resistividad de los patrones curados en el caso de curado térmico con escalón de

temperatura, independientemente de la temperatura final. El mejor valor de resistividad obtenido ha sido de $9.41 \pm 0.12\,\mu\Omega \cdot cm$ (curado con escalón de temperatura a 200 °C), que es aproximadamente seis veces el valor de la resistividad de la plata ($1.59\,\mu\Omega \cdot cm$). Los resultados obtenidos para todos los casos de temperatura final son consistentes con los valores de resistividad especificados por el fabricante de la tinta conductiva utilizada, de 5 a $30\,\mu\Omega \cdot cm$.

El curado eléctrico también se ha estudiado como método alternativo al térmico, sobre el que presenta algunas ventajas como tiempos de curado mucho más rápidos o posibilidad de utilizar sustratos no resistentes a las altas temperaturas. Para estudiar el curado eléctrico y, posteriormente, compararlo con el térmico en términos de comportamiento a altas frecuencias de las estructuras impresas, se diseñaron y fabricaron líneas de transmisión de tipo microstrip con impedancia característica de 50 Ω. Dichas líneas se imprimieron mediante inyección por chorro de tinta sobre poliimida (Kapton® HN) con la cara inferior metalizada para actuar como plano de tierra. Tras una fase previa de pre-curado térmico, las líneas microstrip impresas se curaron eléctricamente aplicando diferentes formas de tensión entre sus extremos. Los mejores resultados se obtuvieron con escaleras de voltaje hasta 25 V en pasos de 5 V, con una duración total de 5 segundos. Aplicando este curado térmico se coniguió reducir la resistividad de las líneas hasta $5\,\mu\Omega \cdot cm$, que es un valor de resistividad tan solo 3.3 veces superior al de la plata. Con este tipo de curado alcanzamos, además, el límite inferior de resistividad posible según el fabricante de la tinta utilizada. A continuación, se analizó el impacto del método de curado en el rendimiento de las líneas microstrip a altas frecuencias. Con ayuda de un analizador vectorial se caracterizaron en RF un total de 10 líneas microstrip impresas: seis de ellas curadas térmicamente a diferentes temperaturas y cuatro curadas eléctricamente. En principio, cabría pensar que las líneas curadas eléctricamente pudieran verse degradadas debido al proceso brusco y repentino de curado. Sin embargo, los estudios realizados en este ámbito, en términos de pérdidas de transmisión, sugieren que el tipo de curado no afecta a priori en el comportamiento de las líneas a altas frecuencias, ya que en ambos casos observamos una tendencia similar. No obstante, esperamos seguir trabajando con más profundidad en este estudio para confirmar dichas conclusiones.

Se ha empleado otra técnica de fabricación para sistemas flexibles, que consiste en la transferencia de patrones sobre tela conductiva. En este ámbito, se ha diseñado una etiqueta RFID de ultra alta frecuencia (Ultra High Frequency, UHF) compatible con la industria textil y, por tanto, compatible con el desarrollo de prendas inteligentes vestibles. Se trata de una etiqueta UHF con una antena circularmente polarizada cuyo rango de lectura medido entre 800 MHz y 1 GHz es superior a 2 metros para cualquier orientación de la etiqueta con respecto al lector. Este trabajo se encuentra en desarrollo, con lo que se pretende aumentar el rango de lectura más allá de los resultados obtenidos mejorando la adaptación entre la impedancia de la antena y la

del chip RFID. Asimismo, dada la naturaleza textil de la etiqueta, debe avanzarse en el estudio de la influencia del cuerpo humano sobre las propiedades de radiación de la antena diseñada.

Como ejemplo de sistema impreso en el que el propio constituyente de la etiqueta posee capacidad sensora, se ha diseñado, fabricado y caracterizado un sistema pasivo y sin chip para medidas de humedad relativa. El sistema está basado en una estructura resonante LC paralela, donde la inductancia L es una espiral plana mientras que la capacidad C está formada por una estructura interdigital. La estrategia de medida se basa en el uso de poliimida como sustrato para la impresión del circuito LC, que se ha llevado a cabo mediante serigrafía. La poliimida es un material que tiene la capacidad de absorber humedad, hecho que influye en sus propiedades eléctricas tales como la permitividad eléctrica. El cambio en esta propiedad eléctrica inducido por la absorción de humedad modifica el valor de la capacidad interdigital impresa, lo cual tiene como efecto un cambio en la frecuencia de resonancia del sistema completo. El sistema ha sido diseñado para resonar a una frecuencia en torno a 13.56 MHz en un ambiente de atmósfera seca. Utilizando una cámara climática y un analizador de impedancias, se ha medido el cambio en la frecuencia de resonancia del sistema al variar la humedad relativa entre el 10% y el 90% aproximadamente, manteniendo una temperatura constante de 20 °C en el interior de la cámara. De esta forma, se ha obtenido un cambio considerable en la frecuencia de resonancia del sistema de unos 685 kHz entre ambos extremos de humedad relativa, con una tasa de variación media de 8.6 kHz/%RH. Además, la variación de la resonancia sigue una tendencia prácticamente lineal con la humedad relativa. A la vista de los resultados, el sistema diseñado podría utilizarse potencialmente en aplicaciones de envasado inteligente de alimentos, ya que la humedad puede relacionarse con el deterioro de los mismos. Los siguientes pasos en el contexto de este trabajo consistirán en la extensión del rango de humedad de medida, así como el desarrollo de un lector inalámbrico que sea capaz de detectar el cambio en la frecuencia de resonancia de este sistema de cara a una aplicación real.

La utilización de dispositivos y teléfonos móviles como lectores para sistemas sensores resulta de gran interés, ya que en este caso no son necesarios lectores dedicados y específicamente diseñados, sino que cualquier persona está en disposición de un sistema lector sin más que sacar el teléfono móvil de su bolsillo. En este ámbito, se ha desarrollado una plataforma sensora basada en teléfono móvil para dosimetría utilizando la interfaz NFC con aplicación potencial en el sector del control de los tratamientos con radioterapia. El sistema utiliza MOSFET comerciales como sensores de radiación ionizante. A través de tecnología NFC, el teléfono móvil actúa como fuente de alimentación, unidad lectora y unidad de almacenamiento de medidas de la etiqueta diseñada. En este caso, el transistor comercial utilizado como dosímetro se conectaba a la etiqueta NFC antes y después de cada sesión de radiación para llevar a cabo la lectura de las medidas. Se ha conseguido una sensibilidad de

4.5±0.15 mV/Gy, que es consistente con resultados obtenidos en trabajos previos. El sistema propuesto se puede considerar por tanto una opción prometedora y de bajo coste para su uso como sistema de control dosimétrico en tratamientos con radioterapia.

A partir de este punto, las contribuciones que se describen forman parte de los trabajos publicados que constituyen la tesis bajo la modalidad de tesis por compendio de publicaciones. En los cuatro casos se trata de dispositivos sensores impresos sobre sustrato flexible para medidas de parámetros como temperatura, luz, humedad o concentración de diferentes gases.

El primer trabajo ha consistido en el diseño, fabricación y caracterización de una etiqueta UHF RFID impresa pasiva con múltiples capacidades sensoras ópticas (Escobedo, Carvajal, et al., 2016). La etiqueta incluye cinco fotodiodos, cubriendo así un amplio rango espectral que abarca desde la región infraroja hasta la ultravioleta. La antena de la etiqueta, basada en un diseño de tipo dipolo, así como las conexiones del circuito, se imprimieron por serigrafía en sustrato flexible polimérico (concretamente, poliimida). El sistema tiene un rango de lectura de 1.1 m. La etiqueta incluye un microcontrolador que actúa, junto con varios transistores, como sistema conmutador para medir los datos provenientes de los cinco sensores ópticos, proporcionando de esta manera una huella espectral de la radiación electromagnética incidente. Además, el chip RFID utilizado contiene un sensor interno de temperatura, con lo que esta etiqueta es capaz de proporcionar hasta seis magnitudes en cada medida, todo ello sin necesidad de batería ya que la energía la recoge del campo electromagnético generado por el lector RFID. Se ha diseñado un procedimiento de normalización de los datos provenientes de los sensores para la construcción de la huella espectral, y se han propuesto y validado dos posibles aplicaciones. En primer lugar, la detección de diversos iluminantes estándares permite el uso de esta etiqueta para detectar diferentes condiciones de luz. En segundo lugar, el sistema fue utilizado para medidas de color a través de la reflexión de un iluminante estándar. En este sentido, se consiguió detectar el nivel de maduración de los plátanos en función de la huella espectral obtenida a través de la etiqueta.

La siguiente contribución consiste en un sistema impreso flexible sobre PEN para la determinación umbral de gases en ambientes sellados (Escobedo, de Vargas-Sansalvador, et al., 2016). En este caso, el sistema está basado en sensores químicos sensibles a determinados gases que presentan respuesta óptica, ya sea de tipo luminiscente o colorimétrica. La etiqueta incluye un LED para excitar ópticamente la membrana sensible y un detector de color de alta resolución para la lectura de la respuesta óptica. Se incluyó un microcontrolador para procesar los datos provenientes del detector de color, permitiendo diferenciar si la concentración de gas obtenida ha superado o no el valor umbral establecido. El sistema se alimenta por completo a través de dos pequeñas celdas solares, de manera que puede operar bajo

luz solar directa o a través de luz artificial como la obtenida con una linterna. La información sobre si el gas detectado se encuentra o no entre los límites establecidos se envía al usuario a través de un simple código de color utilizando dos LED. Se han desarrollado dos prototipos basados en esta arquitectura. La diferencia entre ambos radica en el módulo sensor, que varía en función del gas que se desee monitorizar. En el primer caso, se hizo uso de un sensor químico luminiscente para la detección de oxígeno. En el segundo prototipo, se utilizó una membrana con respuesta colorimétrica para la detección de dióxido de carbono. Los límites de detección obtenidos en ambos casos confirmaron su potencial uso en aplicaciones de envasado en atmósfera modificada.

En tercer lugar, se presenta el desarrollo de una etiqueta NFC impresa, flexible y pasiva para la determinación de oxígeno, dióxido de carbono, amoníaco y humedad relativa (Escobedo et al., 2017). La etiqueta, impresa por serigrafía sobre PET, está basada en la tecnología NFC como fuente de energía y comunicación de datos a través de un teléfono móvil inteligente. Los cuatro sensores químicos utilizados presentan respuesta óptica a la presencia del gas correspondiente, siendo de tipo luminiscente en el caso del oxígeno y de tipo colorimétrico en el resto de gases. Un único LED blanco se utilizó como fuente de excitación óptica para todos los sensores, mientras que las respuestas ópticas son recogidas a través de cuatro detectores de color de alta resolución. Un microcontrolador se encarga de gestionar la lectura de los cuatro sensores cuando el dispositivo móvil se acerca a la etiqueta. Las respuestas obtenidas de los sensores ópticos se calibraron y ajustaron a funciones simples, permitiendo así la predicción de la concentración de cada gas. También se llevó a cabo un estudio de la sensibilidad cruzada de los sensores, obteniendo resultados despreciables en la mayoría de los casos o fácilmente corregibles a partir del resto de medidas. La elección de los gases se realizó por su importancia en aplicaciones de envasado en atmósfera modificada (caso de oxígeno y dióxido de carbono) o aplicaciones de envasado inteligente de alimentos (caso de humedad y amoniaco). Los valores de resolución y límites de detección obtenidos hacen posible el potencial uso de la etiqueta desarrollada en este tipo de aplicaciones.

Por último, se propone una nueva aproximación para la determinación de oxígeno en aplicaciones de envasado inteligente (Escobedo Araque et al., 2018). El sistema propuesto consiste en una membrana sensible a oxígeno con respuesta luminiscente que se adhiere a la superficie interior del alimento envasado. Un teléfono móvil se utiliza tanto para la excitación como para la lectura de la membrana, evitando así la necesidad de electrónica adicional. Se ha desarrollado una aplicación Android™ para tomar una fotografía de la membrana a una distancia fija y predeterminada. La aplicación realiza un procesamiento de imagen sobre la fotografía tomada para detectar la membrana y obtener información colorimétrica sobre la intensidad de la luminiscencia y la absorción de la misma. Estas magnitudes se combinaron para definir un nuevo parámetro que se encuentra relacionado con la concentración de

oxígeno. El parámetro propuesto muestra una sensibilidad mejorada y mayor inmunidad a la deriva térmica comparado con trabajos previos. El sistema ha sido aplicado a la monitorización de carne de cerdo empaquetada, ya que está demostrado que la concentración de oxígeno en un embalaje sellado que contenga carne está relacionada con la actividad bacteriana. Por lo tanto, la medida de oxígeno en el interior del paquete proporciona información sobre el estado de la carne. El paquete con la carne se introdujo en un ambiente controlado de temperatura a 4 °C durante una semana, tiempo en el cual se fueron tomando medidas con el sistema propuesto. Los resultados obtenidos muestran que la plataforma es capaz de proporcionar información precisa sobre la concentración de oxígeno en el interior del paquete, por lo que el sistema es potencialmente válido para aplicaciones de envasado inteligente de alimentos.

Contenido

List of Figures

Publication 1: Passive UHF RFID Tag for Multispectral Assessment

Publication 2: Flexible passive tag based on light energy harvesting for gas threshold determination in sealed environments

Publication 3: Flexible Passive near Field Communication Tag for Multigas Sensing

Publication 4: Non-Invasive Oxygen Determination in Intelligent Packaging Using a Smartphone

List of Tables

Publication 1: Passive UHF RFID Tag for Multispectral Assessment

Publication 2: Flexible passive tag based on light energy harvesting for gas threshold determination in sealed environments

Publication 3: Flexible Passive near Field Communication Tag for Multigas Sensing

Acronyms

ASK   Amplitude Shift Keying

AC   Alternate Current

ADC   Analog to Digital Converter

ADS   Advanced Design System

API   Application Programming Interface

BJT   Bipolar Junction Transistor

CNT   Carbon NanoTubes

CP   Circular Polarization

CTAB   Cetyltrimethylammonium bromide

CVD   Chemical Vapor Deposition

DABCO   1,4-diazabicyclo[2.2.2]octane

DC   Direct Current

DMP   Dimatix Material Printer

DTD   Drop to Drop

DUT   Device Under Test

ECL   Electrochemiluminescence

EEPROM   Electrically Erasable Programmable Read-Only Memory

EM   Electromagnetic

EPC   Electronic Product Code

EPDM   Ethylene Propylene Diene Monomer

FR-4   Flame Retarded Type 4

HEC   2-Hydroxyethyl cellulose

HF   High Frequency

HFSS   High Frequency Structural Simulator

I^{2}C   Inter-Integrated Circuit

IC   Integrated Circuit

ID   Identification

IDE   Interdigitated Electrodes/Integrated Development Environment

IoT   Internet of Things

IR   Infra Red

ISO   International Organization for Standardization

JFET   Junction Field-Effect Transistor

LED   Light Emitting Diode

LF   Low Frequency

LOD   Limit of Detection

MAP   Modified Atmosphere Packaging

MCP   Meta-Cresol Purple

MCU   Microcontroller Unit

MEMS   Micro Electro Mechanical Systems

MF   Medium Frequency

MOSFET   Metal-Oxide-Semiconductor Field-Effect Transistor

NFC   Near Field Communication

NI   Near Infra Red

NP   Nanoparticles

NPOE   2-Nitrophenyl octyl ether

OCP   Over Current Protection

OLED   Organic Light-Emitting Diode

PCB   Printed Circuit Board

PDMS   Polydimethylsiloxane

PE   Printed Electronics

PEN   Polyethylene naphthalate

PET   Polyethylene terephtalate

PI   Polyimide

PLF   Polarization Loss Factor

PS	Polystyrene
PtOEP	Platinum Octaethylporphyrin
PV	Photovoltaic
PVC	Polyvinylchoride
RES	Rapid Electrical Sintering
RFID	Radiofrequency Identification
RF	Radiofrequency
RGB	Red Green Blue
RH	Relative Humidity
RTD	Resistance Temperature Detector
SFE	Sensor Front End
SHF	Super High Frequency
SRE	Serpentine Electrode
SRF	Self Resonance Frequency
SMA	Subminiature version A
SMD	Surface Mount device
SMU	Source/Measure Unit
SPI	Serial Port Interface
SRE	Serpentine Electrode
SRF	Self Resonant Frequency
TBP	Tributyl phosphate
THF	Tetrahydrofuran
TNT	Trinitrotoluene
TOAOH	Tetraoctylammonium hydroxide
TPU	Thermoplastic polyurethane
TTI	Time–Temperature Indicators
TUT	Tampere University of Technology
UHF	Ultra High Frequency

UV	Ultra Violet
VHF	Very High Frequency
VNA	Vector Network Analyzer
VOC	Volatile Organic Compound
WSN	Wireless Sensor Network
XLP	eXtreme Low Power

1. Introduction

1.1 Motivation

The tracking and monitoring of environmental parameters of significant interest such as temperature, humidity, ionizing radiation and substances or gases concentration is a growing demand in different sectors: from personal and clinic healthcare areas to food safety and industrial fields, including applications in the context of Wireless Sensor Networks (WSNs) and Internet of Things (IoT).

Besides, the emergence of Printed Electronics (PE) technology has enabled the development of sensing devices on flexible substrates such as paper, textile or plastic foils. Using printing techniques to fabricate electronic devices promises lower production costs because of the additive nature of the technology and the advantage of large-area processes with reduced infrastructure. In addition, printed devices can benefit from their potential advantages to be flexible, thin, lightweight, conformal, transparent, wearable, easy-to-integrate, cost-effective and environmentally friendly.

The development of printed sensor devices that are selective, sensitive, with fast response, low cost, low power consumption and connected by means of wireless technologies such as Radio Frequency Identification (RFID) or Near Field Communication (NFC) is an option of great scientific and technological interest. Additionally, it is highly desirable to be able to obtain the information from the sensor systems using general-purpose devices that are readily available to all. The combination of printing technologies and sensor devices with wireless connectivity leads to the next paradigm of smart products.

1.2 Objectives

The aim of this thesis is the design, development, fabrication and evaluation of sensor systems fundamentally based on the use of printing technologies on flexible substrate as the main manufacturing process. Methodological objectives include the study, characterization and validation of the main printing techniques used in the development of PE on flexible substrates: inkjet and screen printing. Post-processing of printed patterns will be also addressed as an essential step towards achieving conductive structures after the printing process.

The main strategies to be followed for the development of the printed sensor systems will be:

- Inclusion of commercially available sensors in passive architectures capable of energy harvesting and remote sensor data transmission by means of wireless technologies such as RFID or NFC.

- Integration of novel printed sensors into passive systems with conditioning stages where sensor information can be accessed using RFID/NFC or other wireless mechanisms.

- Design of printed sensor systems in which the monitored magnitude causes a variation in the electrical properties of the system that can be remotely detected.

- Development of smartphone-based sensor platforms in which mobile devices with custom-designed applications allow the powering, data communication and processing of the associated passive sensor systems.

The magnitudes of interest are temperature, humidity, radiation and concentration of different gases related to modified atmosphere and food preservation. The outcomes of this work will be passive sensor systems in the form of smart RFID/NFC tags or other simple and low-cost sensor platforms with feasibility to be used in fields such as environmental assessment, healthcare monitoring and smart packaging applications.

1.3 Outline of the thesis

It must be pointed out that this is a thesis by compendium of publications, which is formed by published papers resulting in my research work during the doctoral period.

Chapter two reviews the background, principles and state-of-the-art of the different technologies related to the proposed objectives of the thesis. This chapter comprises the following parts: an introduction to Printed Electronics, including materials, printing techniques, post-processing treatments (sintering) and printed sensors; a description of the basics of RFID technology and its applications, paying particular attention to high frequency (HF) and ultra-high frequency (UHF) tags; an updated overview of flexible sensor systems; and a summary of the current state and prospects of smartphone-based sensing platforms. In short, this chapter lays the basis for the development of printed sensor systems on flexible substrate.

The third chapter is devoted to methodological aspects. This covers descriptions of the specific printing methods and other fabrication techniques that have been used, as well as the main characterization equipment employed.

Results and their discussion are presented in Chapter 4. This chapter encompasses the research outcomes that are not part of the compendium or have not yet published, as well as the four published papers presented to constitute the thesis by compendium of publications. The first section of this chapter describes the sintering characterization that has been accomplished as a preliminary study towards the development of printed structures. Then, a wearable RFID tag antenna manufactured by a conductive textile transfer technique is presented. In the following sections, two fully-passive sensor systems are shown: a flexible printed humidity measurement system, and a passive dosimetric system based on NFC tag and smartphone. Sections 4.5, 4.6, 4.7 and 4.8 contain the four publications that form the thesis by compendium. The first one consists of a passive printed UHF RFID tag for spectral fingerprint measurement (Escobedo, Carvajal, et al., 2016). The second one is a flexible printed sensor platform for gas monitoring based on light energy harvesting that can be used in sealed environments (Escobedo, de Vargas-Sansalvador, et al., 2016). The third publication presents a fully-passive flexible NFC tag for multigas sensing (Escobedo et al., 2017). The last one consists of a smartphone-based oxygen detection platform (Escobedo Araque et al., 2018).

Finally, Chapter 5 collects the final conclusions drawn from the obtained results, as well as guidance and lines of work for future research.

2. Background

The field of printed sensor systems has witnessed impressive growth in recent years due to its countless possibilities for applications in the whole spectrum of our everyday lives (Mattana & Briand, 2016; Rim, Bae, Chen, De Marco, & Yang, 2016). These possibilities are even further broadened if a wireless technology such as RFID is included to create a low-cost communication interface for data exchange between the sensor system and the end user. The use of RFID technology along with the sensor system allows not only the data transmission of the measured magnitude to an external reader, but also the energy harvesting that makes it possible the design of passive battery-less systems (MacKenzie & Ho, 2015).

Several issues need to be addressed for the development of these types of printed sensor devices. Firstly, we need to study manufacturing aspects for pattern transfer techniques on flexible substrates, such as printing technologies (S. Khan, Lorenzelli, Dahiya, & Member, 2015) or manufacturing of conductive textiles on fabric substrates (Tao, 2015). Moreover, most of manufacturing techniques for printed electronics involve some kind of sintering process to make printed layers electrically conductive (Wünscher, Abbel, Perelaer, & Schubert, 2014). Moreover, we need to consider the sensors as an essential part of our system. Depending on the magnitude of interest and field of application, these sensors can be chemical, physical or biological. Last but not least, we make use of RFID technology as an energy harvesting and data transmission medium. In some cases, the availability of NFC technology in portable and mobile devices such as smartphones allows the use of these devices as external readers for our system (F. Li, Bao, Wang, Wang, & Niu, 2016). Combining all this we are able to develop flexible, printed, low-cost devices for passive, battery-less and remote sensing.

2.1 Printed Electronics

Printed Electronics (PE) refers to a process that merges electronics manufacturing and printing technology to produce electronic circuits with some special features such as flexibility, thinness, lightness, wearability, cost-effectiveness and environmental friendliness. Although this blended technology is not new and it originated before the 1950s, great advances have been made in the past decade thanks to the emergence of printing techniques with nanomaterial technologies (Suganuma, 2014). Among the different applications of printed electronics we can highlight the manufacturing of solar cells and OLEDs (M. Gao, Li, & Song, 2017; D. Li, Lai, Zhang, & Huang, 2018); organic/inorganic photovoltaics (Mayer, Gallinet, Offermans,

Zhurminsky, & Ferrini, 2017); integrated smart systems such as RFID tags (R. Singh, Singh, & Nalwa, 2017), sport fitness and healthcare devices (Y. Khan, Ostfeld, Lochner, Pierre, & Arias, 2016; Lorwongtragool, Sowade, Watthanawisuth, Baumann, & Kerdcharoen, 2014), printed sensors (Mattana & Briand, 2016) or smart textiles (Stoppa & Chiolerio, 2014); and electronics and components such as memories (Myny et al., 2015), antennas (Guo et al., 2017), batteries (R. Kumar et al., 2017), transistors (Mattana et al., 2017), wiring and interconnects (S.-P. Chen, Chiu, Wang, & Liao, 2015) or passive components (Choi, Yoo, Lee, & Lee, 2016; Ostfeld, 2015).

2.1.1 Materials

In the following sections, a brief review of material candidates for printed electronics is presented, including flexible substrates as well as conducting materials such as conductive textiles and inks.

Flexible substrates

The requirements for printed electronic substrates include flexibility, surface smoothness and adhesion, transparency in many cases, thinness and lightness, heat resistance, low thermal expansion, stiffness and low cost among others. Various choices of substrates are available depending on the nature of the printed electronic product. Table 1 lists some flexible substrates commonly used in PE along with their main characteristics.
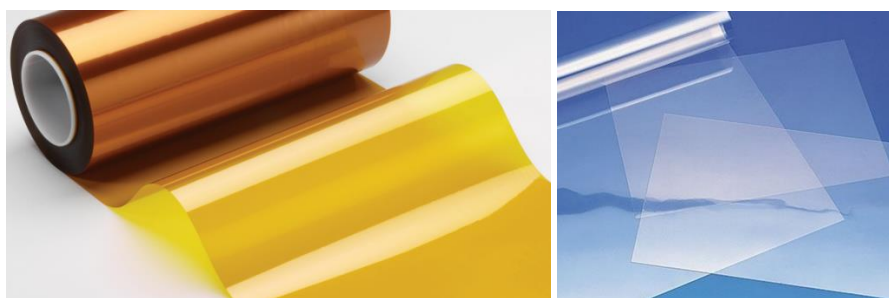
Figure 1. Pictures of two flexible substrates commonly used in PE: polyimide (PI) Kapton roll from Dupont® (left) and polyethylene terephthalate or PET (right).

Polyethylene terephthalate (PET) film is one of the most popular and widely used plastic film for PE due to its high optical transparency and low cost compared with other substrates. However, it has the drawback of poor heat resistance. The heat

resistance improves for polyethylene naphthalate (PEN) and gets much better for polyimide (PI), while transparency decreases and cost increases. PI is also one of the most widely used flexible substrates. Although its application in transparent devices is limited by its intrinsic color, PI can be a good choice for sensor applications thanks to its high moisture absorption (Rivadeneyra, Fernández-Salmerón, Agudo, et al., 2014). Paper substrates are also attractive for PE technology. The major advantages of these substrates are their low cost and biodegradability. Electronic devices utilizing paper as a substrate have the potential for mass production and integration at low cost, which are also disposable and recyclable.

Table 1. Flexible substrates and selected characteristics (Rim et al., 2016; Suganuma, 2014). T_{max} refers to maximum process temperature.

Material	Thickness (μm)	Density (g/cm²)	Transparency (%)	T_{max} (°C)	Other characteristics
PET	16–100	1.4	90	120	Clear, inexpensive, moderate moisture absorption
PEN	12–250	1.4	87	155	Clear, inexpensive, moderate moisture absorption
PI	12–125	1.4	–	300	Orange color, expensive, high moisture absorption
Paper	100	0.6–1.0	–	130	Biodegradable, inexpensive
Glass	50–700	2.5	90	400	Clear, expensive, weak, heavy weight

Besides being flexible, there are other interesting substrates for printed electronics that are elastic and stretchable. Among them, the most popular and commonly used are thermoplastic polyurethane (TPU) and polydimethylsiloxane (PDMS). TPU is a high stretchable material with properties such as low softening temperature, low hardness, abrasion resistance and transparency. Examples of screen-printed stretchable electronics on TPU substrates have been reported for wearable electronics applications (Suikkola et al., 2016). Very recently, TPU has been used as main mechanical carrier in a stretchable electronic platform for soft and smart contact lens applications (Vásquez Quintero, Verplancke, De Smet, & Vanfleteren, 2017). Moreover, TPU can be also laminated onto textiles (X.-D. Liu, Sheng, Gao, Li, & Yang, 2013). PDMS is a silicon-based elastomer that is thermally stable, permeable to gases, simple to handle and manipulate, and with isotropic and homogeneous properties (Mata, Fleischman, & Roy, 2005). It has been used for flexible and stretchable deployments such as soft antennas (Trajkovikj, Zurcher, & Skrivervik, 2013), printed pressure sensors (C.-Y. Li & Liao, 2016) or epidermal strain sensors (Chou, Kim, & Kim, 2016).

Textile materials can also be used as substrates for flexible and printed electronics. The convergence of electronics and textiles (known as e-textiles or "smart textiles") extend the usefulness and functionality of common fabrics by enabling the development of wearable sensing and monitoring devices (An et al., 2017; Castano & Flatau, 2014; Stoppa & Chiolerio, 2014). Besides, some researchers use an approach where rubber materials such as ethylene propylene diene monomer (EPDM) can be integrated into the common textiles for flexible, lightweight body-worn electronics (X. Chen, Ma, Ukkonen, Bjorninen, & Virkki, 2017; Zhigang Wei et al., 2017).

Conductive materials

Many types of printable conductive materials have been studied to achieve low resistances, low processing temperatures, good adhesion, flexibility and stretchability. Among all the potential candidates, metal nanoparticle (NP) inks are considered the best for electrical printing processes due to their ability to create precise patterns with good conductivity (E. S. Park, Chen, Liu, & Subramanian, 2013). NP-based inks are made up of highly conductive materials such as Ag ($\sigma = 6.3 \times 10^7 \ \Omega^{-1} \cdot m^{-1}$), Cu ($\sigma = 5.96 \times 10^7 \ \Omega^{-1} \cdot m^{-1}$), Au ($\sigma = 4.42 \times 10^7 \ \Omega^{-1} \cdot m^{-1}$) or Al ($\sigma = 3.78 \times 10^7 \ \Omega^{-1} \cdot m^{-1}$). Currently, silver NP inks are the most popular due to its high electrical conductivity and low oxidation rate (Chiolerio et al., 2016; Kell et al., 2017). Nevertheless, copper and aluminum inks are recently attracting great attention because of their low price and high conductivity (S.-P. Chen et al., 2015). The use of metallic nanoparticles inks for printed electronics implies the need for a post-printing process in order to sinter the NPs and remove non-conductive organic components to enhance conductivity. This process is called sintering and will be described in Section 2.1.3. Other alternatives to metal NPs for printed electronics are graphite, carbon nanotubes (CNT) and graphene-based conductive inks (Kamyshny & Magdassi, 2014).

As previously mentioned, stretchable electronics is an extension of flexible electronics (Noh, 2016). From the perspective of printed conductors, new electronic inks that exhibit high mechanical durability and elasticity must be functionalized. The most common approach consists of mixing some elastomer with metal nanoparticles such as Ag NPs (Matsuhisa et al., 2017; M. Park et al., 2012). A recent study investigates a hybrid conductive ink composed of graphene and silver NPs (He, Chen, Wang, & Zhu, 2016). Interested readers can find other methods for the design of conductive elastomers for stretchable electronics reviewed in (M. Park, Park, & Jeong, 2014).

As for conductive fabrics, two main approaches exist: conductive threads or uniform electro-textiles. Conductive threads are created from strands of conductive and non-conductive fibers, while electro-textiles are fabricated by incorporating conductive threads into fabrics. Figure 2 shows these two processes as well as some commercially

available electro-textiles such as Shieldit Super, which has been already used for wearable e-textile RFID tags (Virkki, Wei, Liu, Ukkonen, & Björninen, 2017). Conductive materials can be integrated into textile structures by different technologies such as knitting, sewing, embroidering, weaving, coating/laminating or printing (Stoppa & Chiolerio, 2014; Yongsang Kim, Hyejung Kim, & Hoi-Jun Yoo, 2010). While textiles are wearable and washable, electronic devices are not. In this sense, efforts have been made to achieve washable and enduring conductive tracks on textiles (Le Floch et al., 2017; K. Yang, Torah, Wei, Beeby, & Tudor, 2013).
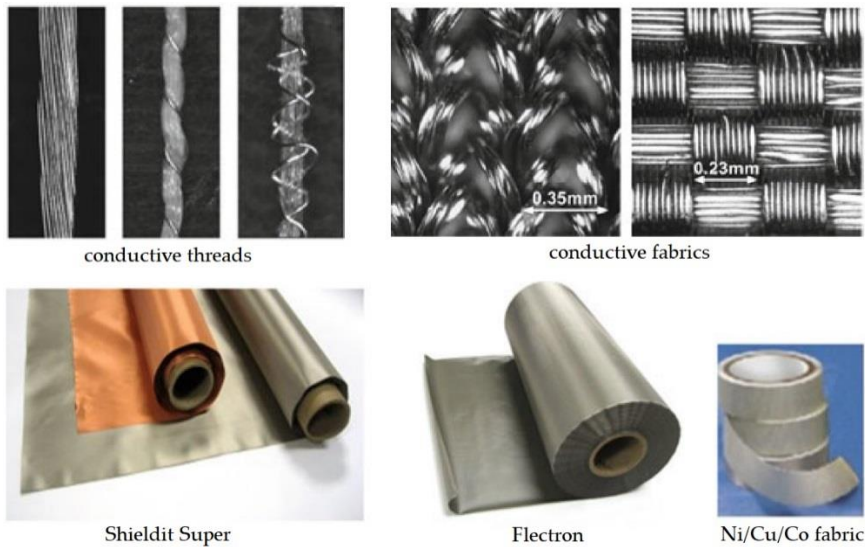
Figure 2. Process for manufacturing conductive fabrics and examples of commercially available conductive fabrics (Tao, 2015).

2.1.2 Printing techniques

Printed conductive patterns and electronic devices are manufactured by a wide range of printing techniques (S. Khan et al., 2015), including inkjet printing, screen printing, gravure printing, flexographic printing, roll-to-roll printing or novel methods such as hybrid 3D printing (Valentine et al., 2017). Roll-to-roll printing enables large-scale production of items such as RFID antennas (Jung et al., 2010). However, shifting from sheet-fed printing to roll-to-roll printing requires time and effort to adjust the different printing parameters and materials to the desired specific application. In this section the attention is focused on the two most commonly used printing methods in research field: screen and inkjet printing, which are also the techniques used throughout this thesis.

Screen printing

Screen printing is the most popular and matured technology for printed electronics and it has been used for many years in electronics manufacturing. In comparison to other printing methods, screen printing is faster, simpler, more affordable and more versatile. A screen printer has a simple setup consisting of a screen, a squeegee, a substrate and a base plate, as shown in Figure 3.
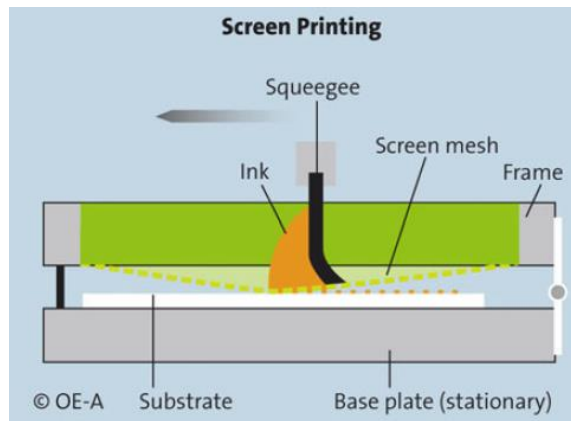
Figure 3. Screen printing process. *Source* OE-A (Kwon, Pode, Kim, & Chung, 2013).

The process is also simple: Firstly, a screen is patterned with an image by closing selected areas. For the ink deposition, the screen is situated some millimeters above the surface of the substrate and the ink is loaded onto the screen. The ink is transferred through the open meshes of the screen onto the substrate by moving the squeegee across the screen, touching momentarily the substrate. A wet film with the desired structure is left behind that dries by the vaporization of the solvent formulation of the ink. The print quality is affected by several parameters such as ink formulation, printing speed, angle and geometry of the squeegee, snap off between screen and substrate, mesh size and material (Soukup, Hamacek, & Reboun, 2012). In particular, the ink viscosity and surface tension of the substrate are critical for correct dispensing of the ink through the screen mask. Screen printing method is usually compatible with high-viscosity inks, as the lower viscosity ones will go through the mesh rather than dispensing out of it (T.-X. Liang, W. Z. Sun, L.-D. Wang, Y. H. Wang, 1996).

The usual thickness of a screen printed layer is in the range of microns, but it can even exceed 100 µm if a thick screen mesh is used. The possibility of printing relatively thick layers can enable the achievement of low-resistance structures by

compensating the high volume resistivity with a thicker layer. As for pattern resolution, which can be higher than 100 μm, we need to consider material, strength and number of meshes in the screen (Parashkov, Becker, Riedl, Johannes, & Kowalsky, 2005). Screens are developed by using different sizes of mesh openings and several materials such as nylon, polyester or stainless steel. Increasing the strength of the mesh material as well as the mesh thread density used in the screen mask will improve printing quality and resolution (Salmerón, Molina-Lopez, et al., 2014).

Inkjet printing

Among the different printing techniques, inkjet printing has raised great attention in recent years since it allows accurate deposition of micro and nanomaterials into functional arrangement in a maskless, additive patterning and non-contact approach (M. Singh, Haverinen, Dhagat, & Jabbour, 2010). These materials or inks essentially consist of a solute dissolved or dispersed in a solvent. The process basically involves the ejection of a fixed quantity of ink in a chamber from a nozzle usually via piezoelectric action, as shown in Figure 4. A chamber filled with ink is contracted in response to the application of an external voltage. This sudden contraction causes a liquid drop to eject from the nozzle. The ejected drop falls until it impinges the substrate.
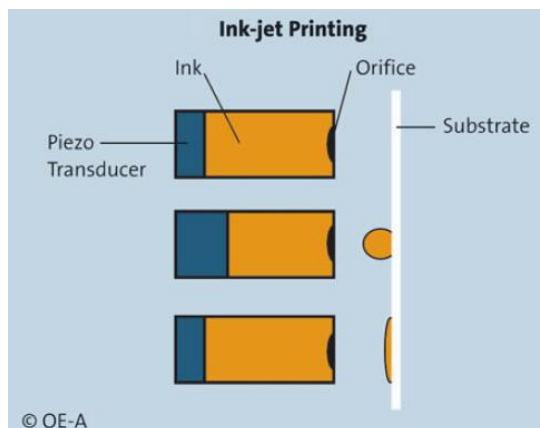
Figure 4. Inkjet deposition mechanism. *Source* OE-A (Kwon et al., 2013).

The viscosity and wettability of the ink affect the amount and shape of the ejected droplet. To print a homogeneous fine line, the inkjet printing parameters such as droplet size, shape, speed and uniformity must be controlled for each nozzle. Additionally, the ejection parameters including the piezo drive waveform, frequency and amplitude affect the shape and direction of droplets during flight, so they also need to be controlled for each nozzle.

The most commonly used inkjet-printable inks for the fabrication of conductive structures and electrodes are the metal nanoparticles-based inks. They allow the fabrication of conductive patterns characterized by an electrical conductivity close to that of bulk metals. These inks are composed of metallic nanoparticles (usually Ag but also Au and Cu) with typical dimensions of a few tens of nm. Each nanoparticle is surrounded by organic molecules to prevent its aggregation and precipitation, and suspended in a mixture of solvents (N. Zhang, Luo, Liu, & Liu, 2016). After printing, these inks require some type of sintering or curing in order to remove the organic components and promote nanoparticles coalescence, giving the printed layers their final desired electrical properties. Below we will discuss about this issue.

2.1.3 Sintering of metal nanoparticle-based conductive inks

Within the context of printed electronics, curing or sintering is a thermally induced process in which the metallic nanoparticles of the inks lose their outer organic shells or surfactants to enter in direct physical contact with one another, thus allowing electrical conductance (C. Y. Lai et al., 2014), as Figure 5 depicts. There are different techniques to achieve sintering (Kamyshny, 2011; Wünscher et al., 2014):

▪ **Thermal sintering:** This is the easiest and most common method for nanoparticles-based ink curing (Vandevenne et al., 2016). Printed patterns are directly exposed to heat, either on a hot plate or inside an oven. Temperatures of 200 °C or even more are commonly employed to achieve thermal sintering. Multiple step sintering can be also performed with a specific temperature step profile for efficient printed line curing (Halonen, Viiru, Ostman, Cabezas, & Mantysalo, 2013; Mościcki, Smolarek-Nowak, Felba, & Kinart, 2017). This process is critical to ensure that all the solvent carrier is fully eliminated from the printed bulk layer before metallization process occurs in between the silver nanoparticles. Insufficient removal of the solvent or additives residue would degrade the electrical performance. However, if higher resistivity is not detrimental to the target application, it is possible to perform thermal sintering at lower temperatures (Z. Wang, Wang, Jiang, & Yu, 2016).
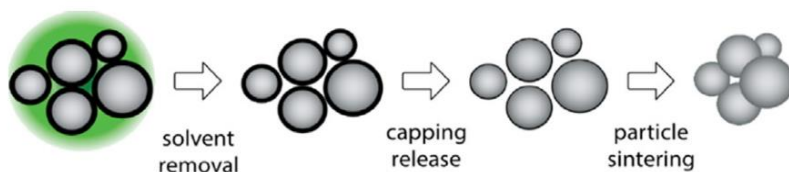
Figure 5. Sintering process of NP-based inks (Vandevenne et al., 2016).

- **Laser and photonic sintering:** In this method a light beam locally heats the printed pattern, thus evaporating the solvent to get the nanoparticles coalescence, as shown in Figure 6 (Ko et al., 2007; Niittynen, Sowade, Kang, Baumann, & Mäntysalo, 2015). In the case of laser sintering a monochromatic light source is employed (Maekawa et al., 2012), while photonic curing utilizes a broad-spectrum light source (Albrecht, Rivadeneyra, Abdellah, Lugli, & Salmerón, 2016), typically in the infrared or ultraviolet range. Both sintering techniques are based on the different absorption properties of the printed metallic structure and the substrate. In this way, the photons emitted by the light source are selectively absorbed by the printed layers to heat the ink without affecting the underlying printing substrate. This is the reason why photonic and laser sintering are often used in cases where the nature of the substrates is not compatible with direct thermal sintering.
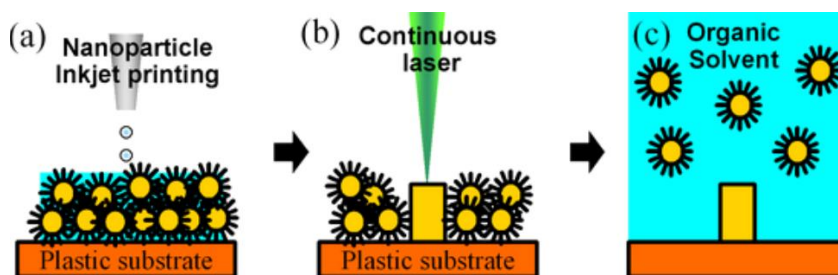
Figure 6. Laser sintering of inkjet-printed pattern. **(a)** Inkjet printing of metallic NPs represented by circles, still separated. **(b)** Laser curing of a conductive line. **(c)** Unsintered ink can be removed with a proper solvent (Ko et al., 2007).

- **Microwave and plasma sintering:** Highly conductive materials such as metals can be fast sintered by microwave radiation (Perelaer, de Gans, & Schubert, 2006), but they have a very limited penetration depth: it ranges from 1.3 to 1.6 μm at 2.54 GHz for Ag, Au and Cu (Kamyshny, 2011). This sintering method is capable of achieving electrical resistivity values similar to thermal sintering within a shorter time (Perelaer, Klokkenburg, Hendriks, & Schubert, 2009). However, it is successful only if the thickness of the printed structure is of the same order as the penetration depth, which limits the usefulness of this technique on a thicker printed layer.

If microwave radiation is combined with plasma, the method is called plasma sintering, see Figure 7 (K.-S. Kim, Bang, Choa, & Jung, 2013). In this case, heat is also directly transferred on the printed layer's surface, which makes this sintering method quicker than conventional microwave plasma (Wolf et al., 2013).
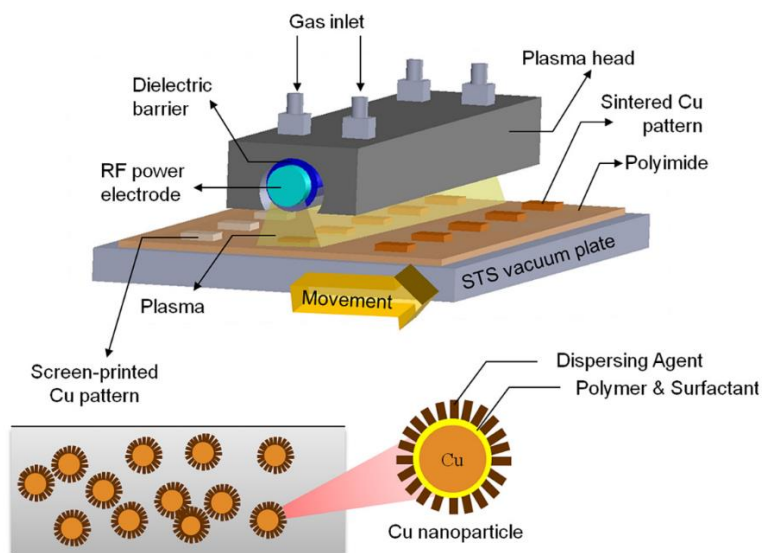
Figure 7. Schematic picture of the atmospheric-pressure plasma sintering (K.-S. Kim, Bang, Choa, & Jung, 2013).

- **Chemical sintering:** This method provides a new approach to achieve coalescence and sintering of metallic nanoparticles at room temperature under chemical agents (Magdassi, Grouchko, Berezin, & Kamyshny, 2010). It was discovered that printed patterns undergo a spontaneous and irreversible coalescence process upon contact with a solution containing oppositely charged polyelectrolytes, thus enabling the formation of low electrical resistivity printed layers even at room temperature (Grouchko, Kamyshny, Mihailescu, Anghel, & Magdassi, 2011). This makes possible the formation of conductive structures on heat sensitive substrates.

- **Electrical sintering:** In this approach, the sintering is reached by applying a voltage over the printed pattern that causes electrical current flow through the structure, as depicted in Figure 8. This leads to a local heating necessary to promote the sintering of the ink by energy dissipation through the Joule effect. As a consequence, the thermal stress of the substrate material is kept to a minimum since the heating is locally produced within the printed layer. Another important advantage of this method is the short sintering time: from microseconds to tens of seconds (Alastalo et al., 2009), so it is commonly referred to as rapid electrical sintering (RES).
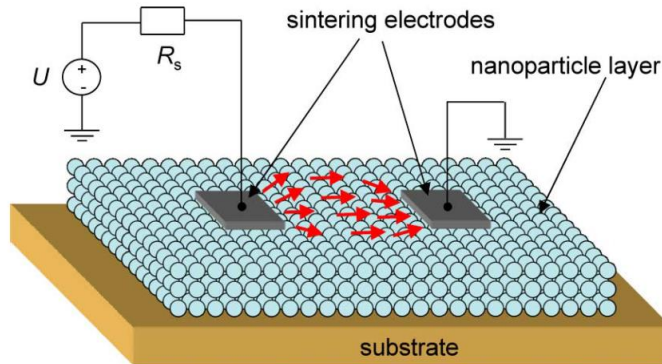
Figure 8. Schematic illustration (drawn out of scale) of a contact-mode electrical sintering setup (M. Allen et al., 2011).

This method was first introduced for silver pattern curing in 2008 (M. L. Allen et al., 2008). Allen et al. demonstrated that the final electrical resistivity of the printed structure can be controlled by regulating the current intensity and duration. First works on RES of printed nanoparticle Au and Ag inks describe the application of a DC current to slightly pre-sintered patterns (D.A. Roberson, Wicker, & MacDonald, 2012).

Before electrical sintering, a low initial conductivity is necessary to change the printed layer from an insulator to a poor resistor, thus allowing the current flow across the pattern to cause ohmic heating and sintering. The initial low conductivity is usually achieved by thermal annealing at low temperatures, which is known as thermal pre-sintering phase. Apart from the initial pattern conductivity, there are other parameters that need to be considered to achieve optimum results, such as input voltage, sintering time or input voltage profile (Jang, Lee, Lee, & Oh, 2013). A high initial resistance of the pre-sintered pattern can be counteracted with a higher input voltage, but too much input energy can cause macroscopic defects in the sintered structure. Some authors have developed a stepwise electrical sintering technique to overcome thermal damage of the sample during RES due to this high initial resistance (H. Lee, Kim, Lee, Moon, & Hwang, 2014).

DC RES requires direct contacting of the printed pattern during sintering, which can become a major obstacle in mass production. For this reason, contactless rapid electrical sintering was implemented using an AC current (M. Allen et al., 2011). In contactless RES, an AC field is applied by electrodes situated slightly above the sample. The electrical field is capable of overcoming the gap to achieve sintering. This method allows the homogeneous sintering of larger areas

compared to DC RES. In summary, electrical sintering stands as a fast and selective curing method that has been used to sinter Ag nanoparticles inks on several substrates such as PI, PET, glass and paper. Conductance values of up to 50% of bulk Ag have been obtained without damaging the underlying substrate (Hummelgård, Zhang, Nilsson, & Olin, 2011; Werner, Godlinski, Zöllmer, & Busse, 2013). The requirement of a thermal pre-sintering step is disadvantageous for high-throughput manufacturing, but it can potentially be replaced by faster sintering approaches like photonic curing.

2.1.4 Printed sensors

Printed Electronics enables the development of sensing systems with unique characteristics such as flexibility, conformability, transparency, wearability and biocompatibility. Flexible printed sensors play an important role in detecting environmental variations such as temperature, illumination, humidity, stress or chemical gases and vapours. With these applications in mind, sensors such as electromechanical sensors, photodetectors and chemical sensors have been developed (Rim et al., 2016). For instance, chemical printed sensors have gained attention in the last years to monitor food quality and safety as well as package integrity (Vanderroost, Ragaert, Devlieghere, & De Meulenaer, 2014). In this regard, flexible chemical sensors are of particular interest to develop intelligent food packaging in order to monitor volatile organic compounds (VOCs) and gas molecules related to food spoilage and package leaking. This allows the evaluation of the product quality and the package integrity, for instance, in modified atmosphere packaging[1] (MAP) applications. Next, we will summarize the current state of the art and trends in the research and development of printed sensors on flexible substrates, both physical and chemical.

Physical printed sensors

In this section there is a briefly review of printed sensors for the detection of physical parameters such as temperature, position, light and mechanical quantities. The majority of printed temperature sensors consist of metallic printed resistors whose resistance varies with temperature within a certain range of interest. There are examples of inkjet-printed silver meander-shaped resistors on different flexible substrates such as PET (Ali, Hassan, Bae, Lee, & Kim, 2016; Molina-Lopez, Quintero,

---

[1] Modified atmosphere packaging (MAP) is a packaging technology in which the air surrounding a food product is replaced by a protective gas mixture (usually CO_2 and N_2) in order to extend shelf life and quality of fresh food products.

Mattana, Briand, & de Rooij, 2013) or PI (Dankoco, Tesfay, Benevent, & Bendahan, 2016). Screen printing technique has also been used for the fabrication of printed temperature sensors on PEN or PET (Aliane et al., 2014).

Printing technologies have been also recently used for the fabrication of photodetectors on flexible substrates. The typical topology consists of a photoactive layer between two transparent electrodes. Several studies can be found in literature on printed photodetectors sensitive to visible-to-infrared wavelengths (Aga, Lombardi, Bartsch, & Heckman, 2014; Azzellino et al., 2013; Maiellaro et al., 2014). Less common, ultraviolet (UV) photodetectors have been also reported with printing technology (Dong et al., 2017; X. Liu et al., 2014).
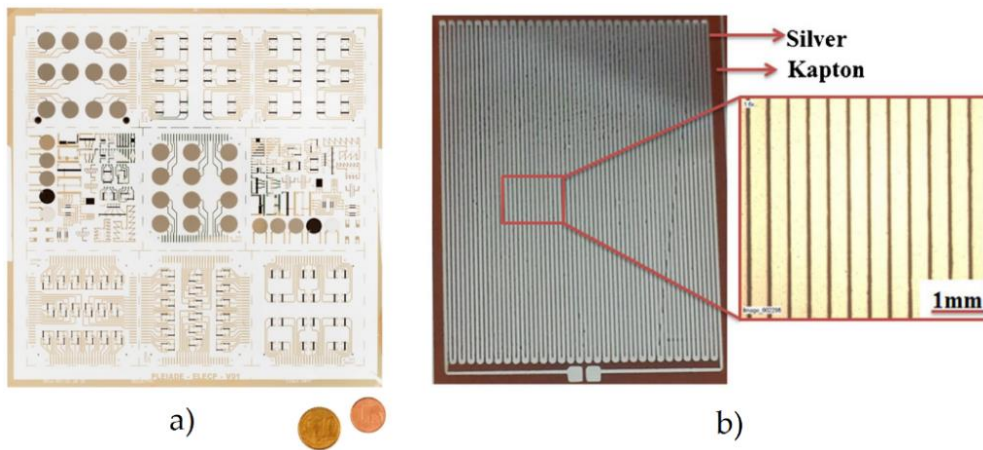
Figure 9. Examples of temperature printed sensors on (a) PEN foil (Aliane et al., 2014) and (b) Kapton, a polyimide substrate (Dankoco et al., 2016).

As for mechanical printed sensors, several mechanical parameters such as acceleration, pressure and strain can be detected and measured. Nowadays, most of accelerometers use Micro Electro-Mechanical Systems (MEMS) technology. Although they are typically fabricated on silicon wafers, also printing methods such as screen printing on polymeric or fabric substrates have been employed recently (Y. Wei, Torah, Yang, Beeby, & Tudor, 2013; Y. Zhang et al., 2017). In order to detect pressure, several transducing principles can be used. The simplest one consist of the capacitance variations of flexible structures under pressure. The typical topology of these capacitive pressure sensors is a parallel plate configuration where a flexible electrode deflects under applied pressure, decreasing the gap between the two electrodes and therefore causing an increase of the capacitance. Narakathu et al.

presented a first example of a screen printed flexible capacitive pressure sensor (Narakathu et al., 2012). Other examples using inkjet printing have been also reported in literature (Joo et al., 2017; Kisic, Blaz, Zlebic, Zivanov, & Nikolic, 2017). Piezoresistivity of printed materials is another phenomenon that can be exploited to detect pressure and strain. This method consists of the change in electrical resistivity of the printed structure produced by the deformation of the material, which is due to the application of an external force. One of the first examples of these printed sensors dates back to last century (Császár, Harsányi, & Agarwal, 1994), but very recent examples can be also found (Giffney, Bejanin, Kurian, Travas-Sejdic, & Aw, 2017; Harada, Honda, Arie, Akita, & Takei, 2014).

Chemical printed sensors

This category includes printed sensors for the detection of chemical analytes such as biomolecules, ions or gaseous species. In the first place, biosensors are devices conceived to analyze species based on biomolecular interactions in real time. In biosensors, one component called 'ligand' or 'receptor' is immobilized on a solid surface while the analyte to be detected is present as a solution. The interaction between these two components, the ligand and the analyte, results in a change of a property of the solid surface that can be measured to determine both the typology and amount of analyte that has reacted.

The largest and the oldest group of chemical and biochemical sensors are the electrochemical sensors, all based on the interaction between electricity and chemicals. The electrochemical sensors can be divided by the measurement mode. Thus, potentiometric sensors measure voltage, amperometric sensors measure current, or conductometric sensors measure conductivity. Electrochemical methods are based on the measurement of basic electrical magnitudes as current, power, resistance and load. They can be classified into two groups: electronic and ionic. The electronic ones are based on changes in properties associated with electrode proccesses, which are electrochemical conversions occurring at an electrode-electrolyte interface where a charge is transferred through the interface and an electric current flows. On the other hand, ionic methods are based on the measurement of the properties of an ionic solution.

The surface where the ligand is immobilized in these electrochemical systems is called working electrode. A variation of the current between the counter and reference electrodes is caused by the reactions between the ligand and the analyte. These variations can be quantified to determine whether an analyte is present into a solution and how much of it (Beni et al., 2015; Chouler, Cruz-Izquierdo, Rengaraj, Scott, & Di Lorenzo, 2018). Different printing techniques have been successfully used for the manufacturing of electrochemical biosensors. Screen printing is by far the

most popular and it has been used for the fabrication of different electrodes (silver, platinum, gold, palladium, graphite) over a variety of substrates (alumina, fiber glass, ceramics, polyvinyl chloride or PVC) (Taleat, Khoshroo, & Mazloum-Ardakani, 2014). One of the first inkjet-printed biosensors was reported in 1992 for glucose determination (Newman, Turner, & Marrazza, 1992). More recently, in (Y. Khan, Pavinatto, et al., 2016) a flexible gold electrode array is presented as a bioelectronic interface. Moreover, the continuous improvement of smartphone electronics and the development of new apps have stimulated research into smartphone-based biosensors (Roda, Michelini, et al., 2016).

Another type of chemical sensors are pH sensors, commonly employed in biology, medicine and health care (Nakata, Arie, Akita, & Takei, 2017) or food industry (Fuertes et al., 2016). These sensors are able to detect the activity of hydrogen ions into an aqueous solution. The most common topology consists of two electrodes (reference and pH electrode) connected to a voltammeter. The potential difference between them is used to derive the pH value (Bandodkar & Wang, 2014). Screen printing is again the most frequently used technique for the fabrication of pH sensors on flexible substrates (Trojanowicz, 2016). Nevertheless, there are some recent studies of inkjet-printed pH sensors (Jović et al., 2017).

Regarding gas and vapours sensors, different transducing principles can be exploited (Briand, Oprea, Courbat, & Bârsan, 2011). Among them, we can highlight the resistive principle, based on metal-oxide and polymeric gas sensitive films (Schiattarella et al., 2018); the capacitive principle, in which there is a change in the dielectric constants of the sensing film; the colorimetric or optical principle, where the optical absorption spectrum is modified by the gaseous analyte; and the resonating principle, involving the modification of the resonant frequency of a resonator due to an addition of mass.

Most of the gas sensors developed on flexible substrates are made on PET, PEN, PI, paper or fabrics using conventional and hybrid printing processes (Rivadeneyra et al., 2016; E. Singh, Meyyappan, & Nalwa, 2017). A large part of the work found in the literature reports flexible humidity sensors (Gaspar, Olkkonen, Passoja, & Smolander, 2017; Mattana et al., 2013; Molina-Lopez, Briand, & de Rooij, 2012; Rivadeneyra, Fernández-Salmerón, Banqueri, et al., 2014; M.-Z. Yang, Dai, & Lu, 2010), sometimes in combination with a temperature sensor (Atamana et al., 2011; Molina-Lopez et al., 2013; Segev-Bar et al., 2017). The most common used sensor architectures are capacitive and resistive transducers, as shown in Figure 10.

Regarding humidity sensors, the transduction mechanism requires the use of chemicals whose electrical permittivity changes accordingly to the relative humidity of the environment. Different strategies have been followed to achieve this sensing capability, such as the deposition of a sensing layer over the electrodes capacitor

(Starke, Turke, Krause, & Fischer, 2011) or the use of a humidity-sensitive substrate as the sensing element (Fernandez-Salmeron, Rivadeneyra, Rodriguez, Capitan-Vallvey, & Palma, 2015; Gaspar et al., 2017). For instance, in (Güder et al., 2016) the authors describe a paper-based moisture sensor that uses the hygroscopic character of paper to measure patterns and rate of respiration. As for the physical structure, the most common one is the interdigitated electrodes (IDE) design, although others have been proposed such as serpentine electrode (SRE) design showing higher sensitivity (Rivadeneyra, Fernández-Salmerón, Banqueri, et al., 2014).
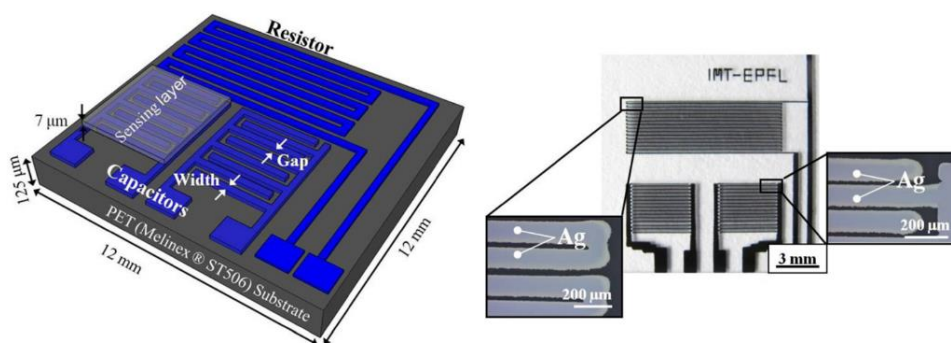
Figure 10. Sketch and picture of two inkjet-printed capacitors for humidity sensing and a resistor for temperature sensing on PET substrate (Molina-Lopez et al., 2013).

Works have been also published on volatile organic compounds ammonia and hydrogen sulfide sensors, using printing technologies to deposit gas-sensitive conducting polymers over the printed electrodes (Danesh et al., 2014; L. Kumar, Rawal, Kaur, & Annapoorni, 2017; Mousavi, Kang, Park, & Park, 2016; E. Singh et al., 2017; Weng, Shepherd, Crowley, Killard, & Wallace, 2010) for healthcare applications (Hibbard et al., 2013) or food industry applications such as rapid spoilage detection and freshness monitoring in foods (S. Li et al., 2017; Matindoust et al., 2017). Other gases that have been detected in the literature using chemical printed sensors are oxygen (Moya et al., 2016), carbon dioxide (B. Andò et al., 2015) or carbon monoxide and nitrogen dioxide. The latter ones are related to atmospheric pollution (Rieu et al., 2016).

Another interesting approach is the optical detection of gases on flexible substrates. In this case, the operating principle consists of the interaction between electromagnetic radiation through the chemical sample, which causes some change in optical parameters that can be related to the magnitude of interest (Janata, 2009; Qazi, Mohammad, & Akram, 2012). A typical optical chemical sensor is composed of a chemical recognition phase, which is called sensing element or receptor, coupled with a transduction element as shown in Figure 11.
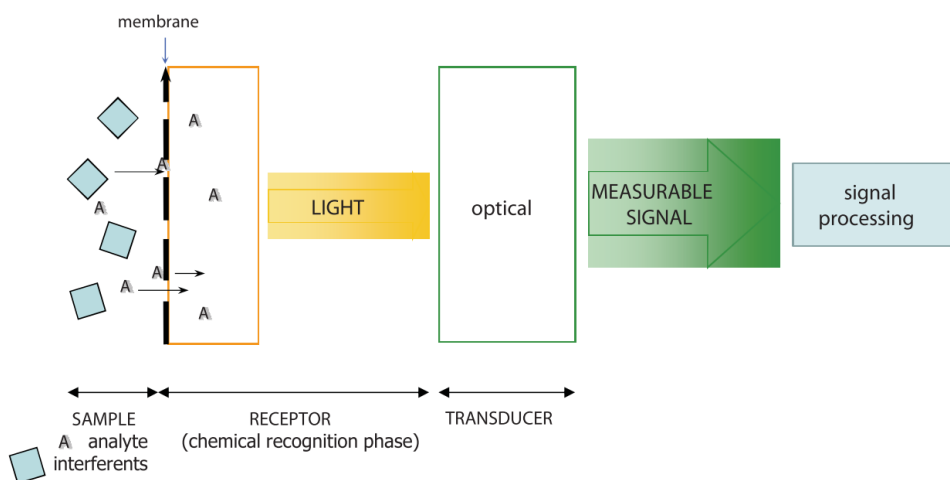
Figure 11. Schematic representation of the elements and operating principle of an optical chemical sensor (Lobnik, Turel, & Urek, 2012).

The sensing element provides an optical signal that is proportional to the concentration of a given compound, and the transducer translates this optical signal into a measurable signal suitable for its processing (Lobnik et al., 2012). This kind of chemical sensors presents some advantages such as facility of use, low cost, no need of physical contact between the sensor and the system used for analysis, immunity to electrical interferences, good sensitivity and reversibility, and no consumption of the analyte during the measurement (F. Baldini J. Homola, S. Martellucci, 2006; Xu dong Wang et al., 2010). Besides these numerous advantages, optical chemical sensors also exhibit some disadvantages. The main ones are the possible interference of the ambient light in the measurement and the long-term stability of the sensor, which can be limited due to the photobleaching effect (Goicoechea, Zamarreño, Matias, & Arregui, 2007).

Optical chemical sensors can cover different regions in the spectrum (UV, visible, IR, NIR) based on several optical principles such as absorbance, reflectance, refraction, luminescence or fluorescence (Hulanicki, Glab, & Ingman, 1991). The most popular methods in optical sensing are those based on light absorption and light emission. Absorption mechanisms, both transmission or reflection, take place when transmitted light with reduced intensity exists after the incident light passes through a sample. Nevertheless, most of absorbance-based sensors undergo a colour change instead of an intensity change (F. Baldini J. Homola, S. Martellucci, 2006). Therefore, this type of sensors is commonly used as colorimetric sensors where the change of colour can be measured and related to the magnitude of interest (Zhiqiang Wei et al., 2017). These colorimetric sensors have been used in smart packaging applications

such as fish spoilage monitoring (Domínguez-Aragón, Olmedo-Martínez, & Zaragoza-Contreras, 2018; Kuswandi et al., 2012; Morsy et al., 2016), milk spoilage determination (Cavallo, Strumia, & Gomez, 2014), meat spoilage monitoring (Y. Chen et al., 2017; Huang et al., 2014; Salinas et al., 2014) or fruit freshness determination (Kuswandi, Maryska, Jayus, Abdullah, & Heng, 2013). Another example for intelligent food packaging appears in (Vu & Won, 2013), where a water-resistant UV-activated O_2 colorimetric indicator is reported. Very recently, a colorimetric CO_2 indicator for cold preserved food has been presented in (Saliu & Della Pergola, 2018).

Molecular emission (fluorescence, phosphorescence, and generally speaking, luminescence) is intrinsically more sensitive than absorption-based methods. In luminescent sensors, a change in the emission properties of a luminophore determines the analyte concentration. The luminescence generated can be determined by measuring its intensity or the luminescence lifetime (Quaranta, Borisov, & Klimant, 2012). Luminescence measurement by means of intensity is simpler and low cost, but it strongly depends on the stability of the light source, the detector sensitivity, and the luminophore stability (Pérez de Vargas-Sansalvador et al., 2009). In recent years, the intensity of the luminescence is being determined using a colorimetric approach (Evans, Douglas, Williams, & Rochester, 2006). This strategy, namely luminescence-based colorimetric sensing, combines the advantages of both luminescence and absorption-based methods (López-Ruiz, López-Torres, Carvajal, De Vargas-Sansalvador, & Martínez-Olmos, 2015; Xu dong Wang et al., 2010). A recent review of luminescent probes as sensors of food quality can be found in (G. Corradini et al., 2016), while a critical review in chemical luminescence-based biosensors is presented in (Roda, Mirasoli, et al., 2016).

Chemical sensing based on optical color changes is gaining increasing interest because of its simplicity of use and its compatibility with portable imaging devices. An extended review of the recent developments related to optical sensors and computer vision-based analytical instruments can be found in (Capitán-Vallvey, López-Ruiz, Martínez-Olmos, Erenas, & Palma, 2015). In two of the publications that sustain this thesis, chemical printed sensors with optical response are used for smart packaging of food and MAP applications (Escobedo et al., 2017; Escobedo, de Vargas-Sansalvador, et al., 2016).

2.2 RFID technology

RFID stands for radio frequency identification, that is, information carried by radio waves. RFID enables product identification and information gathering from distance, without requiring physical connection or line of sight unlike earlier bar-code technology.
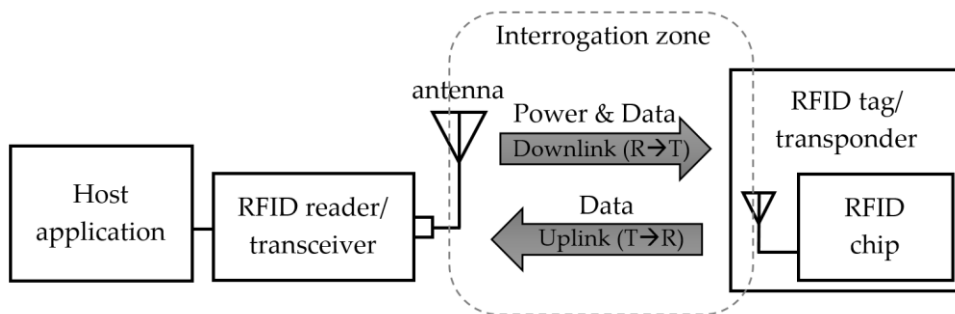
Figure 12. Overview of a generic RFID system.

As shown in Figure 12, a typical RFID system is comprised of three main components: the RFID tag, or transponder, which is located on the object to be identified; the RFID reader, or transceiver, which may be able to both read data from and write data to a transponder; and the data processing subsystem or host, which utilizes the obtained information from the transceiver in some useful manner (Finkenzeller, 2010). The RFID reader can read tags only within the reader's interrogation zone. The RFID tag consists of two main parts: an antenna and a semiconductor integrated chip (IC) attached to it. The RFID antenna is used for electromagnetic wave capture and emission. The antenna must have its impedance matched to the one of the chip in order to achieve maximum energy transmission (Marrocco, 2008). A data-carrying connection link exists between the reader and the tag. It is common to distinguish between the communications channel carrying information from the reader to the tag (the downlink or forward link) and that carrying information from the tag to the reader (the uplink or reverse link).

The chip is an integrated circuit fabricated in silicon. It contains the so-called Electronic Product Code (EPC), which is unique to each tag. In its simplest form, the RFID chip consists of an RF front end, some additional basic signal processing circuits, logic circuitry to implement the algorithms required and Electrically Erasable Programmable Read-Only Memory (EEPROM) for storage. However, there are some RFID chips that include extra functions that are required to add sensing capabilities to RFID tags:

- An interface such as Serial Port Interface (SPI) or Inter-Integrated Circuit (I^2C) in order to enable communication between the RFID chip and other devices, usually microcontrollers and external sensors (Leikanger, Häkkinen, & Schuss, 2017).

- Additional circuitry for signal conditioning to interface external sensors, user memory for saving supplementary information such as sensor data or even integrated on-chip sensors.

- Energy harvesting capabilities to enable the power of external chips and sensors, allowing the development of battery-less designs.

There are not many RFID chips that include these extra functions. Some examples of RFID chips with SPI or I^2C ports are the D18BL01 by Delta (Delta Corporate, Hørsholm, Denmark) or the AS3955 by AMS (AMS AG, Unterpremstaetten, Austria). The latter one also includes a user memory and advanced energy harvesting feature. The EM4325 by EM Microelectronics (EM Microelectronic-Marin SA, Neuchâtel, Switzerland) and the WM72016 by Ramtron Corporate (Ramtron International Corporation, Colorado, USA) include also a built-in temperature sensor. Besides these capabilities, other chips such as SL13A and SL900A by AMS or MLX90129 by Melexis (Melexis Co., Belgium) integrate a sensor front end (SFE) to interface different types of external sensors.

At the highest level, RFID tags can be divided into three classes: active, passive and semi-passive.

- Active tags require a power source. They are usually embedded with a battery for powering the chip and transmitting radio waves to the reader. These tags have wider reading range and faster transmission rate than passive tags, but their cost and size is also higher.

- Passive tags rely on the wave transmitted by the reader for powering the chip, avoiding the necessity of onboard power sources. By means of backscattering mechanism, an electromagnetic wave is sent back to the reader. Compared to active tags, passive tags have several advantages including low cost, long operational life, lightness and small size.

- Semi-passive tags include a battery to provide supply only to the chip. These tags still rely on the reader for electromagnetic wave emission, so the battery remains most of the time inactive and the life span of the tags is increased.

According to their operating frequencies (Figure 13), RFID systems present different characteristics, which are summarized in Table 2 (Bibi, Guillaume, Gontard, & Sorli, 2017).
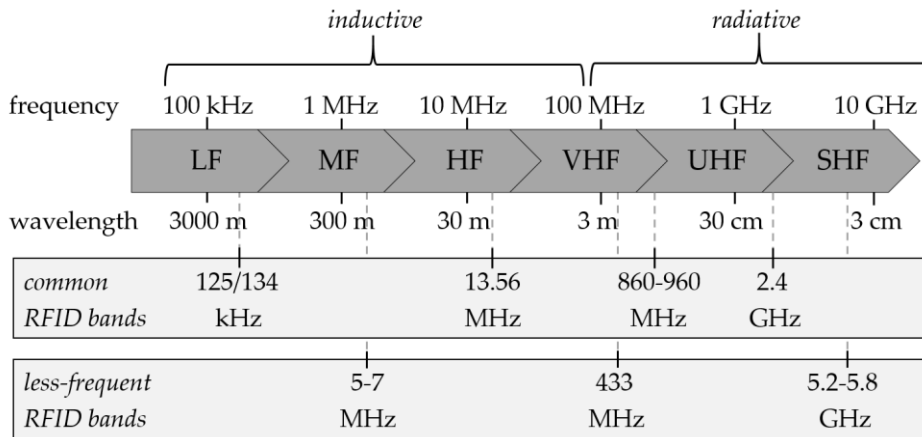
Figure 13. RFID frequency bands.

Low frequency (LF) band is defined between 125 kHz and 134 kHz and its main advantage is having little interferences with liquids and metals. The popular frequency of 13.56 MHz corresponds to high frequency (HF) band. HF tags have a greater reading range and improved data transfer than in the LF domain. Ultra high frequency (UHF) band falls between 860 MHz and 960 MHz, with a greater read range and higher reading speed of tags than in the previous bands. However, RFID tags at this band are impaired by water and metals.

Table 2. Communication frequency bands of RFID tags and their characteristics (Bibi et al., 2017).

Band	Frequency	Coupling type	Communication speed	Free-space reading range
LF	125–134 kHz	Inductive (near field)	Few kb/s	20 cm–100 cm
HF	13.56 MHz	Inductive (near field)	~100 kb/s	0.1 m–1.5 m
UHF	860–960 MHz	Radiative (far field)	Few hundreds of kb/s	3 m –15 m
SHF	2.4 and 5.8 GHz	Radiative (far field)	Few hundreds of kb/s	3 m –30 m

Finally, super high frequency (SHF) band falls within microwave frequency range. The highest data transfer rates are achieved at this frequencies, but the electromagnetic waves are not able to penetrate water and metal and SHF RFID tags have the disadvantage of high cost.

There is a huge range in wavelength corresponding to the range in frequency. The wavelength λ is the distance between successive peaks or troughs of the wave, and so is the ratio of the speed of propagation c to the frequency f:

$$\lambda = \frac{c}{f} \qquad\qquad (2.1)$$

As shown in Figure 13, the wavelengths in most common RFID bands range from about 2000 m to about 12 cm. However, the antenna sizes used in RFID are always about human sized, with the largest ones around 1 m in diameter and the smallest about 1 to 4 cm. In consequence, RFID systems can be also categorized by whether the sizes of the wavelength and antenna are comparable or not.

2.2.1 High Frequency band RFID tags

As Table 2 shows, there are two different fundamental types of interactive modes between the reader and the tag: inductive coupling, where energy is transferred through a magnetic field; and radiative coupling, where energy transfer is performed by an electromagnetic wave.

Systems where the wavelength is much larger than the antenna usually use inductive coupling to communicate between the tag and the reader. This is the case of high frequency (HF) RFID tags, where almost all the available energy from the reader is contained within a region near the reader antenna and comparable to in in size, falling away as the cube of distance as we move away (Dobkin, 2012). Faraday's principle of magnetic induction is the basis of this near-field coupling between a reader and a tag. A reader passes a large alternating current through a coil, resulting in an alternating magnetic field in its neighbouring area (Figure 14). If a tag with a smaller coil is placed in this field, an alternating voltage appears across it. This voltage can be rectified and coupled to a capacitor in order to reserve some charge, which can be used to power the RFID tag chip.
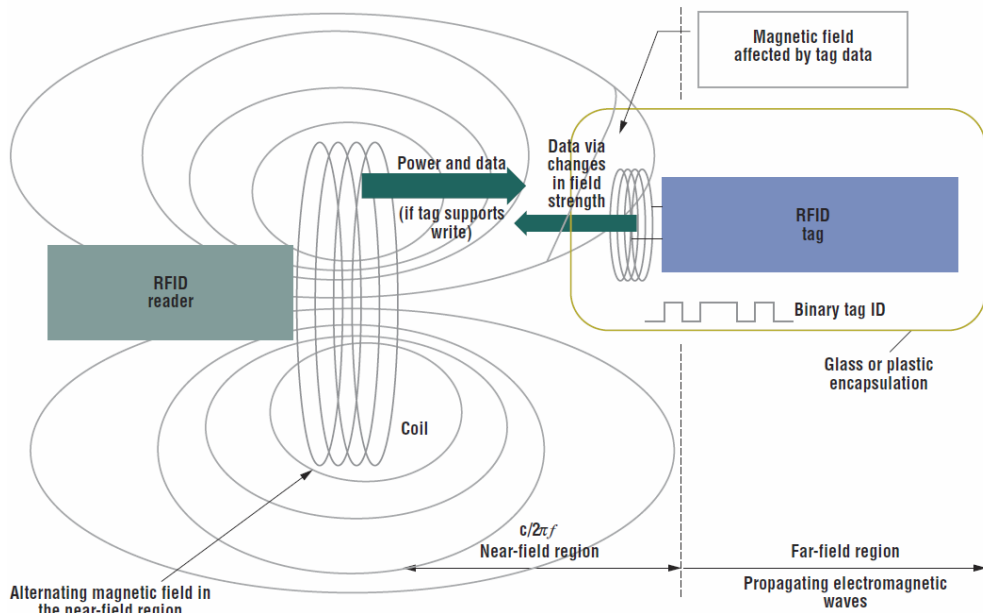
Figure 14. Inductive coupling mechanism for RFID tags operating at less than 100 MHz (Want, 2006). Induction is used for power coupling from reader to tag and load modulation is used to transfer data from tag to reader.

Data is sent back from the tag to the reader using load modulation. Since any current drawn from the tag coil will give rise to its own small magnetic field opposed to the reader's field, the reader coil can detect this as a small increase in current flowing through it. This current will be proportional to the load applied to the tag's coil, hence the name load modulation. If the tag's electronics applies a load to its antenna coil and varies it over time, a signal can be encoded as tiny variations in the magnetic field strength, thus representing the tag's ID. Then, the reader can recover this signal by monitoring changes in the current through its coil antenna.

Near-field coupling is a commonly used approach for implementing passive RFID systems. This has resulted in many standards such as ISO 15693 and 14443, apart from a variety of proprietary solutions. Nevertheless, near-field communication has some limitations. Firstly, the range in which magnetic coupling can be used approximates to $c/(2\pi f)$, so the distance over which near-field communication operates decreases as the operating frequency increases. Another limitation is the amount of energy available in the tag as a function of distance from the reader, as the magnetic field drops off as the cube of distance.

NFC technology

Near-Field Communication (NFC) technology was jointly developed by Philips and Sony in late 2002 for short-range contactless communications in the frequency range of 13.56 MHz (HF band). The protocol, which set out to integrate active signaling between mobile devices utilizing near-field inductive coupling, uses an approach that is compatible with existing RFID standards. The NFC standard provides a mechanism to allow wireless mobile devices communicate with peer devices within few centimeters (up to 10 cm) at 13.56 MHz operating frequency (Coskun, Ozdenizci, & Ok, 2013). The two acting parts of NFC communication are the initiator and the target devices. The first one initiates and guides the data exchange process between both parties, while the NFC target is the device that responds to the requests made by the initiator. NFC protocol distinguishes two operational modes: active and passive.
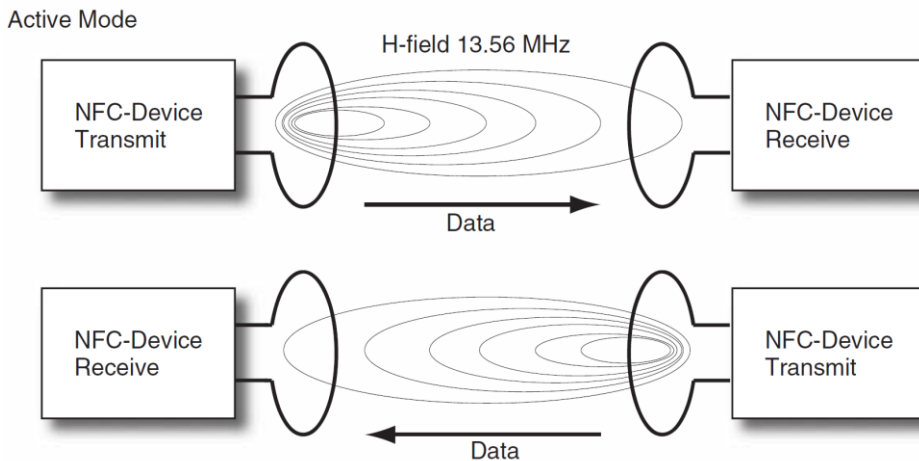
Figure 15. Schematic representation of NFC active operating mode (Finkenzeller, 2010).

In the active mode both devices uses their energy to generate their own RF field in order to alternately transmit the data (Figure 15). The high-frequency current that flows in the antenna of the NFC initiator induces an alternating magnetic field which spreads around the antenna loop. Part of that induced magnetic field moves through the antenna loop of the other NFC device, which is located nearby. Then a voltage is induced in the antenna loop and can be detected by the receiver of the other NFC interface, which acts as the NFC target. The transmission direction is then reversed so as to send data from the NFC target to the NFC initiator, changing the roles. Both NFC interfaces alternately induce magnetic fields where data is only transmitted

from transmitter to receiver. For data transmission between both NFC devices, the amplitude of the emitted magnetic alternating field is modulated by means of Amplitude-shift keying (ASK) modulation.

(a)

(b)
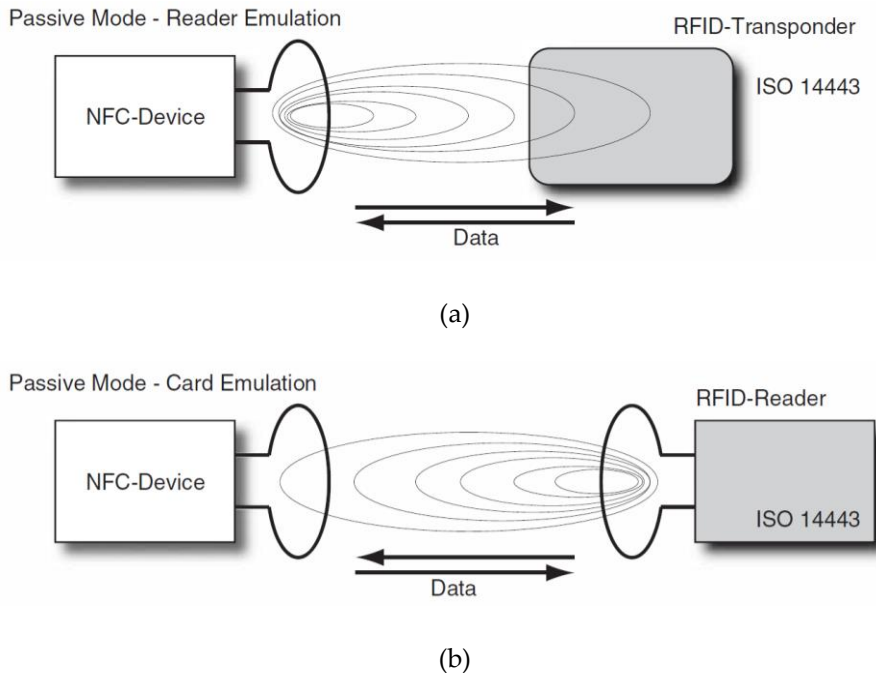
Figure 16. Schematic representation of NFC passive operating modes in (a) reader emulation mode and (b) card emulation mode (Finkenzeller, 2010).

In the passive communication mode only the NFC initiator generates the magnetic alternating field for transmitting data, while the NFC target device makes use of that energy. The field's amplitude is modulated with the pulse of the data to be transmitted (ASK modulation). However, the field is not interrupted after having transmitted the data. It continues in an unmodulated way so that the NFC target is able to transmit data to the NFC initiator by means of load modulation, a well-known method from RFID systems.

The NFC interface that is the target is also able to establish communication with compatible passive transponders that the NFC target supplies and, via load modulation, can transmit data to the NFC interface. This option allows electronic devices that are equipped with NFC interfaces, such as NFC-enabled mobile phones, to read and write on different transponders such as smart labels or tags. Since the

NFC interface behaves in this case similar to an RFID reader, this mode is called reader emulation mode (Figure 16a). On the other hand, if an NFC interface is located close to a compatible RFID reader, both devices are also able to communicate. In this case, the NFC interface adopts the roll of an NFC target. This option enables RFID readers to exchange data with electronic devices equipped with NFC interface, such as NFC-enabled mobile phones. From the reader's perspective, the electronic device (for instance, the mobile phone) acts as a contactless smart card, hence the name card emulation mode (Figure 16b).

NFC tags

Antennas for contactless near-field systems in the 13.56 MHz frequency band are resonant loop antennas. To design passive devices, the NFC tags must extract their power from the magnetic field generated by the reader. The tag and reader antennas are inductances mutually coupled by the magnetic field. The efficient transfer of energy from the reader to the tag depends on how well the loop antenna is tuned to the 13.56 MHz carrier frequency. Therefore, a well-designed NFC tag antenna is crucial for optimal performance.

A loop antenna is a distributed component with inductance L_{ant} as main element, and capacitance C_{ant} and resistance R_{ant} as parasitic network elements. Like for all antennas, the complex impedance varies over frequency. For practical calculations, the equivalent electrical circuit of an NFC tag chip and its antenna is composed of lumped elements, as shown in Figure 17. The NFC chip is represented by a resistor R_{chip} symbolizing its current consumption, in parallel with a capacitor C_{tun} representing the NFC chip internal tuning capacitance.
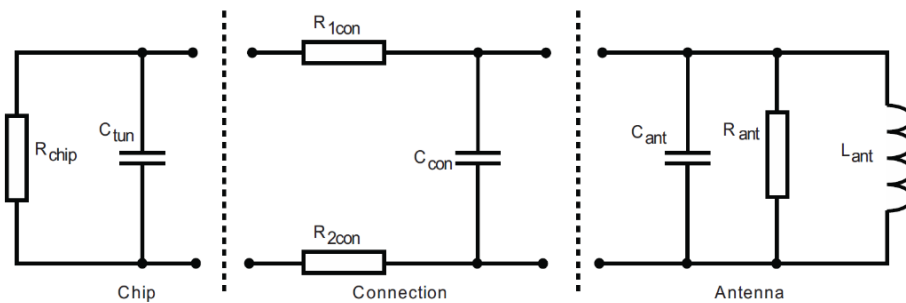
Figure 17. Equivalent circuit model of a NFC tag chip and its antenna (ST Electronics, 2009). Lumped elements represent the NFC chip, the assembly connection of chip and antenna, and the loop antenna (note that C_{ant}, R_{ant} and L_{ant} are frequency dependent).

The model in Figure 17 takes also into account parasitic elements derived from the connections between the chip and the antenna during the assembly phase: R_{1con} and R_{2con} are the equivalent parasitic resistances while C_{con} represents the equivalent parasitic capacitance due to the assembly. As for the loop antenna, its complex impedance can be represented as a simple parallel resonant circuit. The inductance L_{ant} is the main parameter of the antenna loop coil. It consists of mutual inductance due to coupling between the coil turns and self-inductance due to coil length. There is an additional parasitic capacitance C_{ant} because of the electric coupling between the turns and dependent on the relative dielectric constant of the substrate. R_{ant} is the real part of the impedance.

If we represent the reactive part of the impedance over frequency (Figure 18), at low frequencies we can see an inductive behaviour. As frequency increases, there comes a point where the coil inductance becomes zero, which is defined as the self-resonance frequency f_{SRF} of the antenna. From that frequency onwards, the reactive part of the impedance adopts a capacitive behaviour. At self-resonance frequency, the imaginary part of the antenna impedance is null and the antenna is purely resistive. According to Thomson equation (Maxwell, 1892), it can be calculated as:

$$f_{SRF} = \frac{1}{2\pi\sqrt{L_{ant}C_{ant}}}$$

(2.2)
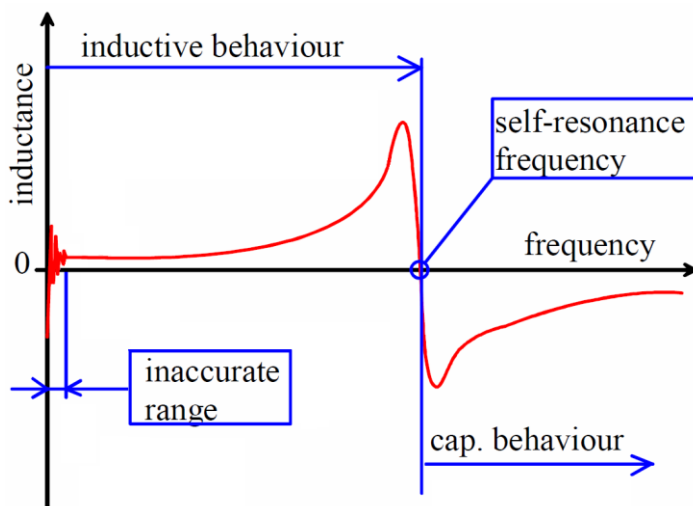
Figure 18. Typical measurement trace of coil inductance over frequency (Gebhart, Neubauer, Stark, & Warnez, 2011).

The antenna resistance can be directly measured at the system carrier frequency of interest, $f_c = 13.56\ MHz$, or it can be measured at the higher antenna self-resonance frequency and then be computed back to the carrier frequency f_c. If AC losses are only caused by the skin effect, like in the case of free air coils, this method is more accurate. The antenna resistance at the frequency of interest can be calculated from Equation 2.3 (Gebhart et al., 2011).

$$R_{ant}(f_c) = \sqrt{\frac{f_{SRF}}{f_c}} R_{ant}(f_{SRF}) \qquad (2.3)$$

From the equivalent inductance and resistance at 13.56 MHz, the quality factor Q of the coil can be calculated from Equation 2.4.

$$Q_{ant}(f_c) = \frac{R_{ant}(f_c)}{2\pi f_c L_{ant}} \qquad (2.4)$$

For practical purposes, the equivalent circuit model in Figure 17 can be further simplified as depicted in Figure 19. In this case, the equivalent resistance R_{eq} is calculated as the parallel association of the chip and antenna resistances:

$$R_{eq} = R_{chip}||R_{ant} = \frac{R_{chip} \times R_{ant}}{R_{chip} + R_{ant}} \qquad (2.5)$$
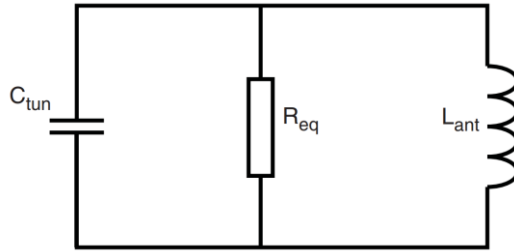
Figure 19. Simplified equivalent circuit model if an NFC tag including the chip, its antenna and connections (ST Electronics, 2009).

In a parallel LC circuit like the one depicted in Figure 19, resonance takes place when the two reactances are equal, so the resonant frequency f_0 can be calculated as:

$$X_{L_{ant}} = X_{C_{tun}} \Rightarrow f_0 = \frac{1}{2\pi\sqrt{L_{ant}C_{tun}}} \qquad (2.6)$$

Therefore, to achieve inductive coupling between an NFC reader and a tag, the coil of the tag must be designed so that its inductance value at the carrier frequency resonance ($f_0 = f_c = 13.56\ MHz$) is:

$$L_{ant} = \frac{1}{(2\pi f_0)^2 C_{tun}}$$

(2.7)

The quality factor Q of the simplified circuit in Figure 19 is defined as 2π times the ratio between the cycle mean stored energy and the cycle mean lost energy (Rhodes, 1976). Since the energy stored in the capacitor is equal to the one stored in the inductor at resonant frequency, Q is calculated as follows:

$$Q = \frac{R_{eq}}{2\pi f_0 L_{ant}}$$

(2.8)

The performance of an antenna is related with its quality factor. In general, a higher Q means a higher power output for a particular sized antenna. However, if Q value is too high, it might conflict with the band-pass characteristics of the reader and create problems in the protocol bit timing (Texas Instruments, 2003).

2.2.2 Ultra High Frequency band RFID tags

Systems where the antenna and the wavelength are comparable in size are typically radiatively coupled. RFID tags based on far-field couplings capture electromagnetic waves propagating from the reader's antenna (Figure 20).

An alternating potential difference appears across the arms of the tag antenna. A diode can rectify this potential and charge a capacitor in order to power the tag's electronics. Unlike the inductive coupling, the tags are beyond the near-field range, so information cannot be transmitted back to the reader by means of load modulation. Instead, backscattering mechanism is used. In this approach, when the signal from reader reaches the RFID tag, some of the energy is reflected back towards the reader, which can detect the energy using a sensitive radio receiver. By changing its antenna's impedance over time, the RFID tag can control how much power of the incoming signal reflects back, in a pattern that encodes the desired information. In practice, a tag's antenna can be detuned by placing a transistor that can switch an antenna load resistor in and out of circuit. As for the range of a far-field RFID system, it is limited by the amount of energy that reaches the tag and by the reader's sensitivity to the reflected signal. In absence of obstacles, the intensity of the electromagnetic wave launched by the reader falls off as the square of the distance travelled. EPCglobal was key to promote the design of UHF tags and define their

protocol specification EPC Class 1 Generation 2 for UHF RFID tags (EPCglobal Inc., 2013).
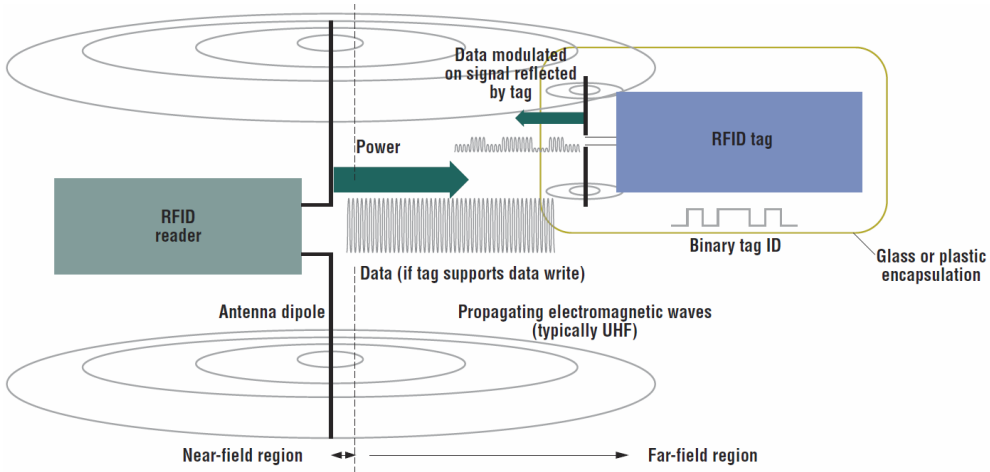
Figure 20. Radiative coupling mechanism for RFID tags operating at greater than 100 MHz (Want, 2006). Electromagnetic wave capture is used to transfer power from reader to tag and backscattering to transfer data from tag to reader.

Most of antennas for UHF RFID tags are commonly modified dipoles manufactured on planar structures. The backscattering modulation allows the communication between the reader and the tag when the microchip matches or mismatches its internal load to the antenna. One of the most important tag performance characteristic is the maximum distance at which the reader can detect the backscattered signal from the tag, denoted as read range. Read range r is sensitive to the tag response threshold, tag orientation, material where it is placed and propagation environment. It can be calculated using Friis free-space formula (Rao, Nikitin, & Lam, 2005):

$$r = \frac{\lambda}{4\pi} \sqrt{\frac{G_t\, G_r\, P_r\, \tau\, PLF}{S_t}} \qquad (2.9)$$

where λ is the wavelength, G_t is the tag antenna gain, G_r is the reader antenna gain, P_r is the effective power transmitted by the reader, PLF is the polarization loss factor, and S_t is the RFID chip sensitivity, that is, the minimum threshold power necessary to provide enough power to the chip. The factor τ is the power transmission coefficient:

$$\tau = \frac{4R_cR_a}{|Z_c + Z_a|^2} \leq 1 \qquad (2.10)$$

This factor accounts for the impedance mismatch between the RFID chip ($Z_c = R_c + jX_c$) and the antenna ($Z_a = R_a + jX_a$). To maximize power transfer and hence tag performance, the RFID tag antenna must be matched to the chip complex impedance (Nikitin et al., 2005). Typically, the power transmission coefficient τ is dominant in frequency dependence and predominantly determines the tag resonance, as depicted in Figure 21.
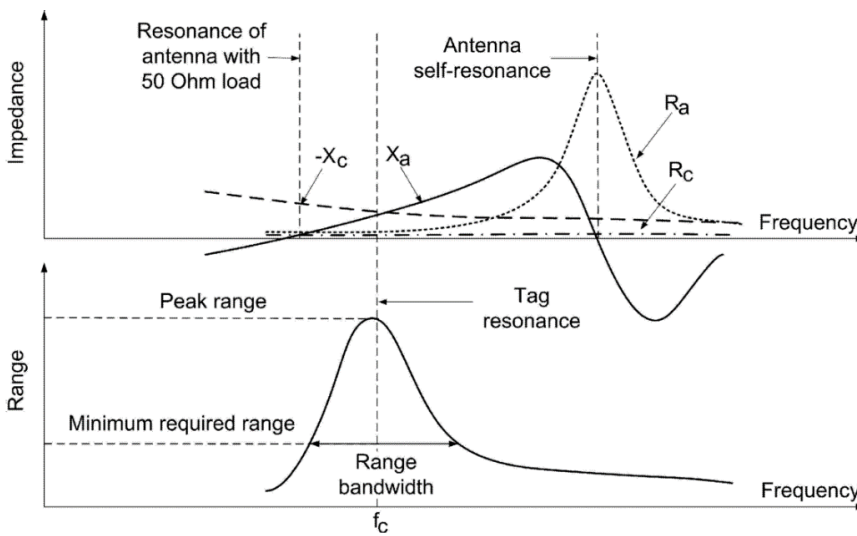
Figure 21. Chip impedance, antenna impedance and read range as functions of frequency in a typical RFID system (Rao et al., 2005).

The power reflection coefficient (Kurokawa, 1965) matching complex antenna to the complex chip impedance is given by:

$$\Gamma = \frac{Z_c - Z_a^*}{Z_c + Z_a} \qquad (2.11)$$

The impedance of the chip Z_c, which is a function of both the frequency and the received input power, has a strongly capacitive input reactance because of the energy-storage stage that includes. Therefore, the antenna impedance must be designed with a large inductive part on its input impedance to achieve the complex conjugate matching (Marrocco, 2008). To maximize the tag read range, the antenna should be conjugate matched to the minimum operational power chip impedance (Loo et al., 2008).

2.3 Flexible sensor platforms

The compatibility of printed electronics and sensors with flexible substrates enables the development of sensor systems in attractive form factors than can be deployed, for instance, into pharmaceutical or intelligent food packaging applications (Biji, Ravishankar, Mohan, & Srinivasa Gopal, 2015; Vanderroost et al., 2014; Zadbuke, Shahi, Gulecha, Padalkar, & Thube, 2013). In addition, the integration of these flexible systems with energy harvesting platforms allows the implementation of passive sensor systems that do not require batteries. Among the different harvesting methods that have been proposed over the years (Shaikh & Zeadally, 2016), the most successful and popular ones are the use of photovoltaic (PV) panels and the use of passive RFID/NFC tags (Ferdous, Reza, & Siddiqui, 2016; Kassal, Steinberg, & Steinberg, 2018).

If average power consumption is low, energy harvesting by means of photovoltaic panels along with some type of energy storage can be an interesting solution (Molina-Farrugia et al., 2017). This is the case of low-power microcontroller-based systems that are only activated to measure a data point or transmit a packet of data, while they spend most of their time in sleep-mode states. To date, there are not many examples of flexible sensor systems powered by PV cells. In (Ostfeld, Gaikwad, Khan, & Arias, 2016), a flexible wearable pulse oximeter for heart rate and blood oxygenation monitoring is reported. The device is powered by a flexible power source integrating a lithium ion battery and amorphous silicon solar module. In (Escobedo, de Vargas-Sansalvador, et al., 2016) we present a passive screen-printed flexible tag for gases determination based on optical chemical sensors that is powered by means of two miniaturized solar cells.

The integration of sensing to RFID tags brings added value to this contactless and non-line-of-sight identification and data transmission technology (Bibi et al., 2017; Catarinucci, Colella, & Tarricone, 2009). There are two main approaches for the addition of sensing capabilities to RFID tags. On the one hand, sensing can be done by studying the variation of materials of RFID tags as a transmission medium of the radio waves, thus considering RFID tags as electromagnetic sensors (Amin, Karmakar, & Jensen, 2016; Y. Xu, Dong, Wang, Jing, & Lu, 2017). On the other hand, an RFID tag can be integrated with additional circuitry and components such as external sensors, microcontroller unit (MCU) and analog to digital converter (ADC) to develop a sensor module (S. Zhang, Li, Cheng, Ma, & Chang, 2015). In this case, the RFID tag is used as a communication interface to transmit sensor data to an end user, while the sensing functions are managed by the external sensors integrated in the tag. Additionally, the RFID tag shall be used as an energy harvesting medium to power the external components and, if applicable, sensors (Meng & Li, 2016).

If the RFID tag is used as an electromagnetic sensor, different changes in the analog response of the tag have been associated to a variation of the sensed magnitude. This approach has been used to develop environment monitoring systems such as humidity sensors in flexible HF tags by exploiting the RFID tag resonance frequency shift measurement. Polyimide, a material sensitive to moisture (see Section 2.1.1), is used as the substrate of a printed inductor coil and an interdigitated capacitor (using screen and inkjet printing techniques) to form an LC resonator for moisture detection (Fernandez-Salmeron et al., 2015). The same operating principle is used in (Virtanen, Ukkonen, Bjorninen, Elsherbeni, & Sydänheimo, 2011) for UHF tags. In (Potyrailo & Surman, 2013), a passive RFID gas sensor with a resonant antenna coated with a gas-sensing film and an IC memory chip is presented (see Figure 22).
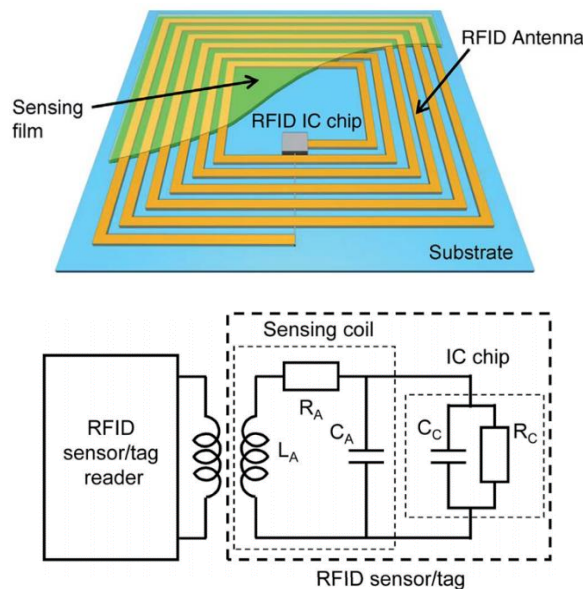
Figure 22. Schematic illustration and equivalent circuit of an RFID tag sensor where the resonant HF antenna is coated with a chemically sensitive film (Potyrailo & Surman, 2013).

In (Feng, Xie, Chen, & Zheng, 2015) a chipless RFID tag consisting of two inkjet-printed planar LC resonators is used for humidity detection utilizing paper substrate as sensing material. Another example to measure threshold humidity in a UHF tag by changing the antenna input impedance was proposed in (J. Gao, Siden, Nilsson, & Gulliksson, 2013). The result is reflected in the change of the minimum transmit power required to power up the tag. Very recently, a flexible RFID tag for humidity and temperature sensing has been proposed (Anum Satti et al., 2018). In this chipless tag, the variations of the monitored magnitudes are associated to changes in the

measured level of the backscattered power. Kim et al. proposed a flexible and stretchable LC resonator-based chipless RFID printed tag for structural strain sensing (J. Kim, Wang, & Kim, 2014). Many other examples of flexible RFID tags as electromagnetic sensors can be found in literature for moisture sensing (Javed et al., 2016; Powell et al., 2016), strain and crack sensing (J. Zhang, Tian, Marindra, Sunny, & Zhao, 2017), gases and vapours (Kutty, Björninen, Syd, & Ukkonen, 2016; Potyrailo, Burns, Surman, Lee, & McGinniss, 2012), chemical sensing for ammonia (Jun et al., 2016) and other magnitudes for food quality and safety including freshness of fruit, fish, milk and bacterial growth (Potyrailo, Nagraj, et al., 2012) among others (Fiddes, Chang, & Yan, 2014; Tanguy, Fiddes, & Yan, 2015).
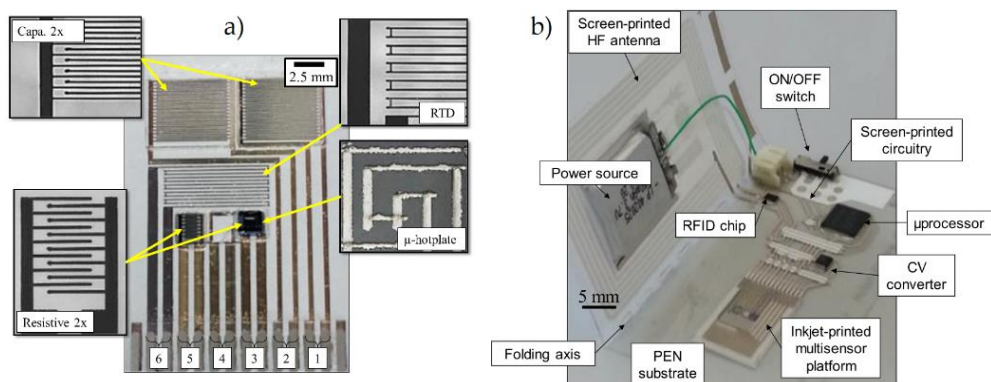
Figure 23. Pictures of (a) the inkjet-printed multisensor platform and (b) the final assembly with the integrated screen-printed HF RFID tag (Quintero et al., 2016).

In the case of flexible RFID sensor tags with external circuitry and sensors, many interesting examples have been proposed for a great variety of application fields (Meng & Li, 2016; Pichorim, Gomes, & Batchelor, 2018). In the field of environment monitoring, Mraović et al. proposed a screen-printed capacitive humidity sensor integrated in a UHF tag and fabricated on recycled paper and cardboard for smart packaging applications (Mraović et al. 2014). A similar approach with polyimide substrate and inkjet printing method can be found in (Salmerón, Rivadeneyra, et al., 2014). In (Fernández-Salmerón et al., 2015), a passive screen-printed UHF tag with multiple sensing capabilities is described, including a pressure sensor and a printed opening detector for packaging monitoring during different stages of the supply chain. An inkjet-printed multisensing platform on flexible polymeric substrate is presented in (Quintero et al., 2016). The platform is integrated into a screen-printed HF RFID smart label (see Figure 23) and it has channels for capacitive vapor detection (i.e. humidity), resistive-based vapor detection (i.e. ammonia) and temperature detection (RTD).

In the field of food and quality safety, an NFC sensor system with a hydrogel-pH-electrode was developed for detecting fish spoilage (Bhadra, Narvaez, Thomson, & Bridges, 2015). As the presence of oxygen is one of the main causes for food spoilage (Rooney, 1995), a screen-printed RFID tag for the determination of oxygen concentration is reported in (Martínez-Olmos et al., 2013). In (Escobedo et al., 2017) we developed a flexible NFC tag for multigas sensing. The four analyzed gases are oxygen and carbon dioxide, which are two of the main gases used in MAP; and ammonia and humidity, which are aimed to reveal the spoilage of the food. In recent years, applications in the field health and bio-monitoring have also begun to emerge. A passive adhesive RFID sweat sensor bandage is presented in (Rose et al., 2015). In (Rakibet, Rumens, Batchelor, Member, & Holder, 2014), an epidermal passive strain sensor integrated in UHF RFID tags is reported. In (Amendola, Bovesecchi, Palombi, Coppa, & Marrocco, 2016), an epidermal RFID sensor is directly stuck over the human skin for remote temperature monitoring. A smart RFID/NFC screen-printed bandage for determination of uric acid status, a key wound biomarker, is presented in (Kassal et al., 2015). Very recently, another wireless smart bandage was presented in (Kassal et al., 2017), in this case for optical determination of pH as another indicator of wound status. In (J. Kim et al., 2016), several battery-free, wireless, epidermal, stretchable optoelectronic devices that exploit NFC technology are presented. Their applications include monitoring of heart rate and arterial blood flow; quantifying of tissue oxygenation and ultraviolet dosimetry; and optical characterization of the skin.

From the above review, we can find that flexible and printed sensor technology is becoming more and more prosperous over the years. The novel properties of flexible electronics such as low weight, mechanical flexibility and simple integration allow them to spread across a wide range of disciplines and application fields, from healthcare, personal and environmental sensing and monitoring to industrial fields such as smart packaging technologies.

2.4 Smartphones for sensing

A smartphone includes all the components required for its use as a reader for sensor systems: a screen to act as a display and a controller; different inputs to capture signals such as camera (Lopez-Ruiz et al., 2014; Masawat, Harfield, & Namwong, 2015), headphone jack (Doeven et al., 2015; Sun, Yao, A.G., & Hall, 2016) and ambient light sensors (Fu et al., 2016); memory to save and store the data; computing capability for sensor data processing; and several wireless connectivity interfaces such as Wi-Fi, Bluetooth, NFC, etc. (Azzarelli, Mirica, Ravnsbæk, & Swager, 2014; D. Zhang et al., 2015). In comparison with traditional instruments, smartphones exhibit some advantages. First, they can directly measure different parameters using their integrated sensors (del Rosario, Redmond, & Lovell, 2015). Secondly, they can

communicate with other devices by means of wireless interfaces. Finally, they can be easily operated by any non-trained user. Furthermore, anyone can develop an own custom mobile application depending on the final use of the smartphone-based sensor platform. Therefore, considering that in recent years the number of smartphones has sharply increased worldwide (eMarketer & Statista Inc., 2016), these devices are an invaluable resource for sensing. In the following paragraphs a brief review of smartphone-based sensor platforms is reported, including optical and electrochemical sensor systems as well as smartphone-based NFC sensor systems.

Smartphone-based platforms for optical sensing take advantage of the digital built-in cameras in the emerging fields of smartphone-based chemical and biosensing (McCracken & Yoon, 2016), with special interest in environmental and health monitoring. In particular, colorimetric detections have been widely reported since mobile phone cameras are able to recognize small differences in color tone that could not be gauged by the naked eye. This capability has been exploited, for instance, to verify the Beer-Lambert law, which relates the intensity of an analyte color in solution to its concentration (Kuntzleman & Jacobson, 2016; Montangero, 2015). In (García et al., 2011) a pioneer mobile phone platform for portable chemical analysis is presented. The platform is able to determine potassium concentration in water by obtaining the characteristic hue value of the captured image of a colorimetric chemical sensor. A similar approach is used in (Lopez-Ruiz et al., 2014) for measurement of nitrite concentration and pH determination in combination with a low-cost paper-based microfluidic device. In (López-Ruiz et al., 2012), a portable instrument is designed for the determination of gaseous oxygen using a mobile device and a luminescence-based O_2 sensor.
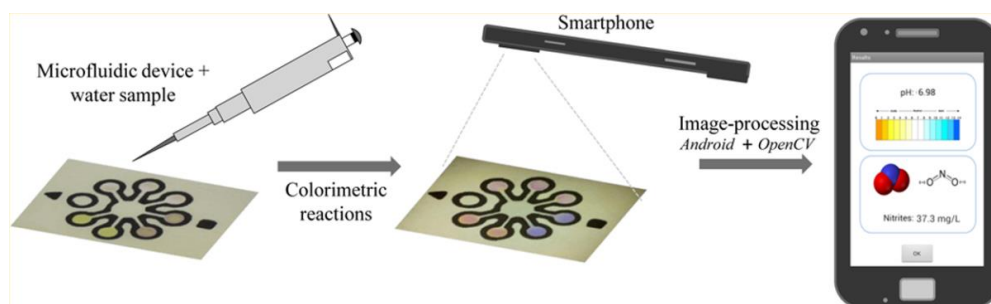
Figure 24. pH detection by using mobile phones as colorimetric readers (Lopez-Ruiz et al., 2014).

Very recently, a Smart Forensic Phone for age estimation based on colorimetric analysis of bloodstain has been reported (Shin et al., 2017). The age for the blood

sample was calculated from the plot of brightness (V) values against time. Another recent example is found in (Araki et al., 2017), where an screen-printed epidermal system combines colorimetric and electronic functions for determination of instantaneous UV exposure levels and skin temperature. The dosimeter is based on digital image capture and analysis using a smartphone activated by proximity to the NFC electronics, so the system can be seen as a combination of smartphone-based optical sensor and smartphone-based NFC sensor. A similar approach has been very recently demonstrated in (Shi et al., 2018), where the authors present a stretchable, skin-mounted UV patch with NFC that measures personal UV doses. Color changes corresponding to UV radiation are analyzed with the smartphone camera. The device described in (Koh et al., 2016) also combines NFC and colorimetric sensing to develop a soft, wearable microfluidic device for the capture, storage and sensing of sweat. There are many other examples in literature of smartphone-based optical platforms in a great variety of application fields, such as food quality controlling (A. Chen et al., 2014; Lin et al., 2018), environmental monitoring (S. A. Lee & Yang, 2014) or healthcare diagnosis (Im et al., 2015; T.-S. Lai, Chang, & Wang, 2017).

Overall, despite the significant advancements in optical smartphone sensing, the insight of these devices for colorimetric diagnostic applications still present challenges such as the interference from uncontrolled or uneven lighting. Some common countermeasures to avoid this difficulty include the use of enclosed lighting or imaging attatchments in the smartphone (Barbosa, Gehlot, Sidapra, Edwards, & Reis, 2015; S. C. Kim, Jalal, Im, Ko, & Shim, 2017; Paterson et al., 2017).

Electrochemical sensing smartphone-based platforms as rapid, portable, low-cost and sensitive detection devices are of great interest for safety monitoring, environment evaluation and clinical diagnostics (Quesada-González & Merkoçi, 2017). One of the most representative works in this field was conducted in 2014 (Nemiroski et al., 2014). In this work, a simple handheld mobile-based device that can perform almost any electrochemical analysis was reported. Different electrochemical detection techniques have been used for applications such as human blood glucose tests (Nemiroski et al., 2014), nitrate sensing in water (Xinhao Wang et al., 2015) or uric acid detection in saliva (Jayoung Kim et al., 2015). In (Deng et al., 2016), an interesting smartphone-interfaced electrochemical device is presented for on-site gender verification. Zhang and co-workers (D. Zhang et al., 2015) proposed another smartphone-based sensor system for bio-detection of 2,4,6-trinitrotoluene (TNT). A hand held paper-pased screen printed electrode for electrochemiluminescence (ECL) was reported in (L. Chen, Zhang, & Xing, 2016) for detection of glucose using a smartphone as a read-out of the ECL signal. More recently, (Ji et al., 2017) presented a smartphone-based system with graphene modified screen printed electrodes for glucose detection. Very recently, a NFC-based

system for potassium concentration measurement in capillary blood has been reported (Kollegger et al., 2018).

In general, the results obtained with the smartphone-based electrochemical sensor systems are in good agreement with those obtained from conventional instruments. Therefore, these platforms have great potential to replace the traditional analytical systems for achieving simpler, cheaper, more portable and less invasive electrochemical sensor devices (Kanchi, Sabela, Mdluli, Inamuddin, & Bisetty, 2018).
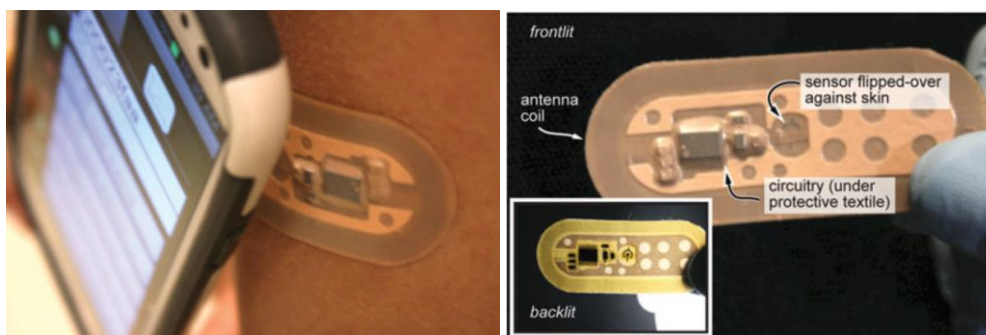
Figure 25. Passive adhesive RFID sweat sensor bandage (Rose et al., 2015).

The inclusion of NFC technology in smartphones as an intrinsic hardware component has enabled the use of these mobile devices as wireless portable readers for NFC sensor tags. The operating principle of these NFC tags was described in Section 2.2.1, and some examples have already been discussed in Section 2.3, such as a passive adhesive RFID sweat sensor patch (Rose et al., 2015). The conventional approach consists of using the NFC module as a wireless communication interface between the sensor system and the smartphone for data transmission and energy harvesting. For instance, in (Prabhakar, Mysore, Saini, Vinoy, & Amruthur, 2015) two NFC products for pervasive health monitoring are described. Firstly, an NFC-based battery charger circuit to charge a thermometer that is equipped with wireless communication; Secondly, an NFC battery-less medical grade thermometer readable by a smartphone. A passive contactless sensor that can be read by any NFC-enabled mobile device is reported in (Steinberg, Tkalčec, & Murković Steinberg, 2016) for monitoring resistivity in porous materials. More recently, in (Lorite et al., 2017) the authors present a smart NFC critical temperature indicator tag for supply chain and storage conditions monitoring of perishable food products. In (Carvajal et al., 2017) a compact dosimetric system based on MOSFETs with an NFC tag and a smartphone is presented. The system is intended to be used for low-cost dosimetry control in radiotherapy treatments.

Smartphone-based NFC sensors can go one step further by using the NFC tag as both the sensor and the interface connection without any extra circuitry. This is the case of (Azzarelli et al., 2014), where chemiresponsive nanomaterials are integrated into the circuitry of commercial NFC tags to achieve portable and inexpensive detection of gas-phase chemicals such as ammonia, hydrogen peroxide and cyclohexanone. Following a similar approach, (G. Xu et al., 2017) describe a flexible NFC tag for biochemical sensing. In this case the tag was modified by removing a section of conducting film on the IC branch. Then, two short wires connected the modified tag with carbonic interdigitated electrodes covered with monolayer chemical vapor deposition (CVD) for gas detection, or gold and platinum electrodes to detect analytes in solution like ions and bacteria. Therefore, there was a threshold value for the activation of the NFC tag depending on the impedance of the sensor electrodes. One of the advantages of NFC sensors on smartphone is their low cost and versatility. The whole sensing process can be completed by any non-professional user without the need of an ad-hoc reader. Furthermore, there is no physical contact or electrical wiring between the sensor tag and the smartphone reader, which allows the positioning of the sensors and the performing of the measurements in many different environments (Kanchi et al., 2018).

3. Methodology

In this chapter we present the main methodological aspects related to the development of the sensor systems that will be described in Chapter 4. The first part is devoted to the fabrication techniques employed, including printing techniques and other manufacturing methods such as copper milling or conductive textile transfer. The second part of the chapter describes the main characterization equipment that has been used, including instruments for thermal and humidity measurements of the developed sensor systems; mechanical and physical characterization of printed patterns; and RF and electrical performance of different printed structures, RFID tags and sensing platforms.

3.1 Fabrication techniques

Among the different printing methods on flexible substrates presented in Section 2.1.2, two of them have been used in this thesis for the development of printed systems: inkjet printing and screen printing. For prototyping on FR-4 substrate, PCB milling has been employed. In addition, a fabrication technique for conductive textile transfer has been used to achieve wearable and light-weight structures compatible with textile manufacturing. In the following subsections, a short description of all the fabrication techniques used in this thesis is included. The different equipment and materials employed in each case are reported as well.

3.1.1 Inkjet printing

The Dimatix Materials Printer DMP-2831™ (Fujifilm Dimatix Inc, Santa Clara, USA) has been used for inkjet printing prototyping (Figure 26). DMP-2831™ is a drop-on-demand printer that employs a piezoelectric element to drive current through the cartridge's nozzles, ejecting droplets on the substrate according to a predefined digital pattern. The printable area is 210 mm × 315 mm if the substrate thickness is below 0.5 mm, and it reduces to 210 mm × 260 mm for 0.5 – 25 mm thick substrates. According to the specifications and our experience, the printer has a repeatability of ± 25 μm. The substrate holder, whose temperature is adjustable up to 60 °C, includes a vacuum platen to fix the substrate. For inkjet printing, flexible polymeric substrates have been used, in particular polyimide (PI) Kapton® HN (DuPont™, Wilmington, DE, USA) with a thickness of 75 μm, relative permittivity (ε_r) of 3.5 at 1 kHz, and loss tangent ($\tan\delta$) of 0.002 (1 kHz).

The nanoparticle-based silver ink SunTronic U5603 (Sun Chemical, New Jersey, USA) was used to inkjet-print the patterns. With a particle size lower than 150 nm and viscosity around 10-13 cPs at 25 °C, this ink has a 20% solid Ag content dissolved in ethanol and ethanediol. According to the manufacturer, afer curing at 150–300 °C the ink can achieve resistivities between 5–30 μΩ·cm.

Figure 26. Fujifilm Dimatix DMP-2831TM inkjet printer.

3.1.2 Screen printing

Screen-printed patterns have been manufactured using a Serfix III screen printing machine (Seglevint SL, Barcelona, Spain). To manufacture the masks, an emulsion of a hardened diazo-photopolymer (Kopimask S. A., Barcelona, Spain) was used. The screens used consist of aluminum rectangular structures of 50 cm × 35 cm with different mesh densities: 90, 120 and 150 Nylon threads per centimeter (T/cm). Polyimide Kapton® HN was also used as substrate for screen printed patterns. Apart from PI, polyethylene naphthalate (PEN, Kaladex PEN Film, DuPont Teijin Films, Japan) in two different thicknesses (75 μm and 100 μm) was chosen because of its high optical transmission in the visible spectrum and good adherence. This material has a dielectric constact of 3.2 at 10 kHz and a dissipation factor of 0.005 at 1 kHz. Its upper working temperature is 155 °C.

The conductive silver-based ink used in screen printing was SunTronic CRSN 2442 (Sun Chemical, New Jersey, USA). With 70% solid Ag content and viscosity of 20–30 cPs (25 °C), this ink has resistivity of 25–50 μΩ·cm after annealing at 120–150 °C, according to the manufacturer.

3.1.3 FR-4 Milling

For electronic system prototyping on FR-4 substrates, a mechanical milling machine model ProtoMat® S100 (LPKF Laser & Electronics AG, Garbsen, Germany) was employed (Figure 27). The minimum conductor width is 100 μm according to the manufacturer. Specific RF tools were used to improve accuracy during the milling process in order to achive more vertical clean edge finish. Repetition accuracy with the employed tools is ± 2.5 μm and positioning accuracy ±5 μm. The FR-4 substrate has a relative permittivity of ε_r = 4.6 and a loss tangent of tanδ = 0.015. Metallization layer is 35 μm thick copper with a conductivity of σ = 4.6 × 10^7 S/m.

Figure 27. LPKF ProtoMat® S100 circuit board milling system.

3.1.4 Conductive textile transfer

A different approach using conductive textile has been also used to achieve light-weight and wearable structures compatible with textile manufacturing. We have used nickel- and copper-plated Shieldit Super Fabric Cat. #A1220 (Less EMF Inc., New York, USA) as the electro-textile conductor and Ethylene-Propylene-Diene-Monomer (EPDM) cell rubber foam as the substrate (Johannes Birkenstock GmbH, Wuppertal, Germany). The electro-textile has a sheet resistance of approximately 0.16 Ω/□, while the dielectric constant and loss tangent of EPDM are 1.26 and 0.007, respectively, at 915 MHz. The fabrication process begins by attaching the electro-textile material on the EPDM substrate. The electro-textile used can be easily ironed on the substrate thanks to the hot melt glue on its backside. Then, the desired patterns are accurately and quickly cut on the electro-textile material by means of a laser cutter (Epilog Fusion Laser Model 13000) without affecting the underlying substrate.

In the cases of inket-printed, screen-printed and conductive textile structures, a conductive resin was used for the bonding of the chips, connectors and external

components to the different substrates. Epoxy EPO-TEK® H20E (Epoxy Technology Inc., Billerica, USA) was used when a thermal curing process was possible. According to the manufacturer, this silver epoxy needs a minimum bond cure of 120 °C during 15 minutes to become electrically conductive. The curing time can be reduced if a higher temperature is used (45 seconds at 175 °C) and vice versa (3 hours at 80 °C). If the thermal curing was not possible due to the substrate heating limitations (like in the case of EPDM), the CircuitWorks CW2400 conductive epoxy was used (Chemtronics, Kennesaw, Georgia, USA). This silver epoxy allows quick room temperature curing.

3.2 Characterization equipment

For thermal and humidity measurements, a climate chamber model VCL4006 (Vötsch Industryetedhnik, Germany) was employed (see Figure 28). This equipment allows a temperature range from -40 °C to 180 °C. Relative humidity inside the chamber can be set from 10% to 98% with a control of the climatic range from 10 °C to 95 °C. With an empty chamber, the temperature rate of change is 3.5 °C/min for heating and 5 °C/min for cooling.

Figure 28. VLC4006 climatic test chamber from Vötsch.

A Dektak XT™ Stimulus Surface Profiling System (Bruker Corporation, Conventry, UK), shown in Figure 29, was used for profile characterization of printed structures. The Bruker Dektak XT is a contact profilometer that is able to measure the thin film thickness of patterned structures by sensing the deflection of a fine stylus that is

raster scanning over features ranging in height from 1 mm down to 5 nm, with a vertical resolution of 0.1 nm.
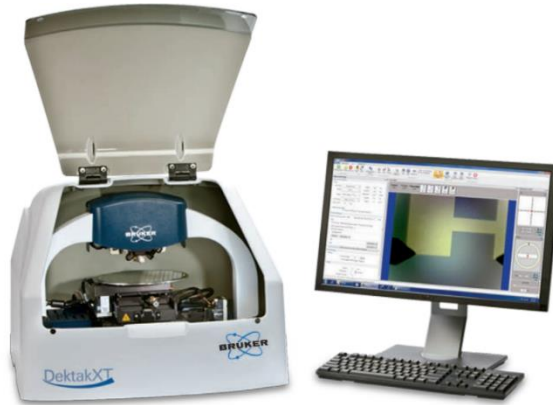
Figure 29. Bruker Dektak XT™ Stimulus Surface Profiling System.

A RF Network Analyzer ENA model E5071C (Keysight Tech., Santa Clara, CA, USA) has been used to measure the RF response of the fabricated UHF antennas and other patterns such as printed microstrip lines. This equipment has 4 ports (Figure 30) and it covers a wide frequency range from 9 kHz to 8.5 GHz. This Network Analyzer also features a wide dynamic range (>123 dB), fast measurement speed (9 msec for 401 points with error correction) and excellent temperature stability (0.005 dB/°C). The N4431B RF Electronic Calibration Module (ECal) was employed along with the Network Analyzer for calibration purposes.

(a)   (b)

Figure 30. (a) RF Network Analyzer ENA model E5071C from Keysight Technologies and **(b)** N4431B RF Electronic Calibration Module (ECal).

For electrical characterization of the fabricated HF antennas and other printed components such as planar inductors or capacitors, a precision impedance analyzer was used, the Agilent 4294A (Keysight Technologies, Santa Clara, California, USA).

This analyzer covers a broad frequency range from 40 Hz to 110 MHz with a basic impedance accuracy of ±0.08 %. The equipment has been used along with a 42941A impedance probe kit to connect the devices under test (DUT) to the analyzer (see Figure 31).
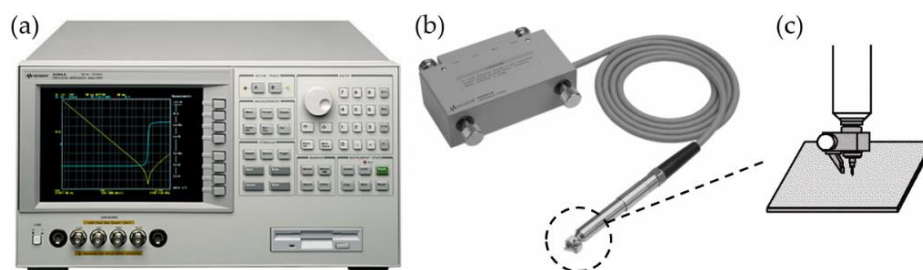
Figure 31. (a) 4294A Precision Impedance Analyzer from Keysight Technologies with **(b)** 42941A impedance probe kit. A detailed view of the pin probe is shown in **(c)**.

A DC Power Analyzer model N6705A (Keysight Technologies) like the one in Figure 32 was employed as a source/measure unit (SMU) to apply voltage on the patterns for electrical sintering.

Figure 32. N6705B DC Power Analyzer used for electrical sintering.

This equipment is a multi-functional power system that combines the functions of a multiple-output DC voltage source with the waveform/data capturing capability of an oscilloscope and data logger. As a multiple-output DC source, the Keysight N6705A provides four configurable outputs. Each output also has arbitrary waveform generation capability, which lets you program predefined voltage and current waveforms. In our equipment, the four available power modules have the following voltage and current combinations:

- Module 1: DC Power N6743B. 100 W output rating (20 V, 5 A).
- Module 2: DC Power N6746B. 100 W output rating (100 V, 1 A).
- Module 3: High-Perform N6751A. 50 W output rating (50 V, 5 A).
- Module 4: Precision N6761A. 50 W output rating (50 V, 1.5 A).

As measurement system, the N6705A displays the average output voltage and current in a meter view. Waveforms are displayed in a scope view, while the data logger view allows measuring, charting and logging average and peak voltage and current measurements over an extended period of time.

3.3 Smartphone applications development

All custom-designed Android™ applications for the different smartphone-based sensor systems have been developed using the Integrated Development Environment (IDE) Android Studio, release 2.3.1 or 2.3.3. Depending on the particular case, the applications have been developed and tested against Application Programming Interface (API) 24, which corresponds to Android version 7.0, or API 22 (Android 5.1). Nevertheless, they are backward compatible with older Android versions. The lowest supported API levels are API 18 (Android 4.3) or 16 (Android 4.1). When image detection and processing tasks have been required, the developed algorithms have been based on computer vision OpenCV 3.1.0 Android library.

Three different smartphones have been used. The oldest one is the Sony Xperia S, which has been used as an NFC-enabled smartphone running Android 4.3 (API level 18). A Nexus 5 smartphone by Google Inc., also equipped with NFC technology, has been used running Android version 6.0.1 (API 23). Finally, a Samsung Galaxy S7 running Android 7.0 (API 24) has been employed, particularly in the cases where image processing tasks were required. This smartphone features a 12-megapixel rear camera with an f/1.6 aperture, focal length of 26mm, optical image stabilization and autofocus.

4. Results and discussion

In this chapter, the different achievements and results obtained during the development of this thesis are presented and discussed. The chapter begins with sintering characterization as a prior step to the development of printed structures. In this regard, both thermal and electrical sintering methods are studied and compared in terms of electrical conductivity and RF performance of sintered patterns. After this, an e-textile tag antenna is presented as a RFID platform compatible with textile manufacturing. Then, two complete passive sensor systems are presented for applications in the fields of smart packaging and healthcare. This includes a flexible printed humidity measurement platform, and a passive NFC tag to be used for dosimetry control in radio-therapy treatments. To conclude the chapter, the four published papers that constitute the thesis by compendium of publications are included. All of them are flexible passive sensor systems capable of detecting and monitoring parameters such as temperature, optical spectrum or different gases concentrations. These platforms are conceived to be used for fruit ripeness detection, food spoilage determination or MAP applications, among others.

4.1 Sintering characterization

After printing, the patterns must be sintered in order to remove organic solvents and fuse the metallic nanoparticles together to form conductive tracks, as explained in Section 2.1.3. As a preliminary step towards the developmeny of printed sensor systems, thermal and electrical sintering methods were studied and compared using two different simple patterns: a meander structure and a microstrip line. Our goal in this work is to investigate if the long duration of thermal sintering is overcome with a short electrical sintering but without losing DC and RF performance.

4.1.1 Thermal sintering

Figure 33 shows the meandered pattern that has been inkjet-printed for the thermal sintering characterization. It consists of fourteen meander-shaped lines, each of them composed of 400 μm width segments separated by 400 μm gaps, making a total length of 110.4 mm. Two squared pads of 5.5 mm × 4.4 mm were printed at both ends of the meandered pattern to provide electrical contacts for measurements. The nanoparticle-based silver ink SunTronic U5603 was used to print 2 layers for each pattern. A drop-to-drop (DTD) space of 25 μm was configured on the Dimatix printer

for around 50 µm diameter landed drops. The patterns were printed on a 75 µm thick PI Kapton® HN. While printing, the substrate temperature was fixed at 40 °C.
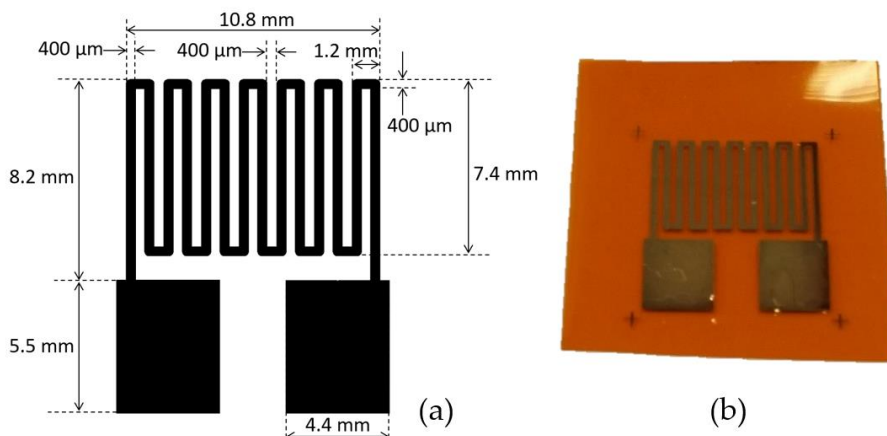
Figure 33. (a) Footprint of the inkjetted meandered structure and **(b)** example of one meandered patterns inkjetted with SunTronic silver ink on PI substrate.

A two-step printing process was carried out. In the first place, only the squared pads were printed, followed by a thermal curing process at 160 °C during 60 minutes in a convection air oven Venticell VC55 (MMM Medcenter Einrichtungen GmbH, Munich, Germany). Then, the meandered lines were printed after a correct alignment of the substrate in the printer. In this way, the two already sintered contact pads were available for electrical measurements during the thermal sintering process of the meandered lines.

Thermal sintering characterization was performed with the printed meander structures by monitoring the change in their resistance during sintering process at different temperatures. Six sintering temperatures were considered, from 100 °C to 200 °C in steps of 20 °C. Furthermore, two different situations were studied: (i) sintering with temperature ramp up to the final temperature and (ii) sintering with temperature step, that is, the printed samples are introduced in the oven once it has reached the desired final temperature. In both cases, the final temperature was kept during 60 minutes and then the oven was automatically turned off. The samples were kept inside the oven until temperature was gradually reduced to approximate ambient temperature.

The process was monitored inside the oven by connecting a 34970A data acquisition unit (Agilent Technologies, California, USA) to the sintered pads of the printed meanders through clamps and heat resistant cables. The acquisition unit was

configured to scan and log four channels during the sintering process. Three of them were dedicated to three printed patterns, while the fourth one was connected to a Pt1000 resistance temperature detector (RTD). The minimum interval scanning time achieved with the equipment was 1.4 seconds, which was more than enough for our purposes.

Resistivity of the printed meanders was calculated based on dimensional measurements of the printed patterns and the measured resistance, as proposed in (David A. Roberson, Wicker, Murr, Church, & MacDonald, 2011). The equation to calculate resistivity ρ is:

$$\rho = R \frac{A}{l} \qquad (4.1)$$

Where R is the measured resistance of the printed trace is, A is the cross-sectional area of the printed trace and l refers to its length. Cross-sectional area of the printed traces was calculated by measuring the lines thickness and width with the Dektak XT™ Stimulus Surface Profiling System. Figure 34 shows an example of the cross section of a printed line measured with the profilometer. The cross-sectional area was approximated by calculating the area beneath the plotted curve. Three profile measurements were taken for one serpentine pattern per temperature, making a total of 18 measurements. The cross-sectional area used for the resistivity calculations was the average of all the measurements.
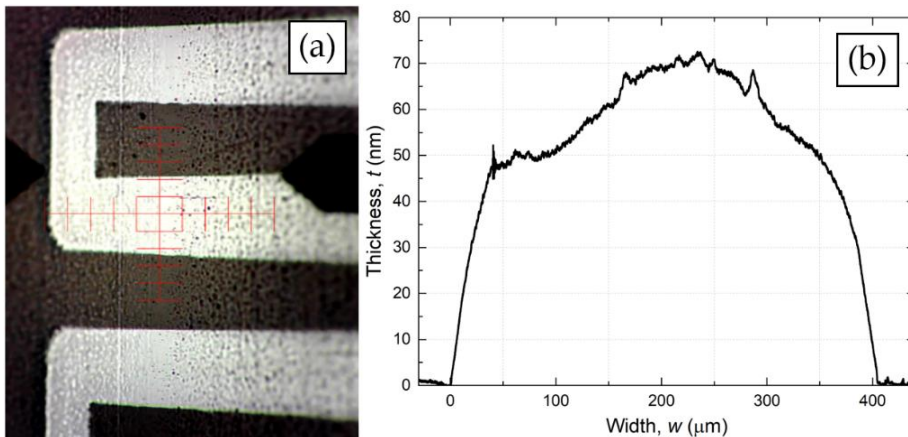
Figure 34. (a) Enlarged view and **(b)** randomly measured profile of a printed line of a meandered pattern on PI Kapton® substrate.

Resistivity change of the printed meanders during thermal sintering with temperature ramp is depicted in Figure 35, while the same experiment with temperature step is shown in Figure 36.
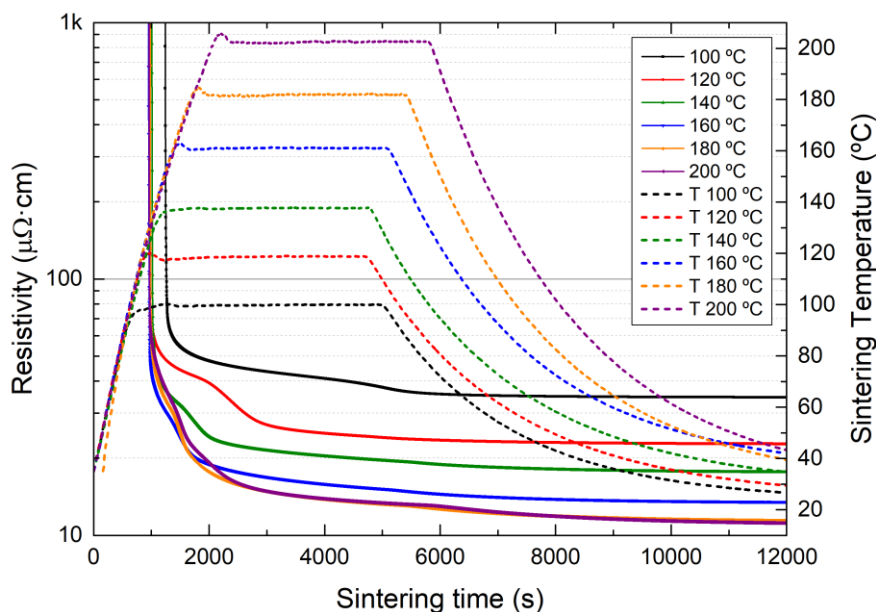
Figure 35. Resistivity change of the meandered patterns during thermal sintering with temperature ramp.

In both cases, a set of three meandered structures have been sintered at each temperature. As expected, the higher temperature, the faster changes in resistivity. We can divide each graph of thermal sintering process into three regions: the first in which the patterns are still non-conductive and the instrument measures an infinite resistance; the second is a transition phase, where resistivity quickly decreases in a short period of time and the actual sintering phenomenon occurs; finally, a third region with low resistivity changes.

These regions can be associated to the two basic stages of any sintering process (Falat, Platek, & Felba, 2012). The first region corresponds to the first sintering stage, which consists of the thermal decomposition and removing of surfacants. In this stage the nanoparticles are still separated by the outer organic layers, so they do not touch each other and therefore the resistance is too high. In the second stage, which corresponds to the other two regions in our graph, the nanoparticle protective shells are removed and the diffusion and recrystallization processes are dominant. At the start of this phase, many new electrical paths between the nanoparticles are created within a short period of time, so the resistivity quickly decreases. After this, the sintering process slows down and the resistivity reduces much more slowly.
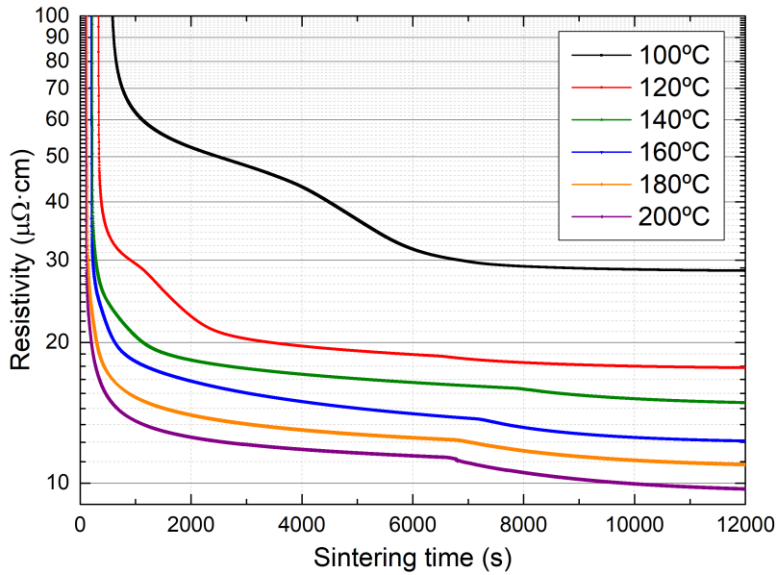
Figure 36. Resistivity change of the meandered patterns during thermal sintering with temperature step.

Table 3 collects the average measured resistivity of each set of meanders for the six final temperatures and the two cases considered, with and without temperature ramp. The numerical data of Table 3 are graphically displayed in Figure 37.

Table 3. Final resistivities as a function of final temperatures with temperature ramp and temperature step in the thermal sintering process.

Final Temperature (°C)	Final Resistivity ($\mu\Omega\cdot$cm)	
	Temp. ramp	Temp. step
100	34.5 ± 0.5	28.2 ± 0.4
120	22.6 ± 2.4	17.4 ± 0.4
140	17.5 ± 1.1	14.5 ± 0.5
160	13.7 ± 1.4	12.13 ± 0.19
180	11.6 ± 2.0	10.62 ± 0.14
200	10.9 ± 0.4	9.41 ± 0.12

As it can be observed, best resistivity values are achieved for the case of sintering with temperature step. The difference is more significant for lower final temperatures than for higher ones. In the case of temperature ramp, the best resistivity value achieved is $\rho = 10.9 \pm 0.4\ \mu\Omega \cdot$ cm for 200 °C, which is roughly seven times the value of bulk silver resistivity, 1.59 $\mu\Omega\cdot$cm (Lide, 2007).
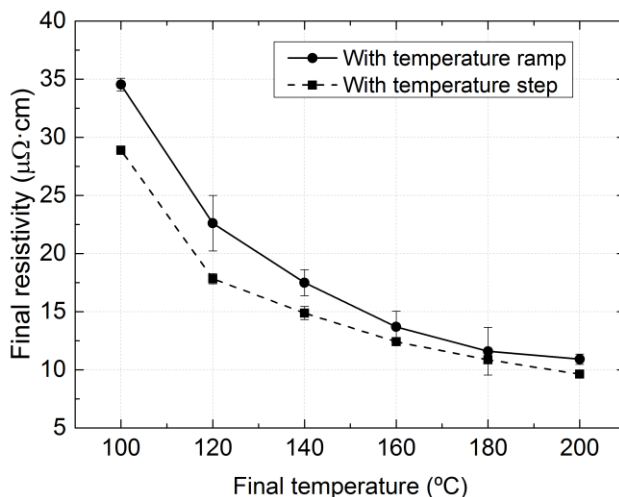
Figure 37. Final resistivities as a function of final temperatures with temperature ramp and temperature step in the thermal sintering process.

The lowest value of $\rho = 9.41 \pm 0.12 \; \mu\Omega \cdot cm$ is achieved with temperature step at for 200 °C, which is about six times the value of bulk silver. These results are consistent with the resistivity of 5—30 μΩ·cm reported on the SunTronic ink manufacturer datasheet. Measured resistivities are higher than bulk silver resistivity because printed silver has smaller grain size and higher porosity than bulk silver. In consequence, electrons scatter more at the grain boundaries of printed silver than on bulk silver (Merilampi, Laine-Ma, & Ruuskanen, 2009; Salmerón, Molina-Lopez, et al., 2014).

To further analysis, the starting times of the thermal sintering process were studied. We have considered the starting time as the moment when the data acquisition unit begins measuring a resistance value. The obtained values for the different temperatures are included in Table 4.

Table 4. Starting times of thermal sintering process for different sintering temperatures with and without temperature ramp.

Final Temperature (°C)	Time when sintering starts (s)		
	Temp. ramp	Temp. step	Time difference
100	1117	490	627
120	919	284	635
140	962	184	778
160	956	175	781
180	947	115	832
200	920	88	832

The first remarkable fact is that sintering phenomenon starts long before in the case with temperature step, which is understandable since the oven already has a high temperature when the samples are placed inside it. In this case, the patterns start sintering just after 88 seconds for the highest temperature, while they need more than 8 minutes for the lowest temperature. In other words, with temperature step the time required to start the sintering process is closely correlated with the temperature. This can be more clearly appreciated in Figure 38, which shows an enlarged view of the first sixteen minutes of the thermal sintering process with temperature step.
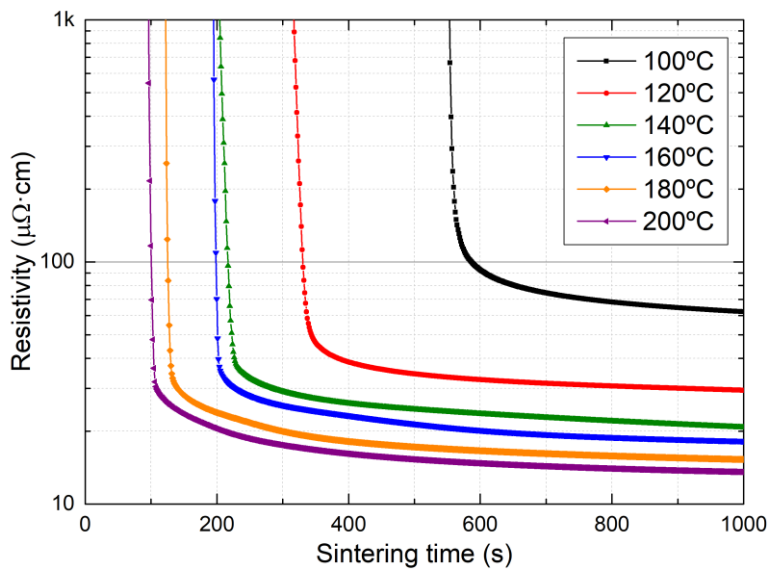
Figure 38. Enlarged view of Figure 36: Resistivity change of the meandered patterns during thermal sintering with temperature step.

With temperature ramp, almost all printed structures start the sintering process at approximately the same time, around 15 minutes after the samples are introduced into the oven. This is true for all temperatures except for the lowest one, 100 °C. At this temperature value, the starting time is about three minutes higher than the average starting time of the other cases. This suggests that the reached value of temperature is not high enough to cause the beginning of the sintering phenomenon, as it happens with higher temperature values. As a consequence, the printed silver tracks need more time to remove the protective surfactants layer. Figure 39 shows an enlarged view of the thermal sintering process with temperature ramp.
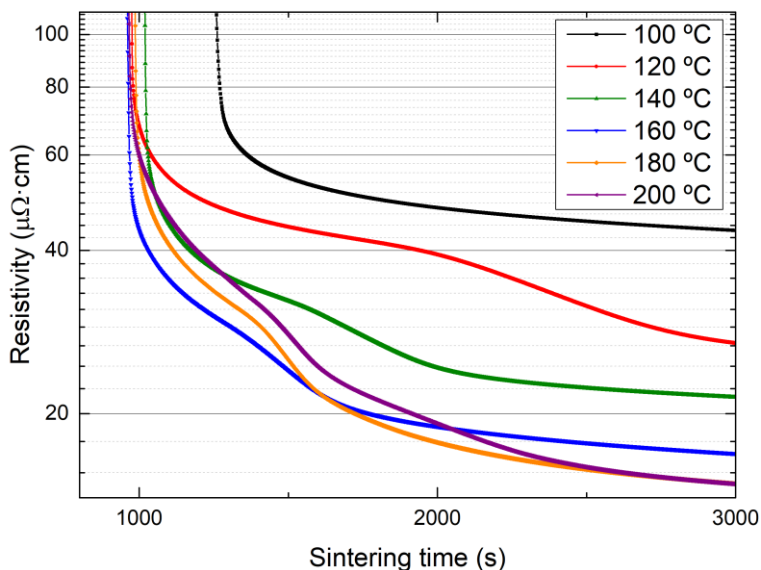
Figure 39. Enlarged view of Figure 35: Resistivity change of the meandered patterns during thermal sintering with temperature ramp.

4.1.2 Electrical sintering

Thermal sintering has some disadvantages. First of all, it is a time-consuming process. Moreover, some substrates can suffer from shrinkage when exposed to typical sintering temperatures. There can be also undesired gas emission from the substrate during the process. Finally, it is not an area-specific process, that is, the whole structure needs to be sintered (M. L. Allen et al., 2008). Electrical sintering is a method that overcomes some of these limitations. The key advantages of electrical sintering are summarized in short sintering times and reduced substrate heating, because heat generates only in the nanoparticle layer.

To test and characterize electrically sintered printed patterns, microstrip lines were designed and fabricated using inkjet printing. A microstrip line is a type of transmission line used for Electromagnetic (EM) wave propagation. Figure 40 shows the geometry of this structure, which consists of three layers: a dielectric substrate with a continuous ground plane on one side and a metallic signal conductor on the other side. The characteristic impedance of the microstrip line depends on the conducting strip width, height and length, as well as on the substrate properties such as thickness, relative permittivity and dissipation factor. Line Calculator tool from Advanced Design System (ADS) simulator (Agilent Technologies, Santa Clara, CA, USA) was used for the combination of PI Kapton HN substrate and SunTronic U5603

silver ink to find the geometric dimensions leading to the desired 50 Ω characteristic impedance. In this case, the 75 μm Kapton substrate with on one side metallized with 30 nm aluminum to act as the ground plane. An additional microstrip line on double sided PCB with FR-4 substrate was designed and fabricated as a reference strip.
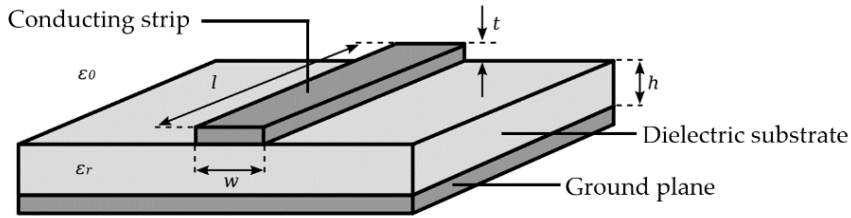
Figure 40. Geometry of a microstrip line composed of three layers: conducting strip with lengh *l*, width *w* and thickness *t*; dielectric layer with thickness *h* and relative permittivity ε_r; and ground plane.

Table 5 shows the geometric dimensions obtained with ADS software for the rigid FR-4 and the flexible inkjet-printed microstrip lines.

Table 5. Microstrip lines dimensions computed with Line Calculator from ADS to get a characteristic impedance of 50 Ω for the two different material combinations used.

Materials	Substrate		Conducting strip	
	Thickness *h*	ε_r	Length *l*	Width *w*
Copper on FR-4 substrate	1.5 mm	4.6	46.5 mm	2.7 mm
Silver ink on Kapton substrate	75 μm	3.5	52.1 mm	168.9 μm

According to the inkjet printed model previously reported in our research group (Salmerón, Molina-Lopez, et al., 2014), the irregularity in the contribution of the outer part of the lines to the total width has to be taken into account if the printed element is comparable in size with the diameter of one printed drop. In this case, the drop-to-drop space is DTD = 25 μm and the desired width is 168.9 μm, so the designed witdh must consider the contribution of the outer drops as depicted in Figure 41.

As in the case of the meanders, a two-step printing process was carried out. Firstly, the pads were printed and cured at 160 °C during 60 minutes in a convection air oven. Then, the lines between the pads were printed. Since the printed line's resistance just after printing was too high to be electrically sintered, a thermal pre-sintering phase was applied in order to establish an initial level of conductance prior to the application of electrical current.
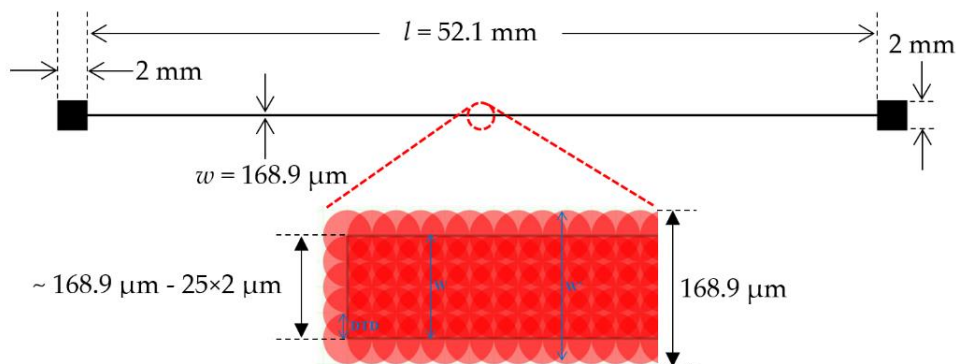
Figure 41. Footprint of the designed microstrip line with dimensions.

The lines were preheated in the oven at 100 °C from 1 to 5 minutes. This preheating time determines the initial resistance of the printed line, which ranges from hundreds of ohms to several kΩ. After this, electrical sintering was carried out. Finally, the Subminiature Version A (SMA) edge connectors were attached using silver Epoxy on both ends of the printed lines in order to characterize their frequency response using the Network Analyzer (ENA). The connectors were reinforced with glue to improve protection against mechanical stress.

Figure 42. (a) Image of some inkjet-printed microstrip lines on PI metallized film with attached SMA connectors. **(b)** Picture with the Dimatix fiducial camera of a printed microstrip line.

Figure 43 shows an example of a measured profile of a printed microstrip, while Table 6 collects the obtained measurements of three samples with the Dektak XT™ surface profilometer. As it can be observed, we obtain an average width of 169.4 ± 2.6 μm, which is very close to the designed value.
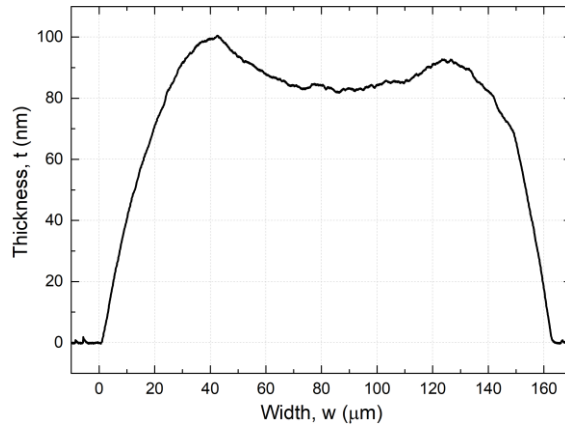
Figure 43. Example of a randomly measured profile of a printed microstrip line on PI Kapton®
HN substrate.

Table 6. Width and effective thichness measurements of three printed microstrip lines with
the Dektak XT™ Stimulus Surface Profiling System.

# Microstrip line	Width (μm)	Effective thickness (μm)
1	171.1	0.697
2	166.4	0.650
3	170.6	0.634
Average	**169.4**	**0.660**
Standard deviation	**2.6**	**0.033**

The N6705A DC Power Analyzer, which was described in Section 3.2, was employed
to apply voltage to the printed lines for electrical sintering. By applying a potential
difference to both ends of the line, the generated electrical power accelerates the free
electrons to move through the conductive ink track. The collisional energy of free
electros with silver nanoparticles in the conductive ink is then changed to thermal
energy by joule heating (see Section 2.1.3). Several arbitrary voltage waveforms were
tested in order to cure the patterns, with different voltage and current values. Best
results were obtained by using a voltage staircase up to 25 V in 5 V steps, in other
words, 5 steps of 5 V each. A current limit of 0.2 A was set in the power analyzer
configuration. This voltage staircase was applied during 5 seconds, so that each 5 V
step was applied for 1 second. The obtained results for five microstrip line samples
are collected in Table 7. An average final resistivity value of 5.2 ± 0.3 μΩ·cm was
obtained, which is approximately 3.3 times the value of bulk silver resistivity, 1.59
μΩ·cm (Lide, 2007). In comparison with the best resistivity values obtained after
thermal sintering, the resistivity with electrical sintering has been reduced by 44.6 %.

Table 7. Initial and final values of resistance and resistivity for different microstrip lines during the electrical sintering tests.

#Sample	Initial Resistance (Ω)	Final Resistance (Ω)	Electrical sintering	Final Resistivity (μΩ·cm)
1	1.1 k	24.1	Voltage	5.17
2	587	24.4	Staircase	5.23
3	579	26.3	25 V, 5 s	5.64
4	1.6 k	23.3	5 steps,	4.99
5	592	23.4	0.2A lim.	5.02
6	400 k	71.1	V. Pulse 40V, 5 s, OCP=0.2A	8.8

Figure 44 shows the variation in the resistivity and the power of a printed microstrip line during electrical sintering when the 25 V voltage staircase is applied. Note that the power variation has an opposite tendency to the resistivity variation. There is an abrupt rise in the power at the same time when the resistivity starts to sharply drop. As it can be seen, actual sintering occurs within a very short time. Then, the power is limited by the maximum current allowed through the sample.
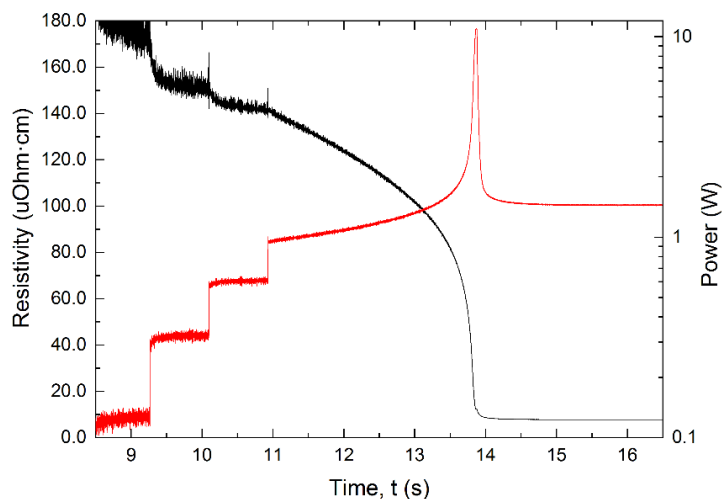
Figure 44. Variation in the resistivity and the power of a printed microstrip line when a 25 V voltage staircase is applied for electrical sintering.

One limitation of the applied staircase waveforms up to 25 V was that sintering was only achieved if the resistance of the preheated samples was relatively low (no higher than some kΩ). In the cases where the initial resistances of the lines were too high,

sintering was not triggered. For this reason, a new arbitrary waveform consisting of a 40 V voltage pulse during 5 secons was tested. The overcurrent protection (OCP) was set to 0.2 A in the N6705A. Last row in Table 7 shows the result obtained for a microstrip line with 400 kΩ initial resistance. In this case, an abrupt reduction in the resistance down to 71 Ω is achieved after the application of a single voltage pulse. Although the final obtained resistivity of 8.8 μΩ·cm is not as low as in the previous cases, it is still lower than the best resistivities achieved with thermal sintering.

4.1.3 RF performance

The electrical responses at high frequencies of several inkjet-printed microstrip transmission lines sintered with the two methods, thermal and electrical, have been used to compare their RF behaviour. To do so, we used a vector network analyzer to obtain the scattering or S-parameters of the microstrip lines, which are defined in terms of voltage travelling waves. An N-port device has N^2 S-parameters. Our microstrip lines are two-port devices, so they have four S-parameters, as depicted in Figure 45. According to the numbering convention, the first number following the "S" is the port where signal emerges, while the second number is the port where signal is applied (see Equation 4.2). The incident terms (a_1, a_2) and output terms (b_1, b_2) represent voltage travelling waves.
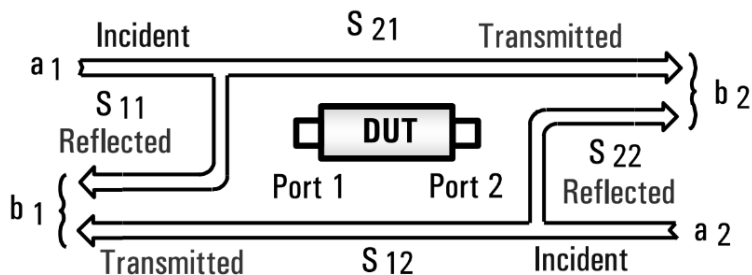
Figure 45. Signal transmission and reflection (Keysight Technologies, 2014).

$$b_1 = S_{11}a_1 + S_{12}a_2$$
$$b_2 = S_{21}a_1 + S_{22}a_2$$
(4.2)

RF performance was assesed by measuring the forward transmission coefficient S_{21}, which is a measure of the signal coming out port 2 relative to the RF stimulus entering port 1. In other words, S_{21} is the ratio of the transmitted voltage to the incident voltage when the output is terminated in a perfect Z_0 (a load that equals the characteristic impendance of the DUT, which is in our case the microstrip line). This condition guarantees that a_2 is zero, since there is no reflection from an ideal load.

$$S_{21} = \frac{\text{Transmitted}}{\text{Incident}} = \frac{b_2}{a_1}\bigg|_{a_2=0} \qquad\qquad (4.3)$$

S_{21} means transmission loss or gain and will be negative if DUT has a loss, and positive if DUT has a gain. To do so, the Network Analyzer described in Section 3.2 was employed along with a custom-made wood structure to avoid mechanical stress of the lines, as depicted in Figure 46.
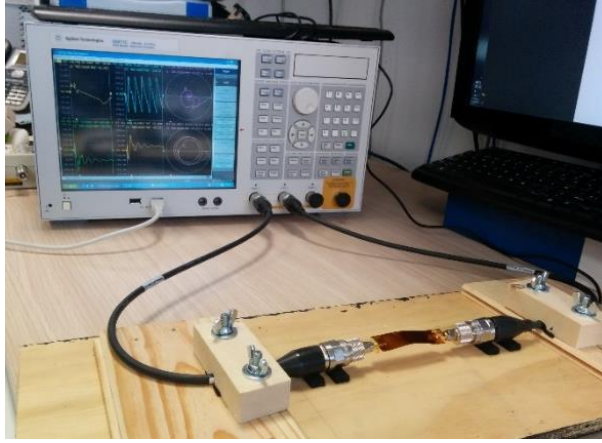
Figure 46. Measurement setup for the RF characterization of the printed microstrip lines, including the E5071C Network Analyzer and the handmade structure.

Figure 47 illustrates the frequency response obtained for several microstrip lines. Apart from the rigid line fabricated on FR-4 substrate, four samples thermally sintered at three different temperatures (100 °C, 160 °C and 200°C) have been measured. As for the electrically sintered lines, three samples sintered with the staircase waveform and one with the voltage pulse have been characterized. The transmission parameter S_{21} is presented in Figure 47 per length unit and normalized to the value obtained at DC, so that the trend of this transmission parameter for each case can be easily compared. The decay of the obtained value for S_{21} as frequency increases is related to the loss phenomena. In a transmission line there are two types of losses: the dielectric substrate loss and the ohmic loss in the conductors because of the skin effect (Pozar, 2012). For typical substrates thicknesses used in PE, ohmic losses become more significant as the frequency rises and they are usually larger than dielectric substrate losses. For this reason, the decay in S_{21} can be attributed to losses in the conductor.
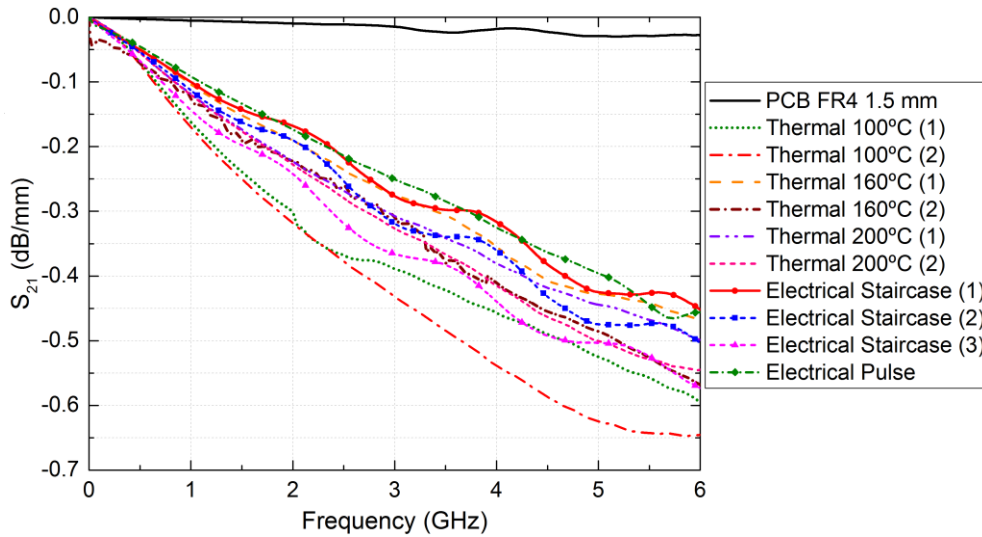
Figure 47. Measured frequency response of the transmission parameter S_{21} for the different microstrip lines fabricated.

In any case, we can see from Figure 47 that frequency response of thermally sintered lines have a similar trend than the response of the electrically sintered ones. This suggests that the abrupt change in resistance during electrical sintering does not degrade the RF behaviour of the lines as would be expected due to mechanical stress of the line caused by an accelerated heating in electrical sintering. Therefore, we can take advantage of the benefits that electrical sintering offers over thermal sintering without renouncing their use at RF. As for the FR-4 microstrip line, we can observe that its losses are significantly lower than inkjetted ones. In the first place, there is a clear difference in the substrate thickness, which is 1.5 mm for the FR-4 lines and about 75 µm for the inkjet-printed lines. On the other hand, conducting strip conductivity and thickness are larger for the rigid FR-4 lines (copper has a resistivity of 1.68 µΩ·cm) than for the printed lines. This results confirm that ohmic losses related to conducting layer properties play a critical role on RF performance.

4.2 Circularly-polarized antenna with conductive fabric

The results reported in this section are the outcome of a short stay in the Faculty of Biomedical Sciences and Engineering at Tampere University of Technology (TUT) in Finland. This Faculty belongs to BioMediTech, which is a multidisciplinary institute for life sciences and medical technology bringing together research groups from TUT and the University of Tampere. During the stay, I was part of the Wireless Identification and Sensing Systems Research Group (WISE). This research group, headed by Professor Leena Ukkonen, who supervised my stay, concentrates on wireless biomedical sensors and wireless health technologies, implantable and body-centric antennas, wireless data and power transfer in biomedical sensing systems and novel antenna and sensor materials and their manufacturing methods. With more than 120 publications in the last five years, WISE develops its research activity in areas such as printed and stretchable electronics (Suikkola et al., 2016), printed RFID tags on flexible substrates (Babar, Elsherbeni, Sydanheimo, & Ukkonen, 2013) or wearable e-textile RFID antennas (X. Chen, Ukkonen, & Bjorninen, 2016; Koski, Sydanheimo, Rahmat-Samii, & Ukkonen, 2014; J. Wang et al., 2016).

During the stay we worked on the design, fabrication and characterization of a planar circularly polarized (CP) e-textile UHF RFID tag antenna. As mentioned in Section 2.2.2, the most popular antennas in UHF band are the dipole-type antennas, whose main advantage is their inherently omni-directional radiation pattern. In the same section we also showed that the attainable read range of an RFID tag is not only determined by the radiation pattern of the tag antenna, but also by the polarization matching between the tag and the reader. This phenomenon is taken into account through the polarization loss factor (PLF). Since dipole-based antennas are linearly polarized, cross-polarization between dipole tag antenna and reader antenna can emerge if linear antennas are used for reading. This can completely prevent the power transfer in certain orientations of the tag. The most common approach to remove the possibility of cross-polarization consists of using circularly polarized antennas on the reader's side. In this case, the polarization loss between the linearly polarized tag antennas and CP reader antennas is 0.5 (-3 dB), no matter what the orientation of the tag is (Björninen, Saghlatoon, Sydänheimo, Rahmat-samii, & Ukkonen, 2014). Another way to have a polarization mismatch loss of -3dB consists of using CP tag antennas with linearly polarized reader antennas. Using CP antennas for reading as well would introduce again the possibility of cross-polarization if the handedness of the tag and reader antenna are opposite.

The proposed CP tag antenna for the UHF RFID band was based on a previous design from the same research group (Björninen, Ukkonen, Sydänheimo, & Elsherbeni,

2010). The starting point for the design was two loops connected in series, which are open-circuited from one corner to produce a circularly polarized radiation as reported in (Morishita, Hirasawa, & Nagao, 1998). Since compact tags are preferred, one of the major challenges in the design of a CP tag antenna is the size limitation (Lu & Chang, 2014), which is not so critical for reader antennas. To achieve size reduction, meandering in one side of each loop was introduced so that the loops appear electrically larger. Tag antenna geometry is shown in Figure 48 and dimensional values are listed in Table 8.
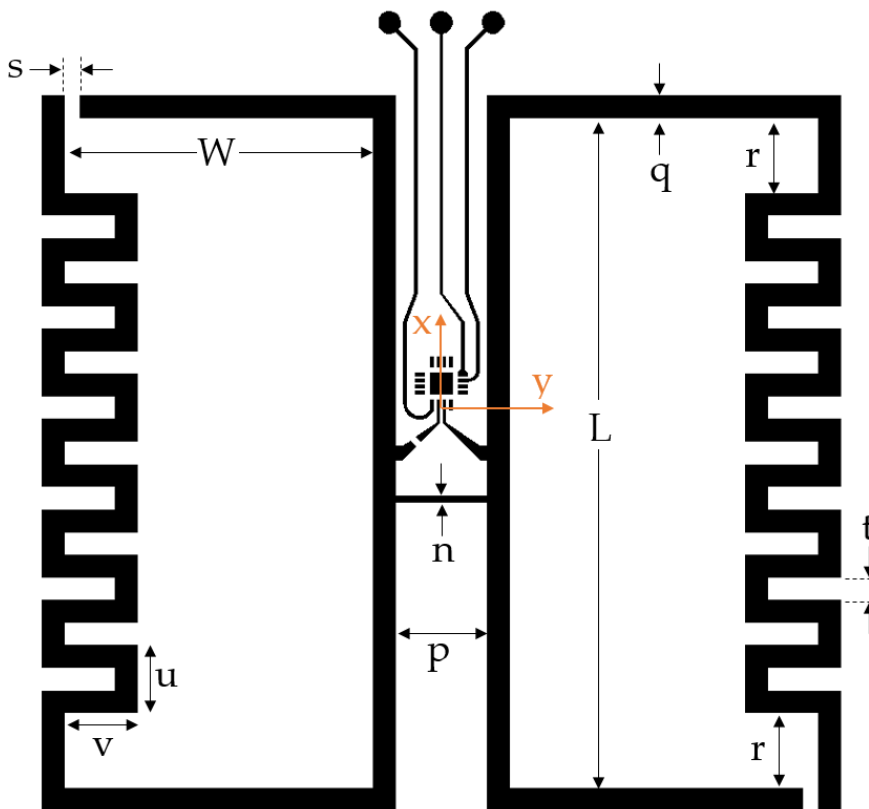
Figure 48. Geometry of the proposed circularly polarized UHF tag antenna.

Table 8. Values of the dimensional parameters shown in Figure 48.

Parameter	L	W	n	p	q	r	s	t	u	v
Value(mm)	88	40.5	1	12	3	9.5	2	2.94	8.94	9.5

The design and simulation of the tag antenna was carried out using Ansys HFSS (High Frequency Structural Simulator) software, the industry standard for simulating high-frequency electromagnetic fields. Figure 49 shows a screenshots of the simulated UHF antenna in HFSS, where the spherical coordinates have been superimposed. The angle θ is known as the elevation angle and ϕ is the azimuth angle, which is measured counterclockwise from the x-axis to the y-axis.
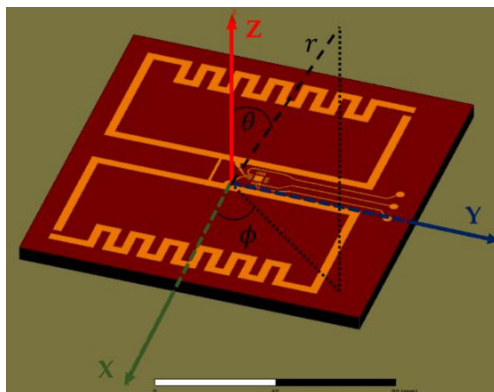
Figure 49. Screenshots of the designed and simulated UHF antenna using Ansys HFSS simulation tool.

Less EMF Shieldit Super Fabric was used as the electro-textile conductor and 5 mm thick EPDM cell rubber foam was used as the substrate. The characteristics of both materials have already been reported in Section 3.1.4. The RFID chip NXP UCODE G2iL was employed in this work. Figure 50 shows a picture of the fabricated UHF RFID tag.
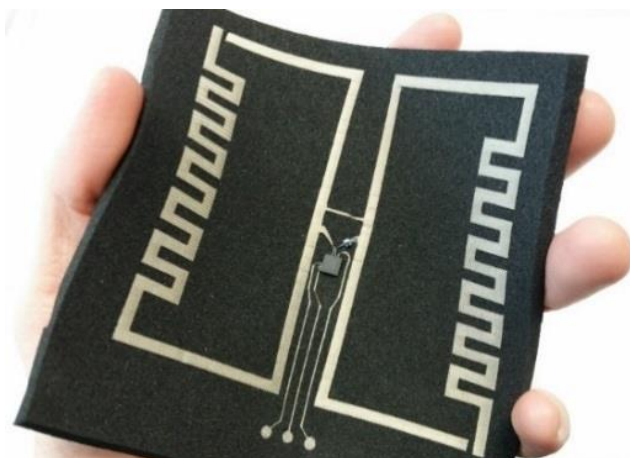
Figure 50. Circularly polarized UHF RFID tag fabricated with conductive fabric.

To estimate the read range of the manufactured tag, measurements were conducted inside an anechoic chamber with Voyantic Tagformance measurement system,[2] as Figure 51 shows. Voyantic Tagformance system is based on a linearly polarized UHF RFID reader with adjustable transmission frequency from 800 MHz to 1 GHz and output power up to 30 dBm. It provides the recording of the backscattered signal strength (down to −80 dBm) from the tag under test. Estimation of read range was done by characterizing the wireless channel from the reader antenna to the tag location and by recording the minimum output power of the reader (threshold power) at which a valid 16-bit random number from the tag is received as a response to a query command.

Figure 51. Measurements conducted inside the anechoic chamber using the Voyantic Tagformance System.

Figure 52 shows the simulated and measured attainable read ranges of the e-texile tag when it is placed vertical (along the X axis, see Figure 48) and horizontal (along the Y axis) with respect to the RFID reader. In the simulation, the two tag orientations were differentiated by considering the θ and ϕ components of the gain when computing the read range according to the Friis equation (Rao et al., 2005).

It can be seen that attainable reading distances above 2 m are achieved on the whole frequency range for both orientations of the tag. In general, the θ component of the read range is around 1 to 1.5 m higher than the ϕ component. This is due to the gain of the designed tag antenna, whose θ component (in the elevation plane) is higher than the gain in the azimuth plane. The largest read range was measured at 800 MHz with a value of approximately 4 m.

---

[2] Voyantic Ltd. http://www.voyantic.com/ , last accessed: 10th Jan. 2018
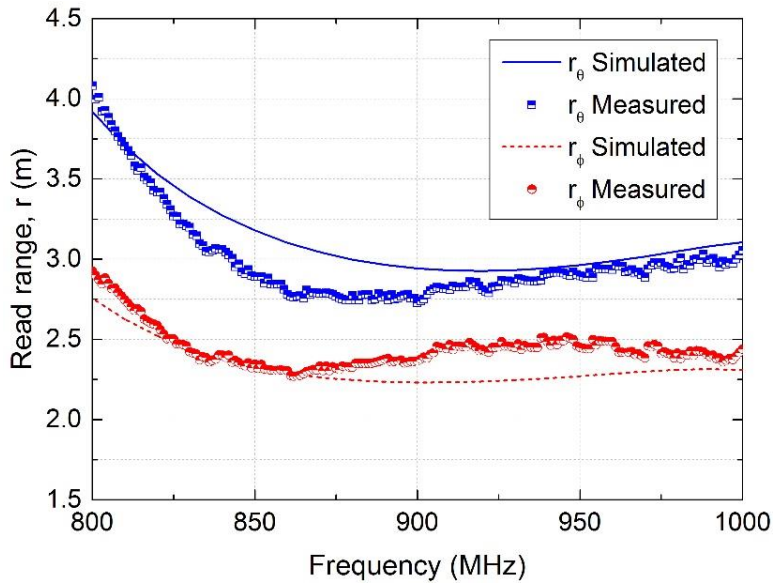
Figure 52. Simulated and measured attainable read ranges of the e-texile tag when placed vertical (blue solid line) and horizontal (red dashed line) with respect to the RFID reader.

This work has allowed us to gain knowledge about conductive pattern transfer onto fabric as well as antenna design. The combination of both insights results in an interesting approach to develop RFID platforms compatible with textile manufacturing. Despite the good results obtained, further work can be performed to extend read range of the tag by improving impedance matching between the RFID chip and the CP antenna. Moreover, on a wider level, it would be interesting to study the influence of the human body on the radiation characteristics of the antenna.

4.3 Passive printed LC-based humidity measurement system

As previously mentioned, transfer of fully passive and printed sensing tags to industry is currently a major challenge. Temperature and humidity are both environmental magnitudes whose monitoring and control are advisable in a huge amount of industrial applications. In that way, here we present the design, fabrication and characterization of a printed chipless passive system for relative humidity measurement based on a parallel LC resonator structure. Figure 53 shows the footprint and geometric dimensions of the printed system, which basically consists of a planar loop inductor in parallel with an IDE capacitor. Physical dimensions are summarized in Table 9. In comparison with other structures, planar IDE capacitors allow more direct interaction between the sensor and the surrounding environment (Molina-Lopez et al., 2012).
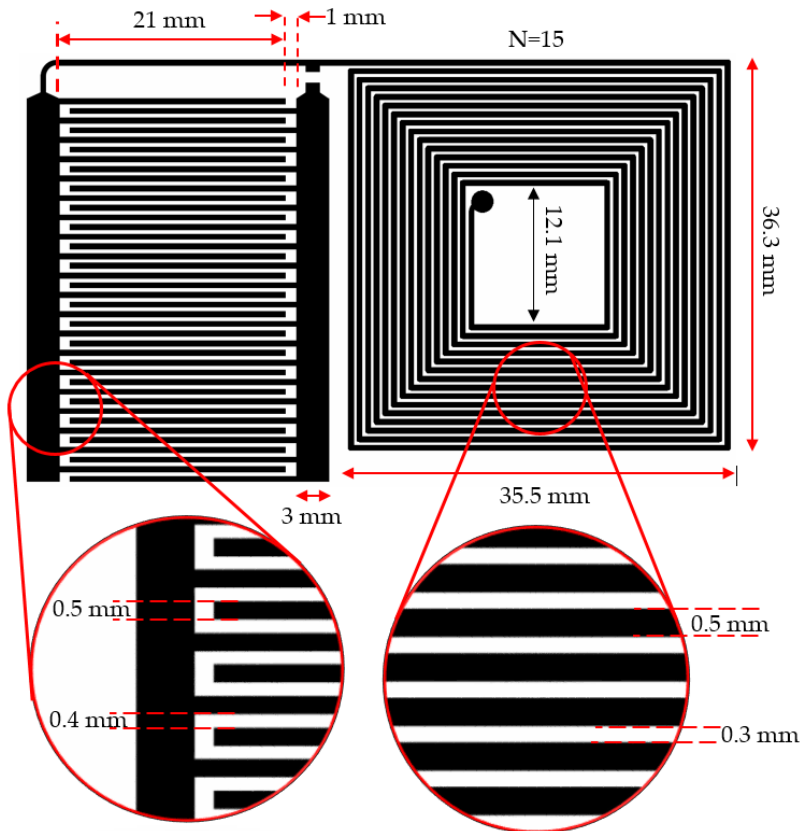
Figure 53. Footprint and geometric dimensions of the passive printed LC-based humidity measurement system.

In the section devoted to chemical printed sensors in Chapter 2, we saw that a possible approach to provide humidity sensitivity consists of depositing a sensing layer on this structure with some humidity-dependent electrical property. The variation of this property with humidity produces changes in the capacitance of the device. But in this case, to simplify the fabrication process we have directly used a polyimide flexible substrate as the sensing element (Boudaden et al., 2018). The electrical permittivity of this material changes accordingly to the relative humidity of the environment. Therefore, the capacitance of the IDE structure will change as a function of humidity. This approach has already been used in literature (Fernandez-Salmeron et al., 2015) but in this case, both elements have been manufactured with screen printing.

Table 9. Physical dimensions of the capacitive interdigitated structure and the planar loop inductor.

	Parameter	Value	Description
	Length	21 mm	Length of each finger
	Width	500 μm	Width of each finger
IDE	Interspacing	400 μm	Distance between consecutive fingers
capacitor	No. Fingers	20	Number of fingers of each electrode
	Separation	1 mm	Distance between finger in one electrode and the backbone of the other electrode
	Width	500 μm	Conductor width
Loop	Interspacing	300 μm	Conductor spacing
inductor	No. Turns	15	Number of turns
	Length 1	35.5 mm	Length of outermost segment
	Length 2	36.3 mm	Length of the other outermost segment

As explained in Section 2.2.1, the resonance frequency in a parallel LC circuit takes place when the two reactances are equal, and it is inversely proportional to inductance and capacitance. The humidity sensing strategy is based on the shift in the resonance frequency because of the change in the capacitance of the printed structure.

The system was screen-printed on 75 μm thick flexible Kapton® HN substrate using the conductive silver-based ink CRSN 2442 (Figure 54). The tag was designed to resonate at approximately 13.56 MHz (HF band). We chose this frequency band to make the system potentially compatible with NFC technology. Physical dimensions, summarized in Table 9, were obtained via numerical simulation. In the case of the loop inductor, ADS simulator from Agilent was used, while COMSOL Multiphysics®

(Comsol Inc., Burlington, MA, USA) was employed to optimize the capacitive structure. The design goal was to achieve the minimum possible dimensions accounting for the limitations of the printed technology employed.

Once the tag was fabricated, the AC electrical characterization was performed by measuring its impedance, both magnitude and phase, using the Precision Impedance Analyzer and the impedance probe kit described in Section 3.2. At dry atmosphere, a capacitance value of 17.96 pF was measured at 13.56 MHz, while the measured inductance at this frequency was 8.06 µH. The measured resonance frequency of the parallel LC circuit at dry atmosphere was 13.88 MHz.
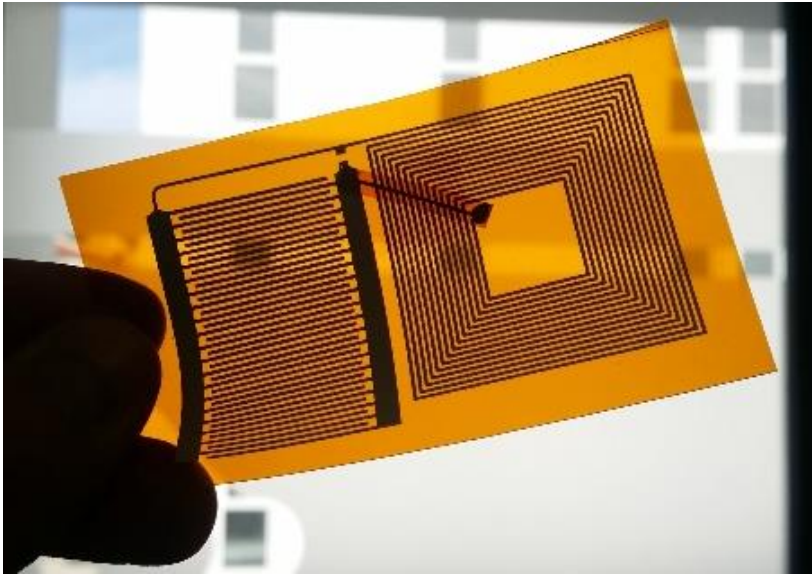
Figure 54. Picture of the LC-based humidity system printed on polyimide Kapton®.

The stationary humidity conditions of the tag were controlled in the climatic chamber VCL4006, where a constant temperature of 20 °C was set. The obtained results, depicted in Figure 55, show that resonance frequency of the LC circuit is shifted from 14.05 MHz at 10% RH to 13.36 MHz when RH is increased up to 90%. Therefore, there is a significant change of about 685 kHz in the resonance frequency of the system. Moreover, a nearly linear behaviour is observed in the resonance frequency shift between these two RH limits.
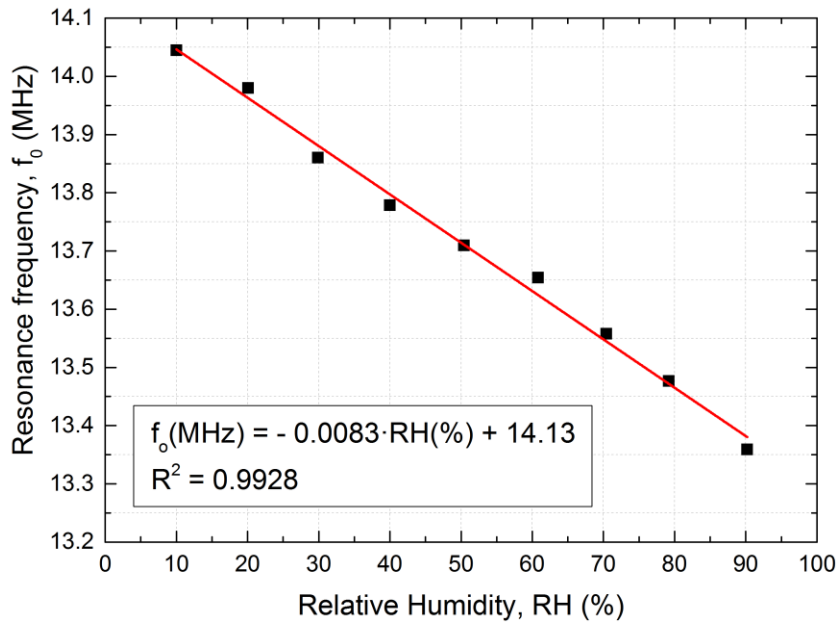
Figure 55. LC resonance frequency as a function of relative humidity.

Considering the flexible nature of the printed system, the reduced dimensions, compact design and chipless approach, this design has the potential to be used in the field of smart packaging applications, since humidity is a magnitude that can reveal the condition of food. To further our research in this regard, we intend to develop a wireless reader unit for this LC-based humidity sensing system (Babu & George, 2016).

4.4 Compact dosimetric system for MOSFETs based on passive NFC tag and smartphone[3]

In-vivo dosimetry is a complementary technique to improve the quality of radiotherapy treatments. The use of small sensor devices to reduce the distortion of the irradiation delivered to the patient is highly advisable. P channel MOSFET (pMOSFET) dosimeters are becoming more popular for in-vivo dosimetry in radiotherapy treatments. There are several commercial dosimetric systems based on pMOSFETs (Best, Ralston, & Suchowerska, 2005; US 8,742,357 B2, 2008) and other systems developed by some research groups (Carvajal et al., 2012; Vasović & Ristić, 2012).

Here we present a dose reader system for commercial pMOSFETs composed of a smartphone and an NFC tag. The sensor module is connected to the NFC tag configured as a reader unit. An Android application has been designed to use an NFC-enabled smartphone for wirelessly powering the system up and reading the dose measurements (Carvajal et al., 2017).

4.4.1 System description

The NFC tag consists of the following functional blocks, depicted in Figure 64: RFID chip and antenna, a charge pump to increase the supply voltage, a current source, conditioning electronic and a socket to connect the sensor module.

The RFID chip SL13A (AMS AG, Unterpremstätten, Austria) along with a custom designed RFID antenna is used for energy harvesting, communication and sensor acquisition purposes (AMS, 2014). This chip operates in HF band and it has a sensor front end (SFE) that is able to measure voltage, current, resistance and capacitance. In this work, the SFE is used as a single voltage input for the built-in ADC of the chip. The ADC input signal must lie between 300 mV and 600 mV. In addition, energy harvesting capabilities of the chosen NFC chip enable the development of battery-free designs. The integrated circuit can provide a regulated voltage of 3.2 V with an output current up to 4 mA if the external RF electromagnetic field from the RFID

---

[3] ©2017 Part of this section, including Figures and Tables, have been reprinted and adapted with permission under the Creative Commons CC-BY-NC-ND 4.0 license http://creativecommons.org/licenses/by-nc-nd/4.0/.

reader is adequate. Therefore, this RFID chip is able to provide up to 12.8 mW without battery, which is enough to supply some additional circuitry.
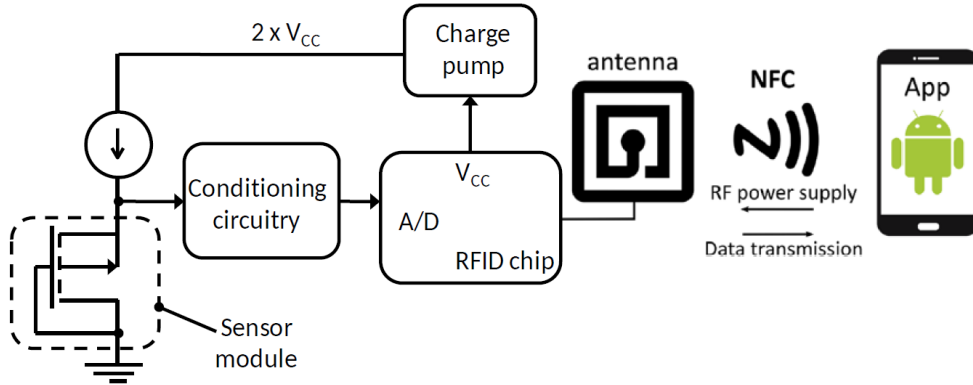
Figure 64. NFC tag and sensor module block diagram of the dosimetric system.

The antenna consists of a PCB custom-designed planar coil and the internal capacitor of the SL13A. The RFID chip communicates with the smartphone through the antenna and, in addition, the energy is harvested through the antenna and supplies the tag. The chosen NFC chip integrates an internal tuning capacitor with a value of 25 pF at the frequency of interest, 13.56 MHz. Thus, according to the theoretical background in Section 2.2.1, a simple coil with a value of 5.5 μH is required to obtain a parallel LC circuit resonant at 13.56 MHz. The designed antenna coil has 12 turns and dimensions of 30 mm × 20 mm. The width of the conductor is 200 μm and the interspacing between the lines is 250 μm. The final number of turns and dimensions were obtained after optimization process with numerical simulations with Advanced Design System (ADS). Antenna and reader tag were fabricated on 1.5 mm thick FR4 substrate using a mechanical milling machine ProtoMat S100, as described in Section 3.1.3. The developed tag is shown in Figure 65. It operates without battery, only with the energy harvested from the electromagnetic field coming from the smartphone NFC link.

For electrical characterization of the tag antenna an impedance analyser was used, the Agilent 4294A. For thermal measurements, four devices were introduced into the climate chamber VCL4006 while the electrical parameters were registered with a multimeter Agilent 34410A (Agilent, USA). For the app, Android Studio 2.3.1 was used. The application was designed and tested against API level 22 (Android 5.1), although the lowest API level compatible is API level 16 (Android 4.1). The smartphone used in this work as the NFC reader was the Sony Xperia S.
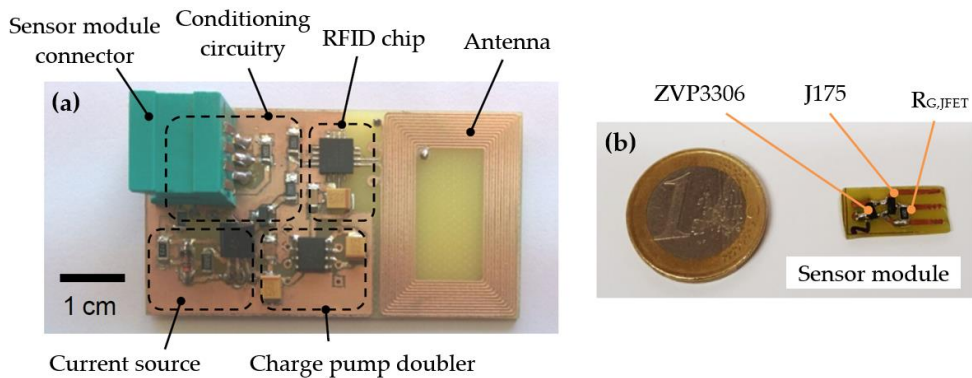
Figure 65. NFC tag with the functional blocks highlighted **(a)** and sensor module **(b)**.

A different set of three sensor modules based on the commercial pMOSFET ZVP3306 (Zetex Diode, USA) were irradiated with a linear accelerator Siemens Artiste (Siemens AG, Germany). A total of 20 Gy were provided in a series of five sessions of 4 Gy each, with a field of 10×10 cm² with photon beams of 6 MV. The sensors were placed at the isocenter of the irradiation source. In order to achieve the electronic equilibrium, a 1.5 cm build-up layer of solid water was placed over the transistors. To control LINAC stability and to verify dose measurements, a PTW23332 ionization chamber (Radiation Products Design, Inc.; Albertville, France) was placed under the sensor modules for every irradiation session.

The easiest way to measure the threshold voltage shifts of pMOSFET as radiation sensor is the measurement of the source voltage shifts at constant current. To do so and carry out dose measurements, a current source has been included in the tag as well as a buffer to avoid that the conditioning circuit loads the current source. The integrated circuit LM334 of Texas Instruments (Dallas, Texas, USA) has been used to implement the current source with the circuit topology recommended by the manufacturer of the LM334 to reduce the thermal drift of the output current, using two resistors and diode (see Figure 66).

The buffer consists of a general propose bipolar transistor model BC848 (Infineon AG, Germany), which avoids the subtraction of drain current by the voltage divider and ADC of the SL13A. The collector current depends on the value of source voltage, V_S, and it must be set for each transistor model and drain current selected, as it is described in following sections for the transistor ZVP3306. The output of the conditioning circuitry must lie between 300 and 600 mV because this is the input voltage range of the ADC. Thus, a voltage divider is required and implemented with R1 and R2 resistors. Moreover, a voltage shift of a reference voltage, V_{ref}, has been included to reduce the voltage before the ADC, as Figure 66 shows.
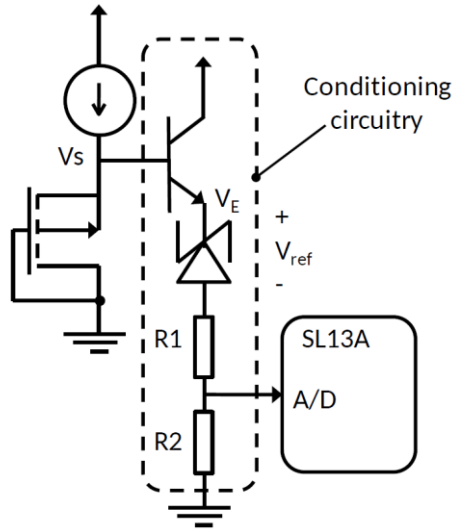
Figure 66. Signal and power conditioning: Buffer, voltage shift and voltage divider schematic circuit of the tag reader.

The ADC input voltage is given by:

$$V_{in}^{ADC} = \frac{R_2}{R_1 + R_2}(V_S - V_{BE} - V_{ref}) \qquad (4.4)$$

The selected Vref was the LM385-1.2 of Texas Instruments (USA) that provides a stable voltage of 1.23 V with a typical thermal dependence of 20 ppm/ºC. The main restriction is that the reverse current must be between 0.01 and 20 mA. Taking into account that the voltage source of the ZVP3306 was around 2.6 V at the chosen bias current, the resistors R1 and R2 were selected as 15 kΩ to ensure a reserve current in the LM385 of 0.03 mA, which is in the correct range of this reference voltage.

The power harvested by the antenna, after being rectified and regulated by the RFID chip, is used to supply the switch capacitor voltage doubler based on ADM660 integrated circuit (Analog Devices, USA). This chip was chosen due to its low quiescent current, 600 µA, and the easy doubler configuration in which only two external capacitors are required. In this way, the regulated voltage of 3.2 V is increased up to 6.4 V in order to increase the maximum drain-source voltage. Assuming a DC/DC efficiency of 80 %, and considering the quiescent current of the ADM660, the total power that must be provided by the SL13A is around 4 mW. This power can be supplied by the SL13A if the inductive coupling between the coil of the smartphone and the coil of the tag is appropriate.

Figure 67 shows the sensor module, which consists of the pMOS transistors as radiation sensor and a JFET that prevents the damage due to electrostatic discharge during the storage and irradiation period. Since a negative voltage is not available in the NFC tag, an N-channel JFET cannot be used. Therefore, a P-channel JFET connecting the source and drain terminals of the pMOS has been used despite its higher ON resistance. The J175 from NXP Semiconductors (Eindhoven, Netherlands) was selected. This device presents a typical ON resistor of 125 Ω and a gate-source cut-off voltage of 3 to 6 V. In our case, the gate was connected directly to the power supply voltage, which was enough to cut off the JFET.
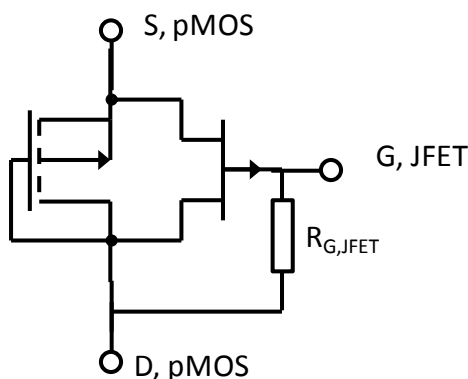
Figure 67. Sensor module schematic.

The pMOSFET drain and BJT collector currents were both selected both to properly bias the device properly for reading out and to reduce the thermal coefficient of the emitter voltage. The thermal behaviour assumed in the present work is a linear model, as already assumed with good results in our previous works (Carvajal et al., 2011; Carvajal, Martínez-García, Guirado, Martínez-Olmos, & Palma, 2016; Carvajal, Martínez-García, Martínez-Olmos, Banqueri, & Palma, 2014). Therefore, the voltage increments due to temperature changes (ΔT) can be written as follows:

$$\Delta V_{in}^{ADC} = \alpha \Delta T, \Delta V_S = \alpha_S \Delta T, \Delta V_{BE} = \alpha_{BE} \Delta T \qquad (4.5)$$

where α is the thermal coefficient of the ADC input voltage, α_S is the thermal coefficient of the source voltage and α_{BE} is the thermal coefficient of the base-emitter voltage. Neglecting the thermal dependence of the voltage divider and the reference voltage, the thermal coefficient of the input A/D converter voltage can be obtained from Equation 4.6 as follows:

$$\alpha = \frac{R_2}{R_1 + R_2}(\alpha_S - \alpha_{BE}) \qquad (4.6)$$

If α_S and α_{BE} are very similar, the thermal dependence of the voltage input of the ADC will be minimized. According to our previous work (Carvajal et al., 2016), the thermal coefficient of the source voltage of the ZVP3306 in saturation region with gate and drain short-circuited and biased at a current of 220 µA was (-2.30 ± 0.12) mV/°C. In the same work, the reverse diode was characterized as temperature sensor, obtaining a thermal coefficient of (-2.332 ± 0.013) mV/°C for a diode current of 30 µA. In the case of our previous reader unit, an operational amplifier instead of a bipolar transistor was used as buffer. Thus, the method described above cannot be applied to reduce the thermal dependence in dose measurements with the previous reader unit. To minimize the thermal drift in that case, the drain current selected to measure the increment of source voltage was 100 µA. At that current, the thermal coefficient was minimum for these transistors (2.04 ± 0.12) mV/°C. To sum up, the drain currents used for dose measurements are 220 µA and 100 µA for the NFC reader and our previous reader respectively, and 30 µA for the collector current of the buffer in the NFC reader.

4.4.2 Android application

The chosen SL13A chip is compliant with the ISO15693 RFID standard and compatible with Android near-field communication (NFC-V standard). The application is based on the use of ISO15693 and cool-Log commands. These latter are EPC (Electronic Product Code) custom commands with the same structure as the standard ISO15693 commands. Figure 68 shows a screenshot of the application user interface. It consists of several text fields showing information about the tag identification number, temperature and the digital value of the external voltage read through the SFE of the chip.

When the phone is approached to the tag, the user can start the application, which programmatically activates the NFC of the phone. The system is powered up by the electromagnetic energy from the mobile NFC link, the tag is detected and the measurements are taken The ADC measurements from the external sensor interface analog input are taken within an independent thread of the application that executes during 10 seconds, reading a value of the ADC each 500 milliseconds. Each measurement is written on a file that is stored in the internal memory of the phone. After that, the NFC is automatically turned off. It is important to switch the NFC on at the beginning of the measurement and then switch it off when the measurement is concluded, because when a pMOSFET is biased an initial decay of source-voltage is

produced due to activation of low state. The effect of this decay is minimized if the time during which the pMOSFET is biased before the source voltage measurement is the same in every measurement. It should be noted that the smartphone needs to be rooted first since Android API does not allow to enable or disable NFC programmatically without root access.
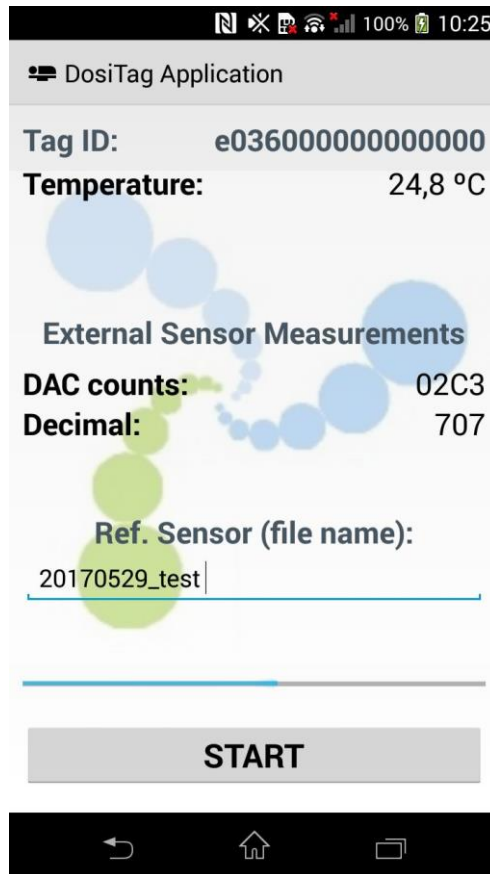
Figure 68. Screenshot of the custom designed Android application for the NFC reader dosimetric system.

The alignment for identification of an NFC tag is not critical if the power consumption of the tag is low, as it happens in typical digital applications such as contactless payments. However, in tags with sensing capabilities with higher power consumption, the inductive coupling between the external NFC reader coil and the tag coil must be good enough. The distance must be as short as possible and both coils should be overlapped, in order to optimize the energy harvested by the tag. In our case, a wood structure was handmade to ensure the adequate and repeatable

inductive coupling. The tag is placed into the structure keeping the sensor socket accessible, as shown in Figure 69.

Figure 69. Experimental setup for NFC measurements using a custom-made wood structure to ensure adequate and repeatable inductive coupling.

4.4.3 Results and discussion

Figure 70 shows the measured inductance and quality factor of the PCB coil without the SL13A chip. The inductance at 13.56 MHz is 5.41 µH, very close to the designed value. In addition, the quality factor achieved using a FR-4 substrate is higher than 60, enough for this type of applications, and the self-resonance frequency is much higher than 13.56 MHz, about 36 MHz in our case. Therefore, the coil can be considered valid for our requirements.

Once the SL13A is attached to the PCB, the resonant circuit is completed. Thus a new frequency characterization was carried out, measuring the impedance and phase of the parallel LC resonant circuit. In order to fine-tune the resonant frequency, a 4.9 pF parallel capacitor has been included. As can be observed in Figure 71, the measured resonant frequency is 13.575 MHz, which is very close to the desired working frequency of 13.56 MHz.
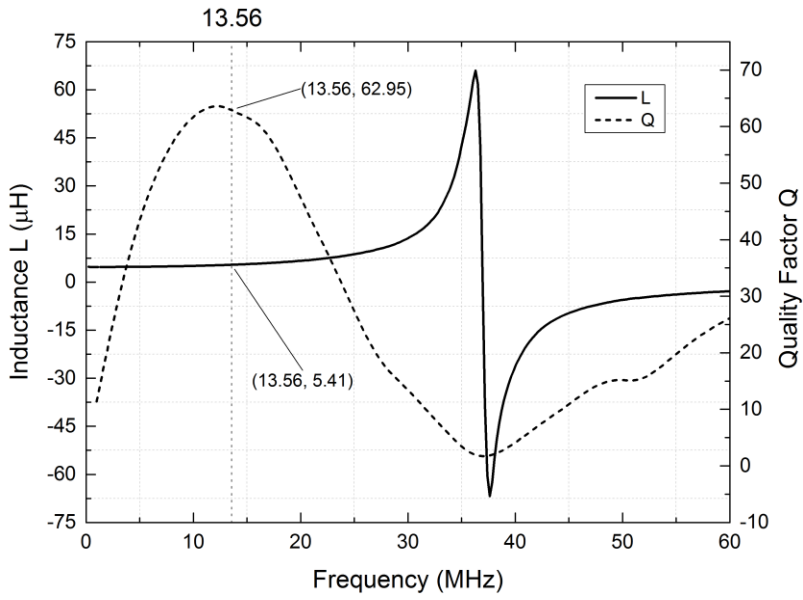
Figure 70. Inductance and quality factor of PCB planar coil without the SL13A chip.
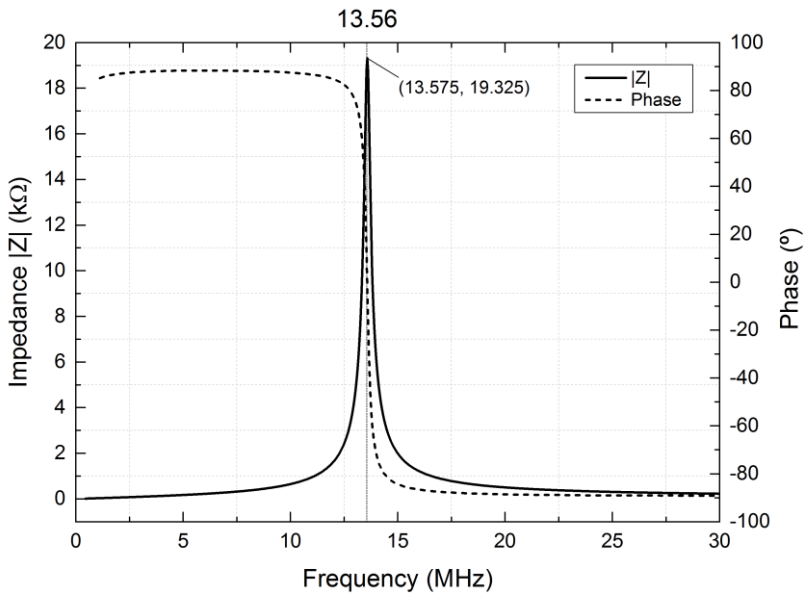
Figure 71. Impedance and phase of the antenna coil with the SL13A chip soldered on the PCB.

The stability of the current source in terms of thermal dependence was measured using a 12 kΩ resistor (equivalent resistance of the ZVP3306 at 220 µA) as load and registering the current. The tag was supplied by a DC power source fixed at 6.4 V and it was placed into the climate chamber. The temperature was varied from 0 °C to 50 °C while the output current was measured. Applying a linear fitting, the thermal drift obtained was lower than 70 nA/°C, which is good enough for our requirements. Therefore, we can consider the current source suitable for our design.

Once the thermal stability of the current source was verified, we studied the thermal dependence of the whole sensor module. Four sensor modules were placed into the climate chamber and the temperature was changed from 0 °C to 50 °C. The source voltage of the pMOS transistor, V_S, and the emitter voltage of the BJT, V_E, were registered (see Figure 66), and the thermal coefficient of these voltages were measured for each sensor module. Finally, the average thermal coefficients of the set of sensor modules was calculated. The global thermal coefficient of the set of sensor modules was reduced from (-1.80 ± 0.15) mV/°C to (0.63 ± 0.10) mV/°C. The thermal compensation was not as good as expected due to the difference between the thermal coefficient of the source voltage obtained in our previous work (Carvajal et al., 2016), (-2.30 ± 0.12) mV/°C; and the thermal coefficient obtained in the present work (-1.80 ± 0.15) mV/°C. Anyway the thermal coefficient reduction is enough for our requirements.

To test the NFC reader unit, a comparison with our previously developed dose reader unit was carried out. Before irradiations, the source voltage for each sensor was measured with our previous reader and the developed NFC reader unit. Five minutes after the irradiation, the source voltage shift was measured. The obtained results from the three analysed sensors using both the NFC reader unit and the previous reader are displayed in Figure 72a and Figure 72b, respectively, and summarised in Table 10 for the three studied sensors.

Table 10. Sensitivities (mV/Gy) found for the three sensor modules using the NFC reader and the previous reader unit.

	# 1	# 2	# 3	Average
NFC reader	4.64 ± 0.03	4.69 ± 0.02	4.92 ± 0.03	4.75 ± 0.15
Previous reader	4.88 ± 0.02	4.89 ± 0.04	4.77 ± 0.03	4.85 ± 0.07
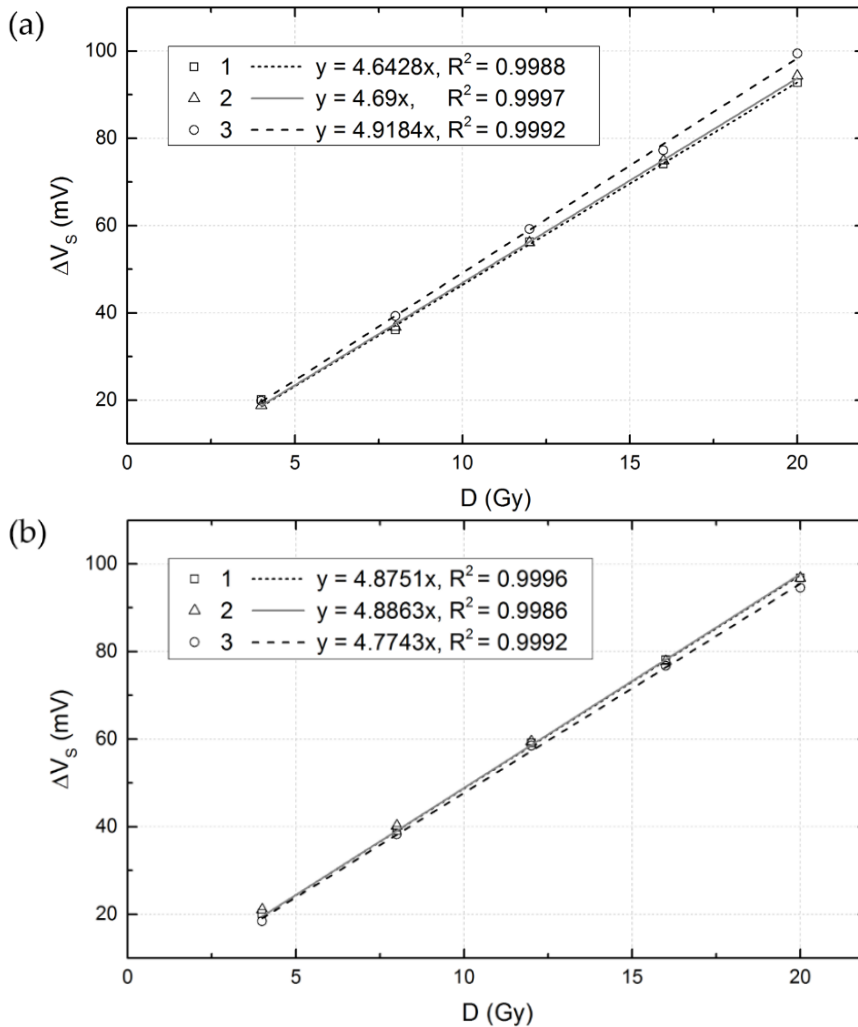
Figure 72. Accumulated source voltage shift versus dose measured by **(a)** the NFC reader unit; **(b)** the previously developed reader.

The average sensitivity found with the NFC reader unit is (4.75 ± 0.15) mV/Gy, which is in good agreement with the sensitivity measured by our previous reader, (4.85 ± 0.08) mV/Gy. As expected, a higher standard deviation is found with the NFC reader unit where the system simplicity does not allow the features of high performance readers. In any case, technical specifications of the presented architecture can be considered suitable to the majority of applications.

4.5. Publication 1

Passive UHF RFID Tag for Multispectral Assessment[4]

Pablo Escobedo [1], Miguel A. Carvajal [1], Luis F. Capitán-Vallvey [2], José Fernández-Salmerón [3], Antonio Martínez-Olmos [1] and Alberto J. Palma [1,*]

[1] ECsens, CITIC-UGR, Department of Electronic and Computer Technology, ETSIIT University of Granada, Granada E-18071, Spain; pabloescobedo@ugr.es (P.E.); carvajal@ugr.es (M.A.C.); amartinez@ugr.es (A.M.-O.)

[2] ECsens, Department of Analytical Chemistry, Faculty of Sciences, University of Granada, Granada E-18071, Spain; lcapitan@ugr.es

[3] Institute for Nanoelectronics, Technical University of Munich, Munich DE-80333, Germany; jfsalmeron@nano.ei.tum.de

[*] Correspondence: ajpalma@ugr.es; Tel.: +34-958-242-300; Fax: +34-958-242-330

Abstract

This work presents the design, fabrication, and characterization of a passive printed radiofrequency identification tag in the ultra-high-frequency band with multiple optical sensing capabilities. This tag includes five photodiodes to cover a wide spectral range from near-infrared to visible and ultraviolet spectral regions. The tag antenna and circuit connections have been screen-printed on a flexible polymeric substrate. An ultra-low-power microcontroller-based switch has been included to measure the five magnitudes issuing from the optical sensors, providing a spectral fingerprint of the incident electromagnetic radiation from ultraviolet to infrared, without requiring energy from a battery. The normalization procedure has been designed applying illuminants, and the entire system was tested by measuring cards from a colour chart and sensing fruit ripening.

1. Introduction

In its simplest form, a radio frequency identification (RFID) tag is composed of an antenna and an integrated circuit (IC). Most popular RFID tags are low-cost passive tags that draw energy from the electromagnetic field radiating from the reader when they are within range of its interrogation zone [1]. In this regard, printed electronics are a good solution to manufacture thin, wearable, flexible, lightweight, and cost-effective electronic devices [2]. There are several examples of RFID tags produced with printing techniques such as screen printing, gravure, flexography, and inkjet printing, among others [3–7].

There is growing interest in including sensing capabilities in RFID tags in order to expand their features, adopting different solutions to achieve this aim. On one hand, some authors have associated the tag's analog response (read range, resonance frequency, backscattered power, etc.) with a variation in the monitored magnitude [4,8–14]. However, although quite valuable results have been achieved, several factors could interfere in link performance, making it difficult to distinguish whether the change in the tag's analog response is in fact due to a variation in magnitude or to some other interference. Moreover, the RFID reader generally needs to include additional circuitry to detect a tag response change. On the other hand, there are some other approaches to design the sensor tag based on passive, semi-passive or active operation modes proposed for packaging surveillance applications [15,16]. Some of these designs combine microcontroller architectures with RFID chips to incorporate different environmental sensors together: temperature, light, and acceleration [17]; temperature, humidity, and gases [18–20]; ion or gas concentration [21–23]; pressure [24–26]; temperature with surface acoustic wave (SAW) sensors [27,28]; or general RFID platforms [29–33]. Other single-chip sensing architectures without a microcontroller unit have also been reported [34–36]. These strategies have the advantage of both processing the sensor data directly in the RFID tag and reducing costs. In addition, chipless RFID tags do not require any IC in the transponder as they encode the data in the frequency or the time domain [37,38]. This chipless approach has been used to develop tags sensing temperature [39], humidity [40,41], surface cracks [42], gases [43,44], and visible radiation [45].

In this work, we present the design, fabrication, characterization, and validation of a passive printed RFID tag with multiple optical sensing capabilities. The main novelty is the ability to measure up to five magnitudes from different sensors with a unique, fully passive printed tag. The tag, directly powered from the electromagnetic field

that the RFID reader radiates, includes five photodiodes to cover a wide spectral range: infrared (IR), visible region (blue (B), green (G), and red ((R) components), and ultraviolet (UV). These sensors provide useful information to detect spectral data, and their practical applications can be extended to areas such as colourimetry and optical chemical sensing [46]. The tag has been printed on a flexible substrate using screen-printing technology, making it adaptable to different shapes and useful in smart packaging applications. The tag architecture boosts the sensing capabilities of the RFID chip, allowing the use of five external sensors with a single chip, as explained in Section 2. In Section 3, two possible applications are tested, both in the context of reflective colour sensing. The first application consists of a simple colour checker of plain-coloured cardboards. In the second application, the tag is used for identifying the stage of banana ripening, from immature to overripe.

2. Materials and Methods

2.1. Sensor Tag Architecture

Figure 1 shows a schematic diagram of the RFID tag architecture. This architecture was presented in rigid FR4 substrate in a previous conference paper [47]. The tag comprises an SL900A RFID chip (AMS AG, Unterpremstaetten, Austria) compatible with the EPC Gen 2 RFID standard [48], a microcontroller unit (MCU) PIC16LF1703 (Microchip Technology Inc., Chandler, AZ, USA), an RGB colour sensor KPS-5130PD7C (Kingbright Electronic Co., Issum, Germany) with three silicon photodiodes (one each for red, green, and blue), a Silicon PIN IR photodiode TEMD7100X01 (Vishay Intertechnology, Inc., Malvern, PA, USA), a UV Schottky-type photodiode GUVA-S12SD (Roithner LaserTechnik GmbH, Vienna, Austria), and extra circuitry to interface the optical sensors.

Moreover, the RFID chip has a fully integrated temperature sensor and two inputs for external sensors. We used this RFID chip in a previous work where two sensors were handled with no MCU (Fernández-Salmerón et al., 2015). Now, we have included a MCU to expand the possibilities of sensor reading with a novel strategy based on controlling a low power array of analog switches as it will be explained below. The tag has a passive architecture, in which the antenna harvests the energy necessary for powering up the system from the reader's EM field. The antenna was designed to resonate at 868 MHz, corresponding to the UHF European RFID band. The radio frequency interface includes an RF Surface Mount Device (SMD) inductor to match the chip input impedance [48].
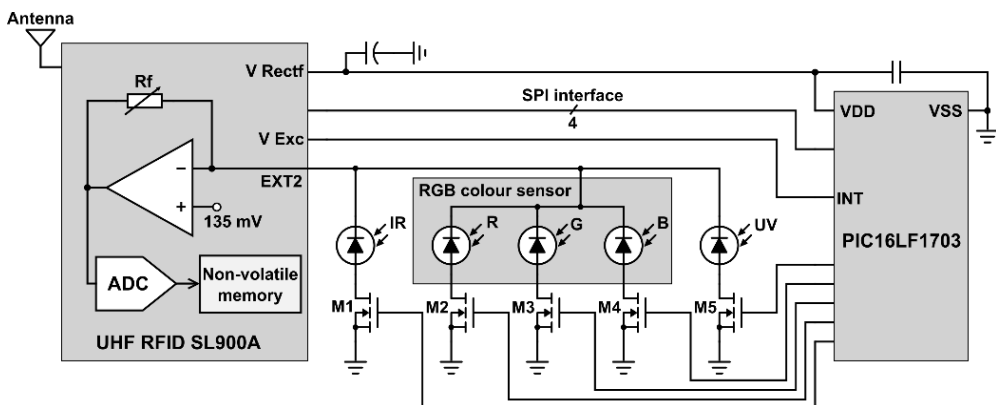
Figure 1. Schematic diagram showing the optical sensor mode of the RFID chip and its connection with the five photodiodes and the microcontroller unit.

The RFID chip is directly connected to the microcontroller, which was selected for its low power consumption (nanoWatt XLP technology). The microcontroller communicates with the RFID chip by means of a Serial Peripheral Interface (SPI) bus. The RGB colour sensor and the IR and UV photodiodes are connected to the Sensor Front End (SFE) of the RFID chip, which comprises different sensor conditioning stages and a 10-bit Analog to Digital Converter (ADC). The voltage input range of the integrated ADC is set with two voltage references (V_{o1} and V_{ref}) selectable in 50 mV steps from 160 mV to 610 mV. In addition, the V_{o1} voltage reference can be directly tied to ground. The V_{ref} voltage defines the lower voltage limit, while the upper voltage limit is defined by $2V_{ref} - V_{o1}$. These voltage references allow the selection of a particular resolution and range. As shown in Figure 1, the sensor conditioning stage internally consists of an operational amplifier with negative feedback, combined with a selectable feedback resistor R_f (185, 400, 875, 1875, or 3875 kΩ). The non-inverting input is fixed at 135 mV. Therefore, this configuration is a current-to-voltage conversion stage with selectable gain by choosing the value of the feedback resistor. It allows measurements with an optical sensor based on a reverse-bias diode current, such as a photodiode. The input voltage in the ADC V_{ad} is related to the reverse diode current:

$$I_D = (V_{ad} - 135 \text{ mV})/R_f \tag{1}$$

Our RGB colour sensor is composed of a three-channel Si photodiode sensitive to red (peak sensitivity wavelength λ_P = 620 nm), green (λ_P = 550 nm), and blue (λ_P = 470 nm) spectral regions. The TEMD7100X01 infrared photodiode has a peak sensitivity at 950 nm and the GUVA-S12SD is sensitive to ultraviolet radiation (λ_P = 350 nm). Each photodiode channel generates a current proportional to the incident radiation.

Figure 2 depicts the spectral sensitivity of each photodiode according to the manufacturer's data [49–51].
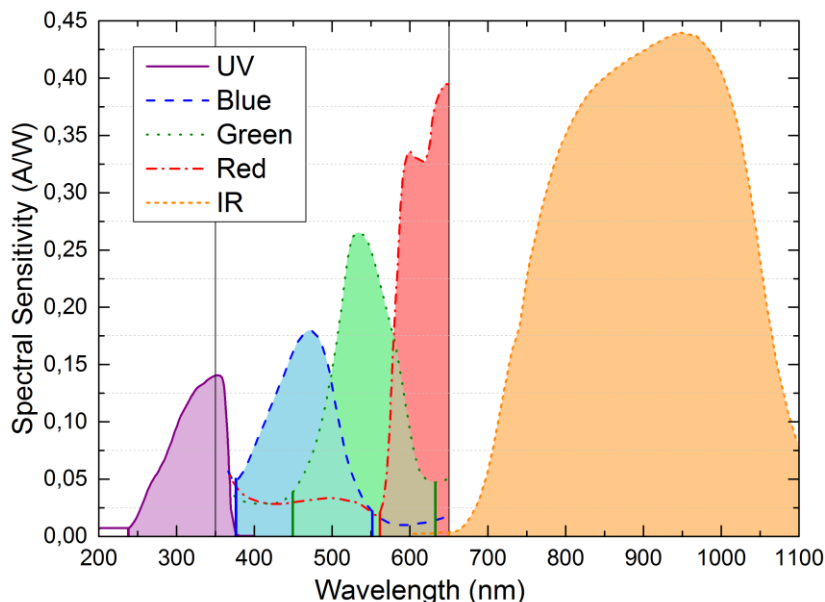
Figure 2. Spectral sensitivities of each photodiode according to manufacturer's data. Vertical lines at 350 nm and 650 nm delimit the available manufacturer's data for the RGB colour sensor.

In theory, the chip does not require any external components to read out a voltage value. However, since we wanted to sequentially measure the output of each photodiode in the same access, we included a switch based on five discrete MOS transistors combined with the microcontroller unit. The transistors are BSS138LT1 NMOS (Semiconductor Components Industries LLC, Phoenix, AZ, USA) with a resistance value in on-region $R_{DS(ON)}$ = 3.5 Ω. Each transistor is connected to the anode of each photodiode (Figure 1). The sensors have a common cathode connected to the inverting input of the operational amplifier (EXT2 pin in the RFID chip). The gates of the five transistors are connected to different microcontroller outputs. The microcontroller generates the switch control signals, sequentially activating each output at a time. Therefore, one photodiode (ultraviolet, blue, green, red, or infrared) is read at each access. Every time an output is active, the microcontroller sends an SPI command to the RFID chip to measure the corresponding photodiode current. Then, the microcontroller saves the sensor readings using SPI commands on a specific location of the RFID chip's non-volatile memory so it can later be accessed by the RFID reader.

At this point, we must state that the proposed switch array to interface more than one sensor can be scaled up not only to five sensors, as presented here, but also to a higher amount of them taking into account the availability of MCU I/O ports that can be used to drive the switches. Therefore, we have designed a generalizable electronic architecture as interface between multiple sensors and a single RFID chip for the development of passive sensing tags.

In order to measure each photodiode output current, it is necessary to properly select the feedback resistor value and the ADC input voltage range. In the case of the feedback resistor, the RFID chip includes an autorange function that automatically selects a proper R_f value to provide unsaturated measurements within the ADC input voltage range. As stated above, the limits of the ADC input voltage are V_{ref} and $2V_{ref}$ − V_{o1}. By default, these reference voltages are $V_{o1} = 0$ V and $V_{ref} = 310$ mV, so the ADC input voltage ranges from 310 mV to 620 mV, leading to a detection range of reverse diode current from 45.24 nA (with $R_f = 3875$ kΩ) to 2.62 μA (with $R_f = 185$ kΩ). Other detection ranges can be easily configured by choosing different values of V_{o1} and V_{ref}. This is done through SPI commands sent from the microcontroller unit to the RFID chip. The minimum detectable current is 32.3 nA and the maximum one is 5.86 μA. Figure 3 shows the fabricated RFID tag with its main components labelled.

A commercial RFID reader compatible with EPC Gen2, DK-UHF RFID HP2 (IDS Microchip AG, Wollerau, Switzerland) is used to power up and read the tag. The latter is done by sending EPC Gen 2 Read commands to access the RFID chip EEPROM memory locations where the measurements have been saved through SPI commands. The RFID reader antenna consists of a circular polarized patch antenna A0025 (Poynting antenna, Samrad, South Africa).
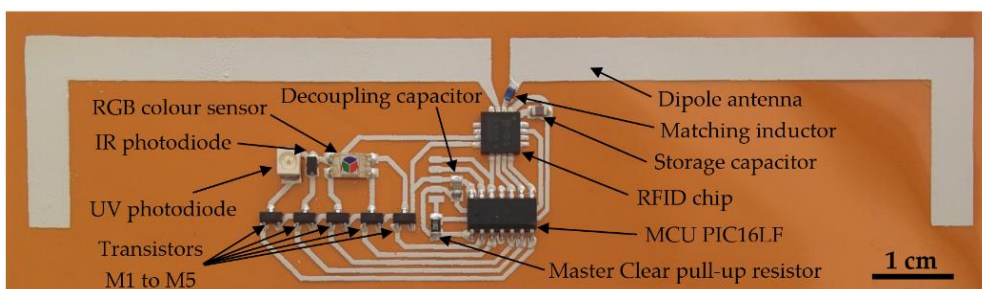
Figure 3. Screen-printed RFID tag on flexible substrate with all components.

2.2. Fabrication Process

The tag pattern is directly printed on polyimide (PI) Kapton® HN (DupontTM, Wilmington, DE, USA), a flexible polymeric substrate. The PI used has a thickness of 75 µm, a relative permittivity (ε_r) of 3.5, and a loss tangent (tanδ) of 0.002. The screen-printing machine is a Serfix III (Seglevint SL, Barcelona, Spain). The screen used to fabricate the single-layer screen-printed tag has a mesh density of 120 nylon threads per centimetre (T/cm). The conductive silver-based ink is CRSN 2442 (Sun Chemical Corporation, Parsippany, NJ, USA). Under these conditions, the printed layer thickness is 13.3 µm and the resistivity is 39 ± 4 µΩ·cm [52]. After printing, the tag is cured at a constant temperature of 150 °C for 20 min to enable the formation of the conductive pattern and obtain the desired resistivity. To assemble the chips and the external components to the substrate, a three-step process was carried out. First, we interconnected the chips and silver pads by using the conductive resin H20E (Epoxy Technology, Inc., Billerica, MA, USA). After this, a double layer of 50-µm-thick dry adhesive, AR Clear 8932 (Adhesives Research, Inc., Glen Rock, PA, USA) was attached to the bottom of the chips to fix them to the substrate. Finally, a heating process was performed in an oven at 120 °C for 20 min to cure the conductive resin. The E5071C Vector Network Analyzer (VNA) (Keysight Tech., Santa Clara, CA, USA) was used to characterize the fabricated antenna. Considering the differential character of the antenna measurement, we defined the S-parameter differential port between port-1 and port-2 through a test fixture simulator included in the VNA. To connect the antenna to the VNA, we used Ultra Miniature Coaxial connectors (U.FL) (Hirose Electric, Tokyo, Japan) attached at the antenna feed point along with SMA to U.FL wires. For calibration purposes, a full custom Short-Open-Load-Thru (SOLT) calibration kit was used [35].

2.3. Methodology

To obtain the optical spectra as reference data in our experimental characterization and validation, we used a high-resolution spectrometer model HR2000+ (Ocean Optics Inc., Dunedin, FL, USA). This device has a spectral response range of 200 to 1100 nm and an optical resolution of 1.10 nm, with a 14-bit ADC module and a fiber light input method. The output of our RFID sensor tag consists of five current values (one for each photodiode) defining a spectral fingerprint. To adapt the spectral fingerprint obtained with our RFID tag, composed of five coordinates, to the spectrum measured by the spectrometer, the following procedure was carried out:

1. Standard normalization of the response of the five photodiodes according to their spectral sensitivities. The aim is to obtain an equivalent spectral graph with the same area under each photodiode response curve, but with a flat spectral

sensitivity. To do that, we divide the area under the spectral sensitivity curve of each photodiode by its bandwidth (see Figure 2). The result of each division is the height of the flat sensitivity whose area is the same as the original spectral sensitivity. Then, we calculate the inverse of these heights. Finally, we normalize them to obtain the normalization factor assigned to each photodiode.

2. Multiplying each current value of the spectral fingerprint (obtained with our RFID tag) by each corresponding normalization factor calculated in Step 1. The result of this step is a set of five coordinates.

3. Assigning each of the five coordinates of the spectral fingerprint to the peak sensitivity wavelength of each photodiode (350, 470, 550, 620, and 950 nm).

4. Considering one of the values of the new spectral fingerprint and its associated wavelength. Then, calculating the factor necessary to get the same value as that obtained with the spectrometer at that particular wavelength.

5. Applying this calculated factor to the five coordinates of the spectral fingerprint.

6. Repeating Steps 4 and 5 for the rest of the coordinates.

7. The final spectral fingerprint is the average of all the values obtained for each photodiode. The error is calculated as the standard deviation of all the values for each photodiode from Steps 5 and 6.

This procedure was developed and optimized by comparing the spectral coordinates from our system to the spectrometer measurements for the studied illuminants. We used seven standard illuminants: white LED (cool and warm), infrared LED, UV lamp, fluorescent light, tungsten halogen lamp, and daylight. As a result, the calculated normalization factors for the five photodetectors were: 1.00 for the UV; 0.75, 0.57, and 0.30 for the blue, green, and red photodiodes, respectively; and 0.29 for the IR photodetector.

The next step was to validate this methodology by identifying cards from a colour chart. We carried out reflective colour-sensing measurements using several plain-coloured cardboards as targets: white, red, green, blue, orange, yellow, and brown. A cool white LED model XPGWHT-L1-0000-00H51 (Cree, Inc., Durham, NC, USA) was used as an illuminant. The geometric setup of the illuminant and detector consists of a typical 45°/0° geometry setup to carry out diffuse reflectance measurements (Figure 4). In this type of reflection, the target surface properties modify the spectrum of the incident light. The RFID reader is placed at the base of the setup to read the output of the photodiodes in the tag. The reader can be moved

away from the target surface up to the maximum read range, which will be shown in the next section. To apply our system in a real situation, we then replaced the cardboards with a banana in order to monitor its stage of ripeness. Bananas change colour from green to yellow as they ripen, then becoming dark brown as they get overripe. The illuminant, setup, and procedure used in the banana experiment were the same as those used with the cardboards.
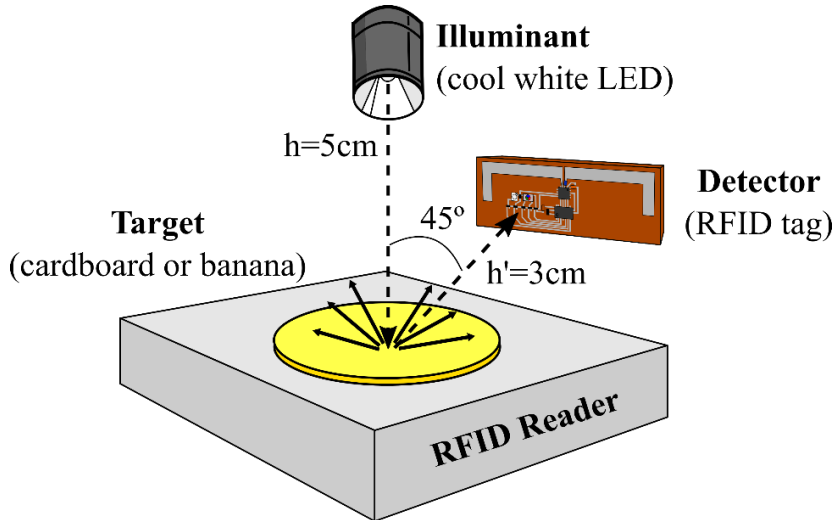
Figure 4. The 45°/0° geometry setup used to carry out diffuse reflectance measurements with the plain-coloured cardboards and the banana.

3. Results and Discussion

3.1. Antenna Characterization

The antenna in Figure 3 is the typical dipole antenna based on the development kit recommended for the SL900A chip by the manufacturer (AG 2014), with final dimensions of the antenna arms of 5.5 mm in width and 79 mm in length. The dipole arms have been bent to optimize the occupied area. The input impedance of the dipole at 868 MHz is $(31.1 + j9.4)\ \Omega$. This dipole is designed to achieve the same real part of the impedance as the RFID chip $(31.1 - j286)\ \Omega$ [53]. The imaginary part is compensated with an SMD matching inductor series 3650 of 51 nH and a quality factor of 60 at 900 MHz (TE Connectivity, Ltd., Schaffhausen, Switzerland) placed on one of its arms. Antenna gain is 0.661 dBi, directivity is 2.401 dBi, and efficiency is 66.97% at the working frequency. These parameters have been obtained by EM simulation with Advanced Design System 2013 (Keysight Technologies Inc., Santa Rosa, CA, USA).

Figure 5 compares the dipole antenna measured response with the simulated one. The obtained resonance value at 868 MHz is −12.5 dB, whereas the simulated one is −13.6 dB. Additionally, we observed a wider range of response. The maximum read range can be calculated using a Friis free-space equation [54]:

$$\text{range}_{\max} = \frac{\lambda}{4\pi} \sqrt{\frac{G_{\text{tag}} \, G_{\text{reader}} \, P_{\text{reader}} \, \tau \, \text{PLF}}{S_{\text{tag}}}} \qquad (2)$$

where λ is the wavelength, G_{tag} is the tag antenna gain, G_{reader} is the reader antenna gain, P_{reader} is the effective power transmitted by the reader, S_{tag} is the RFID chip sensitivity, τ is the power transmission coefficient, and PLF is the polarization loss factor. In our case, the transmission power is 26 dBm and the reader antenna gain is 7 dBi at 868 MHz, according to the manufacturer. The PLF includes the polarization mismatch between the reader antenna (circular polarization) and the tag antenna (linear polarization), with a value of 0.5 (−3 dB). The minimum threshold power necessary to activate the tag and answer the identification inquiries of the EPC protocol is $S_{\text{tag}} = -15$ dBm. However, extra power is required to drive the SFE [35] and power up the microcontroller unit. This power is collected from the reader's radiated EM field. Therefore, the chip sensitivity to read out a value of the photodiode current is increased to −3.98 dBm. Assuming ideal conditions ($\tau = 1$ and $G_{\text{tag}} = 0.661$ dBi as obtained by the EM simulation) and considering the chip sensitivity to be −3.98 dBm, the read range should be 1.5 m, according to Equation (2). The measured read range of 1.1 m for the RFID tag is slightly smaller than the simulated one, perhaps due to the non-ideal behavior of the printed conductive layer, reducing the tag antenna performance. To measure this range, the RFID reader antenna was attached to a tripod and placed in front of the tag at the same height. The measurements were taken in an anechoic chamber.
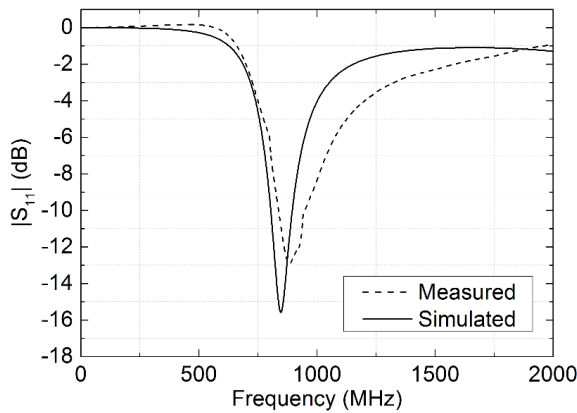
Figure 5. Simulated and measured differential S-parameter of the UHF dipole antenna showing minimal return loss at 868 MHz.

3.2. Tag Performance: Spectral Response

Figure 6 shows the final step of an iterative process where spectral fingerprint coordinates and the full spectral response are fitted. Error bars come from the standard deviations calculated in the final step of the methodology explained in Section 2.3.

Four illuminants are placed directly facing the photodiodes in the tag for this figure. The resulting procedure for computing the spectral fingerprint is an estimation based on the spectral sensitivities provided by each photodiode manufacturer. Despite this, the normalized experimental results can be fitted to the spectral emissions of each illuminant. Therefore, after this optimization process and accounting for the normalization factor correction, the spectral fingerprint obtained allows the identification of the illuminant source applied to the tag.

Figure 6. Comparison of the normalized spectral responses measured with the spectrometer and the spectral fingerprints obtained with the RFID tag for different types of illuminants: cool white LED, ultraviolet lamp, tungsten halogen light, and daylight. Lines are spectrophotometer outputs and dots are spectral fingerprint coordinates.

3.3. Validation and Application in a Real Situation

Apart from the possibility of identifying different illuminants, this passive tag has been used to conduct reflective colour-sensing measurements. We first carried out a validation of this type of measurement using a colour chart as the target. Figure 7 shows the results for seven plain-coloured cardboards: the three primary colours (red, blue, and green), white, yellow, orange, and brown. The illuminant is a cool white LED and the setup is as depicted in Figure 4. It can be observed that the spectrum of the incident light measured with the spectrometer has been modified in accordance with the cardboard surface colour. The spectral fingerprints obtained with the RFID tag also reflect the colour change, and the relative heights of its five coordinates allow the identification of the cardboard colour as well.

(a)   **(b)**

Figure 7. Comparison of the normalized spectral responses measured with the spectrometer and the spectral fingerprints obtained with the RFID tag for reflective colour-sensing experiments with: **(a)** red, green, and blue cardboards; **(b)** white, yellow, orange, and brown cardboards.

Along the same line, we propose an application for our RFID tag in a real situation: identification of the ripening stage of fruit. To this end, we consider a banana as the target and monitor the progress of its ripeness from immature to overripe (see Figure 8a). The banana can be classified as immature, ripe, or overripe according to the relative positions of the five components in its spectral fingerprint. Figure 8b shows photographs of the banana at each ripening stage. Given the colour shift from green to dark brown, an illuminant with a high green component, such as the one used in this study, could be the most suitable one to measure the ripening process.

(a) (b)

Figure 8. (a) Normalized spectral responses measured with the spectrometer and spectral fingerprints obtained with the RFID tag for the progress of banana ripeness from immature to overripe; **(b)** Photographs of the banana tested in its different ripening stages: immature, ripe, and overripe.

Table 1 presents the spectral fingerprint values obtained with our RFID tag for the different targets considered: on one hand, the plain-coloured cardboards used for the validation process, and on the other hand, the banana used for its ripening stage identification. In these cases, most of the information is contained in the blue, green, and red coordinates. This is due to the spectral characteristics of the light source used as an illuminant. Nevertheless, this information is enough to identify the colour in the case of the cardboards and the ripening stage in the case of the banana. Other radiation sources with significant spectral information in the ultraviolet or infrared regions could also be used as illuminants.

Table 1. Spectral fingerprint coordinates obtained with the RFID tag for the reflective colour-sensing experiments with the plain-coloured cardboards and the banana ripening stages.

Target	Spectral Fingerprint Coordinates				
	UV	B	G	R	IR
White cardboard	0.007 ± 0.003	0.37 ± 0.04	0.56 ± 0.05	0.194 ± 0.018	0.0027 ± 0.0006
Red cardboard	0.006 ± 0.004	0.36 ± 0.04	0.51 ± 0.07	0.38 ± 0.05	0.0042 ± 0.0017
Green cardboard	0.005 ± 0.005	0.32 ± 0.03	0.80 ± 0.06	0.154 ± 0.011	0.0036 ± 0.0013
Blue cardboard	0.007 ± 0.003	0.34 ± 0.05	0.52 ± 0.08	0.140 ± 0.020	0.0018 ± 0.0007

Yellow cardboard	0.005 ± 0.005	0.265 ± 0.017	0.98 ± 0.06	0.314 ± 0.018	0.0051 ± 0.0014
Orange cardboard	0.005 ± 0.004	0.34 ± 0.07	0.69 ± 0.14	0.42 ± 0.08	0.0058 ± 0.0021
Brown cardboard	0.006 ± 0.004	0.45 ± 0.04	0.85 ± 0.07	0.29 ± 0.03	0.0050 ± 0.0023
Immature banana	0.0011 ± 0.0003	0.26 ± 0.05	0.90 ± 0.07	0.30 ± 0.06	0.00026 ± 0.00008
Ripe banana	0.00084 ± 0.00007	0.31 ± 0.03	0.968 ± 0.011	0.41 ± 0.04	0.00021 ± 0.00018
Overripe banana	0.008 ± 0.006	0.43 ± 0.04	0.62 ± 0.05	0.2198 ± 0.0021	0.0012 ± 0.0011

4. Conclusions

This work describes a passive printed UHF RFID tag with multiple optical sensor capabilities. Five photodiodes have been integrated on the tag, covering a wide spectral range from ultraviolet to infrared regions. A microcontroller-based switch circuit has been designed and tested to allow the multiplexing of several photodiodes to one SFE input. Furthermore, the chosen RFID chip has a built-in temperature sensor. Therefore, six different magnitudes can be measured in every reading in a fully passive mode. The tag has been manufactured by screen-printing on a flexible polymeric substrate. This system boasts a very high sensing capability, in this case up to six different magnitudes in the same tag. The implemented switch array expands the capabilities of the sensor-enabled RFID chip, which includes at most two inputs for external sensors. As the switching process is sequential, this interface solution is scalable, the number of available MCU I/O pins being the only limitation to the number of sensors that can be interfaced.

The operation of this passive tag has been successfully demonstrated. First, using several standard illuminants, a procedure was defined to obtain the spectral fingerprint of the target illuminant. Therefore, these types of RFID tags would be very useful to detect different light conditions. Subsequently, tag performance was validated through reflective colour-sensing measurements. In this regard, the spectral fingerprints obtained with our RFID tag were modified by the target surface colour, using a cool white LED as an illuminant and different plain-coloured cardboards as targets. As the main limitation, we have detected some influence of the label/illuminant source position on the tag results that should be minimized in later refinements of this design. Also, the measured read range of the tag is limited to 1.1 m. Beyond this range there is no longer sufficient power to drive the SFE of the RFID chip and power up the MCU, whose measured power consumption in operation

mode is 0.42 mW. Finally, we have proposed a real-life application using the same technique to identify the ripeness of a banana from immature to overripe. These results could be extended to the study of other fruits or food in general, and the tag could be used in smart packaging applications.

Author Contributions: P. Escobedo and M.A. Carvajal developed the design of the tag and its experimental characterization and validation. J. Fernández-Salmerón provided the antenna design and its electrical characterization. Luis Fermín Capitán-Vallvey conceived and supervised the screen-printing process, A. Martínez Olmos and Alberto J. Palma supervised the electronic design and the sensor selection. All authors contributed to the discussion of the results and the manuscript writing.

Conflicts of Interest: The authors declare no conflict of interest.

Abbreviations: The following abbreviations are used in this manuscript:

UHF	Ultra high frequency
RFID	Radio frequency identification
IC	Integrated circuit
EM	Electromagnetic
UV	Ultraviolet
IR	Infrared
SMD	Surface mount device
XLP	Extreme low power
SPI	Serial peripheral interface
SFE	Sensor front end
ADC	Analog to digital converter
MOS	Metal-Oxide-Semiconductor
EEPROM	Electrically erasable programmable read-only memory
PI	Polyimide
VNA	Vector network analyzer
LED	Light emitting diode
PLF	Polarization loss factor

References and Notes

1. Finkenzeller, K. *RFID Handbook : Fundamentals and Applications in Contactless Smart Cards, Radio Frequency Identification and Near-Field Communication*, 3rd Ed.; Wiley & Sons, Ltd.: Chichester, UK, 2010.

2. Suganuma, K. Introduction to Printed Electronics. In *SpringerBriefs in Electrical and Computer Engineering*; Springer: New York, NY, USA, 2014; Volume 74.

3. Sutija, D. Printed Sensor Tags and Smart Objects. Available online: http://www.idtechex.com/events/presentations/printed-sensor-tags-and-smartobjects-003757.asp (accessed on 9 November 2015).

4. Virtanen, J.; Ukkonen, L.; Bjorninen, T.; Elsherbeni, A.Z.; Sydänheimo, L. Inkjet-Printed Humidity Sensor for Passive UHF RFID Systems. *IEEE Trans. Instrum. Meas.* **2011**, *60*, 2768–2777.

5. Bozzi, M.; Tentzeris, M.M.; Lakafosis, V.; Le, T.; Kim, S.; Vyas, R.; Georgiadis, A.; Cooper, J.; Cook, B.; Moro, R.; et al. Inkjet-printed antennas, sensors and circuits on paper substrate. *IET Microw. Antennas Propag.* **2013**, *7*, 858–868.

6. Martínez-Olmos, A.; Fernández-Salmerón, J.; Lopez-Ruiz, N.; Rivadeneyra Torres, A.; Capitan-Vallvey, L.F.; Palma, A.J. Screen Printed Flexible Radiofrequency Identification Tag for Oxygen Monitoring. *Anal. Chem.* **2013**, *85*, 11098–11105.

7. Unander, T.; Sidén, J.; Nilsson, H.E. Designing of RFID-based sensor solution for packaging surveillance applications. *IEEE Sens. J.* **2011**, *11*, 3009–3018.

8. Yi, X.; Cho, C.; Cooper, J.; Wang, Y.; Tentzeris, M.M.; Leon, R.T. Passive wireless antenna sensor for strain and crack sensing—Electromagnetic modeling, simulation, and testing. *Smart Mater. Struct.* **2013**, *22*, 085009.

9. Bhadra, S.; Thomson, D.J.; Bridges, G.E. Monitoring acidic and basic volatile concentration using a pH-electrode based wireless passive sensor. *Sens. Actuators B Chem.* **2015**, *209*, 803–810.

10. Cazeca, M.J.; Mead, J.; Chen, J.; Nagarajan, R. Passive wireless displacement sensor based on RFID technology. *Sens. Actuators A Phys.* **2013**, *190*, 197–202.

11. Fernandez-Salmeron, J.; Rivadeneyra, A.; Rodriguez, M.A.C.; Capitan-Vallvey, L.F.; Palma, A.J. HF RFID Tag as Humidity Sensor: Two Different Approaches. *IEEE Sens. J.* **2015**, *15*, 5726–5733.

12. Manzari, S.; Catini, A.; Pomarico, G.; Di Natale, C.; Marrocco, G. Development of an UHF RFID Chemical Sensor Array for Battery-Less Ambient Sensing. *IEEE Sens. J.* **2014**, *14*, 3616–3623.

13. Kimionis, J.; Tentzeris, M.M.; Nikolaou, S. Inkjet-printed UHF RFID folded dipole antennas for remote sensing applications. In Proceedings of the 2014 IEEE Antennas and Propagation Society International Symposium (APSURSI), Memphis, TN, USA, 6–11 July 2014; pp. 332–333.

14. Croux, D.; Vangerven, T.; Broeders, J.; Boutsen, J.; Peeters, M.; Duchateau, S.; Cleij, T.; Deferme, W.; Wagner, P.; Thoelen, R.; et al. Molecular imprinted polymer films on RFID tags: A first step towards disposable packaging sensors. *Phys. Status Solidi* **2013**, *210*, 938–944.

15. Unander, T.; Nilsson, H.-E. Characterization of Printed Moisture Sensors in Packaging Surveillance Applications. *IEEE Sens. J.* **2009**, *9*, 922–928.

16. Nilsson, H.-E.; Unander, T.; Siden, J.; Andersson, H.; Manuilskiy, A.; Hummelgard, M.; Gulliksson, M. System Integration of Electronic Functions in

Smart Packaging Applications. *IEEE Trans. Compon. Packag. Manuf. Technol.* **2012**, *2*, 1723–1734.

17. De Donno, D.; Catarinucci, L.; Tarricone, L. A Battery-Assisted Sensor-Enhanced RFID Tag Enabling Heterogeneous Wireless Sensor Networks. *IEEE Sens. J.* **2014**, *14*, 1048–1055.

18. Smits, E.; Schram, J.; Nagelkerke, M.; Kusters, R.; Heck, G.; Van Acht, V.; Van Koetse, M.; Brand, J.; Van Den Gelinck, G.; Schoo, H. Development of printed RFID sensor tags for smart food packaging. In Proceedings of the 14th International Meeting on Chemical Sensors, Nuremberg, Germany, 20–23 May 2012; pp. 403–406.

19. Pursula, P.; Marttila, I.; Nummila, K.; Seppa, H. High Frequency and Ultrahigh Frequency Radio Frequency Identification Passive Sensor Transponders for Humidity and Temperature Measurement Within Building Structures. *IEEE Trans. Instrum. Meas.* **2013**, *62*, 2559–2566.

20. Oprea, A.; Courbat, J.; Bârsan, N.; Briand, D.; de Rooij, N.F.; Weimar, U. Temperature, humidity and gas sensors integrated on plastic foil for low power applications. *Sens. Actuators B Chem.* **2009**, *140*, 227–232.

21. Steinberg, M.D.; Kassal, P.; Tkalčec, B.; Murković Steinberg, I. Miniaturised wireless smart tag for optical chemical analysis applications. *Talanta* **2014**, *118*, 375–381.

22. Kassal, P.; Steinberg, I.M.; Steinberg, M.D. Wireless smart tag with potentiometric input for ultra low-power chemical sensing. *Sens. Actuators B Chem.* **2013**, *184*, 254–259.

23. Eom, K.H.; Kim, M.C.; Lee, S.; Lee, C.W. The Vegetable Freshness Monitoring System Using RFID with Oxygen and Carbon Dioxide Sensor. *Int. J. Distrib. Sens. Netw.* **2012**, *2012*, 1–6.

24. Fernández-Salmerón, J.; Rivadeneyra, A.; Martínez-Martí, F.; Capitán-Vallvey, L.; Palma, A.; Carvajal, M. Passive UHF RFID Tag with Multiple Sensing Capabilities. *Sensors* **2015**, *15*, 26769–26782.

25. Fernández, I.; Asensio, A.; Gutiérrez, I.; García, J.; Rebollo, I.; de No, J. Study of the Communication Distance of a MEMS Pressure Sensor Integrated in a RFID Passive Tag. *Adv. Electr. Comput. Eng.* **2012**, *12*, 15–18.

26. Beriain, A.; Rebollo, I.; Fernandez, I.; Sevillano, J.F.; Berenguer, R. A passive UHF RFID pressure sensor tag with a 7.27 bit and 5.47 pJ capacitive sensor interface. In Proceedings of the 2012 IEEE/MTT-S International Microwave Symposium Digest, Montreal, QC, Canada, 17–22 June 2012; pp. 1–3.

27. Malocha, D.; Gallagher, M.; Fisher, B.; Humphries, J.; Gallagher, D.; Kozlovski, N. A Passive Wireless Multi-Sensor SAW Technology Device and System Perspectives. *Sensors* **2013**, *13*, 5897–5922.

28. Kang, A.; Zhang, C.; Ji, X.; Han, T.; Li, R.; Li, X. SAW-RFID enabled temperature sensor. *Sens. Actuators A Phys.* **2013**, *201*, 105–113.

29. Vyas, R.; Lakafosis, V.; Rida, A.; Chaisilwattana, N.; Travis, S.; Pan, J.; Tentzeris, M.M. Paper-Based RFID-Enabled Wireless Platforms for Sensing Applications. *IEEE Trans. Microw. Theory Tech.* **2009**, *57*, 1370–1382.

30. Picdi, J.-M.C.; Rmili, B. An ultra low power RFID sensor platform for launchers applications. In Proceedings of the IEEE International Conference on Wireless for Space and Extreme Environments, Baltimore, MD, USA, 7–9 November 2013; pp. 1–5.

31. Wang, J.; Fu, L.; Han, H.; Min, H.; Lee, K.B. A Low-Cost Configurable ISO/IEC/IEEE 21451-7-Compatible Sensor Tag. *IEEE Sens. J.* **2015**, *15*, 2451–2459.

32. Iero, D.; Della Corte, F.G.; Felini, C.; Merenda, M.; Minarini, C.; Rubino, A. RF-powered UHF-RFID analog sensors platform. In Proceedings of the 2015 XVIII AISEM Annual Conference, Trento, Italy, 3–5 February 2015; pp. 1–3.

33. Sample, A.P.; Yeager, D.J.; Powledge, P.S.; Mamishev, A.V.; Smith, J.R. Design of an RFID-Based Battery-Free Programmable Sensing Platform. *IEEE Trans. Instrum. Meas.* **2008**, *57*, 2608–2615.

34. Catarinucci, L.; Colella, R.; Tarricone, L. Enhanced UHF RFID Sensor-Tag. *IEEE Microw. Wirel. Compon. Lett.* **2013**, *23*, 49–51.

35. Salmerón, J.F.; Rivadeneyra, A.; Agudo-Acemel, M.; Capitán-Vallvey, L.F.; Banqueri, J.; Carvajal, M.A.; Palma, A.J. Printed single-chip UHF passive radio frequency identification tags with sensing capability. *Sens. Actuators A Phys.* **2014**, *220*, 281–289.

36. Cho, N.; Song, S.-T.; Kim, S.; Kim, S.; Yoo, H.-J. A 5.1-uW RFID tag chip integrated with sensors for wireless environmental monitoring. In Proceedings of the 31st European Solid-State Circuits Conference, Grenoble, France, 12–16 September 2005; pp. 279–282.

37. Preradovic, S.; Karmakar, N.C. *Multiresonator-Based Chipless RFID*; Springer: New York, NY, USA, 2012.

38. Shao, B. *Fully Printed Chipless RFID Tags towards Item-Level Tracking Applications*; Ph.D. Thisis, KTH Royal Institute of Technology: Stockholm, Sweden, 2014.

39. Preradovic, S.; Karmakar, N. Chipless RFID tag with integrated sensor. In Proceedings of the 2010 IEEE Sensors, Kona, HI, USA, 1–4 November 2010; pp. 1277–1281.

40. Nair, R.; Perret, E.; Tedjini, S.; Barron, T. A humidity sensor for passive chipless RFID applications. In Proceedings of the 2012 IEEE International Conference on RFID-Technologies and Applications (RFID-TA), Nice, France, 5–7 November 2012; pp. 29–33.

41. Amin, E.M.; Bhuiyan, M.S.; Karmakar, N.C.; Winther-Jensen, B. Development of a Low Cost Printable Chipless RFID Humidity Sensor. *IEEE Sens. J.* **2014**, *14*, 140–149.

42. Kalansuriya, P.; Bhattacharyya, R.; Sarma, S.; Karmakar, N. Towards chipless RFID-based sensing for pervasive surface crack detection. In Proceedings of the

2012 IEEE International Conference on RFID-Technologies and Applications (RFID-TA), Nice, France, 5–7 November 2012; pp. 46–51.

43. Shrestha, S.; Balachandran, M.; Agarwal, M.; Phoha, V.V.; Varahramyan, K. A Chipless RFID Sensor System for Cyber Centric Monitoring Applications. *IEEE Trans. Microw. Theory Tech.* **2009**, *57*, 1303–1309.

44. Vena, A.; Sydänheimo, L.; Tentzeris, M.M.; Ukkonen, L. A Fully Inkjet-Printed Wireless and Chipless Sensor for CO_2 and Temperature Detection. *IEEE Sens. J.* **2015**, *15*, 89–99.

45. Amin, E.M.; Bhattacharyya, R.; Sarma, S.; Karmakar, N.C. Chipless RFID tag for light sensing. In *2014 IEEE Antennas and Propagation Society International Symposium (APSURSI)*; IEEE: Memphis, TN, USA, 2014; pp. 1308–1309.

46. Capitán-Vallvey, L.F.; López-Ruiz, N.; Martínez-Olmos, A.; Erenas, M.M.; Palma, A.J. Recent developments in computer vision-based analytical chemistry: A tutorial review. *Anal. Chim. Acta* **2015**, *899*, 23–56.

47. Escobedo-Araque, P.; Martinez-Olmos, A.; Carvajal, M.A.; Palma, A.J.; Fernandez-Salmeron, J. Passive UHF RFID tag for spectral fingerprint measurement. In Proceedings of the 2015 IEEE 15th Mediterranean Microwave Symposium (MMS), Lecce, Italy, 30 November–2 December 2015; pp. 1–4.

48. AG, A. Demo Kit for the SL900A Smart EPC Sensor Tag IC. Available online: http://ams.com/eng/Support/Demoboards/UHF-RFID/UHF-Interface-and-Sensor-Tags/SL900A-Demo-Kit (accessed on 6 October 2015).

49. Kingbright RGB Color Sensor, KPS-5130PD7C datasheet 2013.

50. Roithner LaserTechnik GmbH Ultraviolet Sensor, GUVA-S12SD datasheet, 2011.

51. Vishay Semiconductors Silicon PIN Photodiode, TEMD7100X01 datasheet, 2009.

52. Salmerón, J.F.; Molina-Lopez, F.; Briand, D.; Ruan, J.J.; Rivadeneyra, A.; Carvajal, M.A.; Capitán-Vallvey, L.F.; de Rooij, N.F.; Palma, A.J. Properties and Printability of Inkjet and Screen-Printed Silver Patterns for RFID Antennas. *J. Electron. Mater.* **2014**, *43*, 604–617.

53. Salmerón, J.F.; Molina-lopez, F.; Rivadeneyra, A.; Quintero, A.V.; Capitán-vallvey, L.F.; Rooij, N.F.; De Ozáez, J.B.; Briand, D.; Palma, A.J. Design and Development of Sensing RFID Tags on Flexible Foil Compatible with EPC Gen 2. *IEEE Sens. J.* **2014**, *14*, 4361–4371.

54. Rao, K.V.S.; Nikitin, P.V.; Lam, S.F. Antenna design for UHF RFID tags: A review and a practical application. *IEEE Trans. Antennas Propag.* **2005**, *53*, 3870–3876.

4.6. Publication 2

Flexible passive tag based on light energy harvesting for gas threshold determination in sealed environments[5]

P. Escobedo [a], I.M. Pérez de Vargas-Sansalvador [b], M. Carvajal [a], L.F. Capitán-Vallvey [b], A.J. Palma [a], A. Martínez-Olmos [a],*

a ECsens, CITIC-UGR, Department of Electronics and Computer Technology, University of
   Granada, Granada, 18071, Spain
b ECsens, Department of Analytical Chemistry, University of Granada, Granada, 18071, Spain
* Corresponding author; email: amartinez@ugr.es

Abstract

In this work we describe a passive screen printed flexible tag for gas monitoring that can be used in sealed environments. The developed measurement system is based on chemical sensors that are sensitive to gases concentration presenting optical response, luminescent or colourimetric. The measuring electronics consist of a LED for optical excitation of the sensing membrane and a high resolution digital colour detector for the reading of the optical signal. A microcontroller receives and processes the data enabling the detection threshold for the corresponding gas. The whole system is powered by two miniaturized solar cells that provide 4 V and up to 250 μA each one. This system can run in sunlight or using a bright artificial light as the only energy source. The information of the inner environmental conditions regarding the gas concentration is transmitted to the user through a simple optical code using

colour light-emitting diodes. These LEDs are activated to indicate whether the concentration of the monitored gas is within the expected limits, or not. Two prototypes based on this architecture and only changing the sensing module have been developed and applied for the determination of two common gases: oxygen and carbon dioxide. In the first case, a luminescent chemical sensor is used while in the second, the sensing membrane presents a colourimetric response. Both types of sensors can be used in this design. Resulting limits of detection are compatible with assessment of modified atmosphere packaging.

Keywords: Passive tag; Optical gas sensing; Colour detector; Light energy harvesting; Sealed environment sensing.

1. Introduction

Modification of the atmosphere composition in sealed environments is a common technique to improve the preservation of the contents. It is applied to prevent the inside from biological hazards, plagues, humidity, etc. In the food industry, modified atmosphere packaging (MAP) is traditionally used to preserve the freshness of fresh produce, meats and fish by controlling their biochemical metabolism [1, 2]. It is basically performed by injection of some gas or gas mixtures in the package with the objective of displacing or inhibiting others than can be detrimental to the content. Classical MAP technologies consist of nitrogen flushing, vacuum packaging and carbon dioxide injection [3, 4], and they have been used commercially for many years. Some recent MAP approaches make use of an inert gas (e.g. argon) flushing for fruits and vegetables [5], or carbon monoxide injection and high oxygen flushing for red meats [6].

Other sectors also draw upon atmosphere modification in enclosed environments with protection aims. For example, archaeological and art museums and private collections use storage in sealed chambers where the gas composition has been modified to avoid the deterioration of the items. The use of microclimate boxes with a modified gaseous content has become popular in the last decades. This interest arose from the need to reduce the deteriorating effects of oxygen [7]. The oxygen concentration in a microclimate box can be reduced to less than 0.05% as a method for the treatment of insect-infested museum objects. The Royal Mummy Collection at the Egyptian Museum is stored in sealed glass cases with an oxygen-reduced inert atmosphere of nitrogen at low relative humidity which suppresses both biological activity and oxidation in proteinaceous material [8]. In other cases, an atmosphere with high concentration of carbon dioxide about 60% is used to eliminate insect plagues in museums [9, 10].

In these modified and sealed atmospheres, it is of great importance to monitor the gas mixture composition, in order to maintain the gases proportion and detect small breaches or holes or its modification by bacterial activity. In some cases, this monitoring is accomplished by means of invasive methods such as the circulation of gas samples through pumps or needles to a gas analyzer and its later return to the sealed case [11, 12]. Nevertheless, this strategy is lately being replaced by non-invasive methods that maintain intact the sealing of the package or storage. This has the advantage that no package has to be sacrificed and therefore, it has an advantageous economic impact. These techniques are gaining great diffusion in the sector of intelligent or smart packaging of food and beverages. Intelligent packaging is an extension of the communication function of traditional packaging. It communicates information to the consumer based on its ability to sense, detect, or record external or internal changes in the product's environment. Examples include time−temperature indicators (TTI), gas leakage indicators, ripeness indicators, toxin indicators, biosensors, and radio frequency identification tags [13].

For the transmission to the user of the information regarding the atmosphere conditions inside the package, electronic circuitry is often included in the envelope [14, 15]. Radio frequency identification (RFID) has been adopted as a major technology for the development of tags included or impressed on the packaging for the reading of the gas sensors and the transmission of the data to a remote RFID reader [16-18]. This technology presents the advantage of allowing the design of passive circuits that obtain the required power supply for the operation of the electronics from the near field generated by a remote RFID reader when it is approached to the tag [19, 20]. Therefore no battery is used in these tags, reducing the cost and extending its autonomy. Nevertheless, passive tags based on RFID require the inclusion of a large size antenna, usually screen-printed which limits the integration of the circuit. Moreover, the user needs an external RFID reader for its operation. In the last few years, these RFID passive tags have been combined with alternative sources of energy harvesting, specially solar energy, with the aim of maintaining the sensors working while there is no communication with an external RFID reader, or to increase the power supply for the whole system [21, 22]. Still, these designs are yet dependent on the presence of an external RFID reader and the integration of an antenna for wireless communication and energy harvesting.

In this work we describe a passive tag for gases determination based on optical chemical sensors that can be used in sealed environments. Unlike the mentioned designs based on RFID technology for data transmission and energy harvesting, the tag presented here is powered by means of two miniaturized solar cells. To the authors' knowledge, this is the first report of a passive tag for gas concentration measurement where the power supply relies only on light energy harvesting, and no other source of power supply such as batteries or near field energy harvesting is used,

as it happens in the tags where RFID protocol is implemented. The results of the gas measurement are visually transmitted to the user through a simple colour code. This is done by means of colour light-emitting diodes (LEDs) that are activated to inform whether the monitored gas concentration is below or above a programmed limit. Therefore, this system acts as a threshold detector, which is enough for most of applications in the mentioned field.

The use of the proposed system can be extended for the determination of any gas if a corresponding chemical sensor with optical response, luminescent or colourimetric is included. In order to evaluate the performance of the proposed architecture, in this work two different tags based on this scheme and using both luminescent and colourimetric sensors have been developed for the monitoring of oxygen and carbon dioxide, two of the main gases employed in modified atmosphere techniques [23, 24].

2. Experimental

2.1. Reagents and materials

2-Hydroxyethyl cellulose (HEC, average Mv ~90,000), meta-cresol purple sodium salt (MCP), glycerin, sodium bicarbonate, tetrahydrofuran (THF), platinum octaethylporphyrin (PtOEP), and polystyrene (PS, average MW 280 000; Tg, 100 °C; GPC grade) were all sourced from Sigma–Aldrich Química S.A. (Spain). As reflective layer white duct tape from 3M (Minnesota, USA) was used.

The tag is directly printed on 75 μm thick polyethylene naphthalate (PEN, Kaladex PEN Film, Dupont Teijin Films, Japan). This substrate was chosen because of its high optical transmission in the visible spectrum and good adherence. The screen-printing machine was a Serfix III (Seglevint S.L., Spain). The screen used to fabricate the single-layer pattern has a mesh density of 120 nylon threads per centimeter (T/cm). The conductive silver-based ink is CRSN 2442 (Sun Chemical Corporation, New Jersey, USA). After printing, the pattern was sintered at a constant temperature of 120°C for 5 min. To assemble the chips and external components to the substrate, a two-step process was carried out. First, the chips and silver pads were interconnected using the conductive resin H20E (Epoxy Technology, Inc., Massachusetts, USA). After this, the conductive resin was cured in an oven at 120 °C for 20 minutes.

2.2. Instruments and software

The electrical characterization of the system was carried out using the following laboratory instrumentation: a mixed signal oscilloscope (MSO4101, Tektronix, Oregon, USA), an 81/2-bit Digital Multimeter 3158A (Agilent Technologies,

California, USA), a 15 MHz waveform generator 33120A (Agilent Technologies), a Precision Impedance Analyzer 4294A and an impedance probe kit (42941A) (Agilent Technologies), a DC power supply E3630A (Agilent Technologies) and a balance DV215CD (Ohaus Co., New Jersey, USA). A user interface made in Visual Basic was used in a computer for calibration purposes.

The standard mixtures for instrument calibration and characterization were prepared using N_2 as the inert gas by controlling the flow rates of the different high purity gases O_2, CO_2 and N_2, entering a mixing chamber using a computer-controlled mass flow controller (Air Liquid España S.A., Spain) operating at a total pressure of 760 Torr and a flow rate of 500 cm^3 min^{-1}.

2.3. System description

2.3.1. Membranes preparation

Sensing membranes containing luminophore for O_2 were prepared from a cocktail that contains 100 mg of PS dissolved in 1 mL of freshly distilled THF, using an ultrasonic bath, and 0.5 mg PtOEP. The sensor preparation consists of the casting on one side of the support with 20 μL of cocktail A. After that, the support was left to dry in darkness in a desiccator that had a saturated THF atmosphere for 1 hour at room temperature [25].

Sensing membranes for CO_2 were prepared from a cocktail containing 12.5 mg of HEC, 1.4 mg MCP, 2.25 mg $NaHCO_3$ and 37.5 mg glycerin all dissolved in 1 mL of water, using an ultrasonic bath. The sensor preparation consists of the casting on one side of the Mylar support with 20 μL of cocktail B. After that, the support was left to dry in darkness in a desiccator for 6 h at room temperature.

2.3.2. Description of the instrument

The novel architecture consists of a small electronic tag screen printed on a flexible substrate of dimensions 38 × 19 mm^2. This tag is intended to be attached on the external surface of the sealed case that contains the modified atmosphere to be monitored, or it can even be directly printed on the envelope of the package. The optical gas sensor is printed or deposited on the inner surface of the cage or container, aligned with the sensing electronics. This measurement technique has been previously described by the authors [19]. As explained above in the Introduction section, the objective of this work is to develop a flexible screen printed passive tag that does not require the use of RFID technology for the communication with the user. The benefits of this approach are the elimination of the large-size antenna needed in this protocol and an easier interaction with the user because it does not

require an external RFID reader to power the tag and obtain the data. This implies that any non-expert user can read the information provided by the tag. The approach followed in this work for generating the power supply of the prototype is based on light energy harvesting. The whole design is based on the specification that the system is powered through two mini solar cells model CPC1824 (IXYS Integrated Circuits Division, California, USA). Each cell provides an output of 4 V and a current up to 100 µA at direct sunlight (6000 lux), according to the manufacturer specifications. Nevertheless, it has been proved that a bright light with intensity higher than 6000 lux produces an output current up to 250 µA, value that depends on the intensity of the incident light and the load applied to the cells.

Figure 1 shows the electrical characterization of a single solar cell in terms of output current I and power P versus output voltage V when it is illuminated by the light source used in this study. The light source is a 5 watt compact LED hand torch that contains a white LED model CREE XPG R5 (Cree, Inc. North Carolina, USA). This device generates a white light with an intensity of 400 lumen. The maximum available output power under these conditions is achieved at the Maximum Power Point (MPP), which in this case is 0.8 mW at 3.7 V. Due to the selection of components of ultra low power consumption the maximum power required for our tag is around 1.5 mW. Therefore, at least two solar cells must be included in the design to generate a maximum power of 1.6 mW. When these two cells are arranged in parallel configuration, the output voltage of the structure is 4V, and the supplied current is 190 µA, which is very close to the MPP, as it can be seen in Figure 1.
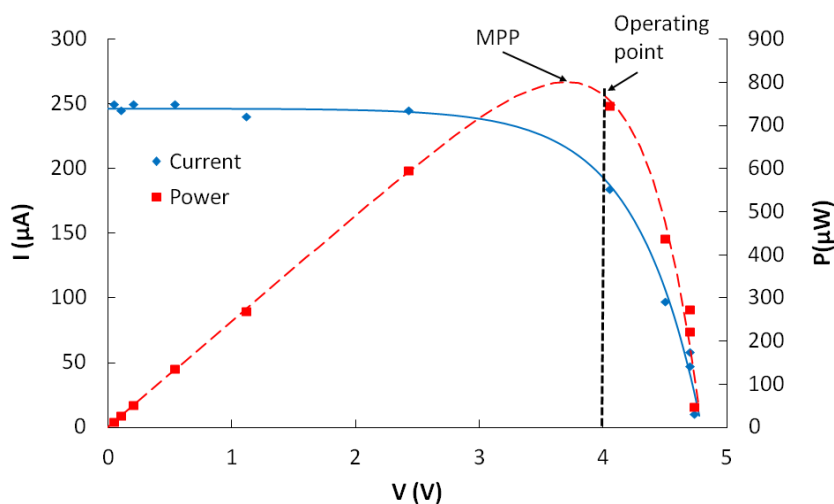
Figure 1. Electrical characterization of a single solar cell illuminated in the tests conditions.

The sensing module of the system is composed of an excitation LED and a high resolution digital colour detector. The LED must be selected according to the application of the system, i.e., the chemical sensor used to measure a given gas. If the sensor presents luminescent response, that is, it emits a luminescence when it is excited at a given wavelength, the LED is chosen to excite at this particular excitation wavelength. If the sensor used is a colourimetric one, i.e. it shows colour variation with the concentration of the gas, the LED selected is white.

A digital colour detector is used to register the optical response of the chemical sensor. The model used in this design is the S11059-02DT (Hamamatsu Photonics, Japan), which is an I²C interface-compatible colour detector sensitive to red (λ_{peak}=615 nm), green (λ_{peak}=530 nm), blue (λ_{peak}=460 nm), and infrared (λ_{peak}=855 nm) radiation. It outputs detected results as 16-bit digital data for each colour. Besides its high resolution and compatibility, it has been selected over other detectors used in previous works [19, 26] due to its very low power consumption (250 μW in operation mode), which makes this device optimal for passive designs. The output of the colour detector is serially sent as digital words to the microcontroller model PIC16LF1703 (Microchip Technology Inc., Arizona, USA). This device is selected because of its extreme low-power features such as an operating current in the range of microamperes. A temperature sensor model MCP9700A (Microchip Technology Inc.) is included in the design. This sensor presents an accuracy of ±1°C and a very low current consumption of 6 μA. A temperature sensor is necessary when the chemical sensor used in a given application presents temperature drifts that have to be corrected by the microcontroller [27].

Both the colour detector and the microcontroller are digital components, so they are not affected by variations in the power supply provided by the solar cells that can arise from changes in the intensity or angle of the incident light, as long as the voltage and current are enough to allow their operation. The temperature sensor is an analog device, but it shows a stable output that is not affected by variations in the power supply, as long as it remains above 2.3 V to keep the sensor activated. The only device that could produce a misreading of the gas concentration if variations in the output voltage and current of the solar cells are produced is the excitation LED. The intensity of the light emitted by this LED affects the response of the optical chemical sensor when it is luminescent type, or directly the measurement of the colour detector when the sensor presents a colourimetric response. The emission of the excitation LED must be stable, but it depends on its polarization current and voltage. Therefore, a voltage reference consisting of a Zener diode is included in the design, configured in parallel to the excitation LED, as it is shown in Figure 2.
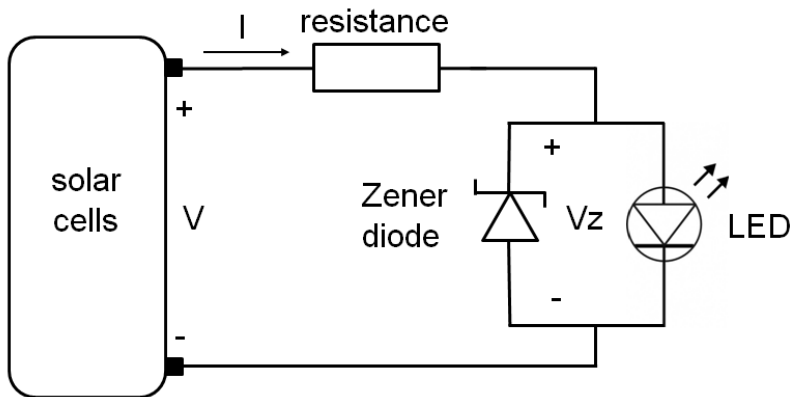
Figure 2. Polarization of the excitation LED

The Zener diode is reverse polarized, establishing a voltage drop of *Vz* from anode to cathode of the excitation LED. This voltage drop must match the required polarization voltage for the excitation LED, so both Zener and LED diodes must be designed to be complementary. With the structure depicted in Figure 2, variations in the output voltage caused by the solar cells are absorbed by the serial resistance, while variations in the output current are absorbed by the Zener diode. In that way, the polarization of the excitation LED remains fully stable.
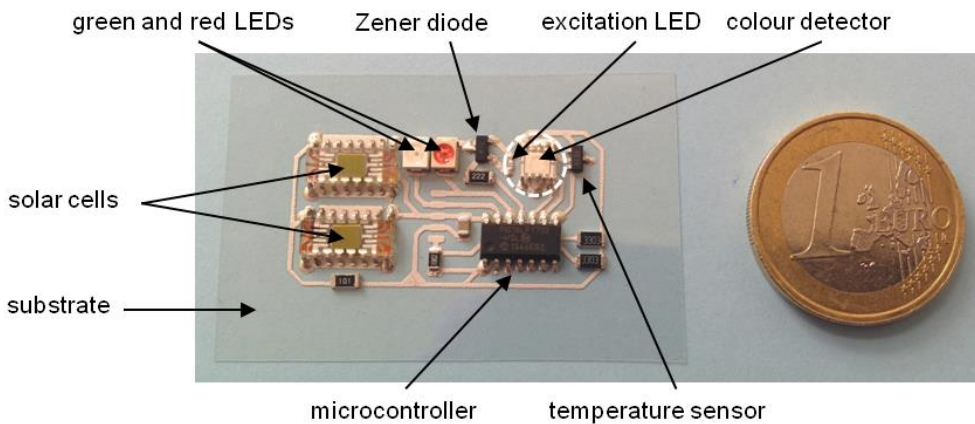
Figure 3. Photography showing the different smart tag components. The white circle indicates the region where the sensing membrane is placed.

Figure 3 presents a photography of a generic developed tag based on the described scheme. As it has been explained above, the selection of the excitation LED and the associate Zener diode depends on the specific application of the tag, and more particularly, on the optical gas sensor included in the system. The rest of the components are common to any tag developed following the presented architecture.

When the sensing module performs a measurement, the data regarding the colour detection and temperature are received by the microcontroller, where the calibration curves are previously stored. The microcontroller generates an estimation of the gas concentration based on these data and the result is compared to a pre-established threshold that determines whether the concentration is correct inside the sealed environment or not. The microcontroller activates the green or red LED to inform the user about the result of this measurement, therefore making unnecessary the presence of a wireless data transmission protocol such as RFID.

3. Results and Discussion

The measurement platform described in the previous section has been applied to the determination of two common gases in modified atmospheres, namely oxygen and carbon dioxide. The system is able to monitor only one gas, hence two different tags have been developed in order to measure O_2 and CO_2. The gas sensors employed present different optical responses; therefore the configuration of the tags must be distinct, as it is explained below.

In the case of O_2, a chemical sensor based on luminescence quenching of the complex PtOEP is used. This sensor has a long lifetime, the long term stability of luminophore membranes shows a phosphorescence decreases by some 20% after 210 days [27] and a low price of $3{,}2{\cdot}10^{-3}$ € per sensing membrane.

This luminophore produces an emission at the wavelength of 645 nm corresponding to red region of the visible spectrum when it is optically excited at 537 nm, which corresponds to green light [28]. An excitation LED model SMP2-UPGC (Bivar Inc., California, USA.) with peak emission at 536 nm is used due to its low power consumption. For a direct polarization voltage of 2.5 V, this LED requires a low current of only 40 µA. The corresponding Zener diode used to fix the polarization of the excitation LED to 2.5 V according to Figure 2 is the model LM285-2.5-N (Texas Instruments, Texas, USA) which is reverse polarized with a small current of 20 µA.
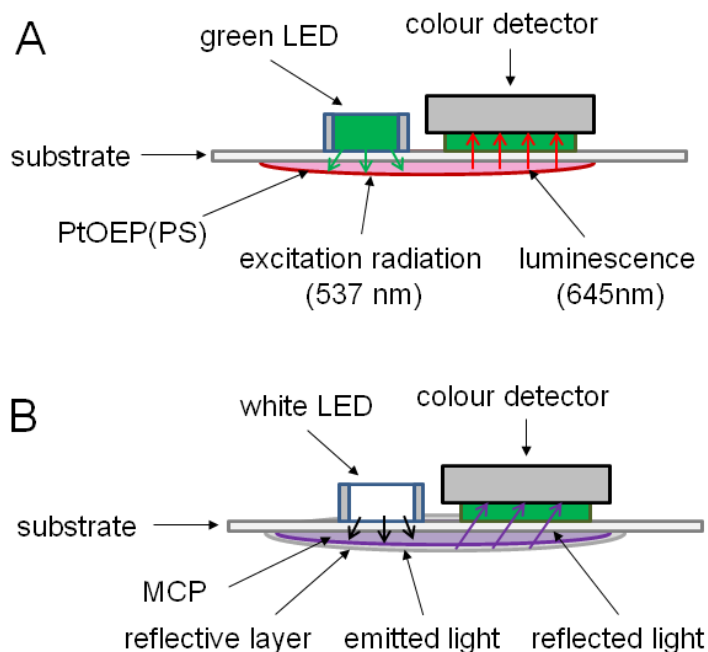
Figure 4. Sensing set-ups showing the excitation and reading devices of the O_2 sensor **(A)** and CO_2 sensor **(B)**.

The emitted luminescence of the oxygen sensitive luminophore in response to the optical excitation is captured with the colour detector as it is schematized in the Figure 4A. The output digital word corresponding to the red component of the colour detector is a direct measurement of the intensity [26] when the system is optically isolated. The internal filters of the colour detector avoid the influence of the excitation green light on the measurement of the luminescence emitted by the oxygen sensor, since the output of this device corresponding to the incident red light is only affected by this luminescence. The intensity of this luminescence under stable optical excitation is attenuated when the concentration of the surrounding oxygen increases, as it is shown in the Figure 5A.
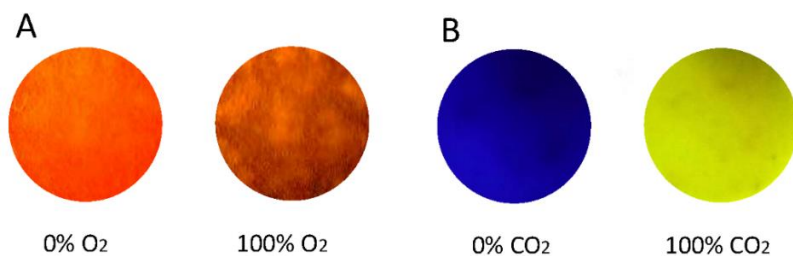
Figure 5. Optical response of the O_2 **(A)** and CO_2 **(B)** sensors.

This system has been calibrated in the full range 0–100%, with 6 replicas at room temperature (21°C) for each concentration. For data acquisition, the microcontroller programmer model Pickit 3 (Microchip Technology Inc.) is configured in debugger mode and used to obtain the colour measurements. The results are shown in Figure 6, where logarithmic scale in the vertical axis is used for a better visualization of the data. Error bars are included in the graphic but they are too small to be appreciated. The intensity is directly taken as the red coordinate reading from the colour detector when a stable optical excitation is applied.
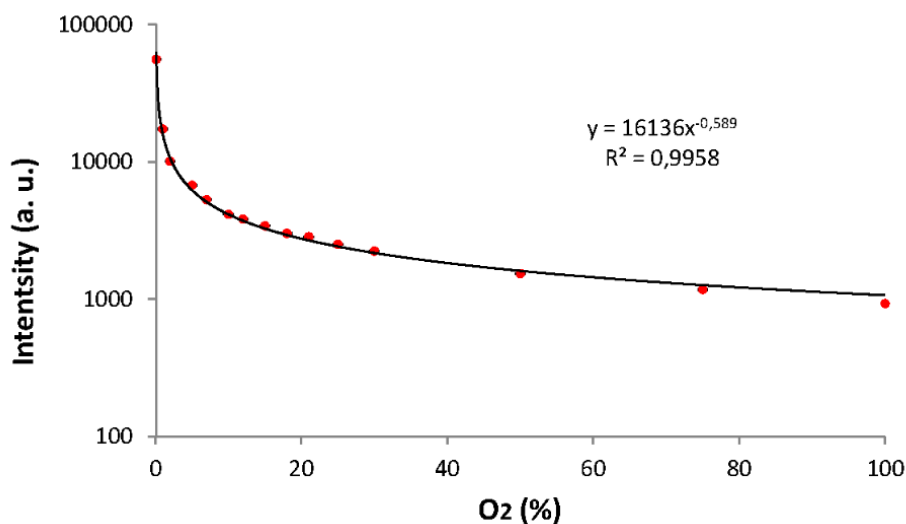
Figure 6. Calibration curve of the system with the O_2 sensor.

As it was expected, the measured data can be fitted to a potential curve in the form [24, 26] $I = \alpha \cdot [O_2]^\beta$, with α = 16136.42 and β = -0.5894, being the coefficient of correlation, R^2 = 0.9958.

The CO_2 sensor is based on the acidity of this molecule [29]. The sensor contains an acid-base indicator (MCP) showing an optical response in the form of colour variations when the concentration of the surrounding CO_2 changes. The colour of this sensor varies from dark blue to yellow when the concentration of carbon dioxide raises from 0 to 100% as it is shown in Figure 5B. This sensor has been proved to be stable for 9 months [30]. It also has a very low cost of $5 \cdot 10^{-5}$ € per sensing membrane. The advantages of using of water-based sensors instead of the widely used organic-based sensors for CO_2 are their less toxicity and higher stability since quaternary ammonium salts are not used [25]. These characteristics gain great importance

especially for food industry applications. The drawback of CO_2 water-based sensors compared to organic-based sensors is the higher response times [30].

Since the response of this sensor is colourimetric, the measurement protocol is slightly different than the previous case. Figure 4B presents the arrangement of the sensing module in the case of colourimetric sensors. Here the excitation LED used is white, considering that the parameter to be determined now is the colour of the membrane. The model of the LED used is LW-QH8G (OSRAM Licht AG, Germany), which can be polarized at 2.5 V with a low current of 30 µA. Being the polarization voltage the same as the one in the configuration for the oxygen sensor, the same Zener diode is used. Since the excitation and detection devices are placed on the same side of the tag, the colour measurement is carried out by reflection of the emitted white light. As it is depicted in the Figure 4B, a reflective layer is attached to the gas sensitive membrane. This layer consists simply of a white porous adhesive paper that allows the flux of gas through it. Using this configuration of the tag, the CO_2 sensor has been calibrated in the full range 0 to 100%. To quantify the colour variation of the membrane, an intensity parameter has been defined from the values of the R, G and B coordinates given by the colour detector [31]:

$$I = \sqrt{R^2 + G^2 + B^2}$$ (1)

Figure 7 presents the data obtained in the calibration process.
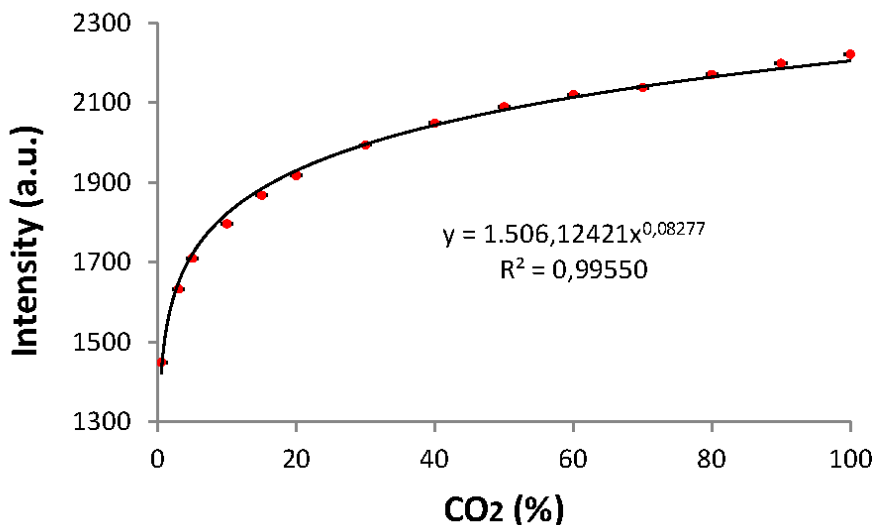
Figure 7. Calibration of the system with the CO_2 sensor.

In this case, the measured data can be again fitted to a potential curve in the form $I = \alpha \cdot [CO_2]^\beta$, being now $\alpha = 1506.12$ and $\beta = 0.0828$, and $R^2 = 0.9955$.

The resolution of this system can be obtained from the potential curves found in the fitting of the experimental data, taking derivatives in both sides of the equation and approximating these derivatives to increments [28]. By doing so, the obtained expression for the resolution is:

$$\Delta X = \frac{\left(\frac{I}{\alpha}\right)^{1/\beta}}{\beta I} \Delta I \tag{2}$$

where X is the concentration of O_2 or CO_2 and ΔI is the error or uncertainty in the determination of the intensity I. This intensity is defined as the value of the red component of the detected light in the case of the oxygen sensor.

Therefore, for this case, $\Delta I = \Delta R$ is the resolution in the quantification of the R coordinate. In the case of the carbon dioxide sensor, the intensity is defined as expressed in Equation 1. The uncertainty in the determination of this intensity is calculated by taking derivatives again:

$$\Delta I = \frac{R}{I}\Delta R + \frac{G}{I}\Delta G + \frac{B}{I}\Delta B \tag{3}$$

In the ideal case where no external source of error in the measurement of the gas affects the response of the system, the errors ΔR, ΔG and ΔB are given by the resolution of the colour detector, that is, $1/2^{16} = 15 \cdot 10^{-6}$ arbitrary units since this device codifies the measured light in 16-bits words. In practice, the response of the system is affected by small instabilities of the concentration in the gases mixture surrounding the gas sensor, temperature drifts, etc. The experimental resolution in this study is calculated by taking the errors ΔR, ΔG and ΔB as the standard deviation of the measurements for six replicas, which take values in the range 0.5 to 2 arbitrary units. These uncertainties are much higher than the used in the theoretical study; therefore significative differences in the theoretical and experimental resolutions are expected.

The limit of detection (LOD) was obtained using the standard criteria: $LOD = y_b + 3s_b$, where y_b is the average blank signal and s_b is the standard deviation of the blank, which is determined using at least 10 replicas. Table 1 presents the obtained values of resolution and LOD for both study cases. As it can be seen, very good specifications are achieved with the presented system. In particular, the low values of the LOD in oxygen and carbon dioxide, 170 ppm (0.017%) and 720 ppm (0.072%) respectively, make the developed tag optimal for its use in the determination of the concentration of these gases in sealed environments such as microclimate boxes or MAPs.

Table 1. Resolution and LOD of the two tags.

Gas	Theoretical resolution (ppm)	Experimental resolution (ppm)	LOD (ppm)
O_2	1.3×10^{-5} (at 1%) 1.6×10^{-3} (at 21%) 3.4×10^{-2} (at 100%)	6.4 (at 1%) 100 (at 21%) 2057 (at 100%)	170
CO_2	1.4×10^{-3} (at 0.5%) 2.2×10^{-2} (at 15%) 1.5×10^{-1} (at 100%)	93 (at 0.5%) 1416 (at 15%) 9594 (at 100%)	720

In these cases, the O_2 concentration can be reduced up to a 0.05%, and the CO_2 is usually maintained above 2%. The limits achieved with the presented system cover these values more than enough, so a high resolution threshold detector can be implemented with the proposed tag for any application in modified atmospheres controlling.

4. Conclusions

In this work the architecture of a full passive tag for the detection of gas threshold concentration in sealed environments is presented. The power supply is provided by means of two mini solar cells that are able to harvest light energy from solar radiation or from a bright artificial light source such as a hand torch. The selection of very low consumption components for the measurement electronics allow the use of this power source, with a total power consumption below 1.6 mW. The determination of the gas concentration is based on chemical sensors with optical response that is registered through a high resolution digital colour detector. This system has been evaluated for the measurement of two gases O_2 and CO_2, by means of two different developed tags, although any gas sensor showing optical response can be used. Results show that a high experimental resolution of 6.4 and 93 ppm in the best case, and a low limit of detection of 170 and 720 ppm for oxygen and carbon dioxide respectively, are achieved using both luminescent and colourimentric sensors. A threshold of gas concentration can be programmed in the microcontroller, and the system generates an optical output through green and red LEDs to inform the user if the monitored gas inside the package or cage is below of above this limit.

To the best of our knowledge, this is the first report on an electronic system with these characteristics which does not require the use of a RFID protocol for data transmission and energy harvesting, relying the power supply only on light energy harvesting. The use of this tag covers a wide range of applications in different areas where the monitoring of gases composition in modified atmospheres is required.

References

[1] J.H. Han, Innovations in food packaging, Academic Press, 2013.

[2] M.L. Rooney, Active food packaging, Springer US, 1995.

[3] J.F. Chapon, C. Blanc, P. Varoquaux, A modified atmosphere system using a nitrogen generator. Postharvest Biol. Technol. 31 (2004) 21–28.

[4] P. Singh, A.A. Wani, A.A. Karim, H.C. Langowski, The use of carbon dioxide in the processing and packaging of milk and dairy products: a review, Int. J. Dairy Technol. 65 (2012) 161-177.

[5] Gordon L. Robertson, Food packaging: principles and practice, CRC Press, 2012.

[6] F. De Santos, M. Rojas, G. Lockhorn, M.S. Brewer, Effect of carbon monoxide in modified atmosphere packaging, storage time and endpoint cooking temperature on the internal color of enhanced pork, Meat Sci. 77 (2007) 520–528.

[7] K. Dardes, A. Rothe, The structural conservation of panel paintings, Proceedings of a Symposium at the J. Paul Getty Museum, 24–28 April 1995.

[8] S. Maekawa, Oxygen-free museum cases, Getty Publications, 1999.

[9] National Park Service, Controlling insect pests: alternatives to pesticides. Conserve O Gram, number 3/8, August 1998.

[10] C. Selwitz, S. Maekawa, Inert gases in the control of museum insect pests. The Getty Conservation Institute, 1998.

[11] N. Valentin, M. Lidstrom, F. Preuss, Microbial control by low oxygen and low relative humidity environment. Stud. Conserv. 35 (1990) 222-230.

[12] M. Rust, J. Kennedy, The feasibility of using modified atmospheres to control insect pests in museum, Report, GCI Scientific Program, March 1993.

[13] D. Restuccia, U.G. Spizzirri, Ortensia I. Parisi, G. Cirillo, M. Curcio, F.a Iemma, F. Puoci, G. Vinci, N. Picci, New EU regulation aspects and global market of active and intelligent packaging for food industry applications. Food Control 21 (2010) 1425–1435.

[14] K. Marsh, B. Bugusu, Food packaging—roles, materials, and environmental issues, J. Food Sci. 72 (2007) 39-55.

[15] K.L. Yam, D.S. Lee, Emerging food packaging technologies: principles and practice, Elsevier 2012.

[16] S. Bhadra, C. Narvaez, D.J. Thomson, G.E. Bridges, Non-destructive detection of fish spoilage using a wireless basic volatile sensor, Talanta 134 (2015) 718–723.

[17] A. Ramos, P. Clément, A. Lazaro, E. Llobet, D. Girbau. Nitrogen dioxide wireless sensor based on carbon nanotubes and UWB RFID technology, IEEE Antennas Wirel. Propag. Lett. 14 (2015) 1145-1148.

[18] Z. Zou, Q. Chen, I. Uysal, L. Zheng. Radio frequency identification enabled wireless sensing for intelligent food logistics. Phil. Trans. R. Soc. A 372 (2014) 1-17.

[19] A. Martínez-Olmos, J. Fernández-Salmerón, N. Lopez-Ruiz, A. Rivadeneyra Torres, L.F. Capitan-Vallvey, A.J. Palma, Screen printed flexible radiofrequency identification tag for oxygen monitoring, Anal. Chem. 85 (2013), 11098–11105.

[20] C. Occhiuzzi, A. Rida, G. Marrocco, M. Tentzeris, RFID passive gas sensor integrating carbon nanotubes, IEEE Trans. Microw. Theory Tech. 59 (2011) 2674-2684.

[21] A. Ramos, D. Girbau, A. Lázaro. A. Collado, A. Georgiadis. Solar-powered wireless temperature sensor based on UWB RFID with self-calibration, IEEE Sens. J. 15 (2015) 3764-3772.

[22] L. Vojtěch, L. Kypus, L. Kvarda, N. Thiard, J. Yannis. Solar and wireless energy harvesting semi-active UHF RFID tag design and prototyping, 16th International Conference on Mechatronics, 3-5 December 2014.

[23] X. Meng, S. Kim, P. Puligundla, S. Ko, Carbon dioxide and oxygen gas sensors-possible application for monitoring quality, freshness, and safety of agricultural and food products with emphasis on importance of analytical signals and their transformation, Korean Soc. Appl. Biol. Chem. 57 (2014), 723–733.

[24] S. Maekawa, K. Elert, The use of oxygen-free environments in the control of museum insect pests, Getty Publications, 2003.

[25] I.M. Pérez de Vargas-Sansalvador, M.A. Carvajal, O.M. Roldán-Muñoz, J. Banqueri, M.D. Fernández-Ramos, L.F. Capitán-Vallvey, Phosphorescent sensing of carbon dioxide based on secondary inner-filter quenching, Anal. Chim. Acta 655 (2009) 66–74.

[26] N. López-Ruiz, D. Hernández-Bélanger, M.A. Carvajal, L.F. Capitán-Vallvey, A.J. Palma, A. Martínez-Olmos, Fast lifetime and amplitude determination in luminescence exponential decays, Sens. Actuator B-Chem. 216 (2015) 595–602.

[27] I.M. Pérez de Vargas, A. Martínez-Olmos, A.J. Palma, M.D. Fernández-Ramos, L.F. Capitán-Vallvey, Compact optical instrument for simultaneous determination of oxygen and carbon dioxide, Microchim. Acta 172 (2011) 455–464.

[28] N. López-Ruiz, A. Martínez-Olmos, I.M. Pérez de Vargas-Sansalvador, M.D. Fernández-Ramos, M.A. Carvajal, L.F. Capitan-Vallvey, A.J. Palma, Determination of O_2 using colour sensing from image processing with mobile devices, Sens. Actuator B-Chem. 171– 172 (2012) 938– 945.

[29] I.M. Pérez de Vargas-Sansalvador, C. Fay, T. Phelan, M.D. Fernandez-Ramos, L.F. Capitan-Vallvey, D. Diamond and F. Benito-Lopez, A new light emitting diode–light emitting diode portable carbon dioxide gas sensor based on an interchangeable membrane system for industrial applications. Anal. Chim. Acta 699 (2011) 216-222.

[30] A. Mills, G.A. Skinner, Water-based colourimetric optical indicators for the detection of carbon dioxide, Analyst 135 (2010) 1912-1917.

[31] J. Park, W. Hong, C.S. Kim, Color intensity method for hydrogel oxygen sensor array, IEEE Sens. J. 10 (2010) 1855-1862.

4.7. Publication 3

Flexible Passive near Field Communication Tag for Multigas Sensing[6]

P. Escobedo [a], M.M. Erenas [b], N. López-Ruiz [c], M.A. Carvajal [a], S. Gonzalez-Chocano [b], I. de Orbe-Payá [b], L.F. Capitán-Valley [b], A.J. Palma [a], A. Martínez-Olmos [a],*

[a] ECsens, CITIC-UGR, Department of Electronics and Computer Technology, University of Granada, Granada, 18071, Spain
[b] ECsens, Department of Analytical Chemistry, University of Granada, Granada, 18071, Spain
[c] Department of Electronics Technology, University Carlos III, Madrid, 28911, Spain
[*] Corresponding author; email: amartinez@ugr.es

Abstract

In this work we present a full-passive flexible multi-gas sensing tag for the determination of oxygen, carbon dioxide, ammonia and relative humidity readable by a smartphone. This tag is based on NFC technology for energy harvesting and data transmission to a smartphone. The gas sensors show an optic response that is read through high-resolution digital colour detectors. A white LED is used as the common optical excitation source for all the sensors. Only a reduced electronics with very low power consumption is required for the reading of the optical responses and data transmission to a remote user. An application for Android operating system has been developed for the power supplying and data reception from the tag. The responses of the sensors have been calibrated and fitted to simple functions, allowing a fast prediction of the gases concentration. Cross-sensitivity has been also evaluated finding that in most of the cases is negligible or easily correctable using the rest of the readings. The election of the target gases has been due to their importance in the monitoring of modified atmosphere packaging. Resolutions and limits of detection measured are suitable for such kind of application.

---

[6] Reprinted (adapted) with permission from Escobedo, P.; Erenas-Rodríguez, M. M.; López-Ruiz, N.; Carvajal-Rodríguez, M. A.; González-Chocano, S.; de Orbe-Payá, I.; Capitán-Vallvey, L- F-; Palma-López, A. J.; Martínez-Olmos, A. *Flexible passive Near Field Communication Tag for Multigas Sensing*. Analytical Chemistry 2017, 89, 1697-1703. Copyright 2018 American Chemical Society.

The control of the conditions for food and beverage preservation in packaging systems has been widely studied in the last decade. The importance of guaranteeing the safe condition of the food, protecting it from external contamination, has led to an increasing interest of the companies in intelligent packaging technologies as well as the presence of this kind of systems on the markets. The research carried out on this subject has provided some innovations such as smart and active packaging, modified atmosphere packaging (MAP), and edible films/coatings.[1] Smart packaging is a system that allows the monitoring of the properties of packaged foods and its environment, communicating their state to the manufacturer, retailer and consumer.[2] Active packaging includes additives or components that have an active participation in the preservation of the food and beverage. MAP is used as a technique to modify the environmental conditions inside the packaging in order to introduce some gas or gas mixtures to avoid the spoilage of the contained food.[1,3] Some of the traditional MAP technologies use nitrogen flushing, vacuum packaging and carbon dioxide injection.[4,5] In recent studies, different gases have been introduced in the modified atmosphere such as argon for fruits and vegetables,[6] or carbon monoxide and high oxygen concentrations for red meats.[7] MAP technology is often combined with smart packaging in order to inform the user if the atmosphere within the package suffers any modification due to small breaks in the envelope that might produce the spoilage of the content.

For the reading and transmission to the user of the information regarding the atmosphere conditions inside the package, electronic circuitry is often included in the envelope.[8,9] This electronics should be small size and low-power consumption.[10] In this field, radio frequency identification (RFID) and more recently near field communication (NFC) has been adopted as a major technology for the development of tags included or impressed on the packaging for the reading of the gas sensors and the transmission of data to a remote RFID/NFC reader.[11-13] This short-range radio technology presents the advantage of allowing the design of passive circuits that obtain the required power supply for the operation of the electronics from the near field generated by a remote reader, such as an NFC-enabled mobile device, when it is approached to the tag.[14,15] Therefore no battery is used in these tags, reducing the cost and enabling autonomous operation.

In the recent years, many passive RFID tags with sensing capabilities conceived for monitoring the status of food in smart packaging have been reported.[16,17] Most of them are based on gases detection inside the package.[18,19] Recently, the availability of NFC-enabled mobile devices such as smartphones has avoided the necessity of a specific RFID reader for data collection from the RFID tags. As a consequence, the

smart packaging based on this technology is being lately oriented to this protocol for data transmission.[20,21] Previous work of the authors presented the implementation of passive tags conceived to be used in smart packaging for the monitoring of gases concentration in modified atmospheres.[14,22] In these papers, we proved the feasibility of the development of low cost battery-free electronics systems based on optical sensors for the control of the gases commonly presented in modified atmosphere composition and the rapid detection of the envelope damages that can alter this composition producing the content spoilage.

In this paper we propose a passive tag for multi-gas sensing based on RFID/NFC technology for energy harvesting and data transmission with new sensing capabilities: the number of gas sensors has been incremented to four. Furthermore, we have developed an Android application that allows in-situ measurement of the four gases concentration using an NFC-enabled mobile phone. The analysed gases used for evaluating the status of the inner modified atmosphere are oxygen and carbon dioxide, which are two of the main gases used in MAPs.[23-25] The other two gas sensors measured by our prototype are aimed to detect and quantify the presence of ammonia and humidity, two magnitudes that can reveal the spoilage of the food.[26-28] The detection of these four gases is based on the use of chemical sensors with optical response. This approach allows a physical separation of the sensors, which can be placed inside the package in contact with the inner atmosphere, whereas the reading and processing electronics remain on the outside of the package. In addition, a temperature sensor is included in order to compensate the temperature drifts of the gas sensors, as well as to evaluate temperature variations of the environment than could also affect the content.[29]

Experimental Section

Reagents and materials

The chemicals used for the preparation of the sensing cocktails are: tributyl phosphate (TBP), o-nitrophenyloctylether (NPOE), α-naphtholphthalein, crystal violet, bromophenol blue sodium salt, 5,10,15,20-tetrakis (pentafluorophenyl)-21H,23H-porphine palladium(II) (PdTFPP), tetraoctylammonium hydroxide (TOAOH), cetyltrimethylammonium bromide (CTAB), ethanol, toluene, acetone, butyl acetate, polystyrene, ethyl cellulose, cellulose acetate, and nafion 5%WT. All the reagents used are analytical-reagent grade purchased from Sigma-Aldrich (Madrid, Spain).

The tag is screen printed on flexible substrate, specifically on 100 μm thick polyethylene naphthalate (PEN, Kaladex PEN Film, Dupont Teijin Films, Tokyo,

Japan), using silver conductive ink model CRSN 2442 (Sun Chemical Corporation, Parsippany, New Jersey, USA). PEN film was chosen because of its high light transmittance of 87% and good adherence. The screen-printing machine was a Serfix III (Seglevint S.L., Barcelona, Spain). The screen used to fabricate the single-layer pattern has a mesh density of 140 nylon threads per centimeter (T/cm). After printing, the pattern was sintered at a constant temperature of 120 °C for 5 min in a convection oven (Venticell, Medcenter Einrichtungen Gmbh, Planegg, Germany). After sintering, four circles to contain the four sensing membranes were screen printed using vinyl matt ink (Areny Color SL, Alicante, Spain) on the other side of the tag. These circles act as barriers to prevent the membranes from spreading. Finally, to assemble the chips and external components to the substrate, a two-step process was carried out. First, the chips and silver pads were interconnected using the conductive resin H20E (Epoxy Technology Inc., Billerica, Massachusetts, USA). After this, the conductive resin was cured in the hot air oven at 120 °C for 20 min.

Instruments and software

The electrical characterization of the system was carried out using the following laboratory instrumentation: a mixed signal oscilloscope (MSO4101, Tektronix, Oregon, USA), an 8 1/2-bit Digital Multimeter 3158A (Agilent Technologies, Santa Clara, California, USA), a 15 MHz waveform generator 33120A (Agilent Technologies), a Precision Impedance Analyzer 4294A and an impedance probe kit (42941A) (Agilent Technologies), a DC power supply E3630A (Agilent Technologies) and a balance DV215CD (Ohaus Co., Parsippany, New Jersey, USA). The standard mixtures for instrument calibration and characterization were prepared using N_2 as the inert gas by controlling the flow rates of the different high purity gases O_2, CO_2, NH_3 and N_2, entering a mixing chamber using a computer-controlled mass flow controller (Air Liquid España S.A., Madrid, Spain) operating at a total pressure of 760 Torr and a flow rate of 500 cm3 min−1. Advanced Design Simulator (ADS, Agilent Technologies, Santa Clara, California, USA), a software based on the momentum method, has been used for the design and simulation of the printed antenna. To implement the Android application in the mobile phone, Android Studio 2.1.2 was chosen as the integrated development environment (IDE).

System description

Membranes preparation

The composition of the different sensing membranes and their preparation depends on the analyte that is going to be detected as well as the quantities of each one. The carbon dioxide sensing cocktail is prepared by the mixture of 64 µL of TBP, 320 µL

of solution of 4.7 mg of α-naphtholphthalein in 4.27 mL of toluene/ethanol (80/20), 58.3 mg of ethyl cellulose in 1 ml of toluene and 600 µL of TOAOH.30 Ammonia sensing cocktail is composed by 40 mg of cellulose acetate, 2 mg of bromophenol blue sodium salt, 37 mg of NPOE, 4.5 mg of CTAB in 2 mL of acetone.31 Oxygen sensing cocktail is prepared by the solution of 4.9 mg of PdTFPP in 5 mL of polystyrene 60 mg/mL in butyl acetate. Finally, the humidity sensing cocktail is prepared by the mixture of 1.27 mL of a solution of crystal blue 1.75 mM in methanol and 1 mL of nafion 5%WT.32

Afterwards, 7 µL of each sensing solutions were dropped using a micropipette in the round designed area for that purpose and let it dry at room temperature for 2 hours in the darkness. Once the sensing membranes are dried, the tag can be used for the determination of the four gases.

Description of the passive sensing tag

The proposed architecture consists of a RFID tag printed on a flexible substrate for the monitoring of four different gases by means of chemical sensors with optical response. The system is fully passive, therefore no battery is needed to supply the prototype. Instead, the power supply is obtained from the energy harvested from the near electromagnetic field induced by an external RFID reader. In this case, the reader is an NFC-enabled mobile phone. Since the system is battery-free, it has been designed using very low consumption devices. Figure 1 shows a block diagram of the proposed system.
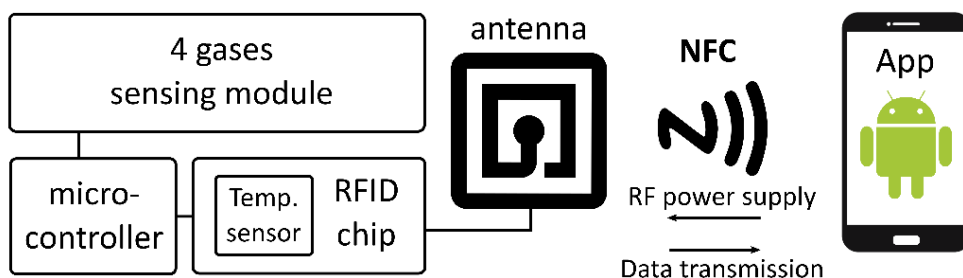
Figure 1. Block diagram of the complete system.

The analysis of the concentration of these gases is based on optical chemical sensors that are disposed on the inner face of tag in form of membranes. These membranes are optically excited and their optical responses are registered and related to the concentration of the objective gases. The printed interconnections and the required electronics for excitation and reading of the gas sensors and the data transmission is

attached to the external face of tag, therefore the sensing membranes are the only elements that can be placed inside the package.

The sensing module is presented in the scheme of Figure 2. It consists of four gas sensors disposed in form of round membranes. These sensors are excited using a common white light-emitting diode (LED) situated in the centre of the sensing membranes (Figure 2(A)). In this way, the four sensors are excited together. For the reading of the optical response of the gas sensors, a digital colour detector is situated on the external surface of the flexible substrate directly facing each sensing membrane (Figure 2(B)).
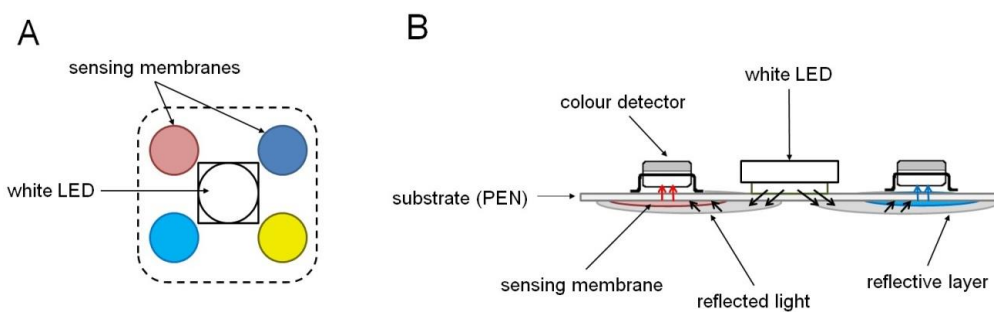
Figure 2. Bottom view **(A)** and lateral view **(B)** schemes of the sensing module.

In order to ensure that the emitted white light reaches by reflection the sensing membrane, a reflective layer permeable to gases consisting of white duct tape from 3M (St. Paul, Minnesota, USA) is placed covering each membrane and part of the white LED. The optical response of each membrane, luminescent or colourimetric, is registered by the corresponding colour detector.

Figure 3 presents the complete system. A wide-surface diffused white LED model ASMT-MYH0-NDF00 (Avago Technologies, San José, California, USA) is used as the common optical excitation for the four sensing membranes. This LED has a very low power consumption of only 0.8 mW. The colour detector used in this design is the S11059-02DT (Hamamatsu Photonics, Hamamatsu, Japan), which is an I2C interface-compatible digital detector sensitive to red (λ_{peak}=615 nm), green (λ_{peak}=530 nm), blue (λ_{peak}=460 nm), and infrared (λ_{peak}=855 nm) radiation. The measured incident radiation is codified in four words of 16 bits, one for each colour. Besides its high resolution, it has been selected due to its very low power consumption of 250 µW, which makes this device optimal for passive designs.
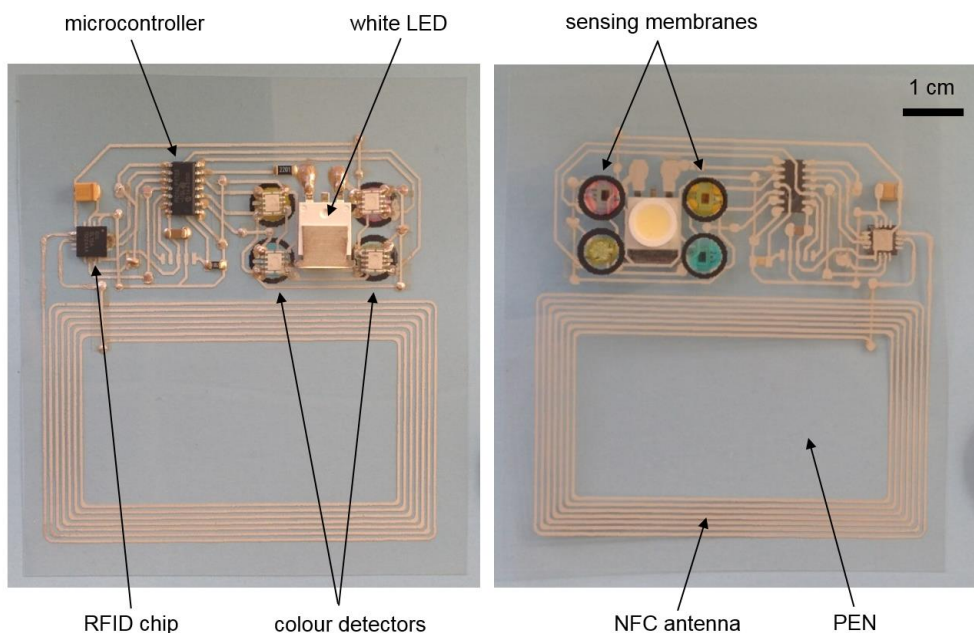
Figure 3. Photography of both sides of the developed tag.

The digital outputs of the four colour detectors are directly transmitted by means of the I2C bus to the microcontroller model PIC16LF1703 (Microchip Technology Inc., Chandler, Arizona, USA), which also presents very good features regarding low power consumption. In this application, the consumption of the whole system is 8.5 mW in operation mode. The RFID chip is a device which integrates a radio-frequency (RF) interface that allows a wireless communication with an external RFID reader. The model selected here is the SL13A (IDS Microchip AG, Switzerland, since 2012 acquired by AMS AG, Unterpremstätten, Austria), which is a widely-used interface for the development of RFID/NFC tags.[33-35] This device is compliant with the ISO15693 RFID standard. It is also compatible with Android near-field communication (NfcV standard). This component can be powered from the electromagnetic field induced in the antenna by the external reader, which makes it suitable for the development of passive tags. The SL13A integrates an on-chip 8kbit EEPROM and a built-in temperature sensor. In addition, this device is able to power supply the rest of the circuitry with a voltage output of 3.4 V and a maximum current of 4 mA, that is, a maximum power of 13.2 mW, which is enough for this application. The antenna is a custom-designed screen printed inductor. Resonance is achieved at $\omega_0 = \sqrt{LC}$, being about 25 pF the capacitance of the RFID chip at the frequency of interest, 13.56 MHz. Thus, the inductance value required for the resonation of the system at the frequency of 13.56 MHz is about 5.5 µH. The designed printed inductor has seven turns and dimensions of 65 mm × 40 mm, being 500 µm the width of the

conductor and the interspacing between the lines. The frequency response of the antenna as well as the resonant frequency of the full system antenna-RFID chip has been evaluated. The measured values of inductance and quality factor at the frequency of interest are 5.32 µH and 1.43, respectively. The impedance of the tag reaches a value of 817 Ω at the resonant frequency, in this case 13.68 MHz. Although this value is not exactly the desired working frequency of 13.56 MHz, it is valid for a wireless operation following the ISO15693 protocol specification.

Android application

An Android application has been developed to use an NFC-enabled smartphone as the external reader for the sensing tag. The application has been designed and tested against API 23. However, to support different Android versions, the lowest API level compatible with the application is API 16. The application user interface consists of several text fields showing information about the tag identification number, current temperature, values of each colour detector and gases concentration computed from these values.
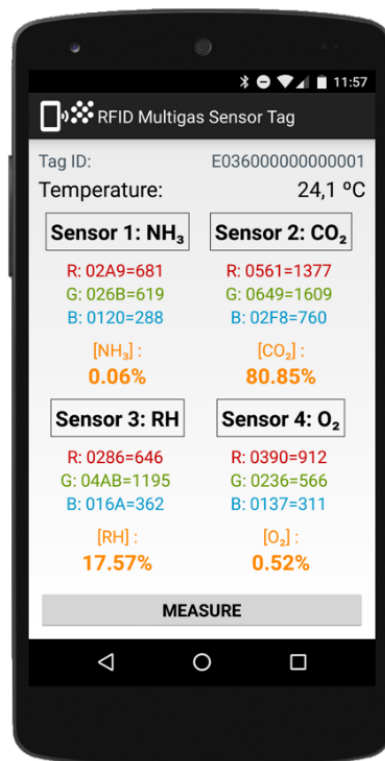
Figure 4. Smartphone running the Android application.

When the smartphone is approached to the tag, it is detected, the Android application is started and the system is powered up. After this, the white LED switches on, the microcontroller sequentially reads the digital outputs of the four colour detectors by means of the I2C (Inter-Integrated Circuit) protocol and it computes the different gases concentrations. Then, the microcontroller saves all these measurements using the SPI (Serial Peripheral Interface) protocol on specific locations of the RFID chip's non-volatile memory. These memory locations are accessed by the Android application through the NFC interface using the ISO 15693 NFC protocol, and the results are displayed on the screen of the smartphone, as shown in Figure 4. This whole procedure takes 812 ms to complete. The application also gets the temperature value measured by the RFID on-chip temperature sensor. The explained procedure is repeated each time the user clicks on the Measure button of the application user interface.

Results and Discussion

The multi-gas sensing tag has been applied to monitor the concentrations of oxygen, carbon dioxide, ammonia and humidity. The concentration of O_2 in a MAP is very low, usually ranging from 0.05% to 2%, while the CO_2 is flushed into the package to obtain a high concentration above 60%.[22] The concentration of ammonia will depend on the spoilage status of the food and it is found in low concentrations in the order of tens of ppm.[36] The relative humidity of the MAP can take both low and high values depending on the application.[27,37]

The four gas sensors show an optical response to the presence of the corresponding gas, being the response of the O_2 sensor luminescent and the response of the rest of the sensors colourimetric. Previous work of the authors proved the feasibility of the structure shown in Figure 1(B) for the reading of the optical response of sensors both luminescent or colourimetric.[22] There, a white LED was used as optical source for colourimetric sensors, and a specific LED for the excitation of luminescent sensors that require an optical source of a certain wavelength. In this work, we have been able to use a common white LED for the excitation of all sensors by means of a redesign and optimization of the sensing area. The spectrum of this LED contains the wavelengths necessary for the excitation of the luminescent sensor.

Stability of the power supply

The power supply of the tag provided by the RFID/NFC chip SL13A from the electromagnetic energy harvesting has been evaluated in order to prove its stability and analyze its possible influence on the response of the digital colour detectors.
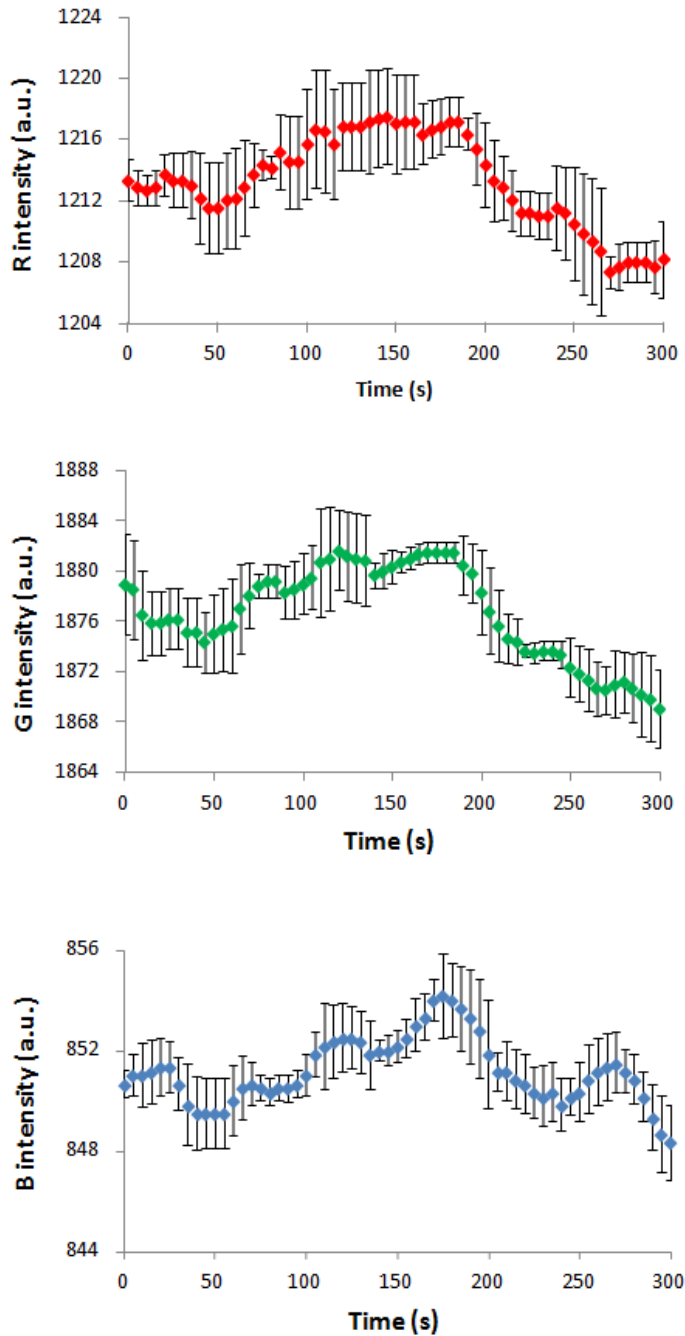
Figure 5. Output signals of the colour detector over time.

Two external parameters can affect the stability of the regulated voltage generated by the SL13A: the powering time and the position of the smartphone when it is approximated to the tag antenna. Since the SL13A chip requires an induced electromagnetic field in the antenna high enough to provide the regulated power supply, not every position of the smartphone is able to activate the tag. When it is adequately placed, only a small displacement is allowed to avoid the deactivation of the system. Within this accepted range of positions of the smartphone, the voltage output of the SL13A presents a drop of 5% of its nominal value. Since the colour detector is a digital device that can be powered with a voltage from 2.25 to 3.6 V this variation in the power supply has no effect on the output signals, according to manufacturer.

The influence of the powering time on the response of the colour detector is depicted on Figure 5. This graphic shows the measurements of a stable incident light taken every 5 seconds from the moment of activation of the tag by the smartphone up to 5 minutes. Each point in the curves is calculated as the mean value of six replicas, and the error bars are obtained as the standard deviation of these replicas.

As it can be seen, some fluctuation of the measured values is present. Nevertheless, the dispersion of the data is very low with a maximum value of 0.25%, which is below the maximum error obtained in the determination of each measurement from the set of six replicas. Therefore, this fluctuation is assumed to be produced by uncertainty inherent to the colour detector rather than due to the powering time.

System calibration

The multi-gas sensing tag has been calibrated obtaining the response of the different gas sensors to variations in the concentration of the corresponding sensed gas. The measurements are carried out when the tag is powered by the smartphone.

Figure 6A presents the calibration curve of the oxygen sensor. The response of the sensor is characterized by the intensity of the emitted red radiation that reaches the colour detector. This radiation corresponds to the luminescence generated by the complex PdTFPP when it is optically excited.[38] The output data word of the colour detector corresponding to red light is a direct measurement of this luminescence. The mean of 6 replicas at room temperature (21°C) is taken as the representative data for each concentration. An offset signal in the output of the colour detector is induced by the light emitted by the excitation white LED. Nevertheless, since it is a constant interference, it can be easily compensated or included in the calibration curve. As it was expected, the fitting equation is a potential function in the form $I = \alpha \cdot [O_2]^{\beta}$.[39]
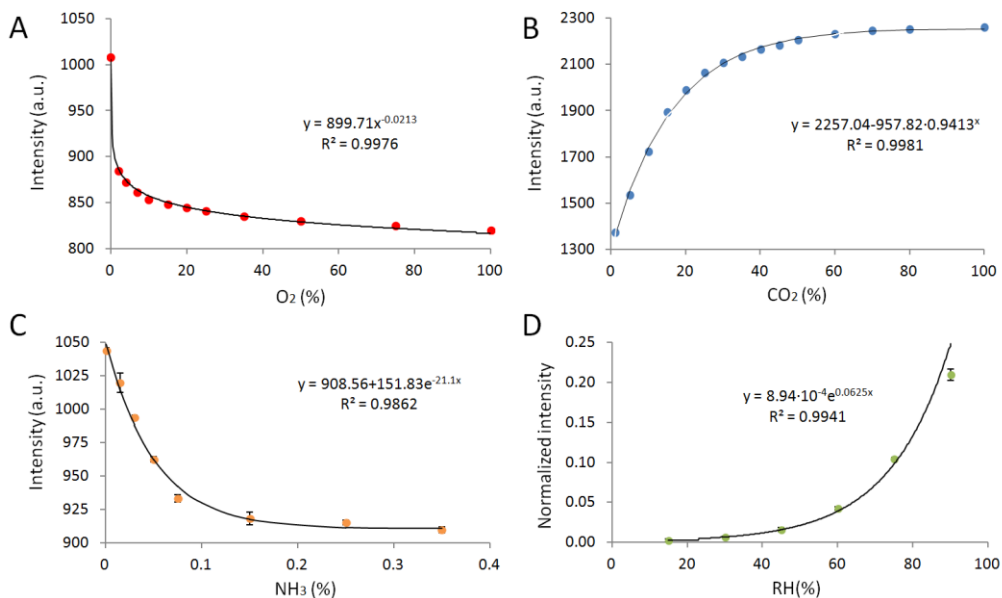
Figure 6. Calibration curves of the gas sensors.

The other three sensors are colourimetric-type. That means that the sensing membranes show a colour shift when the concentration of the surrounding target gas varies. Figures 6B to 6D show the calibration and fitting curves of the CO_2, NH_3 and humidity sensors, respectively. The response of these sensors is quantified by means of the colour intensity parameter given by[40]:

$$I = \sqrt{R^2 + G^2 + B^2} \tag{1}$$

where R, G and B are the red, green and blue components of radiation measured by the digital colour detector, respectively. For the calibration curve of the CO_2 and NH_3 sensors, the intensity is fitted directly to a prediction function which is used to generate a value of the corresponding gas concentration from the colour measurements. Nevertheless, the data obtained from the calibration of the humidity sensor must be further processed to generate a simple fitting function as it is shown in Figure 6D, where a normalized value of the colour intensity in the form $\log(I_0/I)$ is presented, being I_0 the intensity measured for 0% relative humidity. Oxygen, carbon dioxide and relative humidity are calibrated in the full range 0 to 100%. Ammonia is measured from 0 to 0.35 %.

From the fitting functions presented in Figure 6 some technical specifications such as resolution and limit of detection (LOD) can be obtained. The resolution is calculated

by taking derivatives in both sides of the equation and approximating these derivatives to increments[41]:

$$\Delta X = \frac{\partial f(I)}{\partial I} \Delta I \qquad (2)$$

where X is the concentration of gas, $f(I)$ is the corresponding fitting function and ΔI is the error or uncertainty in the determination of the intensity I, which is taken as the standard deviation of the replicas made during the calibration processes. The LOD was obtained using the standard criteria: $LOD = y_b + 3s_b$, where y_b is the average blank signal and s_b is the standard deviation of the blank, which is determined using at least 10 replicas. Repeatability of the measurements is quantified through the coefficient of variation (CV) of the signal, defined as the ratio between the standard deviation of a set of replicas and its mean value.

Table 1 shows the results of the resolution, LOD and repeatability obtained for the four gas sensors. As it can be seen, these specifications allow the use of the developed tag for the monitoring of the selected gases taking into consideration the usual ranges found in MAPs.

Table 1. Technical specifications of the sensing tag.

Gas	Concentration (%)	Resolution (%)	CV (%)	LOD (%)
O_2	0	$1.9 \cdot 10^{-4}$	0.09	$1.3 \cdot 10^{-3}$
	2	$9.4 \cdot 10^{-2}$	0.09	
	20	$9.1 \cdot 10^{-1}$	0.81	
CO_2	5	$7.4 \cdot 10^{-2}$	0.21	0.23
	50	$9.4 \cdot 10^{-1}$	0.13	
	100	3.8	0.07	
NH_3	$1.5 \cdot 10^{-2}$	$3.3 \cdot 10^{-3}$	0.71	$7.9 \cdot 10^{-4}$
	$5.0 \cdot 10^{-2}$	$2.0 \cdot 10^{-3}$	0.22	
	$3.5 \cdot 10^{-1}$	$1.6 \cdot 10^{-1}$	0.25	
RH	15	0.8	0.21	1.8
	45	1.1	0.24	
	90	0.1	0.44	

Cross-Sensitivity

The possible interferences of the gases in the response of the selective sensors have been evaluated. For this purpose, the maximum variation of the output signal of the sensors in the presence of the rest of gases is obtained for a fixed concentration of the target gas. In addition, the influence of the temperature on the response of the selective sensors has been also quantified as the variation of the output signal to an increment of 25 °C. Table 2 shows the obtained results.

As it can be seen, the interference produced by the gases on the response of the other gases selective sensors is very low, below the 3%, and the maximum deviation of the signal is always obtained when the interfering gas is present in a very high concentration near the 100%, which is not a realistic case in MAPs. This implies that in a practical case the cross-sensitivity can be neglected. There is only one exception, the influence of the ammonia on the response of the humidity sensor. The maximum variation of the output signal of this sensor is above 21%. This means that an important interference is produced by this gas and it should be corrected when the determination of the gases concentration is carried out from the readings of the sensors.

Table 2. Cross-sensitivities between the sensors of the tag.

Selective sensor	Interferent	Signal variation (%)
O_2 (0%)	CO_2 (100%)	0.2
	NH_3 (100%)	2.2
	RH (90%)	2.4
	T	14.1
CO_2 (0%)	O_2 (100%)	2.8
	NH_3 (100%)	2.1
	RH (90%)	0.1
	T	2.6
NH_3 (0%)	O_2 (100%)	1.9
	CO_2 (100%)	2.9
	RH (90%)	1.7
	T	1.8
RH (35%)	O_2 (100%)	0.4
	CO_2 (50%)	0.7
	NH_3 (100%)	21.1
	T	2.3

On the other hand, the temperature shows a strong influence in the response of the oxygen sensor, which is a well-known effect.[42] The reading of the oxygen sensor should be also corrected with the value of the temperature;[14] that is the reason for using a RFID chip with a built-in temperature sensor.

Conclusions

In this work, a passive multi-gas sensing RFID/NFC tag is presented for the determination of a high number of parameters (oxygen, carbon dioxide, ammonia, relative humidity and temperature) that are readable with a smartphone. The gases concentrations are determined by means of chemical sensors with optical response. The tag response to the different gases concentrations has been calibrated, obtaining very good values for resolution, repeatability and limit of detection. This makes the proposed system suitable for its use in smart packaging applications. Cross-sensitivity has been also evaluated, obtaining an interference below the 3% in all cases with few exceptions, where the measurements are easily corrected by software in the microcontroller from the full set of readings.

The tag is completely passive and the required power supply for its operation is harvested from the near field generated by an NFC-enabled mobile phone. In this application, the power consumption of the tag is only 8.5 mW in sensing mode. Thanks to the use of digital colour detectors for the reading of the chemical sensors' response, the system is robust against fluctuations in the power supply. In addition to powering the system up, the mobile phone is used to collect and display the results on a custom Android application in less than one second. The wireless communication between the tag and the phone is achieved via the ISO 15693 standard. The use of a smartphone as exciter/receiver instead of a specific RFID reader allows the operation of the tag by any non-expert and non-trained user. This tag can be applied to a wide range of applications in modified atmospheres where the monitoring of gases composition is required, or in smart packaging applications where the control of the conditions for food and beverage preservation needs to be guaranteed.

Author Information: Corresponding Author: *E-mail: amartinez@ugr.es. ORCID ID A.Martínez-Olmos: 0000-0001-6765-789X. Notes: The authors declare no competing financial interest.

References

(1) Han, J.H., Innovations in Food Packaging. Academic Press, 2005.

(2) Kerry, J.P.; O'Grady M.N.; Hogan S.A. Meat Sci. 2006, 74, 113-130.

(3) Rooney, M.L. Active Food Packaging, Springer US, 1995.

(4) Chapon, J.F.; Blanc, C.; Varoquaux, P. Postharvest Biol. Technol. 2004, 31, 21–28.

(5) Singh, P.; Wani, A.A.; Karim, A.A.; Langowski, H.C. Int. J. Dairy Technol. 2012, 65, 161-177.

(6) Robertson, G.L. Food Packaging: Principles and Practice, CRC Press, 2012.

(7) De Santos, F.; Rojas, M; Lockhorn, G.; Brewer, M.S. Meat Sci. 2007, 77, 520–528.

(8) Marsh, K., Bugusu, B. J. Food Sci. 2007, 72, 39-55.

(9) Yam, K.L.: Lee, D.S. Emerging food packaging technologies: principles and practice, Elsevier 2012.

(10) Potyrailo, R.A.; Nagraj, N.; Tang, Z.; Mondello, F.J.; Surman, C.; Morris, W. J. Agric. Food Chem. 2012, 60, 8535-8543.

(11) Bhadra, S.; Narvaez, C.; Thomson, D.J.; Bridges, G.E. Talanta 2015, 134, 718–723.

(12) Ramos, A.; Clément, P.; Lazaro, A.; Llobet, E.; Girbau, D. IEEE Antennas Wirel. Propag. Lett. 2015, 14, 1145-1148.

(13) Zou, Z.; Chen, Q.; Uysal, I.; Zheng. Phil. Trans. R. Soc. A 2014, 372, 1-17.

(14) Martínez-Olmos, A.; Fernández-Salmerón, J.; Lopez-Ruiz, N.; Rivadeneyra Torres, A.; Capitan-Vallvey, L.F.; Palma, A.J. Anal. Chem. 2013, 85, 11098–11105.

(15) Occhiuzzi, C.; Rida, A.; Marrocco, G.; Tentzeris, M. IEEE Trans. Microw. Theory Tech. 2011, 59, 2674-2684.

(16) Meng, X.; Kim, Puligundla, P.; Ko S. J. Korean Soc. Appl. Biol. Chem. 2014, 57, 723–733.

(17) Tanguy, N.R.; Fiddes, L.K.; Yan, N. ACS Appl. Mater. Interfaces 2015, 7, 11939–11947.

(18) Matindoust, S.; Baghaei-Nejad, M.; Abadi, M.H.S.; Zhuo, Z.; Li-Rong, Z. Sens. Rev. 2016, 36, 169–183.

(19) Fiddes, L.K.; Yan, N. Sens. Actuators B-Chem. 2013, 186, 817– 823.

(20) Azzarelli, J.M.; Mirica, K.A.; Ravnsbæk, J,B, Swager, T.M. Proc. Natl. Acad. Sci. U. S. A. 2014, 111, 18162–18166.

(21) Kassala, P.; Steinberg, I.M.; Steinberg, M.D. Sens. Actuators B-Chem. 2013, 184, 254– 259.

(22) Escobedo, P.; Pérez de Vargas-Sansalvador, I.M.; Carvajal, M.; Capitán-Vallvey, L.F.; Palma, A.J.; Martínez-Olmos, A. Sens. Actuators B-Chem. 2016, 236, 226–232.

(23) Jacxsens, L.; Devlieghere, F.; Van der Steen, C.; Debevere, J. Int. J. Food Microbiol. 2001, 71, 197–210.

(24) Kirtil, E.; Kilercioglu, M.; Oztop, M.H. Modified atmosphere packaging of foods, Reference Module in Food Sciences Elsevier, 2015.

(25) Weigel, C.; Schneider, M.; Schmitt, J.; Hoffmann, M.; Kahl, S.; Jurisch, R. J. Sens.

Sens. Syst. 2015, 4, 179–186.

(26) Kuswandi, B.; Jayus; Restyana, A.; Abdullahb, A.; Heng, L.Y.; Ahmad, M. A novel colorimetric food package label for fish spoilage based on polyaniline film, Food Control 2012, 25, 184-189.

(27) Nopwinyuwong, A.; Trevanich, S.; Suppakul, P. Talanta 2010, 81, 1126–1132.

(28) Gao, J.; Sidén, J.; Nilsson, H.E.; Gulliksson, M. IEEE Sens. J. 2013, 13, 1824-1834.

(29) Ki-Hwan, E.; Kyo-Hwan, H.; Sen, L.; Joo-Woong, K. Int. J. Distrib. Sens. Netw. 2014, 2014, 591812.1-591812.9.

(30) Amao, Y.; Komori. T. Talanta 2005, 66.4, 976–81.

(31) Werner, T.; Klimant, I.; Wolfbeis, O.S. Analyst 1995, 1627-1631.

(32) Raimundo Jr., I.M.; Narayanaswamy, R. Analyst 1999, 124.11, 1623–1627.

(33) Windl, R; Bruckner, F.; Abert, C.; Suess, D; Huber, T.; Vogler, C.; Satz, A; J. Appl. Phys. 2015, 117, 17C125.1- 17C125.4.

(34) Kumar, P.; Reinitz, H.W.; Simunovic, J.; Sandeep, K.P.; Franzon, P.D. J. Food Sci. 2009, 74, R101-R106.

(35) Pursula, P.; Marttila, I.; Nummila, K.; Seppä, H. IEEE Trans. Instrum. Meas. 2013, 62, 2559-2566.

(36) Pacquit, A.; Lau, K.T.; McLaughlin, H.; Frisby, J.; Quilty, B.; Diamond, D. Talanta 2006, 69, 515–520.

(37) Yahia, E.M.; Guevara, J.C.; Tijskens, L.M.M.; Cedeño, L. Acta Hort. 2005, 647, 97-104.

(38) López-Ruiz, N.; Martínez-Olmos, A.; Pérez de Vargas-Sansalvador, I.M.; Fernández-Ramos, M.D.; Carvajal, M.A.; Capitan-Vallvey, L.F.; Palma, A.J. Sens. Actuators B-Chem. 2012, 171, 938-945.

(39) López-Ruiz, N.; Hernández-Bélanger, D.; Carvajal, M.A.; Capitán-Vallvey, L.F.; Palma, A.J.; Martínez-Olmos, A.; Sens. Actuators B-Chem. 2015, 216, 595-602.

(40) Park, W.; Hong, W.; Kim, C.S. IEEE Sens. J. 2010, 10, 1855–1862.

(41) Pérez de Vargas-Sansalvador, I.M.; Martinez-Olmos, A.; Palma, A.J.; Fernández-Ramos, M.D.; Capitán-Vallvey L.F. Microchim. Acta 2011, 172, 455-464.

(42) Koren, K.; Borisov, S.M.; Klimant, I. Sens. Actuators B-Chem. 2012, 169, 173–181.

4.8. Publication 4

Non-Invasive Oxygen Determination in Intelligent Packaging Using a Smartphone [7]

Pablo Escobedo Araque, Isabel M. Pérez de Vargas Sansalvador, Nuria López Ruiz, Miguel M. Erenas, Miguel. A. Carvajal Rodríguez, and Antonio Martínez Olmos

P. Escobedo Araque, M. A. Carvajal Rodríguez, and A. Martínez Olmos are with the Department of Electronics and Computer Technology, University of Granada, 18071 Granada, Spain (e-mail: pabloescobedo@ugr.es; carvajal@ ugr.es; amartinez@ugr.es).

I. Pérez de Vargas Sansalvador and M. M. Erenas are with the Department of Analytical Chemistry, University of Granada, 18071 Granada, Spain (e-mail: isabelpdv@ugr.es; erenas@ugr.es).

N. López Ruiz is with the Department of Electronics Technology, Carlos III University of Madrid, 28911 Leganés, Spain (e-mail: nulopezr@ing.uc3m.es).

Abstract

Here, we present a technique for the determination of the gaseous oxygen concentration inside packed food. It is based on the use of a luminescent membrane sensitive to O_2 that is optically excited and read by a smartphone. The flash of the smartphone along with an optical filter is used as the light source for the optical stimulation of the membrane. The luminescence generated, which is quenched by the surrounding gaseous oxygen, is registered by the rear camera of the same device. The response parameter is defined by combining the registered intensities at two different wavelength ranges corresponding to the emission and the absorption peaks of the sensitive membrane. Thanks to this novel response parameter, the sensitivity is increased and, more importantly, the thermal dependence of the membrane is significantly reduced. This approach allows the use of a luminescent O_2-sensitive membrane for intelligent packaging with no need of any associated electronics for its excitation and reading. This means that an oxygen sensor is developed, where a luminescent compound acts as an indicator, therefore combining the advantages of both schemes, that is, the simplicity and reduced cost of indicators with the high sensitivity and accuracy of selective sensors.

Index Terms: Intelligent packaging, oxygen sensing, optical sensor, luminescent membrane, smartphone, Android™ application.

I. Introduction

Along with its primary objective of containment and transportability, the main aim of packaging is the protection and preservation of food and beverage from external contamination. Thanks to the presence of an appropriate packaging, the content can be prevented from deterioration, its shelf life is extended and its quality and safety preserved. In the last decades there has been an increasing interest regarding research and development of new technology in food and beverage packaging, due to the growing requirement from the final consumers to receive a guarantee of freshness, quality and safety of the product.

Three major strategies have been followed in order to add new functionalities to packaging systems: active and intelligent packaging (AP and IP), edible films/coatings and modified atmosphere packaging (MAP) [1]. Active packaging allows incorporation of additives, such as gas scavengers or temperature and moisture controllers among others to enhance the quality and sensory aspects of packaged foods [2]. Intelligent packaging is oriented to gather information related to the status of the content, and transmit it to the consumer [3]. Edible films are defined as thin layers of materials that can be consumed and provides barriers to moisture,

oxygen and solute movement for the food [4]. MAP may be defined as an active packaging method in which an altered atmosphere is created in the headspace, which retards chemical deterioration while simultaneously delays the growth of spoilage organisms [5]. One of the most important parameters to sense in intelligent packaging and MAP is the concentration of gaseous oxygen within the package, since oxygen is the main cause of food spoilage [6], [7]. The presence of an atmosphere with some elevated concentration of O_2 (above 2%) facilitates processes such as promotion of microbial growth, lipid oxidation, protein decomposition, and discoloration [8]. In IP and MAP there are two main technologies for monitoring the analytes of interest: indicators and sensors [9]. Indicators are molecules that displays an optical effect with a specific analyte such as oxygen [10]. They can be disposed as two-dimensional membranes, aimed to provide direct information about the presence and/or concentration range of a substance. For oxygen determination, many indicators have been developed following this principle. Some of them are designed to react to the mere presence of oxygen, showing a color drift in this case [11], while others present a wide color displacement related to the oxygen concentration, thus allowing a qualitative detection of the oxygen [8], [12]. In this last case, the color difference should be significant for different concentrations to prevent the misreading of the consumer. Another type of optical oxygen indicators are those based on a luminescent response. In such systems, the luminescence generated by an optically excited luminophore is related, in terms of intensity or lifetime, to the concentration of the surrounding molecular oxygen [13]. These indicators also provide qualitative information about the oxygen concentration within the package [14], [15]. The drawback of luminescent indicators is that they require an external light source. Sensors are more complex systems or devices that include control and processing electronics, interconnection network and software. A sensor contains one or more detectors that generate a signal proportional to the monitored analyte or magnitude. This signal is processed and transmitted as information to a user or consumer, thus providing quantitative data. Oxygen sensors are able to provide the value of the oxygen concentration with very high resolution [16]–[18].

In the last two decades there has been a great effort to adapt or create oxygen sensors that are suitable to be included in intelligent packaging [8], [19]–[21]. The most promising oxygen sensors are based on luminescent detectors, following the same operation principle than the luminescent-based indicators. They offer fast responses, do not consume any analyte and present high sensitivity and accuracy. Many examples of oxygen sensors for intelligent packaging have been proposed based on this type of sensors [22]–[27]. The main drawback in all cases is that they require the presence of a light source, a light detector, processing and communication electronics and powering. This leads to a whole circuitry that must be included in the package in a process that becomes very expensive and complex. As a consequence, the inclusion of full sensing capabilities in intelligent packaging may result prohibitive.

In previous works the authors proposed some designs for gas sensing including oxygen [23], [28], [29]. These prototypes are based on passive flexible tags that generate power supply from energy harvesting, therefore they are suitable to be used as sensors in intelligent packaging and MAPs. Nevertheless, they are still complex and expensive. In this work, we present a new approach in which the luminescent oxygen sensor is simplified by removing the whole electronics, thus reducing it to a single oxygen sensitive membrane. The optical excitation of this membrane is carried out by the application of the flash light of a smartphone along with an optical filter at a fixed distance, and the emitted luminescence is registered in a photography taken with the rear camera of the smartphone. Similar schemes can be found in the literature but using optical fibers as an alternative to the free-space orientation of the proposed sensor [30], [31]. The processing capabilities of this device allow the evaluation of the intensity of this luminescence, thus generating an accurate prediction of the inner oxygen concentration. In this way, the sensitive membrane is treated as an indicator since no electronics are used, but it maintains its sensor characteristics. The system offers the advantages of both schemes: the simplicity and very low cost of an indicator together with the high sensibility and accuracy of a sensor. Moreover, the scan of the luminescent membrane using the camera of the smartphone removes the subjectivity of the consumer in the reading of the provided information.

II. Materials and Methods

A. Reagents and Materials

Platinum octaethylporphyrin complex (PtOEP), 1,4-diazabicyclo[2.2.2] octane (DABCO, 98%), tetrahydrofuran (THF) and polystyrene (PS, average MW 280,000, Tg: 100 °C, GPC grade) were all supplied by Sigma–Aldrich Química S.A. (Madrid, Spain). The gases O_2 and N_2 (>99%) were supplied in gas cylinders by Air Liquide S.A. (Madrid, Spain).

B. Instruments and Software

In order to calibrate and characterise the proposed system, standard gas mixtures were prepared using nitrogen as inert gas and oxygen, controlling the different percentages using mass flow controllers (Iberfluid, Barcelona, Spain), work pressure 1 atm and flow rate 5 Nl·min−1.

For the monitoring of freshness in pork meat, a thermostatic chamber, with a lateral hole for the connection to a computer and gas tubing entrance, made possible to maintain a controlled temperature between −50 °C and +50 °C with an accuracy of

±0.1 °C for thermal characterization. A heat sealer PFS-300MM Electric Impulse Sealing Machine C. (Media w.s. trade S.L. Barcelona, Spain), high barrier bag material BB3055 specific for meat products were obtained from Sealed Air (Seville, Spain) and a CheckPoint – Handheld Gas Ana-lyzer (O_2/CO_2) Dansensor A/S (Rønnedevej 18, DK-4100 Ringsted, Denmark) was used as reference method for O_2 measurement inside meat packages.

The smartphone used in this work was the Samsung Galaxy S7. This smartphone features a 12-megapixel rear camera with an f/1.6 aperture, focal length of 26mm, optical image stabilization and autofocus. The Android™ version running on the device was 7.0 Nougat, which corresponds to Application Programming Interface (API) level 24.

C. Sensing Membrane Preparation

The cocktail for the preparation of the oxygen-sensitive membrane was made by dissolving 0.5 mg of PtOEP and 12 mg of DABCO in 1 ml of a solution of 5% (w/v) of PS in freshly distilled THF. The sensitive membrane was cast by placing a volume of 20 μL of the cocktail on an inert support using a spin-coater at 180 rpm under ambient atmospheric conditions. After the deposition, the sensing membranes were left to dry in darkness in a THF atmosphere for at least 1 h. The obtained membranes were homogeneous, transparent and pink colored. When they are not in use, they must be kept in darkness to extend their lifetime.

D. System Description

The proposed system is composed of two elements: the oxygen sensitive membrane that is attached to the inner surface of the food package, in contact with the inner atmosphere; and a smartphone used to excite the membrane and register the emitted optical signal generated through a programmed application, as it is schematised in Figure 1.

The flash light is turned on and the device is placed at a fixed distance of the membrane. This light contains the wavelength required for the optical excitation of the sensitive membrane. To reduce optical interference with the rest of wavelengths, an optical filter is attached to the flash light of the smartphone. The filter is a non-commercial 50 μm-thick green plastic film. Several films with different green tones have been tested until achieving the maximum transmittance at the desired wavelengh. Under stable excitation, the generated luminescence presents an intensity that is proportional to the concentration of the surrounding oxygen. In this situation, the smartphone takes a photograph of the excited membrane and processes

it to obtain a value of the emitted intensity. An accurate prediction of the oxygen concentration inside the package is computed from this emitted intensity value [17].
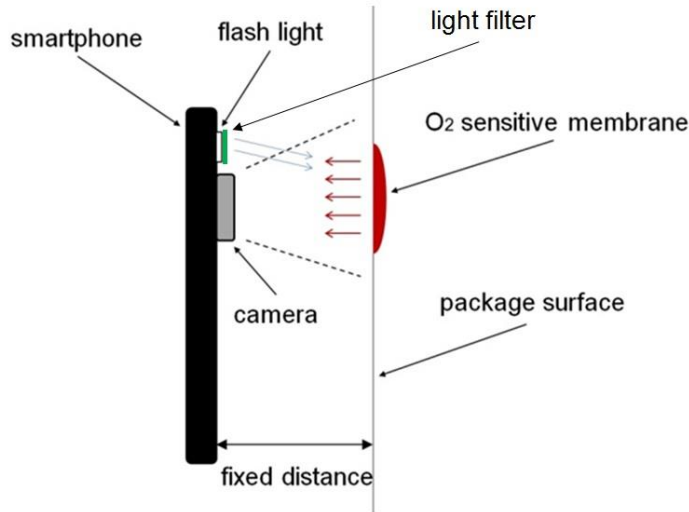
Fig 1. Scheme of the system used to sense O_2.

E. Android Application

A custom developed Android application allows the user to obtain the oxygen concentration by simply approaching the phone to the oxygen sensitive membrane. The application user interface consists of a single white reference circle that is superimposed onto the camera preview. Firstly, the application automatically turns the camera flash light on to excite the membrane. When the camera is aimed at the circular membrane, the application is able to detect it and distinguish it from the background. In order to take the photograph, the user must match the reference on-screen circle with the detected membrane. When both shapes match, a photograph is automatically taken and saved. In this way, the distance between the phone camera and the sensitive membrane is always identical and fixed, so that the same conditions from calibration are achieved. The next screen of the application shows the taken photograph and computes the average red (R), green (G) and blue (B) components inside the detected membrane. After the image processing, which takes less than two seconds, the oxygen concentration computed from these RGB components according to the previous calibration is displayed on the screen, as shown in Figure 2. Finally, the application saves the processed photograph along with the obtained results to the phone internal memory.
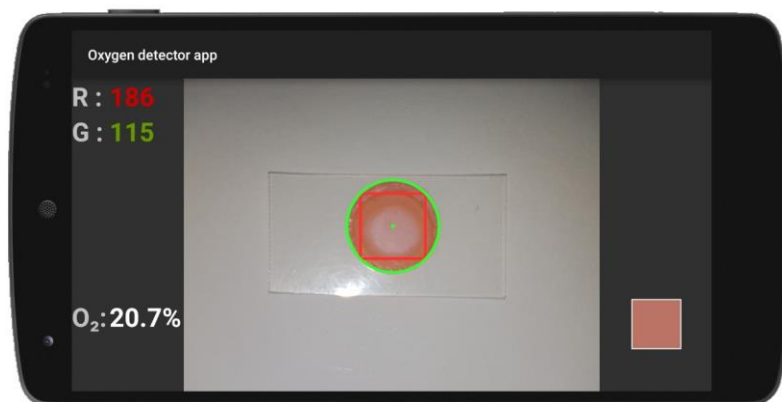
Fig 2. Screenshot of the developed Android application.

The application has been designed using the integrated development environment (IDE) Android Studio 2.3.3. It has been developed and tested against API 24 (Android 7.0), although it is compatible with different Android versions as the lowest supported API level is API 18 (Android 4.3). The algorithms developed to accomplish the detection and processing tasks are based on computer vision OpenCV 3.1.0 Android library. This application is extendable to any Android-based device (smartphone and tablet). For other mobile operating systems, the application should be translated into their appropiate programming language.

III. Results and Discussion

For the determination of O_2, a chemical sensor based on luminescence quenching of the complex PtOEP is used. When this luminophore is optically excited at the wavelengths of 380 and 532 nm, it produces a luminescent emission in the red region of the spectrum with a peak at 645 nm [17]. Figure 3 presents the normalized emission spectrum of this luminophore together with the spectrum of the filtered flashlight of the smartphone.

As it can be seen, the filtered excitation light presents a maximum at the wavelength of 529 nm, which fits almost perfectly with the absorbance peak of the luminophore. Therefore, assuming that the system is optically isolated, only the green light of the filtered source and the red luminescence emitted by the oxygen sensitive membrane have influence on the registered photograph.
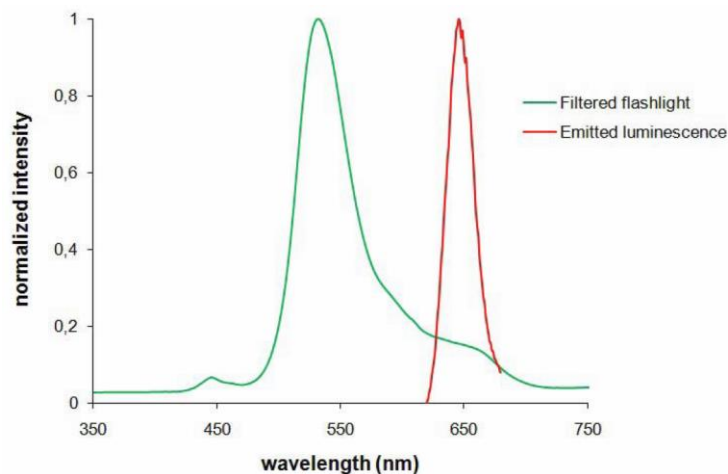
Fig 3. Normalized emission spectra of the luminophore and emitted light of the smartphone flashlight with external filter.

Figure 4 shows an example of the response of the system. Here the original and false-color images of an oxygen sensitive membrane immersed in atmospheres with different oxygen concentrations are depicted. As it is expected, the intensity of the red luminescence decays when the oxygen concentration is increased [32].
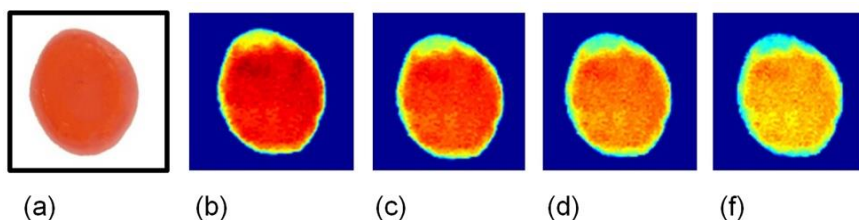
Fig 4. Oxygen sensitive membrane (a) and false-color processed images under growing oxygen concentrations 0%, 30%, 50% and 100% (b-f).

A. System Characterization

The sensing membrane based on PtOEP(PS) has been widely used for oxygen detection, and it is well known that it shows no cross-sensitivity to carbon dioxide or humidity; nevertheless, the temperature has a strong influence on its response. Therefore, this membrane has to be fully characterized by analysing the emitted luminescence at different oxygen concentrations and temperatures. With this aim, two independent calibrations have been carried out. On the one hand, a calibration of this membrane in the full oxygen range 1-100% at room temperature (20°C). On the other hand, a calibration over the temperature range from 0 to 40°C at open air

oxygen concentration (20.9%). In both cases 6 replicas for each concentration are taken. The obtained results are presented in Figures 5 and 6, respectively.
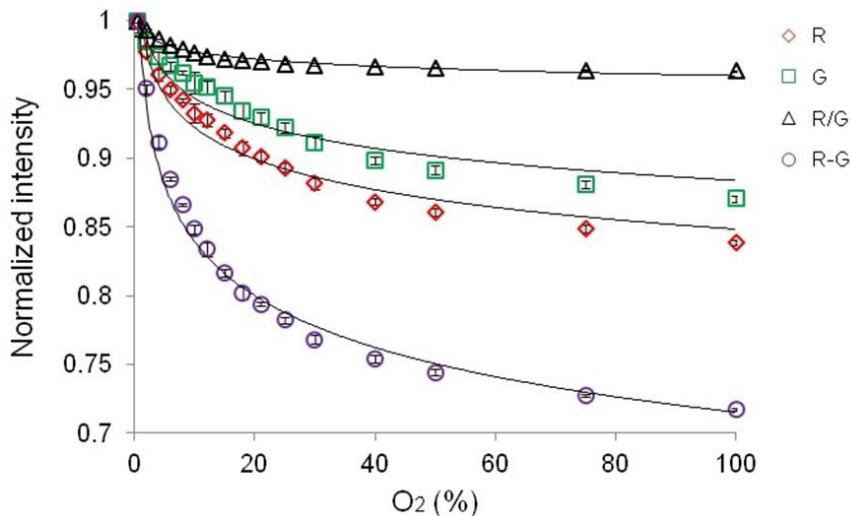
Fig 5. Calibration and fitting curves for O_2 at room temperature using different intensity quantification parameters.

In previous works, the intensity of the luminescence generated by the oxygen sensitive membrane was quantified by means of the red component of the image [17], [28] from the red-green-blue (RGB) space, since it corresponds purely to this luminescence assuming that the system is optically isolated from external light. In other cases, a combination of this R component and the corresponding to the wavelength of the optical source for the excitation has been proposed [23], since it can reduce the influence of small fluctuations of the source. In this work, other parameters for the quantification of the image intensity are evaluated and shown in the Figures 5 and 6. The considered parameters are the R component, thus only including the intensity of the emitted luminescence; the G component, which provides information about the absorbance of the membrane, is also affected by the concentration of the surrounding oxygen; and two relationships derived from these components: the R/G ratio and the R-G difference, where the information about the emitted and absorbed intensities are combined.

From the results shown in Figure 5, it can be observed that the fitting curve of the normalized intensity to the oxygen concentration, whichever parameter is selected to be representative of the intensity of the image, responds to a potential equation of the form I = $\alpha \cdot [O_2]\beta$. Nevertheless, the wider signal variation in the full range of O_2 is obtained for the parameter R-G, which means that improved sensitivity is obtained

if this parameter is used to quantify the intensity of the image. For this case, the fitting curve expression is:

$$I_n = \frac{I}{I_0} = 1.0057\,[O_2]^{-0.076} \tag{1}$$

where I is the intensity given by R-G in the processed image, I_0 the intensity at the minimum oxygen concentration and I_n the normalized intensity. The coefficient of correlation of this fitting curve is $R^2 = 0.9947$.
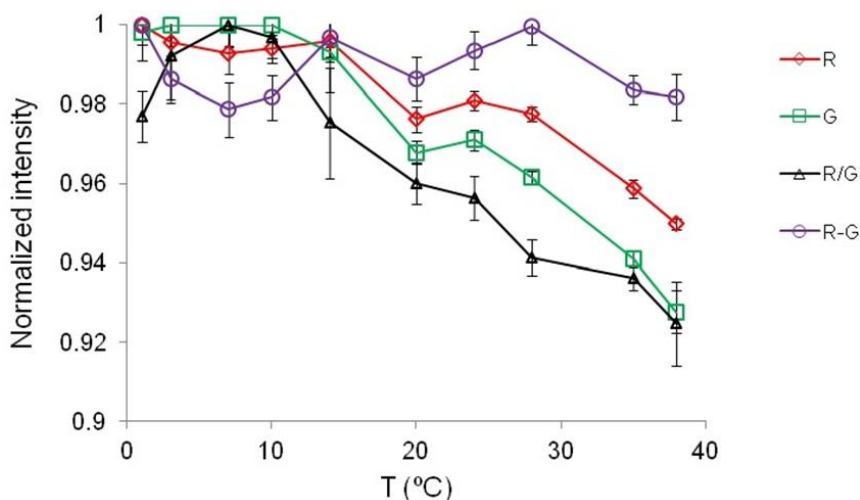
Fig 6. Calibration curves of temperature at open air using different intensity quantification parameters.

From the curves presented in Figure 6, it can be concluded that the intensity of the image calculated as intensity of the luminescence (R), absorbance (G) or a combination of these two magnitudes (R/G, R-G) decays with temperature. This is a common effect in luminescence sensors that has been widely explained in the existing literature [17], [33], [34]. Nevertheless, the published studies show that the influence of the temperature on the response of the luminescent membrane is not well-defined but it shows a behaviour that is not monotonically decreasing and therefore it cannot be fitted to a simple function [35], as it is confirmed by the curves depicted in Figure 6. Therefore, it is difficult to carry out a thermal compensation of the response of the sensitive membrane since there is no accurate fitting expression for this dependence. In addition, a thermal compensation requires the presence of a temperature sensor. In this work, this sensor is not available since our aim is to avoid any electronics from the envelope, and the current smartphones do not include it. In view of this situation and in the light of the curves of Figure 5, the R-G parameter is the most suitable to

represent the image intensity since it has the lowest variation with temperature, which is limited to 2.1%, while the variation of the rest of parameters is above 5%. Consequently, we can assume that the error in the determination of the R-G parameter is 2.1% in the worst case and no further thermal compensation is required.

In summary, from the calibrations presented in Figures 5 and 6, the novel intensity parameter defined as R-G, where information about luminescence and absorbance is combined, is used to relate the image of the sensitive membrane to the oxygen concentration. This parameter offers advantages such as increased sensitivity and less temperature dependence.

The resolution of the system can be obtained from Equation (1) taking derivatives in both sides of the equation and approximating them to increments [23]. By doing so, the obtained expression for the resolution is:

$$\Delta O_2 = \frac{\left(\frac{I_n}{\alpha}\right)^{1/\beta}}{\beta I_n} \Delta I_n \tag{2}$$

where ΔI_n is the error in the determination of the normalized intensity I_n, which is taken as 2.1% because of the temperature influence as explained above. In this case, the average obtained resolution for the prediction of the oxygen concentration is 30%. If the package is kept at a constant temperature as it happens in the storage of foods, the thermal drift is minimized, and the error in its determination is given by the accuracy of the system. This parameter is taken as the standard deviation of the replicas taken for each measurement of Figure 5, obtaining a value of 0.31%, which leads to a resolution of 4.4% of the predicted oxygen concentration.

B. Case Study

The proposed system has been applied to the monitoring of freshness in pork meat. It is known that the concentration of oxygen in a sealed package containing the meat is related to the bacterial activity [36]. Therefore, a measurement of the inner O_2 concentration provides direct information about the state of the content. For this experiment raw pork was purchased fresh, 500 g packaged inside an O_2 impermeable bag, and sealed using the impulse bag sealer. Two identical oxygen membranes have been used, one inside the packed fresh pork and the other one as reference outside the package.

The objective of the reference membrane is to show that the changes in the response of the internal membrane are not produced by external variations but only by the modification of the internal atmosphere. Figure 7 shows the analysed package.

Fig 7. Pork meat in a sealed package where internal and external sensitive membranes have been attached.

This package has been stored in a controlled-temperature environment at 4°C for a week. During this time, measurements of the internal oxygen concentration have been carried out by using the gas analyser as well as the proposed system. 6 replicas for each measurement were taken. Figure 8 presents the obtained results. In Figure 8-A the evolution of the normalized intensity parameter R-G in both external and internal sensitive membranes is depicted. As it can be seen, the response of the reference membrane remains constant, while the corresponding to the sensing membrane grows over time. The variation of the signal generated by the internal membrane is processed and translated into variation in the predicted oxygen concentration within the package, as it is shown in Figure 8-B, where it is compared to the direct oxygen measurements obtained with the gas analyser. As it was expected, the oxygen concentration decays over time as a result of the bacterial activity. The predicted values of oxygen obtained with the novel system are in good concordance with the direct measurements taken using the reference method.

IV. Conclusion

In this work a novel approach for oxygen determination in intelligent packaging is proposed. In the presented scheme, an oxygen sensitive membrane with luminescent response is attached to the inner surface of the packed food. A smartphone is used for simultaneous excitation and reading of the membrane, thus avoiding the necessity of any additional electronics integrated in the envelope to complete the oxygen sensor. This leads to a system where the sensitive membrane acts as an indicator since no other elements in the package are required to provide information about the oxygen concentration.
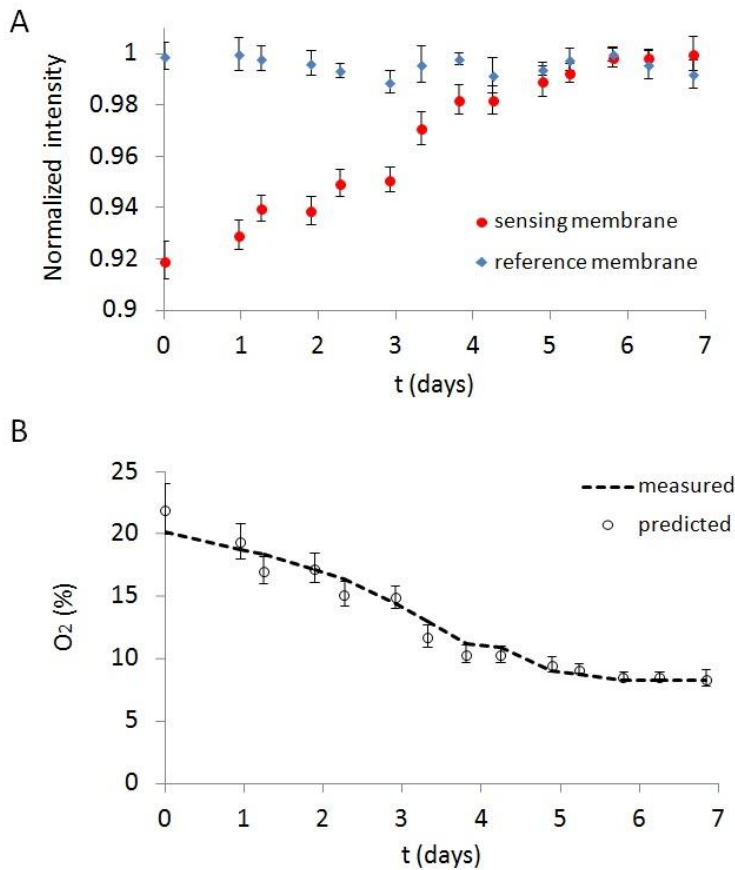
Fig 8. Response of the internal and external membranes (A) and oxygen concentration within the package (B).

Moreover, the system also has the advantage of providing qualitative information, that is, accurate predictions of the oxygen concentration inside the package, as a full sensor. An easy-to-use Android app has been developed to take a photograph of the membrane at a fixed distance. The application also processes it in order to obtain the colorimetric information about the intensity of the luminescence and the absorbance of the membrane. These magnitudes are combined to define a new intensity parameter that is related to the oxygen concentration. This parameter shows improved sensitivity and immunity to thermal drift. The system has been applied to the monitoring of pork meat freshness sealed in a package and stored into a temperature-controlled environment. The results show that the developed system is able to provide accurate information about the oxygen concentration inside the package, information that is directly related to the bacterial activity and therefore to the state of meat.

References

[1] J. H. Han, Innovations in Food Packaging, 2nd ed. San Diego, CA, USA: Academic, 2013.

[2] R. Ahvenainen, Novel Food Packaging Techniques. Cambridge, U.K.: Woodhead Pub., 2003.

[3] K. L. Yam, P. T. Takhistov, and J.Miltz, "Intelligent packaging: Concepts and applications," J. Food Sci., vol. 70, no. 1, pp. R1–R10, 2005.

[4] T. Bourtoom, "Edible films and coatings: Characteristics and properties," Int. Food Res. J., vol. 15, no. 3, pp. 237–248, 2008.

[5] B. A. Blakistone, Principles and Applications of Modified Atmosphere Packaging of Foods, 2nd ed. Gaithersburg, MD, USA: Aspen, 1999.

[6] M. L. Rooney, Active Food Packaging. New York, NY, USA: Springer, 1995.

[7] J. Bonilla, L. Atarés, M. Vargas, and A. Chiralt, "Edible films and coatings to prevent the detrimental effect of oxygen on food quality: Possibilities and limitations," J. Food Eng., vol. 110, no. 2, pp. 208–213, 2012.

[8] A. Mills, K. Lawrie, J. Bardin, A. Apedaile, G. A. Skinner, and O'Rourke, "An O_2 smart plastic film for packaging," Analyst, vol. 137, pp. 106–112, Jan. 2012.

[9] M. Ghaani, C. A. Cozzolino, G. Castelli, and S. Farris, "An overview of the intelligent packaging technologies in the food sector," Trends Food Sci. Technol., vol. 51, pp. 1–11, Mar. 2016.

[10] X. Wang and O. S. Wolfbeis, "Optical methods for sensing and imaging oxygen: Materials, spectroscopies and applications," Chem. Soc. Rev., vol. 43, no. 10, pp. 3666–3761, 2014.

[11] C. H. Vu and K. Won, "Novel water-resistant UV-activated oxygen indicator for intelligent food packaging," Food Chem., vol. 140, pp. 52–56, Sep. 2013.

[12] K. Lawrie, A. Mills, and D. Hazafy, "Simple inkjet-printed, UV-activated oxygen indicator," Sens. Actuator B, Chem., vol. 176, pp. 1154–1159, Jan. 2013.

[13] A. Mills, "Oxygen indicators and intelligent inks for packaging food," Chem. Soc. Rev., vol. 34, pp. 1003–1011, Dec. 2005.

[14] R. C. Evans, P. Douglas, J. A. Williams, and D. L. Rochester, "A novel luminescence-based colorimetric oxygen sensor with a 'traffic light' response," J. Fluorescence, vol. 16, pp. 201–206, Mar. 2006.

[15] A. Mills, C. Tommons, R. T. Bailey, M. C. Tedford, and P. J. Crilly, "UVactivated luminescence/colourimetric O_2 indicator," Int. J. Photoenergy, vol. 2008, pp. 1–6, 2008.

[16] C. Baleizão, S. Nagl, M. Schäferling, M. N. Berberan-Santos, and O. S. Wolfbeis, "Dual fluorescence sensor for trace oxygen and temperature with unmatched range and sensitivity," Anal. Chem., vol. 80, pp. 6449–6457, Aug. 2008.

[17] N. López-Ruiz et al., "Determination of O₂ using colour sensing from image processing with mobile devices," Sens. Actuator B, Chem. vols. 171–172, pp. 938–945, Aug./Sep. 2012.

[18] R. Ambekar, J. Park, D. B. Henthorn, and C. S. Kim, "Photopatternable polymeric membranes for optical oxygen sensors," IEEE Sensors J., vol. 9, no. 2, pp. 169–175, Feb. 2009.

[19] J. Ehgartner, H. Wiltsche, S. M. Borisov, and T. Mayr, "Low cost referenced luminescent imaging of oxygen and pH with a 2-CCD colour near infrared camera," Analyst, vol. 139, no. 19, pp. 4924–4933, 2014.

[20] F. C. O'Mahony, T. C. O'Riordan, N, Papkovskaia, V. I. Ogurtsov, J. P. Kerry, and D. B. Papkovsky, "Assessment of oxygen levels in convenience-style muscle-based sous vide products through optical means and impact on shelf-life stability," Packag. Technol. Sci., vol. 17, no. 4, pp. 225–234, 2004.

[21] M. Fitzgerald, D. B. Papkovsky, M. Smiddy, J. P. Kerry, C. K. O'Sullivan, D. J. Buckley, and G. G. Guilbault, "Nondestructive monitoring of oxygen profiles in packaged foods using phasefluorimetric oxygen sensor," J. Food Sci., vol. 66, no. 1, pp. 105–110, 2001.

[22] A. Hempel, M. G. O'Sullivan, D. B. Papkovsky, and J. P. Kerry, "Nondestructive and continuous monitoring of oxygen levels in modified atmosphere packaged ready-to-eat mixed salad products using optical oxygen sensors, and its effects on sensory and microbiological counts during storage," J. Food Sci., vol. 78, pp. 1057–1062, Jul. 2013.

[23] A. Martínez-Olmos, J. Fernández-Salmerón, N. Lopez-Ruiz, A. R. Torres, L. F. Capitan-Vallvey, and A. J. Palma, "Screen printed flexible radiofrequency identification tag for oxygen monitoring," Anal.Chem., vol. 85, no. 22, pp. 11098–11105, 2013.

[24] Z. Zou, Q. Chen, I. Uysal, and L. Zheng, "Radio frequency identification enabled wireless sensing for intelligent food logistics," Philos. Trans. Roy. Soc. A, vol. 372, pp. 1–17, Jun. 2014.

[25] K. H. Eom, M. C. Kim, S. Lee, and C. W. Lee, "The vegetable freshness monitoring system using RFID with oxygen and carbon dioxide sensor," Int. J. Distrib. Sens. Netw., vol. 8, no. 6, pp. 1–6, 2012.

[26] K. Eom, W. Lee, and J. Shin, "Integration of an oxygen indicator sensor with a passive UHF band RFID tag," Contemp. Eng. Sci., vol. 9, no. 18, pp. 889–896, 2016.

[27] W. Kozak and U. Samotyja, "The use of oxygen content determination method based on fluorescence quenching for rapeseed oil shelf-life assessment," Food Control, vol. 33, pp. 162–165, Sep. 2013.

[28] P. Escobedo, I. M. P. de Vargas-Sansalvador, M. Carvajal, L. F. Capitán-Vallvey, A. J. Palma, and A. Martínez-Olmos, "Flexible passive tag based on

light energy harvesting for gas threshold determination in sealed environments," Sens. Actuator B, Chem., vol. 236, pp. 226–232, Nov. 2016.

[29] P. Escobedo et al., "Flexible passive near field communication tag for multigas sensing," Anal. Chem., vol. 89, no. 3, pp. 1697–1703, 2017.

[30] K. Bremer and B. Roth, "Fibre optic surface plasmon resonance sensor system designed for smartphones," Opt. Exp., vol. 23, pp. 17179–17184, Jun. 2015.

[31] A. Sultangazin, J. Kusmangaliyev, A. Aitkulov, D. Akilbekova, M. Olivero, and D. Tosi, "Design of a smartphone plastic optical fiber chemical sensor for hydrogen sulfide detection," IEEE Sensors J., vol. 17, no. 21, pp. 6935–6940, Nov. 2017.

[32] J. Park, W. Hong, and C.-S. Kim, "Color intensity method for hydrogel oxygen sensor array," IEEE Sensors J., vol. 10, no. 12, pp. 1855–1862, Dec. 2010.

[33] V. C. Fernicola, L. Rosso, R. Galleano, T. Sun, Z. Y. Zhang, and K. T. V. Grattan, "Investigations on exponential lifetime measurements for fluorescence thermometry," Rev. Sci. Instrum., vol. 71, no. 7, pp. 2938–2943, 2000.

[34] X. Zhaoa, W. Zhenga, D. Donga, and L. Jiao, "Temperature effect on fluorescence of PtOEP embedded in sol–gel membrane used in oxygen sensor," Optik-Int. J. Light Electron Opt., vol. 124, pp. 6799–6802, Dec. 2013.

[35] R. Shinar, Z. Zhou, B. Choudhury, and J. Shinar, "Structurally integrated organic light emitting device-based sensors for gas phase and dissolved oxygen," Anal. Chim. Acta, vol. 568, pp. 190–199, May 2006.

[36] I. M. P. de Vargas-Sansalvador, M. M. Erenas, D. Diamond, B. Quilty, and L. F. Capitan-Vallvey, "Water based-ionic liquid carbon dioxide sensor for applications in the food industry," Sens. Actuator B, Chem., vol. 253, pp. 302–309, Dec. 2017.

5. Conclusions and future work

This research has focused on the design, development and validation of sensor systems primarilly based on the use of printing technologies on flexible substrates as the key fabrication process. Below is included a summary of the main conclusions and future work of the contributions of this thesis:

1. Two sintering methods, thermal and electrical sintering, have been studied and compared as post-printing treatments in terms of electrical and RF performance. Regarding thermally sintered printed patterns, we have demonstrated that lower resistivity values are achieved if the heating treatment is done with temperature step rather than temperature ramp. In both cases, resistivity decreases with heating temperature. For the same sintering time, resistivity shows about 67% decrease when final temperature is 200 °C compared to the final temperature of 100 °C. The best resistivity value of 9.4 μΩ · cm, which is approximately six times the value of bulk silver resistivity, was achieved with a temperature step of 200 °C. The results are in good agreement with the expected resistivity values reported in the datasheet of the conductive ink. Electrical sintering was tested to overcome the limitations of thermal sintering, particularly the long sintering times. With this sintering method, we succeeded in improving the resistivity values down to 5 μΩ · cm, which is only 3.3 times higher than that of bulk silver. In this case, we reached the lower limit for resistivity specified in the conductive ink datasheet. RF performance of printed microstrip lines was also tested to study the potentiall impact of the sintering method at high frequencies. Our investigations into this area suggest that sintering type, thermal or electrical, does not affect the RF behaviour of the printed lines, since the obtained transmission loss parameter has a similar trend in both cases.

2. Another fabrication approach to achieve flexible systems, consisting of conductive textile transfer, has been employed to develop a UHF RFID tag compatible with textile manufacturing. We have simulated, designed, manufactured and tested a circularly polarized antenna attached to a flexible substrate as a first step to transfer to fabric. Attainable read ranges above 2 m have been achieved on the whole frequency range (800 MHz – 1 GHz) for all tag orientations thanks to a circulary polarized antenna. We have adquired new knowledge in the field of the transfer of conductive patterns onto fabric and in antenna design from the stay in the Technical University of Tampere. Nevertheless, further work can be done to achieve better matching between the chip and antenna impedances so as to extend reading distance beyond the obtained limits. In addition, considering the textile character of the tag, further

research could be undertaken to account for the influence of the human body on the electromagnetic properties of the antenna.

3. A screen-printed passive chipless system for relative humidity sensing based on a parallel LC resonator structure has been developed. Sensing strategy is based on the change in the resonance frequency of the LC circuit when exposed to different levels of humidity. A relative humidity range from 10% to about 90% has been tested. We have obtained satisfactory preliminary results showing a very regular trend, nearly linear, in the resonance frequency change with relative humidity. Further investigation needs to be carried out to complete this study, but we have found a substantial change of around 685 kHz in the resonance frequency between both relative humidity limits. Given the flexible character of the system, this design could be directly used as a humidity sensor for smart packaging applications if an analog reader capable of measuring the resonance frequency is employed. Next steps will be the enhancement of this frequency shift and the development of the wireless reader for this LC-based humidity measurement system.

4. An NFC-based smartphone-based sensor platform has been developed to act as dose reader system with potential application in the field of in-vivo dosimetry in radiotherapy treatments. We have succeeded in reducing the main uncertainty source, the thermal drift, by using a bipolar buffer. To do so, the commercial pMOSFET used as dosimeter and the bipolar transistors have been biased at appropriate drain and collector currents respectively, achieving a reduction of the thermal coefficient of 65 % in average. A custom-developed Android application has been designed to control the measurement process and the data storage. To test the NFC reader unit, a comparison with a previously developed dose reader of our research group (Carvajal et al., 2016) was carried out, obtaining average sensitivities of (4.75 ± 0.15) mV/Gy and (4.85 ± 0.08) mV/Gy, respectively. The results are in good agreement except for the uncertainty, which is higher for the NFC reader although still acceptable for dose measurements. In any case, a previous calibration would be required for accurate dose measurements.

5. Four passive printed sensor systems on flexible substrate have been developed, capable of detecting and monitoring parameters such as temperature, light or different gases concentrations. The four works have been published and constitute the thesis by compendium of publications. In the first one, a passive screen-printed UHF RFID tag with multiple optical sensor capabilities has been designed (Escobedo, Carvajal, et al., 2016). The tag provides a spectral fingerprint of the incident electromagnetic radiation, from ultraviolet to infrared. The tag has been validated as a proof of concept by means of two procedures. Firstly, using

several standard illuminants to detect different light conditions. Secondly, through reflective colour-sensing measurements. A potential application consisting of detecting the ripeness of a banana from immature to overripe has been proposed and validated. Therefore, the tag could be used in the field of smart packaging applications.

6. In the second paper of the compendium, a full passive tag for the detection of gas threshold concentration in sealed environments has been reported (Escobedo, de Vargas-Sansalvador, et al., 2016). In this case, the system harvests the necessary energy by means of two mini solar cells. The platform, which has been screen printed on flexible PEN substrate, has been evaluated for the measurement of oxygen and carbon dioxide. Two different tags based on chemical sensors with optical response to these gases have been developed. We have obtained a high experimental resolution of 6.4 and 93 ppm in the best case, and a low limit of detection of 170 and 720 ppm for oxygen and carbon dioxide, respectively. The obtained results prove that the tag has the potential to be used in modified atmosphere packaging applications.

7. In the third publication, a passive smartphone-based NFC system for multigas sensing has been presented (Escobedo et al., 2017). The tag, which has been screen-printed on flexible substrate, can detect and monitorize four different gases: oxygen and carbon dioxide, which are commonly used for evaluating the status of inner modified atmospheres; and humidity and ammonia, which are aimed to detect the spoilage of food. A custom Android application has been developed to power the system up and read the measurements from the tag. The tag response to the different gases concentrations has been calibrated. Resulting values of resolution, limits of detection and cross-sensitivity are compatible with smart packaging applications.

8. The last paper of the compendium lies in the field of smartphone-based optical sensor platforms, where a novel approach for oxygen determination in intelligent packaging has been proposed. In the presented system, an oxygen sensitive flexible membrane with luminescent response is attached to the inner surface of packed food. A smartphone is used for simultaneous excitation and reading of the membrane, thus avoiding the necessity of any additional electronics integrated in the envelope to complete the oxygen sensor. An easy-to-use Android app has been developed to take a photograph of the membrane at a fixed distance. The application processes the taken photograph in order to obtain the colorimetric information about the intensity of the luminescence and the absorbance of the membrane. These magnitudes were combined to define a new intensity parameter related to the oxygen concentration. This parameter showed improved sensitivity and immunity to thermal drift. In particular, the proposed

system has been applied to the monitoring of freshness in sealed pork meat, since it is known that oxygen concentration in a sealed package containing meat is related to the bacterial activity. The obtained results show that the developed system is able to provide accurate information about the oxygen concentration inside the package, information that is directly related to the bacterial activity and therefore to the state of meat.

6. Scientific Contributions

Journals papers

Escobedo, P.; Pérez de Vargas-Sansalvador, I.M.; López-Ruiz, N.; Erenas-Rodríguez, M.M.; Carvajal-Rodríguez, M.A.; Martínez-Olmos, A. *Non-invasive oxygen determination in intelligent packaging using a Smartphone*. IEEE Sensors Journal 2018, 18, 11. DOI: 10.1109/JSEN.2018.2824404. **Impact Factor (2016): 2.512. Rank 12/58 in Instruments & Instrumentation (Q1).**

Carvajal, M.A.; **Escobedo, P.**; Jiménez-Melguizo, M.; Martínez-García, M.S.; Martínez-Martí, F.; Martínez-Olmos, A.; Palma, A.J. *A compact dosimetric system for MOSFETs based on passive NFC tag and smartphone*. Sensors Actuators A Phys. 2017, 267, 82–89. DOI: 10.1016/j.sna.2017.10.015. **Impact Factor (2016): 2.499. Rank 13/58 in Instruments & Instrumentation (Q1)**.

Escobedo, P.; Erenas-Rodríguez, M.M.; López-Ruiz, N.; Carvajal-Rodríguez, M.A.; González-Chocano, S.; de Orbe-Payá, I.; Capitán-Vallvey, L.F; Palma-López, A.J.; Martínez-Olmos, A. *Flexible passive Near Field Communication Tag for Multigas Sensing*. Analytical Chemistry 2017, 89, 1697-1703. DOI: 10.1021/acs.analchem.6b03901. **Impact Factor (2016): 6.32. Rank 4/76 in Analytical Chemistry (Q1)**.

Escobedo, P.; Carvajal, M.; Capitán-Vallvey, L.F.; Fernández-Salmerón, J.; Martínez-Olmos, A.; Palma, A.J. *Passive UHF RFID tag for multispectral assessment*. Sensors 2016, 16, 7, 1085. DOI: 10.3390/s16071085. **Impact Factor: 2.677. Rank 10/58 in Instruments & Instrumentation (Q1)**.

Escobedo, P.; Pérez de Vargas-Sansalvador, I.M.; Carvajal, M.A.; Capitán-Vallvey, L.F.; Palma, A.J.; Martínez-Olmos, A. *Flexible passive tag based on light energy harvesting for gas threshold determination in sealed environments*. Sensors Actuators B Chem. 2016, 236, 226–232. DOI: 10.1016/j.snb.2016.05.158. **Impact Factor: 5.401. Rank 2/58 (TOP 3) in Instruments & Instrumentation (Q1)**.

Cornejo García, J.M.; **Escobedo, P.**; Rodríguez, D. *Status of the Project TRAPSENSOR*. Hyperfine Interactions 2014, 227, 223-237. DOI: 10.1007/s10751-014-1029-4. **Impact Factor (2007): 0.209. Rank 31/32 in Physics, Atomic, Molecular & Chemical (Q4)**.

Submitted Journal papers

Escobedo, P.; Pérez de Vargas-Sansalvador; López-Ruiz, N.; Capitán-Vallvey, L.F.; Palma, A.J.; Carvajal, M.A; Martínez-Olmos, A. *Thermoelectric energy harvesting for oxygen determination in refrigerated intelligent packaging*. Submitted to Sensors & Actuators: B. Chemical (IF: 5.401. Rank 2/58 (TOP 3) in Instruments & Instrumentation, Q1). May, 2018.

Escobedo, P.; Martínez-Olmos, A.; Fernández-Salmerón, J.; Rivadeneyra, A.; Capitán-Vallvey, L.F.; Palma, A.J.; Carvajal, M.A. *Compact readout system for chipless passive LC tags and its application for humidity monitoring.* Submitted to Sensors & Actuators A: Physical (IF: 2.499. Rank 13/58 in Instruments & Instrumentation, Q1). May, 2018.

Tabraue-Chávez, Mavys; Luque-González, María Angélica; Marín-Romero, Antonio; Sánchez-Martín, Rosario María; **Escobedo, Pablo**; Capitán-Vallvey, Luis Fermín; Palma, Alberto J.; Pernagallo, Salvatore; Díaz-Mochón, Juan José. *A colorimetric molecular assay based on dynamic chemistry for simple and accurate discrimination of Trypanosomatid species.* Submitted to Lab on a Chip (IF: 6.045. Rank 18/87 in Nanoscience & Nanotechnology, Q1). May, 2018.

International Conferences

Escobedo, P.; Palma, A.J.; Martinez-Olmos, A.; Lallena, M; Guirado, D.; Carvajal, M.A.; *Radiation effects on light-dependent resistances* (Poster). The 6th Internacional Conference on Radiation and Applications in Various fields of Research (RAD 2018). Ohrid, Macedonia (FYROM), 18-22 June 2018.

Carvajal, M.A.; Jiménez-Melguizo, M.; **Escobedo, P.;** Guirado, D.; Martinez-Olmos, A.; Palma, A.J.; *MOSFET probe for Intra Operative Radiotherapy.* The 6th Internacional Conference on Radiation and Applications in Various fields of Research (RAD 2018). Ohrid, Macedonia (FYROM), 18-22 June 2018.

Carvajal, M.A.; **Escobedo-Araque, P.**; Jiménez-Melguizo, M.; Martínez, S.; Martínez-Martí, F.; Martinez-Olmos, A.; Palma, A.J. *NFC tag for readout of MOSFET dosimeters*. The 5th Internacional Conference on Radiation and Applications in Various fields of Research (RAD 2017). Budva, Montenegro, 12-16 June 2017.

Palma, A.J.; M.; Martínez-García, S.; Torres-del-Río, J.; **Escobedo-Araque, P.**; Jakcsic, A.; González-de-Rivera, G.; Banqueri-Ozáez, J.; Carvajal, M.A. *Response of different electrical parameters of irradiated pMOSFET* (Poster). The 5th Internacional Conference on Radiation and Applications in Various fields of Research (RAD 2017). Budva, Montenegro, 12-16 June 2017.

López-Ruiz, N.; Erenas-Rodríguez, M.; **Escobedo-Araque, P.**; Capitán-Vallvey, L.F.; Palma-López, A.J.; Martínez Olmos, A. *Portable Instrumentation based on Raspberry Pi for optical detection of explosives* (Poster). EUROPT(R)ODE XIII - Conference on Optical Chemical Sensors and Biosensors. Graz University of Technology. Graz, Austria, 20-23 March 2016.

Escobedo-Araque, P.; Martínez-Olmos, A.; Carvajal, M.A.; Palma, A.J.; Fernandez-Salmeron, J. *Passive UHF RFID tag for spectral fingerprint measurement*. In Proceedings of the 2015 IEEE 15th Mediterranean Microwave Symposium (MMS), Lecce, Italy, 30 November - 2 December 2015; pp. 1-4. DOI: 10.1109/MMS.2015.7375454.

Bibliography

Let others boast of pages they have written,
I take pride in those I've read.[8]
"A Reader" by Jorge Luis Borges

Aga, R. S., Lombardi, J. P., Bartsch, C. M., & Heckman, E. M. (2014). Performance of a Printed Photodetector on a Paper Substrate. *IEEE Photonics Technology Letters*, *26*(3), 305–308. https://doi.org/10.1109/LPT.2013.2292830

Alastalo, A. T., Mattila, T., Allen, M. L., Aronniemi, M. J., Leppäniemi, J. H., Ojanperä, K. A., … Seppä, H. (2009). Rapid Electrical Sintering of Nanoparticle Stuctures. *Mater. Res. Soc. Symp. Proc.*, *1113*(Materials Research Society).

Albrecht, A., Rivadeneyra, A., Abdellah, A., Lugli, P., & Salmerón, J. F. (2016). Inkjet printing and photonic sintering of silver and copper oxide nanoparticles for ultra-low-cost conductive patterns. *Journal of Materials Chemistry C*, *4*(16), 3546–3554. https://doi.org/10.1039/C6TC00628K

Ali, S., Hassan, A., Bae, J., Lee, C. H., & Kim, J. (2016). All-Printed Differential Temperature Sensor for the Compensation of Bending Effects. *Langmuir*, *32*(44), 11432–11439. https://doi.org/10.1021/acs.langmuir.6b02885

Aliane, A., Fischer, V., Galliari, M., Tournon, L., Gwoziecki, R., Serbutoviez, C., … Coppard, R. (2014). Enhanced printed temperature sensors on flexible substrate. *Microelectronics Journal*, *45*(12), 1621–1626. https://doi.org/10.1016/j.mejo.2014.08.011

Allen, M., Alastalo, A., Suhonen, M., Mattila, T., Leppaniemi, J., & Seppa, H. (2011). Contactless Electrical Sintering of Silver Nanoparticles on Flexible Substrates. *IEEE Transactions on Microwave Theory and Techniques*, *59*(5), 1419–1429. https://doi.org/10.1109/TMTT.2011.2123910

Allen, M. L., Aronniemi, M., Mattila, T., Alastalo, A., Ojanperä, K., Suhonen, M., & Seppä, H. (2008). Electrical sintering of nanoparticle structures. *Nanotechnology*, *19*(17), 175201. https://doi.org/10.1088/0957-4484/19/17/175201

Amendola, S., Bovesecchi, G., Palombi, A., Coppa, P., & Marrocco, G. (2016). Design,

---

[8] Translated from the Spanish by Normal Thomas di Giovanni. Original quote: *Que otros se jacten de las páginas que han escrito, a mí me enorgullecen las que he leído* («Un Lector», Jorge Luis Borges).

Calibration and Experimentation of an Epidermal RFID Sensor for Remote Temperature Monitoring. *IEEE Sensors Journal*, *16*(19), 7250–7257. https://doi.org/10.1109/JSEN.2016.2594582

Amin, E. M., Karmakar, N. C., & Jensen, B. W. (2016). Fully printable chipless RFID multi-parameter sensor. *Sensors and Actuators A: Physical*, *248*, 223–232. https://doi.org/10.1016/j.sna.2016.06.014

AMS. (2014). *SL13A: Smart Sensory Tag Chip For Unique Identification, Monitoring and Data Logging*. Retrieved from http://ams.com/eng/Products/Wireless-Connectivity/Sensor-Tags-Interfaces/SL13A

An, B. W., Shin, J. H., Kim, S.-Y., Kim, J., Ji, S., Park, J., … Park, J.-U. (2017). Smart Sensor Systems for Wearable Electronic Devices. *Polymers*, *9*(12), 303. https://doi.org/10.3390/polym9080303

Andò, B., Baglio, S., Di Pasquale, G., Pollicino, A., D'Agata, S., Gugliuzzo, C., … Re. (2015). An Inkjet Printed CO2 Gas Sensor. *Procedia Engineering*, *120*, 628–631. https://doi.org/10.1016/j.proeng.2015.08.755

Anum Satti, J., Habib, A., Anam, H., Zeb, S., Amin, Y., Loo, J., & Tenhunen, H. (2018). Miniaturized humidity and temperature sensing RFID enabled tags. *International Journal of RF and Microwave Computer-Aided Engineering*, *28*(1), e21151. https://doi.org/10.1002/mmce.21151

Araki, H., Kim, J., Zhang, S., Banks, A., Crawford, K. E., Sheng, X., … Rogers, J. A. (2017). Materials and Device Designs for an Epidermal UV Colorimetric Dosimeter with Near Field Communication Capabilities. *Advanced Functional Materials*, *27*(2), 1604465. https://doi.org/10.1002/adfm.201604465

Atamana, C., Kinkeldei, T., Vasquez-Quintero, a., Molina-Lopez, F., Courbat, J., Cherenack, K., … De Rooij, N. F. (2011). Humidity and temperature sensors on plastic foil for textile integration. *Procedia Engineering*, *25*, 136–139. https://doi.org/10.1016/j.proeng.2011.12.034

Azzarelli, J. M., Mirica, K. A., Ravnsbæk, J. B., & Swager, T. M. (2014). Wireless gas detection with a smartphone via rf communication. *Proceedings of the National Academy of Sciences*, *111*(51), 18162–18166. https://doi.org/10.1073/pnas.1415403111

Azzellino, G., Grimoldi, A., Binda, M., Caironi, M., Natali, D., & Sampietro, M. (2013). Fully Inkjet-Printed Organic Photodetectors with High Quantum Yield. *Advanced Materials*, *25*(47), 6829–6833. https://doi.org/10.1002/adma.201303473

Babar, A. A., Elsherbeni, A. Z., Sydanheimo, L., & Ukkonen, L. (2013). RFID Tags for Challenging Environments: Flexible High-Dielectric Materials and Ink-Jet Printing Technology for Compact Platform Tolerant RFID Tags. *IEEE Microwave*

Magazine, *14*(5), 26–35. https://doi.org/10.1109/MMM.2013.2259391

Babu, A., & George, B. (2016). A Linear and High Sensitive Interfacing Scheme for Wireless Passive LC Sensors. *IEEE Sensors Journal*, *16*(23), 1–1. https://doi.org/10.1109/JSEN.2016.2614816

Bandodkar, A. J., & Wang, J. (2014). Non-invasive wearable electrochemical sensors: a review. *Trends in Biotechnology*, *32*(7), 363–371. https://doi.org/10.1016/j.tibtech.2014.04.005

Barbosa, A. I., Gehlot, P., Sidapra, K., Edwards, A. D., & Reis, N. M. (2015). Portable smartphone quantitation of prostate specific antigen (PSA) in a fluoropolymer microfluidic device. *Biosensors and Bioelectronics*, *70*, 5–14. https://doi.org/10.1016/j.bios.2015.03.006

Beni, V., Nilsson, D., Arven, P., Norberg, P., Gustafsson, G., & Turner, A. P. F. (2015). Printed Electrochemical Instruments for Biosensors. *ECS Journal of Solid State Science and Technology*, *4*(10), S3001–S3005. https://doi.org/10.1149/2.0011510jss

Best, S., Ralston, A., & Suchowerska, N. (2005). Clinical application of the OneDose™ Patient Dosimetry System for total body irradiation. *Physics in Medicine and Biology*, *50*(24), 5909–5919. https://doi.org/10.1088/0031-9155/50/24/010

Bhadra, S., Narvaez, C., Thomson, D. J., & Bridges, G. E. (2015). Non-destructive detection of fish spoilage using a wireless basic volatile sensor. *Talanta*, *134*, 718–723. https://doi.org/10.1016/j.talanta.2014.12.017

Bibi, F., Guillaume, C., Gontard, N., & Sorli, B. (2017). A review: RFID technology having sensing aptitudes for food industry and their contribution to tracking and monitoring of food products. *Trends in Food Science & Technology*, *62*, 91–103. https://doi.org/10.1016/j.tifs.2017.01.013

Biji, K. B., Ravishankar, C. N., Mohan, C. O., & Srinivasa Gopal, T. K. (2015). Smart packaging systems for food applications: a review. *Journal of Food Science and Technology*, *52*(10), 6125–6135. https://doi.org/10.1007/s13197-015-1766-7

Björninen, T., Saghlatoon, H., Sydänheimo, L., Rahmat-samii, Y., & Ukkonen, L. (2014). Antennas for Small Metal Mountable Passive UHF RFID Tags: Challenges and Advances. *Forum for Electromagnetic Research Methods and Application Technologies (FERMAT)*, (1), 1–9. Retrieved from http://www.e-fermat.org/files/articles/1537fc0291abc0.pdf

Björninen, T., Ukkonen, L., Sydänheimo, L., & Elsherbeni, A. Z. (2010). Circularly Polarized Tag Antenna for UHF RFID. In *26th Annual Review of Progress in Applied Computational Electromagnetics* (pp. 371–375). Tampere. Retrieved from https://engineering.olemiss.edu/~atef/pdfs/proceedings/2010/Circularly_Polarized_Tag_Antenna.pdf

Boudaden, J., Steinmaßl, M., Endres, H., Drost, A., Eisele, I., Kutter, C., & Müller-Buschbaum, P. (2018). Polyimide-Based Capacitive Humidity Sensor. *Sensors*, *18*(5), 1516. https://doi.org/10.3390/s18051516

Briand, D., Oprea, A., Courbat, J., & Bârsan, N. (2011). Making environmental sensors on plastic foil. *Materials Today*, *14*(9), 416–423. https://doi.org/10.1016/S1369-7021(11)70186-9

Capitán-Vallvey, L. F., López-Ruiz, N., Martínez-Olmos, A., Erenas, M. M., & Palma, A. J. (2015). Recent developments in computer vision-based analytical chemistry: A tutorial review. *Analytica Chimica Acta*, *899*, 23–56. https://doi.org/10.1016/j.aca.2015.10.009

Carvajal, M. A., Escobedo, P., Jiménez-Melguizo, M., Martínez-García, M. S., Martínez-Martí, F., Martínez-Olmos, A., & Palma, A. J. (2017). A compact dosimetric system for MOSFETs based on passive NFC tag and smartphone. *Sensors and Actuators A: Physical*, *267*, 82–89. https://doi.org/10.1016/j.sna.2017.10.015

Carvajal, M. A., Martínez-García, M. S., Guirado, D., Martínez-Olmos, A., & Palma, A. J. (2016). Thermal compensation technique using the parasitic diode for DMOS transistors. *Sensors and Actuators A: Physical*, *249*, 249–255. https://doi.org/10.1016/j.sna.2016.09.004

Carvajal, M. A., Martínez-García, M. S., Martínez-Olmos, A., Banqueri, J., & Palma, A. J. (2014). A simplified thermal model for lateral MOSFET and its application to temperature monitoring. *Semiconductor Science and Technology*, *29*(9), 095017. https://doi.org/10.1088/0268-1242/29/9/095017

Carvajal, M. A., Martínez-Olmos, A., Morales, D. P., Lopez-Villanueva, J. A., Lallena, A. M., & Palma, A. J. (2011). Thermal drift reduction with multiple bias current for MOSFET dosimeters. *Physics in Medicine and Biology*, *56*(12), 3535–3550. https://doi.org/10.1088/0031-9155/56/12/006

Carvajal, M. A., Simancas, F., Guirado, D., Vilches, M., Lallena, A. M., & Palma, A. J. (2012). A compact and low cost dosimetry system based on MOSFET for in vivo radiotherapy. *Sensors and Actuators A: Physical*, *182*, 146–152. https://doi.org/10.1016/j.sna.2012.05.024

Castano, L. M., & Flatau, A. B. (2014). Smart fabric sensors and e-textile technologies: a review. *Smart Materials and Structures*, *23*(5), 053001. https://doi.org/10.1088/0964-1726/23/5/053001

Catarinucci, L., Colella, R., & Tarricone, L. (2009). A Cost-Effective UHF RFID Tag for Transmission of Generic Sensor Data in Wireless Sensor Networks. *IEEE Transactions on Microwave Theory and Techniques*, *57*(5), 1291–1296.

https://doi.org/10.1109/TMTT.2009.2017296

Cavallo, J. A., Strumia, M. C., & Gomez, C. G. (2014). Preparation of a milk spoilage indicator adsorbed to a modified polypropylene film as an attempt to build a smart packaging. *Journal of Food Engineering*, *136*, 48–55. https://doi.org/10.1016/j.jfoodeng.2014.03.021

Chen, A., Wang, R., Bever, C. R. S., Xing, S., Hammock, B. D., & Pan, T. (2014). Smartphone-interfaced lab-on-a-chip devices for field-deployable enzyme-linked immunosorbent assay. *Biomicrofluidics*, *8*(6), 064101. https://doi.org/10.1063/1.4901348

Chen, L., Zhang, C., & Xing, D. (2016). Paper-based bipolar electrode-electrochemiluminescence (BPE-ECL) device with battery energy supply and smartphone read-out: A handheld ECL system for biochemical analysis at the point-of-care level. *Sensors and Actuators B: Chemical*, *237*, 308–317. https://doi.org/10.1016/j.snb.2016.06.105

Chen, S.-P., Chiu, H.-L., Wang, P.-H., & Liao, Y.-C. (2015). Inkjet Printed Conductive Tracks for Printed Electronics. *ECS Journal of Solid State Science and Technology*, *4*(4), P3026–P3033. https://doi.org/10.1149/2.0061504jss

Chen, X., Ma, S., Ukkonen, L., Bjorninen, T., & Virkki, J. (2017). Antennas and antenna-electronics interfaces made of conductive yarn and paint for cost-effective wearable RFIDs and sensors. In *2017 IEEE MTT-S International Microwave Symposium (IMS)* (pp. 827–830). IEEE. https://doi.org/10.1109/MWSYM.2017.8058707

Chen, X., Ukkonen, L., & Bjorninen, T. (2016). Passive E-Textile UHF RFID-Based Wireless Strain Sensors With Integrated References. *IEEE Sensors Journal*, *16*(22), 7835–7836. https://doi.org/10.1109/JSEN.2016.2608659

Chen, Y., Fu, G., Zilberman, Y., Ruan, W., Ameri, S. K., Zhang, Y. S., … Sonkusale, S. R. (2017). Low cost smart phone diagnostics for food using paper-based colorimetric sensor arrays. *Food Control*, *82*, 227–232. https://doi.org/10.1016/j.foodcont.2017.07.003

Chiolerio, A., Rajan, K., Roppolo, I., Chiappone, A., Bocchini, S., & Perrone, D. (2016). Silver nanoparticle ink technology: state of the art. *Nanotechnology, Science and Applications*, *9*, 1. https://doi.org/10.2147/NSA.S68080

Choi, K.-H., Yoo, J., Lee, C. K., & Lee, S.-Y. (2016). All-inkjet-printed, solid-state flexible supercapacitors on paper. *Energy & Environmental Science*, *9*(9), 2812–2821. https://doi.org/10.1039/C6EE00966B

Chou, N., Kim, Y., & Kim, S. (2016). A Method to Pattern Silver Nanowires Directly on Wafer-Scale PDMS Substrate and Its Applications. *ACS Applied Materials &*

Interfaces, *8*(9), 6269–6276. https://doi.org/10.1021/acsami.5b11307

Chouler, J., Cruz-Izquierdo, Á., Rengaraj, S., Scott, J. L., & Di Lorenzo, M. (2018). A screen-printed paper microbial fuel cell biosensor for detection of toxic compounds in water. *Biosensors and Bioelectronics*, *102*(November 2017), 49–56. https://doi.org/10.1016/j.bios.2017.11.018

Coskun, V., Ozdenizci, B., & Ok, K. (2013). A Survey on Near Field Communication (NFC) Technology. *Wireless Personal Communications*, *71*(3), 2259–2294. https://doi.org/10.1007/s11277-012-0935-5

Császár, C., Harsányi, G., & Agarwal, R. P. (1994). A very low-cost pressure sensor with extremely high sensitivity. *Sensors and Actuators A: Physical*, *42*(1–3), 417–420. https://doi.org/10.1016/0924-4247(94)80024-3

Danesh, E., Molina-Lopez, F., Camara, M., Bontempi, A., Quintero, A. V., Teyssieux, D., … Persaud, K. C. (2014). Development of a new generation of ammonia sensors on printed polymeric hotplates. *Analytical Chemistry*, *86*(18), 8951–8958. https://doi.org/10.1021/ac501908c

Dankoco, M. D., Tesfay, G. Y., Benevent, E., & Bendahan, M. (2016). Temperature sensor realized by inkjet printing process on flexible substrate. *Materials Science and Engineering: B*, *205*, 1–5. https://doi.org/10.1016/j.mseb.2015.11.003

del Rosario, M., Redmond, S., & Lovell, N. (2015). Tracking the Evolution of Smartphone Sensing for Monitoring Human Movement. *Sensors*, *15*(8), 18901–18933. https://doi.org/10.3390/s150818901

Deng, W., Dou, Y., Song, P., Xu, H., Aldalbahi, A., Chen, N., … Zuo, X. (2016). Lab on smartphone with interfaced electrochemical chips for on-site gender verification. *Journal of Electroanalytical Chemistry*, *777*, 117–122. https://doi.org/10.1016/j.jelechem.2016.08.007

Dobkin, D. M. (2012). *The RF in RFID: UHF RFID in practice* (Second). Newnes.

Doeven, E. H., Barbante, G. J., Harsant, A. J., Donnelly, P. S., Connell, T. U., Hogan, C. F., & Francis, P. S. (2015). Mobile phone-based electrochemiluminescence sensing exploiting the 'USB On-The-Go' protocol. *Sensors and Actuators B: Chemical*, *216*, 608–613. https://doi.org/10.1016/j.snb.2015.04.087

Domínguez-Aragón, A., Olmedo-Martínez, J. A., & Zaragoza-Contreras, E. A. (2018). Colorimetric sensor based on a poly(ortho -phenylenediamine- co -aniline) copolymer for the monitoring of tilapia (Orechromis niloticus) freshness. *Sensors and Actuators B: Chemical*, *259*, 170–176. https://doi.org/10.1016/j.snb.2017.12.020

Dong, Y., Zou, Y., Song, J., Li, J., Han, B., Shan, Q., … Zeng, H. (2017). An all-inkjet-printed flexible UV photodetector. *Nanoscale*, *9*(25), 8580–8585. https://doi.org/

10.1039/C7NR00250E

eMarketer, & Statista Inc. (2016). *Number of Smartphone Users Worldwide from 2014 to 2020*. Retrieved from https://www.statista.com/statistics/330695/number-of-smartphone-users-worldwide/

EPCglobal Inc. (2013). EPC ™ Radio-Frequency Identity Protocols Generation-2 UHF RFID. Specification for RFID Air Interface.

Escobedo Araque, P., Perez de Vargas Sansalvador, I. M., Lopez Ruiz, N., Erenas Rodriguez, M. M., Carvajal Rodriguez, M. A., & Martinez Olmos, A. (2018). Non-Invasive Oxygen Determination in Intelligent Packaging Using a Smartphone. *IEEE Sensors Journal*, *18*(11), 4351–4357. https://doi.org/10.1109/JSEN.2018.2824404

Escobedo, P., Carvajal, M. A., Capitán-Vallvey, L., Fernández-Salmerón, J., Martínez-Olmos, A., & Palma, A. (2016). Passive UHF RFID Tag for Multispectral Assessment. *Sensors*, *16*(7), 1085. https://doi.org/10.3390/s16071085

Escobedo, P., de Vargas-Sansalvador, I. M. P., Carvajal, M., Capitán-Vallvey, L. F., Palma, A. J., & Martínez-Olmos, A. (2016). Flexible passive tag based on light energy harvesting for gas threshold determination in sealed environments. *Sensors and Actuators B: Chemical*, *236*, 226–232. https://doi.org/10.1016/j.snb.2016.05.158

Escobedo, P., Erenas, M. M., López-Ruiz, N., Carvajal, M. A., Gonzalez-Chocano, S., de Orbe-Payá, I., … Martínez-Olmos, A. (2017). Flexible Passive near Field Communication Tag for Multigas Sensing. *Analytical Chemistry*, *89*(3), 1697–1703. https://doi.org/10.1021/acs.analchem.6b03901

Evans, R. C., Douglas, P., Williams, J. A. G., & Rochester, D. L. (2006). A novel luminescence-based colorimetric oxygen sensor with a "traffic light" response. *Journal of Fluorescence*, *16*(2), 201–206. https://doi.org/10.1016/j.entcs.2005.10.013

F. Baldini J. Homola, S. Martellucci, A. N. C. (2006). *Optical Chemical Sensors*. (F. Baldini, A. N. Chester, J. Homola, & S. Martellucci, Eds.), *NATO Science Series II: Mathematics, Physics and Chemistry* (Vol. 224). Dordrecht: Kluwer Academic Publishers. https://doi.org/10.1007/1-4020-4611-1

Falat, T., Platek, B., & Felba, J. (2012). Sintering process of silver nanoparticles in ink-jet printed conductive microstructures-Molecular dynamics approach. In *13th International Conference on Thermal, Mechanical and Multi-Physics Simulation and Experiments in Microelectronics and Microsystems, EuroSimE 2012* (pp. 1–5). Retrieved from http://ieeexplore.ieee.org/xpls/abs_all.jsp?arnumber=6191782

Feng, Y., Xie, L., Chen, Q., & Zheng, L.-R. (2015). Low-Cost Printed Chipless RFID Humidity Sensor Tag for Intelligent Packaging. *IEEE Sensors Journal*, *15*(6),

3201–3208. https://doi.org/10.1109/JSEN.2014.2385154

Ferdous, R. M., Reza, A. W., & Siddiqui, M. F. (2016). Renewable energy harvesting for wireless sensors using passive RFID tag technology: A review. *Renewable and Sustainable Energy Reviews*, *58*, 1114–1128. https://doi.org/10.1016/j.rser.2015.12.332

Fernández-Salmerón, J., Rivadeneyra, A., Martínez-Martí, F., Capitán-Vallvey, L., Palma, A., & Carvajal, M. (2015). Passive UHF RFID Tag with Multiple Sensing Capabilities. *Sensors*, *15*(10), 26769–26782. https://doi.org/10.3390/s151026769

Fernandez-Salmeron, J., Rivadeneyra, A., Rodriguez, M. A. C., Capitan-Vallvey, L. F., & Palma, A. J. (2015). HF RFID Tag as Humidity Sensor: Two Different Approaches. *IEEE Sensors Journal*, *15*(10), 5726–5733. https://doi.org/10.1109/JSEN.2015.2447031

Fiddes, L. K., Chang, J., & Yan, N. (2014). Electrochemical detection of biogenic amines during food spoilage using an integrated sensing RFID tag. *Sensors and Actuators B: Chemical*, *202*, 1298–1304. https://doi.org/10.1016/j.snb.2014.05.106

Finkenzeller, K. (2010). *RFID Handbook: : Fundamentals and Applications in Contactless Smart Cards, Radio Frequency Identification and near-Field Communication* (Third Edit). Chichester, UK: John Wiley & Sons, Ltd. https://doi.org/10.1002/9780470665121

Fu, Q., Wu, Z., Xu, F., Li, X., Yao, C., Xu, M., … Tang, Y. (2016). A portable smart phone-based plasmonic nanosensor readout platform that measures transmitted light intensities of nanosubstrates using an ambient light sensor. *Lab on a Chip*, *16*(10), 1927–1933. https://doi.org/10.1039/C6LC00083E

Fuertes, G., Soto, I., Carrasco, R., Vargas, M., Sabattin, J., & Lagos, C. (2016). Intelligent Packaging Systems: Sensors and Nanosensors to Monitor Food Quality and Safety. *Journal of Sensors*, *2016*, 1–8. https://doi.org/10.1155/2016/4046061

G. Corradini, M., Lavinia Wang, Y., Le, A., M. Waxman, S., Zelent, B., Chib, R., … D. Ludescher, R. (2016). Identifying and selecting edible luminescent probes as sensors of food quality. *AIMS Biophysics*, *3*(2), 319–339. https://doi.org/10.3934/biophy.2016.2.319

Gao, J., Siden, J., Nilsson, H.-E., & Gulliksson, M. (2013). Printed Humidity Sensor With Memory Functionality for Passive RFID Tags. *IEEE Sensors Journal*, *13*(5), 1824–1834. https://doi.org/10.1109/JSEN.2013.2244034

Gao, M., Li, L., & Song, Y. (2017). Inkjet printing wearable electronic devices. *J. Mater. Chem. C*, *5*(12), 2971–2993. https://doi.org/10.1039/C7TC00038C

García, A., Erenas, M. M., Marinetto, E. D., Abad, C. A., de Orbe-Paya, I., Palma, A.

J., & Capitán-Vallvey, L. F. (2011). Mobile phone platform as portable chemical analyzer. *Sensors and Actuators B: Chemical*, *156*(1), 350–359. https://doi.org/10.1016/j.snb.2011.04.045

Gaspar, C., Olkkonen, J., Passoja, S., & Smolander, M. (2017). Paper as Active Layer in Inkjet-Printed Capacitive Humidity Sensors. *Sensors*, *17*(7), 1464. https://doi.org/10.3390/s17071464

Gebhart, M., Neubauer, R., Stark, M., & Warnez, D. (2011). Design of 13.56 MHz Smartcard Stickers with Ferrite for Payment and Authentication. In *2011 Third International Workshop on Near Field Communication* (pp. 59–64). IEEE. https://doi.org/10.1109/NFC.2011.14

Giffney, T., Bejanin, E., Kurian, A. S., Travas-Sejdic, J., & Aw, K. (2017). Highly stretchable printed strain sensors using multi-walled carbon nanotube/silicone rubber composites. *Sensors and Actuators A: Physical*, *259*, 44–49. https://doi.org/10.1016/j.sna.2017.03.005

Goicoechea, J., Zamarreño, C. R., Matias, I. R., & Arregui, F. J. (2007). Minimizing the photobleaching of self-assembled multilayers for sensor applications. *Sensors and Actuators, B: Chemical*, *126*(1), 41–47. https://doi.org/10.1016/j.snb.2006.10.037

Grouchko, M., Kamyshny, A., Mihailescu, C. F., Anghel, D. F., & Magdassi, S. (2011). Conductive inks with a "built-in" mechanism that enables sintering at room temperature. *ACS Nano*, *5*(4), 3354–3359. https://doi.org/10.1021/nn2005848

Güder, F., Ainla, A., Redston, J., Mosadegh, B., Glavan, A., Martin, T. J., & Whitesides, G. M. (2016). Paper-Based Electrical Respiration Sensor. *Angewandte Chemie International Edition*, *55*(19), 5727–5732. https://doi.org/10.1002/anie.201511805

Guo, X., Hang, Y., Xie, Z., Wu, C., Gao, L., & Liu, C. (2017). Flexible and wearable 2.45 GHz CPW-fed antenna using inkjet-printing of silver nanoparticles on pet substrate. *Microwave and Optical Technology Letters*, *59*(1), 204–208. https://doi.org/10.1002/mop.30261

Halonen, E., Viiru, T., Ostman, K., Cabezas, A. L., & Mantysalo, M. (2013). Oven Sintering Process Optimization for Inkjet-Printed Ag Nanoparticle Ink. *IEEE Transactions on Components, Packaging and Manufacturing Technology*, *3*(2), 350–356. https://doi.org/10.1109/TCPMT.2012.2226458

Harada, S., Honda, W., Arie, T., Akita, S., & Takei, K. (2014). Fully Printed, Highly Sensitive Multifunctional Artificial Electronic Whisker Arrays Integrated with Strain and Temperature Sensors. *ACS Nano*, *8*(4), 3921–3927. https://doi.org/10.1021/nn500845a

He, H., Chen, Z., Wang, F., & Zhu, W. (2016). Investigation on Graphene / Ag Nano-

Particles composite ink for flexible electronics. *2016 17th International Conference on Electronic Packaging Technology, ICEPT 2016*, 1337–1340. https://doi.org/10.1109/ICEPT.2016.7583371

Hibbard, T., Crowley, K., Kelly, F., Ward, F., Holian, J., Watson, A., & Killard, A. J. (2013). Point of care monitoring of hemodialysis patients with a breath ammonia measurement device based on printed polyaniline nanoparticle sensors. *Analytical Chemistry*, *85*(24), 12158–12165. https://doi.org/10.1021/ac403472d

Huang, X. W., Zou, X. B., Shi, J. Y., Guo, Y., Zhao, J. W., Zhang, J., & Hao, L. (2014). Determination of pork spoilage by colorimetric gas sensor array based on natural pigments. *Food Chemistry*, *145*, 549–554. https://doi.org/10.1016/j.foodchem.2013.08.101

Hulanicki, A., Glab, S., & Ingman, F. (1991). Chemical sensors: definitions and classification. *Pure and Applied Chemistry*, *63*(9), 1247–1250. https://doi.org/10.1351/pac199163091247

Hummelgård, M., Zhang, R., Nilsson, H.-E., & Olin, H. (2011). Electrical Sintering of Silver Nanoparticle Ink Studied by In-Situ TEM Probing. *PLoS ONE*, *6*(2), e17209. https://doi.org/10.1371/journal.pone.0017209

Im, H., Castro, C. M., Shao, H., Liong, M., Song, J., Pathania, D., … Lee, H. (2015). Digital diffraction analysis enables low-cost molecular diagnostics on a smartphone. *Proceedings of the National Academy of Sciences*, *112*(18), 5613–5618. https://doi.org/10.1073/pnas.1501815112

Janata, J. (2009). *Principles of Chemical Sensors*. *Journal of the Franklin Institute* (Vol. 252). Boston, MA: Springer US. https://doi.org/10.1007/b136378

Jang, S., Lee, D. J., Lee, D., & Oh, J. H. (2013). Electrical sintering characteristics of inkjet-printed conductive Ag lines on a paper substrate. *Thin Solid Films*, *546*, 157–161. https://doi.org/10.1016/j.tsf.2013.05.015

Javed, N., Habib, A., Amin, Y., Loo, J., Akram, A., & Tenhunen, H. (2016). Directly printable moisture sensor tag for intelligent packaging. *IEEE Sensors Journal*, *16*(16), 6147–6148. https://doi.org/10.1109/JSEN.2016.2582847

Ji, D., Liu, L., Li, S., Chen, C., Lu, Y., Wu, J., & Liu, Q. (2017). Smartphone-based cyclic voltammetry system with graphene modified screen printed electrodes for glucose detection. *Biosensors and Bioelectronics*, *98*(July), 449–456. https://doi.org/10.1016/j.bios.2017.07.027

Joo, Y., Yoon, J., Ha, J., Kim, T., Lee, S., Lee, B., … Hong, Y. (2017). Highly Sensitive and Bendable Capacitive Pressure Sensor and Its Application to 1 V Operation Pressure-Sensitive Transistor. *Advanced Electronic Materials*, *3*(4), 1600455.

https://doi.org/10.1002/aelm.201600455

Jović, M., Hidalgo-Acosta, J. C., Lesch, A., Costa Bassetto, V., Smirnov, E., Cortés-Salazar, F., & Girault, H. H. (2017). Large-scale layer-by-layer inkjet printing of flexible iridium-oxide based pH sensors. *Journal of Electroanalytical Chemistry*, (November), 0–1. https://doi.org/10.1016/j.jelechem.2017.11.032

Jun, J., Oh, J., Shin, D. H., Kim, S. G., Lee, J. S., Kim, W., & Jang, J. (2016). Wireless, Room Temperature Volatile Organic Compound Sensor Based on Polypyrrole Nanoparticle Immobilized Ultrahigh Frequency Radio Frequency Identification Tag. *ACS Applied Materials & Interfaces*, *8*(48), 33139–33147. https://doi.org/10.1021/acsami.6b08344

Jung, M., Kim, J., Noh, J., Lim, N., Lim, C., Lee, G., … Cho, G. (2010). All-Printed and Roll-to-Roll-Printable 13.56-MHz-Operated 1-bit RF Tag on Plastic Foils. *IEEE Transactions on Electron Devices*, *57*(3), 571–580. https://doi.org/10.1109/TED.2009.2039541

Kamyshny, A. (2011). Metal-based Inkjet Inks for Printed Electronics. *The Open Applied Physics Journal*, *4*(1), 19–36. https://doi.org/10.2174/1874183501104010019

Kamyshny, A., & Magdassi, S. (2014). Conductive Nanomaterials for Printed Electronics. *Small*, *10*(17), 3515–3535. https://doi.org/10.1002/smll.201303000

Kanchi, S., Sabela, M. I., Mdluli, P. S., Inamuddin, & Bisetty, K. (2018). Smartphone based bioanalytical and diagnosis applications: A review. *Biosensors and Bioelectronics*, *102*, 136–149. https://doi.org/10.1016/j.bios.2017.11.021

Kassal, P., Kim, J., Kumar, R., de Araujo, W. R., Steinberg, I. M., Steinberg, M. D., & Wang, J. (2015). Smart bandage with wireless connectivity for uric acid biosensing as an indicator of wound status. *Electrochemistry Communications*, *56*, 6–10. https://doi.org/10.1016/j.elecom.2015.03.018

Kassal, P., Steinberg, M. D., & Steinberg, I. M. (2018). Wireless chemical sensors and biosensors: A review. *Sensors and Actuators B: Chemical*, *266*, 228–245. https://doi.org/10.1016/j.snb.2018.03.074

Kassal, P., Zubak, M., Scheipl, G., Mohr, G. J., Steinberg, M. D., & Murković Steinberg, I. (2017). Smart bandage with wireless connectivity for optical monitoring of pH. *Sensors and Actuators B: Chemical*, *246*, 455–460. https://doi.org/10.1016/j.snb.2017.02.095

Kell, A. J., Paquet, C., Mozenson, O., Djavani-Tabrizi, I., Deore, B., Liu, X., … Malenfant, P. R. L. (2017). Versatile Molecular Silver Ink Platform for Printed Flexible Electronics. *ACS Applied Materials & Interfaces*, acsami.7b02573. https://doi.org/10.1021/acsami.7b02573

Keysight Technologies. (2014). Network Analyzer Basics. Retrieved from http://literature.cdn.keysight.com/litweb/pdf/5965-7917E.pdf

Khan, S., Lorenzelli, L., Dahiya, R. S., & Member, S. (2015). Technologies for Printing Sensors and Electronics Over Large Flexible Substrates : A Review, *15*(6), 3164.

Khan, Y., Ostfeld, A. E., Lochner, C. M., Pierre, A., & Arias, A. C. (2016). Monitoring of Vital Signs with Flexible and Wearable Medical Devices. *Advanced Materials*, *28*(22), 4373–4395. https://doi.org/10.1002/adma.201504366

Khan, Y., Pavinatto, F. J., Lin, M. C., Liao, A., Swisher, S. L., Mann, K., … Arias, A. C. (2016). Inkjet-Printed Flexible Gold Electrode Arrays for Bioelectronic Interfaces. *Advanced Functional Materials*, *26*(7), 1004–1013. https://doi.org/10.1002/adfm.201503316

Kim, J., Imani, S., de Araujo, W. R., Warchall, J., Valdés-Ramírez, G., Paixão, T. R. L. C., … Wang, J. (2015). Wearable salivary uric acid mouthguard biosensor with integrated wireless electronics. *Biosensors and Bioelectronics*, *74*, 1061–1068. https://doi.org/10.1016/j.bios.2015.07.039

Kim, J., Salvatore, G. A., Araki, H., Chiarelli, A. M., Xie, Z., Banks, A., … Rogers, J. A. (2016). Battery-free, stretchable optoelectronic systems for wireless optical characterization of the skin. *Science Advances*, *2*(8), e1600418–e1600418. https://doi.org/10.1126/sciadv.1600418

Kim, J., Wang, Z., & Kim, W. S. (2014). Stretchable RFID for Wireless Strain Sensing With Silver Nano Ink. *IEEE Sensors Journal*, *14*(12), 4395–4401. https://doi.org/10.1109/JSEN.2014.2335743

Kim, K.-S., Bang, J.-O., Choa, Y.-H., & Jung, S.-B. (2013). The characteristics of Cu nanopaste sintered by atmospheric-pressure plasma. *Microelectronic Engineering*, *107*, 121–124. https://doi.org/10.1016/j.mee.2012.08.019

Kim, S. C., Jalal, U. M., Im, S. B., Ko, S., & Shim, J. S. (2017). A smartphone-based optical platform for colorimetric analysis of microfluidic device. *Sensors and Actuators B: Chemical*, *239*, 52–59. https://doi.org/10.1016/j.snb.2016.07.159

Kisic, M., Blaz, N., Zlebic, C., Zivanov, L., & Nikolic, I. (2017). Fully ink-jet printed capacitive pressure sensor. In *2017 40th International Spring Seminar on Electronics Technology (ISSE)* (pp. 1–4). IEEE. https://doi.org/10.1109/ISSE.2017.8000994

Ko, S. H., Pan, H., Grigoropoulos, C. P., Luscombe, C. K., Fréchet, J. M. J., & Poulikakos, D. (2007). All-inkjet-printed flexible electronics fabrication on a polymer substrate by low-temperature high-resolution selective laser sintering of metal nanoparticles. *Nanotechnology*, *18*(34), 345202. https://doi.org/10.1088/0957-4484/18/34/345202

Koh, A., Kang, D., Xue, Y., Lee, S., Pielak, R. M., Kim, J., … Rogers, J. A. (2016). A soft, wearable microfluidic device for the capture, storage, and colorimetric sensing of sweat. *Science Translational Medicine 8*(366). https://doi.org/10.1126/scitranslmed.aaf2593

Kollegger, C., Greiner, P., Siegl, I., Steffan, C., Wiessflecker, M., Pekec, B., … Deutschmann, B. (2018). Intelligent NFC potassium measurement strip with hemolysis check in capillary blood. *E & i Elektrotechnik Und Informationstechnik*, *135*(1), 83–88. https://doi.org/10.1007/s00502-017-0572-5

Koski, K., Sydanheimo, L., Rahmat-Samii, Y., & Ukkonen, L. (2014). Fundamental Characteristics of Electro-Textiles in Wearable UHF RFID Patch Antennas for Body-Centric Sensing Systems. *IEEE Transactions on Antennas and Propagation*, *62*(12), 6454–6462. https://doi.org/10.1109/TAP.2014.2364071

Kumar, L., Rawal, I., Kaur, A., & Annapoorni, S. (2017). Flexible room temperature ammonia sensor based on polyaniline. *Sensors and Actuators, B: Chemical*, *240*, 408–416. https://doi.org/10.1016/j.snb.2016.08.173

Kumar, R., Shin, J., Yin, L., You, J.-M., Meng, Y. S., & Wang, J. (2017). All-Printed, Stretchable Zn-Ag 2 O Rechargeable Battery via Hyperelastic Binder for Self-Powering Wearable Electronics. *Advanced Energy Materials*, *7*(8), 1602096. https://doi.org/10.1002/aenm.201602096

Kuntzleman, T. S., & Jacobson, E. C. (2016). Teaching Beer's Law and Absorption Spectrophotometry with a Smart Phone: A Substantially Simplified Protocol. *Journal of Chemical Education*, *93*(7), 1249–1252. https://doi.org/10.1021/acs.jchemed.5b00844

Kurokawa, K. (1965). Power Waves and the Scattering Matrix. *IEEE Transactions on Microwave Theory and Techniques*, *13*(2), 194–202. https://doi.org/10.1109/TMTT.1965.1125964

Kuswandi, B., Jayus, Restyana, A., Abdullah, A., Heng, L. Y., & Ahmad, M. (2012). A novel colorimetric food package label for fish spoilage based on polyaniline film. *Food Control*, *25*(1), 18–189. https://doi.org/10.1016/j.foodcont.2011.10.008

Kuswandi, B., Maryska, C., Jayus, Abdullah, A., & Heng, L. Y. (2013). Real time on-package freshness indicator for guavas packaging. *Journal of Food Measurement and Characterization*, *7*(1), 29–39. https://doi.org/10.1007/s11694-013-9136-5

Kutty, A. A., Björninen, T., Syd, L., & Ukkonen, L. (2016). *A Novel Carbon Nanotube Loaded Passive UHF RFID Sensor Tag with Built-in Reference for Wireless Gas Sensing*. TUT. https://doi.org/10.1109/MWSYM.2016.7540328

Kwon, J. H., Pode, R., Kim, H. D., & Chung, H. K. (2013). *Applications of Organic and Printed Electronics*. (E. Cantatore, Ed.), *Applications of Organic and Printed*

Electronics. Boston, MA: Springer US. https://doi.org/10.1007/978-1-4614-3160-2

Lai, C. Y., Cheong, C. F., Mandeep, J. S., Abdullah, H. B., Amin, N., & Lai, K. W. (2014). Synthesis and Characterization of Silver Nanoparticles and Silver Inks: Review on the Past and Recent Technology Roadmaps. *Journal of Materials Engineering and Performance*, *23*(10), 3541–3550. https://doi.org/10.1007/s11665-014-1166-6

Lai, T.-S., Chang, T.-C., & Wang, S.-C. (2017). Gold nanoparticle-based colorimetric methods to determine protein contents in artificial urine using membrane micro-concentrators and mobile phone camera. *Sensors and Actuators B: Chemical*, *239*, 9–16. https://doi.org/10.1016/j.snb.2016.07.158

Le Floch, P., Yao, X., Liu, Q., Wang, Z., Nian, G., Sun, Y., … Suo, Z. (2017). Wearable and Washable Conductors for Active Textiles. *ACS Applied Materials & Interfaces*, *9*(30), 25542–25552. https://doi.org/10.1021/acsami.7b07361

Lee, H., Kim, D., Lee, I., Moon, Y.-J., & Hwang, J.-Y. (2014). Stepwise current electrical sintering method for inkjet-printed conductive ink. *Japanese Journal of Applied Physics*, *53*(05HC07), 1–3. From http://dx.doi.org/10.7567/JJAP.53.05HC07

Lee, S. A., & Yang, C. (2014). A smartphone-based chip-scale microscope using ambient illumination. *Lab Chip*, *14*(16), 3056–3063. https://doi.org/10.1039/C4LC00523F

Leikanger, T., Häkkinen, J., & Schuss, C. (2017). Interfacing external sensors with Android smartphones through near field communication. *Measurement Science and Technology*, *28*(4), 044006. https://doi.org/10.1088/1361-6501/aa57da

Li, C.-Y., & Liao, Y.-C. (2016). Adhesive Stretchable Printed Conductive Thin Film Patterns on PDMS Surface with an Atmospheric Plasma Treatment. *ACS Applied Materials&Interfaces*, *8*(18), 11868–11874. https://doi.org/10.1021/acsami.6b02844

Li, D., Lai, W.-Y., Zhang, Y.-Z., & Huang, W. (2018). Printable Transparent Conductive Films for Flexible Electronics. *Advanced Materials*, *1704738*, 1704738. https://doi.org/10.1002/adma.201704738

Li, F., Bao, Y., Wang, D., Wang, W., & Niu, L. (2016). Smartphones for sensing. *Science Bulletin*, *61*(3), 190–201. https://doi.org/10.1007/s11434-015-0954-1

Li, S., Chen, S., Zhuo, B., Li, Q., Liu, W., & Guo, X. (2017). Flexible Ammonia Sensor Based on PEDOT:PSS/Silver Nanowire Composite Film for Meat Freshness Monitoring. *IEEE Electron Device Letters*, *38*(7), 975–978. https://doi.org/10.1109/LED.2017.2701879

Lide, D. R. (2007). Electrical resistivity of pure metals. In *CRC Handbook of Chemistry and Physics, Internet Version* (87th ed.). Boca Raton, FL: Taylor and Francis. Retrieved from http://hbcponline.com

Lin, B., Yu, Y., Cao, Y., Guo, M., Zhu, D., Dai, J., & Zheng, M. (2018). Point-of-care testing for streptomycin based on aptamer recognizing and digital image colorimetry by smartphone. *Biosensors and Bioelectronics*, *100*(378), 482–489. https://doi.org/10.1016/j.bios.2017.09.028

Liu, X.-D., Sheng, D.-K., Gao, X.-M., Li, T.-B., & Yang, Y.-M. (2013). UV-assisted surface modification of PET fiber for adhesion improvement. *Applied Surface Science*, *264*, 61–69. https://doi.org/10.1016/j.apsusc.2012.09.107

Liu, X., Gu, L., Zhang, Q., Wu, J., Long, Y., & Fan, Z. (2014). All-printable band-edge modulated ZnO nanowire photodetectors with ultra-high detectivity. *Nature Communications*, *5*, 1–9. https://doi.org/10.1038/ncomms5007

Lobnik, A., Turel, M., & Urek, Š. (2012). Optical chemical sensors: Design and applications. *Advances in Chemical Sensors*, 1–28. https://doi.org/10.5772/31534

Loo, C.-H., Elmahgoub, K., Yang, F., Elsherbeni, A. Z., Kajfez, D., Kishk, A. A., … Ruuskanen, P. (2008). Chip impedance matching for UHF RFID tag antenna design. *Progress In Electromagnetics Research*, *81*, 359–370. https://doi.org/10.2528/PIER08011804

Lopez-Ruiz, N., Curto, V. F., Erenas, M. M., Benito-Lopez, F., Diamond, D., Palma, A. J., & Capitan-Vallvey, L. F. (2014). Smartphone-Based Simultaneous pH and Nitrite Colorimetric Determination for Paper Microfluidic Devices. *Analytical Chemistry*, *86*(19), 9554–9562. https://doi.org/10.1021/ac5019205

López-Ruiz, N., López-Torres, J., Carvajal, M. A., De Vargas-Sansalvador, I. P., & Martínez-Olmos, A. (2015). Wearable system for monitoring of oxygen concentration in breath based on optical sensor. *IEEE Sensors Journal*, *15*(7), 4039–4045. https://doi.org/10.1109/JSEN.2015.2410789

López-Ruiz, N., Martínez-Olmos, A., Pérez de Vargas-Sansalvador, I. M., Fernández-Ramos, M. D., Carvajal, M. a., Capitan-Vallvey, L. F., & Palma, A. J. (2012). Determination of O2 using colour sensing from image processing with mobile devices. *Sensors and Actuators B: Chemical*, *171–172*, 938–945. https://doi.org/10.1016/j.snb.2012.06.007

Lorite, G. S., Selkälä, T., Sipola, T., Palenzuela, J., Jubete, E., Viñuales, A., … Toth, G. (2017). Novel, smart and RFID assisted critical temperature indicator for supply chain monitoring. *Journal of Food Engineering*, *193*, 20–28. https://doi.org/10.1016/j.jfoodeng.2016.06.016

Lorwongtragool, P., Sowade, E., Watthanawisuth, N., Baumann, R. R., & Kerdcharoen, T. (2014). A novel wearable electronic nose for healthcare based on flexible printed chemical sensor array. *Sensors (Switzerland)*, *14*(10), 19700–19712. https://doi.org/10.3390/s141019700

Lu, J.-H., & Chang, B.-S. (2014). Compact circularly polarized tag antenna for UHF RFID system. In *2014 International Symposium on Antennas and Propagation Conference Proceedings* (pp. 625–626). IEEE. https://doi.org/10.1109/ISANP.2014.7026806

MacKenzie, J. D., & Ho, C. (2015). Perspectives on Energy Storage for Flexible Electronic Systems. *Proceedings of the IEEE*, *103*(4), 535–553. https://doi.org/10.1109/JPROC.2015.2406340

Maekawa, K., Yamasaki, K., Niizeki, T., Mita, M., Matsuba, Y., Terada, N., & Saito, H. (2012). Drop-on-Demand Laser Sintering With Silver Nanoparticles for Electronics Packaging. *IEEE Transactions on Components, Packaging and Manufacturing Technology*, *2*(5), 868–877. 10.1109/TCPMT.2011.2178606

Magdassi, S., Grouchko, M., Berezin, O., & Kamyshny, A. (2010). Triggering the sintering of silver nanoparticles at room temperature. *ACS Nano*, *4*(4), 1943–1948. https://doi.org/10.1021/nn901868t

Maiellaro, G., Ragonese, E., Gwoziecki, R., Jacobs, S., Marjanovic, N., Chrapa, M., … Palmisano, G. (2014). Ambient Light Organic Sensor in a Printed Complementary Organic TFT Technology on Flexible Plastic Foil. *IEEE Transactions on Circuits and Systems I: Regular Papers*, *61*(4), 1036–1043. https://doi.org/10.1109/TCSI.2013.2286031

Marrocco, G. (2008). The art of UHF RFID antenna design: Impedance-matching and size-reduction techniques. *IEEE Antennas and Propagation Magazine*, *50*(1), 66–79. https://doi.org/10.1109/MAP.2008.4494504

Martínez-Olmos, A., Fernández-Salmerón, J., Lopez-Ruiz, N., Rivadeneyra Torres, A., Capitan-Vallvey, L. F., & Palma, A. J. (2013). Screen Printed Flexible Radiofrequency Identification Tag for Oxygen Monitoring. *Analytical Chemistry*, *85*(22), 11098–11105. https://doi.org/10.1021/ac4028802

Masawat, P., Harfield, A., & Namwong, A. (2015). An iPhone-based digital image colorimeter for detecting tetracycline in milk. *Food Chemistry*, *184*, 23–29. https://doi.org/10.1016/j.foodchem.2015.03.089

Mata, A., Fleischman, A. J., & Roy, S. (2005). Characterization of Polydimethylsiloxane (PDMS) Properties for Biomedical Micro/Nanosystems. *Biomedical Microdevices*, *7*(4), 281–293. https://doi.org/10.1007/s10544-005-6070-2

Matindoust, S., Farzi, A., Baghaei Nejad, M., Shahrokh Abadi, M. H., Zou, Z., & Zheng, L.-R. (2017). Ammonia gas sensor based on flexible polyaniline films for rapid detection of spoilage in protein-rich foods. *Journal of Materials Science: Materials in Electronics*, *28*(11), 7760–7768. https://doi.org/10.1007/s10854-017-6471-z

Matsuhisa, N., Inoue, D., Zalar, P., Jin, H., Matsuba, Y., Itoh, A., … Someya, T. (2017). Printable elastic conductors by in situ formation of silver nanoparticles from silver flakes. *Nature Materials*, *16*(8), 834–840. https://doi.org/10.1038/nmat4904

Mattana, G., & Briand, D. (2016). Recent advances in printed sensors on foil. *Materials Today*, *19*(2), 88–99. https://doi.org/10.1016/j.mattod.2015.08.001

Mattana, G., Kinkeldei, T., Leuenberger, D., Ataman, C., Ruan, J. J., Molina-Lopez, F., … de Rooij, N. F. (2013). Woven Temperature and Humidity Sensors on Flexible Plastic Substrates for E-Textile Applications. *IEEE Sensors Journal*, *13*(10), 3901–3909. https://doi.org/10.1109/JSEN.2013.2257167

Mattana, G., Loi, A., Woytasik, M., Barbaro, M., Noël, V., & Piro, B. (2017). Inkjet-Printing: A New Fabrication Technology for Organic Transistors. *Advanced Materials Technologies*, *2*(10), 1700063. https://doi.org/10.1002/admt.201700063

Maxwell, J. C. (1892). *A Treatise on Electricity and Magnetism* (3rd ed.). Oxford: Claredon.

Mayer, J. A., Gallinet, B., Offermans, T., Zhurminsky, I., & Ferrini, R. (2017). Self-contained optical enhancement film for printed photovoltaics. *Solar Energy Materials and Solar Cells*, *163* (December 2016), 51–57. https://doi.org/10.1016/j.solmat.2017.01.015

McCracken, K. E., & Yoon, J.-Y. (2016). Recent approaches for optical smartphone sensing in resource-limited settings: a brief review. *Analytical Methods*, *8*(36), 6591–6601. https://doi.org/10.1039/C6AY01575A

Meng, Z., & Li, Z. (2016). RFID Tag as a Sensor - A Review on the Innovative Designs and Applications. *Measurement Science Review*, *16*(6), 305–315. https://doi.org/10.1515/msr-2016-0039

Merilampi, S., Laine-Ma, T., & Ruuskanen, P. (2009). The characterization of electrically conductive silver ink patterns on flexible substrates. *Microelectronics Reliability*, *49*(7), 782–790. https://doi.org/10.1016/j.microrel.2009.04.004

Molina-Farrugia, B., Rivadeneyra, A., Fernández-Salmerón, J., Martínez-Martí, F., Banqueri, J., & Carvajal, M. A. (2017). Read Range Enhancement of a Sensing RFID Tag by Photovoltaic Panel. *Journal of Sensors*, *2017*, 1–7. https://doi.org/10.1155/2017/7264703

Molina-Lopez, F., Briand, D., & de Rooij, N. F. (2012). All additive inkjet printed humidity sensors on plastic substrate. *Sensors and Actuators B: Chemical*, *166–167*, 212–222. https://doi.org/10.1016/j.snb.2012.02.042

Molina-Lopez, F., Quintero, A. V., Mattana, G., Briand, D., & de Rooij, N. F. (2013). Large-area compatible fabrication and encapsulation of inkjet-printed humidity sensors on flexible foils with integrated thermal compensation. *Journal of*

Micromechanics and Microengineering, *23*(2), 025012. https://doi.org/10.1088/0960-1317/23/2/025012

Montangero, M. (2015). Determining the Amount of Copper(II) Ions in a Solution Using a Smartphone. *Journal of Chemical Education*, *92*(10), 1759–1762. https://doi.org/10.1021/acs.jchemed.5b00167

Morishita, H., Hirasawa, K., & Nagao, T. (1998). Circularly polarised wire antenna with a dual rhombic loop. *IEE Proceedings - Microwaves, Antennas and Propagation*, *145*(3), 219. https://doi.org/10.1049/ip-map:19981864

Morsy, M. K., Z??r, K., Kostesha, N., Alstr??m, T. S., Heiskanen, A., El-Tanahi, H., … Emn??us, J. (2016). Development and validation of a colorimetric sensor array for fish spoilage monitoring. *Food Control*, *60*, 346–352. https://doi.org/10.1016/j.foodcont.2015.07.038

Mościcki, A., Smolarek-Nowak, A., Felba, J., & Kinart, A. (2017). Ink for Ink-Jet Printing of Electrically Conductive Structures on Flexible Substrates with Low Thermal Resistance. *Journal of Electronic Materials*, *46*(7), 4100–4108. https://doi.org/10.1007/s11664-017-5320-4

Mousavi, S., Kang, K., Park, J., & Park, I. (2016). A room temperature hydrogen sulfide gas sensor based on electrospun polyaniline–polyethylene oxide nanofibers directly written on flexible substrates. *RSC Advances*, *6*(106), 104131–104138. https://doi.org/10.1039/C6RA20710C

Moya, A., Sowade, E., del Campo, F. J., Mitra, K. Y., Ramon, E., Villa, R., … Gabriel, G. (2016). All-inkjet-printed dissolved oxygen sensors on flexible plastic substrates. *Organic Electronics*, *39*, 168–176. 10.1016/j.orgel.2016.10.002

Myny, K., Smout, S., Rockelé, M., Bhoolokam, A., Ke, T. H., Steudel, S., … Heremans, P. (2015). A thin-film microprocessor with inkjet print-programmable memory. *Scientific Reports*, *4*(1), 7398. https://doi.org/10.1038/srep07398

Nakata, S., Arie, T., Akita, S., & Takei, K. (2017). Wearable, Flexible, and Multifunctional Healthcare Device with an ISFET Chemical Sensor for Simultaneous Sweat pH and Skin Temperature Monitoring. *ACS Sensors*, *2*(3), 443–448. https://doi.org/10.1021/acssensors.7b00047

Narakathu, B. B., Eshkeiti, A., Reddy, A. S. G., Rebros, M., Rebrosova, E., Joyce, M. K., … Atashbar, M. Z. (2012). A novel fully printed and flexible capacitive pressure sensor. In *2012 IEEE Sensors* (pp. 1–4). IEEE. https://doi.org/10.1109/ICSENS.2012.6411354

Nemiroski, A., Christodouleas, D. C., Hennek, J. W., Kumar, A. A., Maxwell, E. J., Fernandez-Abedul, M. T., & Whitesides, G. M. (2014). Universal mobile electrochemical detector designed for use in resource-limited applications.

Proceedings of the National Academy of Sciences, *111*(33), 11984–11989. https://doi.org/10.1073/pnas.1405679111

Newman, J. D., Turner, A. P. F., & Marrazza, G. (1992). Ink-jet printing for the fabrication of amperometric glucose biosensors. *Analytica Chimica Acta*, *262*(1), 13–17. https://doi.org/10.1016/0003-2670(92)80002-O

Niittynen, J., Sowade, E., Kang, H., Baumann, R. R., & Mäntysalo, M. (2015). Comparison of laser and intense pulsed light sintering (IPL) for inkjet-printed copper nanoparticle layers. *Scientific Reports*, *5*(1), 8832. https://doi.org/10.1038/srep08832

Nikitin, P. V., Rao, K. V. S., Lam, S. F., Pillai, V., Martinez, R., & Heinrich, H. (2005). Power reflection coefficient analysis for complex impedances in RFID tag design. *IEEE Transactions on Microwave Theory and Techniques*, *53*(9), 2721–2725. https://doi.org/10.1109/TMTT.2005.854191

Noh, J.-S. (2016). Conductive Elastomers for Stretchable Electronics, Sensors and Energy Harvesters. *Polymers*, *8*(4), 123. https://doi.org/10.3390/polym8040123

Ostfeld, A. E. (2015). Screen printed passive components for flexible power electronics. *Scientific Reports*, *5*, 15959. https://doi.org/10.1038/srep15959

Ostfeld, A. E., Gaikwad, A. M., Khan, Y., & Arias, A. C. (2016). High-performance flexible energy storage and harvesting system for wearable electronics. *Scientific Reports*, *6*(1), 26122. https://doi.org/10.1038/srep26122

Parashkov, R., Becker, E., Riedl, T., Johannes, H.-H., & Kowalsky, W. (2005). Large Area Electronics Using Printing Methods. *Proceedings of the IEEE*, *93*(7), 1321–1329. https://doi.org/10.1109/JPROC.2005.850304

Park, E. S., Chen, Y., Liu, T.-J. K., & Subramanian, V. (2013). A New Switching Device for Printed Electronics: Inkjet-Printed Microelectromechanical Relay. *Nano Letters*, *13*(11), 5355–5360. https://doi.org/10.1021/nl4028632

Park, M., Im, J., Shin, M., Min, Y., Park, J., Cho, H., … Kim, K. (2012). Highly stretchable electric circuits from a composite material of silver nanoparticles and elastomeric fibres. *Nature Nanotechnology*, *7*(12), 803–809. https://doi.org/10.1038/nnano.2012.206

Park, M., Park, J., & Jeong, U. (2014). Design of conductive composite elastomers for stretchable electronics. *Nano Today*, *9*(2), 244–260. https://doi.org/10.1016/j.nantod.2014.04.009

Paterson, A. S., Raja, B., Mandadi, V., Townsend, B., Lee, M., Buell, A., … Willson, R. C. (2017). A low-cost smartphone-based platform for highly sensitive point-of-care testing with persistent luminescent phosphors. *Lab on a Chip*, *17*(6), 1051–1059. https://doi.org/10.1039/C6LC01167E

Perelaer, J., de Gans, B.-J., & Schubert, U. S. (2006). Ink-jet Printing and Microwave Sintering of Conductive Silver Tracks. *Advanced Materials*, *18*(16), 2101–2104. https://doi.org/10.1002/adma.200502422

Perelaer, J., Klokkenburg, M., Hendriks, C. E., & Schubert, U. S. (2009). Microwave flash sintering of inkjet-printed silver tracks on polymer substrates. *Advanced Materials*, *21*(47), 4830–4834. https://doi.org/10.1002/adma.200901081

Pérez de Vargas-Sansalvador, I. M., Carvajal, M. A., Roldán-Muñoz, O. M., Banqueri, J., Fernández-Ramos, M. D., & Capitán-Vallvey, L. F. (2009). Phosphorescent sensing of carbon dioxide based on secondary inner-filter quenching. *Analytica Chimica Acta*, *655*(1–2), 66–74. https://doi.org/10.1016/j.aca.2009.09.037

Pichorim, S., Gomes, N., & Batchelor, J. (2018). Two Solutions of Soil Moisture Sensing with RFID for Landslide Monitoring. *Sensors*, *18*(2), 452. https://doi.org/10.3390/s18020452

Potyrailo, R. A., Burns, A., Surman, C., Lee, D. J., & McGinniss, E. (2012). Multivariable passive RFID vapor sensors: roll-to-roll fabrication on a flexible substrate. *The Analyst*, *137*(12), 2777. https://doi.org/10.1039/c2an16278d

Potyrailo, R. A., Nagraj, N., Tang, Z., Mondello, F. J., Surman, C., & Morris, W. (2012). Battery-free Radio Frequency Identification (RFID) Sensors for Food Quality and Safety. *Journal of Agricultural and Food Chemistry*, *60*(35), 8535–8543. https://doi.org/10.1021/jf302416y

Potyrailo, R. A., & Surman, C. (2013). A passive radio-frequency identification (RFID) gas sensor with self-correction against fluctuations of ambient temperature. *Sensors and Actuators B: Chemical*, *185*(4), 587–593. 10.1016/j.snb.2013.04.107

Powell, A. W., Coles, D. M., Taylor, R. A., Watt, A. A. R., Assender, H. E., & Smith, J. M. (2016). Plasmonic Gas Sensing Using Nanocube Patch Antennas. *Advanced Optical Materials*, *4*(4), 634–642. https://doi.org/10.1002/adom.201500602

Pozar, D. M. (2012). *Microwave Engineering*. *John Wiley & Sons, Inc.* (Fourth). https://doi.org/TK7876.P69 2011

Prabhakar, T. V., Mysore, U., Saini, U., Vinoy, K. J., & Amruthur, B. (2015). NFC for Pervasive Healthcare Monitoring. In *2015 28th International Conference on VLSI Design* (Vol. 2015–Febru, pp. 75–80). IEEE. 10.1109/VLSID.2015.18

Qazi, H., Mohammad, A., & Akram, M. (2012). Recent Progress in Optical Chemical Sensors. *Sensors*, *12*(12), 16522–16556. https://doi.org/10.3390/s121216522

Quaranta, M., Borisov, S. M., & Klimant, I. (2012). Indicators for optical oxygen sensors. *Bioanalytical Reviews*, *4*(2–4), 115–157. https://doi.org/10.1007/s12566-012-0032-y

Quesada-González, D., & Merkoçi, A. (2017). Mobile phone-based biosensing: An emerging "diagnostic and communication" technology. *Biosensors and Bioelectronics*, *92*(June 2016), 549–562. https://doi.org/10.1016/j.bios.2016.10.062

Quintero, A. V., Molina-Lopez, F., Smits, E. C. P., Danesh, E., van den Brand, J., Persaud, K., … Briand, D. (2016). Smart RFID label with a printed multisensor platform for environmental monitoring. *Flexible and Printed Electronics*, *1*(2), 025003. https://doi.org/10.1088/2058-8585/1/2/025003

Rakibet, O. O., Rumens, C. V, Batchelor, J. C., Member, S., & Holder, S. J. (2014). Epidermal Passive RFID Strain Sensor for Assisted Technologies, *13*, 814–817. https://doi.org/10.1109/LAWP.2014.2318996

Rao, K. V. S., Nikitin, P. V., & Lam, S. F. (2005). Antenna design for UHF RFID tags: a review and a practical application. *IEEE Transactions on Antennas and Propagation*, *53*(12), 3870–3876. https://doi.org/10.1109/TAP.2005.859919

Rhodes, D. R. (1976). Observable stored energies of electromagnetic systems. *Journal of the Franklin Institute*, *302*(3), 225–237. https://doi.org/10.1016/0016-0032(79)90126-1

Rieu, M., Camara, M., Tournier, G., Viricelle, J.-P., Pijolat, C., de Rooij, N. F., & Briand, D. (2016). Fully inkjet printed SnO2 gas sensor on plastic substrate. *Sensors and Actuators B: Chemical*, *236*, 1091–1097. https://doi.org/10.1016/j.snb.2016.06.042

Rim, Y. S., Bae, S.-H., Chen, H., De Marco, N., & Yang, Y. (2016). Recent Progress in Materials and Devices toward Printable and Flexible Sensors. *Advanced Materials*, *28*(22), 4415–4440. https://doi.org/10.1002/adma.201505118

Rivadeneyra, A., Fernández-Salmerón, J., Agudo-Acemel, M., López-Villanueva, J. A., Capitán-Vallvey, L. F., & Palma, A. J. (2016). Hybrid Printed Device for Simultaneous Vapors Sensing. *IEEE Sensors Journal*, *16*(23), 8501–8508. https://doi.org/10.1109/JSEN.2016.2606415

Rivadeneyra, A., Fernández-Salmerón, J., Agudo, M., López-Villanueva, J. a., Capitan-Vallvey, L. F., & Palma, A. J. (2014). Design and characterization of a low thermal drift capacitive humidity sensor by inkjet-printing. *Sensors and Actuators B: Chemical*, *195*, 123–131. https://doi.org/10.1016/j.snb.2013.12.117

Rivadeneyra, A., Fernández-Salmerón, J., Banqueri, J., López-Villanueva, J. a., Capitan-Vallvey, L. F., & Palma, A. J. (2014). A novel electrode structure compared with interdigitated electrodes as capacitive sensor. *Sensors and Actuators B: Chemical*, *204*, 552–560. https://doi.org/10.1016/j.snb.2014.08.010

Roberson, D. A., Wicker, R. B., & MacDonald, E. (2012). Ohmic Curing of Printed Silver Conductive Traces. *Journal of Electronic Materials*, *41*(9), 2553–2566. https://doi.org/10.1007/s11664-012-2140-4

Roberson, D. A., Wicker, R. B., Murr, L. E., Church, K., & MacDonald, E. (2011). Microstructural and Process Characterization of Conductive Traces Printed from Ag Particulate Inks. *Materials*, *4*(12), 963–979. https://doi.org/10.3390/ma4060963

Roda, A., Michelini, E., Zangheri, M., Di Fusco, M., Calabria, D., & Simoni, P. (2016). Smartphone-based biosensors: A critical review and perspectives. *TrAC Trends in Analytical Chemistry*, *79*, 317–325. https://doi.org/10.1016/j.trac.2015.10.019

Roda, A., Mirasoli, M., Michelini, E., Di Fusco, M., Zangheri, M., Cevenini, L., … Simoni, P. (2016). Progress in chemical luminescence-based biosensors: A critical review. *Biosensors and Bioelectronics*, *76*, 164–179. https://doi.org/10.1016/j.bios.2015.06.017

Rooney, M. L. (1995). *Active Food Packaging*. Springer US.

Rose, D. P., Ratterman, M. E., Griffin, D. K., Hou, L., Kelley-Loughnane, N., Naik, R. R., … Heikenfeld, J. C. (2015). Adhesive RFID Sensor Patch for Monitoring of Sweat Electrolytes. *IEEE Transactions on Biomedical Engineering*, *62*(6), 1457–1465. https://doi.org/10.1109/TBME.2014.2369991

Rozenfeld, A. (2008). *US 8,742,357 B2*. Australia.

Salinas, Y., Ros-Lis, J. V., Vivancos, J. L., Martínez-Máñez, R., Marcos, M. D., Aucejo, S., … Garcia, E. (2014). A novel colorimetric sensor array for monitoring fresh pork sausages spoilage. *Food Control*, *35*(1), 166–176. https://doi.org/10.1016/j.foodcont.2013.06.043

Saliu, F., & Della Pergola, R. (2018). Carbon dioxide colorimetric indicators for food packaging application: Applicability of anthocyanin and poly-lysine mixtures. *Sensors and Actuators, B: Chemical*, *258*, 1117–1124. https://doi.org/10.1016/j.snb.2017.12.007

Salmerón, J. F., Molina-Lopez, F., Briand, D., Ruan, J. J., Rivadeneyra, A., Carvajal, M. A., … Palma, A. J. (2014). Properties and Printability of Inkjet and Screen-Printed Silver Patterns for RFID Antennas. *Journal of Electronic Materials*, *43*(2), 604–617. https://doi.org/10.1007/s11664-013-2893-4

Salmerón, J. F., Rivadeneyra, A., Agudo-Acemel, M., Capitán-Vallvey, L. F., Banqueri, J., Carvajal, M. a., & Palma, A. J. (2014). *Printed single-chip UHF passive radio frequency identification tags with sensing capability*. *Sensors and Actuators A: Physical* (Vol. 220). https://doi.org/10.1016/j.sna.2014.10.023

Schiattarella, C., Polichetti, T., Villani, F., Loffredo, F., Alfano, B., Massera, E., … Di Francia, G. (2018). Inkjet Printed Graphene-Based Chemiresistive Sensors to NO2. In B. Andò, F. Baldini, C. Di Natale, G. Marrazza, & P. Siciliano (Eds.) (Vol. 431, pp. 111–118). Springer, Cham. 10.1007/978-3-319-55077-0_15

Segev-Bar, M., Bachar, N., Wolf, Y., Ukrainsky, B., Sarraf, L., & Haick, H. (2017). Multi-Parametric Sensing Platforms Based on Nanoparticles. *Advanced Materials Technologies*, *2*(1), 1600206. https://doi.org/10.1002/admt.201600206

Shaikh, F. K., & Zeadally, S. (2016). Energy harvesting in wireless sensor networks: A comprehensive review. *Renewable and Sustainable Energy Reviews*, *55*, 1041–1054. https://doi.org/10.1016/j.rser.2015.11.010

Shi, Y., Manco, M., Moyal, D., Huppert, G., Araki, H., Banks, A., … Pielak, R. M. (2018). Soft, stretchable, epidermal sensor with integrated electronics and photochemistry for measuring personal UV exposures. *PLOS ONE*, *13*(1), e0190233. https://doi.org/10.1371/journal.pone.0190233

Shin, J., Choi, S., Yang, J.-S., Song, J., Choi, J.-S., & Jung, H.-I. (2017). Smart Forensic Phone: Colorimetric analysis of a bloodstain for age estimation using a smartphone. *Sensors and Actuators B: Chemical*, *243*, 221–225. https://doi.org/10.1016/j.snb.2016.11.142

Singh, E., Meyyappan, M., & Nalwa, H. S. (2017). Flexible Graphene-Based Wearable Gas and Chemical Sensors. *ACS Applied Materials & Interfaces*, *9*(40), 34544–34586. https://doi.org/10.1021/acsami.7b07063

Singh, M., Haverinen, H. M., Dhagat, P., & Jabbour, G. E. (2010). Inkjet Printing-Process and Its Applications. *Advanced Materials*, *22*(6), 673–685. https://doi.org/10.1002/adma.200901141

Singh, R., Singh, E., & Nalwa, H. S. (2017). Inkjet printed nanomaterial based flexible radio frequency identification (RFID) tag sensors for the internet of nano things. *RSC Adv.*, *7*(77), 48597–48630. https://doi.org/10.1039/C7RA07191D

Soukup, R., Hamacek, A., & Reboun, J. (2012). Organic based sensors: Novel screen printing technique for sensing layers deposition. In *2012 35th International Spring Seminar on Electronics Technology* (pp. 19–24). IEEE. https://doi.org/10.1109/ISSE.2012.6273101

ST Electronics. (2009). AN2866 Application note. How to design a 13.56 MHz customized tag antenna.

Starke, E., Turke, A., Krause, M., & Fischer, W.-J. (2011). Flexible polymer humidity sensor fabricated by inkjet printing. In *2011 16th International Solid-State Sensors, Actuators and Microsystems Conference* (pp. 1152–1155). IEEE. https://doi.org/10.1109/TRANSDUCERS.2011.5969254

Steinberg, M. D., Tkalčec, B., & Murković Steinberg, I. (2016). Towards a passive contactless sensor for monitoring resistivity in porous materials. *Sensors and Actuators B: Chemical*, *234*, 294–299. https://doi.org/10.1016/j.snb.2016.04.169

Stoppa, M., & Chiolerio, A. (2014). Wearable electronics and smart textiles: a critical

review. *Sensors (Basel, Switzerland)*, *14*(7), 11957–92. https://doi.org/10.3390/s140711957

Suganuma, K. (2014). *Introduction to Printed Electronics* (Vol. 74). New York, NY: Springer New York. https://doi.org/10.1007/978-1-4614-9625-0

Suikkola, J., Björninen, T., Mosallaei, M., Kankkunen, T., Iso-Ketola, P., Ukkonen, L., … Mäntysalo, M. (2016). Screen-Printing Fabrication and Characterization of Stretchable Electronics. *Scientific Reports*, *6*(April), 25784. https://doi.org/10.1038/srep25784

Sun, A. C., Yao, C., A.G., V., & Hall, D. A. (2016). An efficient power harvesting mobile phone-based electrochemical biosensor for point-of-care health monitoring. *Sensors and Actuators B: Chemical*, *235*, 126–135. https://doi.org/10.1016/j.snb.2016.05.010

T.-X. Liang, W. Z. Sun, L.-D. Wang, Y. H. Wang, and H.-D. L. (1996). Effect of surface energies on screen printing resolution. *IEEE Trans. Compon., Packag. Manuf. Technol. B, Adv. Packag*, *19*(2), 423–426.

Taleat, Z., Khoshroo, A., & Mazloum-Ardakani, M. (2014). Screen-printed electrodes for biosensing: a review (2008–2013). *Microchimica Acta*, *181*(9–10), 865–891. https://doi.org/10.1007/s00604-014-1181-1

Tanguy, N. R., Fiddes, L. K., & Yan, N. (2015). Enhanced Radio Frequency Biosensor for Food Quality Detection Using Functionalized Carbon Nanofillers. *ACS Applied Materials & Interfaces*, *7*(22), 11939–11947. 10.1021/acsami.5b01876

Tao, X. (2015). *Handbook of Smart Textiles*. (X. Tao, Ed.), *Handbook of Smart Textiles*. Singapore: Springer Singapore. https://doi.org/10.1007/978-981-4451-45-1

Texas Instruments. (2003). *HF Antenna Design Notes*. *Technical Application Report 11-08-26-003*. Retrieved from http://www.ti.com/lit/an/scba034/scba034.pdf

Trajkovikj, J., Zurcher, J.-F., & Skrivervik, A. K. (2013). PDMS, A Robust Casing for Flexible W-BAN Antennas [EurAAP Corner]. *IEEE Antennas and Propagation Magazine*, *55*(5), 287–297. https://doi.org/10.1109/MAP.2013.6735538

Trojanowicz, M. (2016). Impact of nanotechnology on design of advanced screen-printed electrodes for different analytical applications. *TrAC Trends in Analytical Chemistry*, *84*, 22–47. https://doi.org/10.1016/j.trac.2016.03.027

Valentine, A. D., Busbee, T. A., Boley, J. W., Raney, J. R., Chortos, A., Kotikian, A., … Lewis, J. A. (2017). Hybrid 3D Printing of Soft Electronics. *Advanced Materials*, *29*(40), 1703817. https://doi.org/10.1002/adma.201703817

Vanderroost, M., Ragaert, P., Devlieghere, F., & De Meulenaer, B. (2014). Intelligent food packaging: The next generation. *Trends in Food Science & Technology*, *39*(1),

47–62. https://doi.org/10.1016/j.tifs.2014.06.009

Vandevenne, G., Marchal, W., Verboven, I., Drijkoningen, J., D'Haen, J., Van Bael, M. K., … Deferme, W. (2016). A study on the thermal sintering process of silver nanoparticle inkjet inks to achieve smooth and highly conducting silver layers. *Physica Status Solidi (A)*, *213*(6), 1403–1409. 10.1002/pssa.201533007

Vasović, N. D., & Ristić, G. S. (2012). A new microcontroller-based RADFET dosimeter reader. *Radiation Measurements*, *47*(4), 272–276. https://doi.org/10.1016/j.radmeas.2012.01.017

Vásquez Quintero, A., Verplancke, R., De Smet, H., & Vanfleteren, J. (2017). Stretchable Electronic Platform for Soft and Smart Contact Lens Applications. *Advanced Materials Technologies*, *2*(8), 1700073. 10.1002/admt.201700073

Virkki, J., Wei, Z., Liu, A., Ukkonen, L., & Björninen, T. (2017). Wearable Passive E-Textile UHF RFID Tag Based on a Slotted Patch Antenna with Sewn Ground and Microchip Interconnections. *International Journal of Antennas and Propagation*, *2017*, 1–8. https://doi.org/10.1155/2017/3476017

Virtanen, J., Ukkonen, L., Bjorninen, T., Elsherbeni, A. Z., & Sydänheimo, L. (2011). Inkjet-Printed Humidity Sensor for Passive UHF RFID Systems. *IEEE Transactions on Instrumentation and Measurement*, *60*(8), 2768–2777. https://doi.org/10.1109/TIM.2011.2130070

Vu, C. H. T., & Won, K. (2013). Novel water-resistant UV-activated oxygen indicator for intelligent food packaging. *Food Chemistry*, *140*(1–2), 52–56. https://doi.org/10.1016/j.foodchem.2013.02.056

Wang, J., Liu, J., Virkki, J., Bjo rninen, T., Syda nheimo, L., Cheng, L., & Ukkonen, L. (2016). Brush-painting and photonical sintering of copper and silver inks on cotton fabric to form antennas for wearable ultra-high-frequency radio-frequency identification tags. *Textile Research Journal*, *86*(15), 1616–1624. https://doi.org/10.1177/0040517515596969

Wang, X. dong, Chen, H. xu, Zhao, Y., Chen, X., Wang, X. ru, & Chen, X. (2010). Optical oxygen sensors move towards colorimetric determination. *TrAC - Trends in Analytical Chemistry*, *29*(4), 319–338. https://doi.org/10.1016/j.trac.2010.01.004

Wang, X., Gartia, M. R., Jiang, J., Chang, T.-W., Qian, J., Liu, Y., … Liu, G. L. (2015). Audio jack based miniaturized mobile phone electrochemical sensing platform. *Sensors and Actuators B: Chemical*, *209*, 677–685. https://doi.org/10.1016/j.snb.2014.12.017

Wang, Z., Wang, W., Jiang, Z., & Yu, D. (2016). Low temperature sintering nano-silver conductive ink printed on cotton fabric as printed electronics. *Progress in*

Organic Coatings, *101*, 604–611. https://doi.org/10.1016/j.porgcoat.2016.08.019

Want, R. (2006). An Introduction to RFID Technology. *IEEE Pervasive Computing*, *5*(1), 25–33. https://doi.org/10.1109/MPRV.2006.2

Wei, Y., Torah, R., Yang, K., Beeby, S., & Tudor, J. (2013). Screen printing of a capacitive cantilever-based motion sensor on fabric using a novel sacrificial layer process for smart fabric applications. *Measurement Science and Technology*, *24*(7), 075104. https://doi.org/10.1088/0957-0233/24/7/075104

Wei, Z., Liu, A., Chen, X., Waris, B., Ukkonen, L., Bjorninen, T., & Virkki, J. (2017). Comparison of wearable passive UHF RFID tags based on electro-textile dipole and patch antennas in body-worn configurations. In *2017 IEEE Radio and Wireless Symposium (RWS)* (pp. 204–206). IEEE. https://doi.org/ 10.1109/RWS.2017.7885988

Wei, Z., Zhou, Z. K., Li, Q., Xue, J., Di Falco, A., Yang, Z., … Wang, X. (2017). Flexible Nanowire Cluster as a Wearable Colorimetric Humidity Sensor. *Small*, *13*(27), 1–7. https://doi.org/10.1002/smll.201700109

Weng, B., Shepherd, R. L., Crowley, K., Killard, A. J., & Wallace, G. G. (2010). Printing conducting polymers. *The Analyst*, *135*(11), 2779. https://doi.org/ 10.1039/c0an00302f

Werner, C., Godlinski, D., Zöllmer, V., & Busse, M. (2013). Morphological influences on the electrical sintering process of Aerosol Jet and Ink Jet printed silver microstructures. *Journal of Materials Science: Materials in Electronics*, *24*(11), 4367–4377. https://doi.org/10.1007/s10854-013-1412-y

Wünscher, S., Abbel, R., Perelaer, J., & Schubert, U. S. (2014). Progress of alternative sintering approaches of inkjet-printed metal inks and their application for manufacturing of flexible electronic devices. *J. Mater. Chem. C*, *2*(48), 10232–10261. https://doi.org/10.1039/C4TC01820F

Xu, G., Zhang, Q., Lu, Y., Liu, L., Ji, D., Li, S., & Liu, Q. (2017). Passive and wireless near field communication tag sensors for biochemical sensing with smartphone. *Sensors and Actuators, B: Chemical*, *246*, 748–755. https://doi.org/ 10.1016/j.snb.2017.02.149

Xu, Y., Dong, L., Wang, H., Jing, J., & Lu, Y. (2017). A review of passive self-sensing tag. *Sensor Review*, *37*(3), 338–345. https://doi.org/10.1108/SR-01-2017-0001

Yang, K., Torah, R., Wei, Y., Beeby, S., & Tudor, J. (2013). Waterproof and durable screen printed silver conductive tracks on textiles. *Textile Research Journal*, *83*(19), 2023–2031. https://doi.org/10.1177/0040517513490063

Yang, M.-Z., Dai, C.-L., & Lu, D.-H. (2010). Polypyrrole Porous Micro Humidity Sensor Integrated with a Ring Oscillator Circuit on Chip. *Sensors*, *10*(11), 10095–

10104. https://doi.org/10.3390/s101110095

Yongsang Kim, Hyejung Kim, & Hoi-Jun Yoo. (2010). Electrical Characterization of Screen-Printed Circuits on the Fabric. *IEEE Transactions on Advanced Packaging*, *33*(1), 196–205. https://doi.org/10.1109/TADVP.2009.2034536

Zadbuke, N., Shahi, S., Gulecha, B., Padalkar, A., & Thube, M. (2013). Recent trends and future of pharmaceutical packaging technology. *Journal of Pharmacy and Bioallied Sciences*, *5*(2), 98. https://doi.org/10.4103/0975-7406.111820

Zhang, D., Jiang, J., Chen, J., Zhang, Q., Lu, Y., Yao, Y., … Liu, Q. (2015). Smartphone-based portable biosensing system using impedance measurement with printed electrodes for 2,4,6-trinitrotoluene (TNT) detection. *Biosensors and Bioelectronics*, *70*, 81–88. https://doi.org/10.1016/j.bios.2015.03.004

Zhang, J., Tian, G., Marindra, A., Sunny, A., & Zhao, A. (2017). A Review of Passive RFID Tag Antenna-Based Sensors and Systems for Structural Health Monitoring Applications. *Sensors*, *17*(2), 265. https://doi.org/10.3390/s17020265

Zhang, N., Luo, J., Liu, R., & Liu, X. (2016). Tannic acid stabilized silver nanoparticles for inkjet printing of conductive flexible electronics. *RSC Advances*, *6*(87), 83720–83729. https://doi.org/10.1039/C6RA19800G

Zhang, S., Li, S., Cheng, S., Ma, J., & Chang, H. (2015). Research on smart sensing RFID tags under flexible substrates in printed electronics. In *2015 16th International Conference on Electronic Packaging Technology (ICEPT)* (pp. 1006–1009). IEEE. https://doi.org/10.1109/ICEPT.2015.7236749

Zhang, Y., Li, Z., Xu, K., Gao, C., Hao, Y., Meng, F., & Gui, Y. (2017). A low-cost flexible electrochemical accelerometer using graphene-integrated microchannel. *Proceedings of the IEEE International Conference on Micro Electro Mechanical Systems (MEMS)*, 1268–1271. https://doi.org/10.1109/MEMSYS.2017.7863648